

Highly concentrated H_2O_2 preparation, stabilization and decomposition over manganese oxide-based catalysts for space propulsion

Thesis - AE5810 / SK-MRES

A.B. de Roos



Utrecht University



SolvGE

Highly concentrated H₂O₂ preparation, stabilization and decomposition over manganese oxide-based catalysts for space propulsion

Master thesis

by

A.B. de Roos

to obtain the degree of Master of Science
at Delft University of Technology and Utrecht University.

Student number: 4373022 (TUD), 6049362 (UU)

Project duration: May 3, 2021 – July 12, 2022

Supervisors:

Dr. B. V. S. Jyoti,

Dr. F. Meirer,

Dr. M. Monai,

Ir. J. Quesada Mañas,

Prof. Dr. E. T. C. Vogt,

TU Delft, SolvGE

Utrecht University

Utrecht University

SolvGE

Utrecht University



Utrecht University



Preface

"If I have seen further it is by standing on the shoulders of giants"

Sir Isaac Newton

This thesis report is written as a part of the master degrees Nanomaterials Science (Utrecht University) and Aerospace Engineering (Delft University of Technology). Part of the research was conducted at SolvGE, a spin-off of Delft University of Technology, which specializes in the purification of hydrogen peroxide. They were kind enough to supply their Research Grade Printer to conduct experiments with concentrated hydrogen peroxide in the lab in Utrecht.

This work focuses on the issues that hamper implementation of a green space propellant, hydrogen peroxide. Here I have tried to combine my two expertises by applying intricate knowledge on chemistry (particularly catalysis) to solve a pressing issue in the space industry. I hope my work will contribute to making the world just a bit better for the generations to come.

On a personal level, this research learned me that *done is done*, even when it is not: scientific studies are paved with shortcomings and offer many interesting side-roads that are worth exploring. Unfortunately, we are merely passersby on this world, and hence can solely see the shadows of the Truth. This discomforting experience served as a personal mirror and taught me the humbleness necessary to appreciate the art of science to its full extent.

A.B. de Roos
Delft, July 2022

Layman's abstract

The European Union is planning to ban the currently most used satellite fuel, since it is both very toxic and carcinogenic. Therefore the space industry needs an alternative fuel to propel their satellites. Hydrogen peroxide is non-toxic and yet offers similar performance. Because of three main reasons it has still not been widely implemented.

First of all, peroxide is well-known for its strong bleaching power. This bleaching is in fact a chemical reaction that breaks apart the peroxide molecule. Controlled destruction of very pure peroxide produces hot gasses that can propel a satellite. However, the destruction reaction needs a chemical stimulus to start, which is given by a so-called catalyst. Such a catalyst should not burn up during the lifetime of a satellite, which is very challenging because of these hot gasses. Therefore no satellites are currently equipped with such a catalyst to start peroxide destruction. We have found a new type of catalyst for this purpose. They are formed by mixing ceramic materials with a manganese oxide pigment. These result in strong ceramics after firing in a kiln. We have tested several of these dyed ceramics for their ability to enhance the destruction reaction of peroxide. Our research shows that pink alumina ceramics offer both high performance and long lifetime with a limited amount of pigment. This research is an important step required for the acceptance of peroxide as a space fuel.

Secondly, this strong bleaching power on its own results in a limited shelf-life. This is caused by the presence of pollutants, which are (inevitably) introduced during manufacturing or storage. The peroxide reacts with these pollutants, which decreases the mileage of the satellite. And since there are no gas stations in space, this decreases the satellite's lifetime. This problem can be solved when the tanks are furnished with a stabilizing coating. We have tested such a coating (based on tin) that removes the pollutants from the peroxide. Our research shows that these coatings indeed increase the shelf-life of peroxide. Over time though, we have seen that the peroxide attacks the tank wall material and that the coating detaches. Thus, the adhesion of the coating needs to be improved before it can be applied in tanks.

Lastly, watered down peroxide is available at every pharmacy, but satellites require highly concentrated peroxide. This pure peroxide is not widely available or very expensive. A novel machine developed by SolvGE can purify watered down peroxide so that it can be used in satellites. This new machine can still be improved, because the waste contains peroxide. We have found a way to recycle this waste without polluting the peroxide. Our tests showed that by simply cooling down the exhaust, we can recover highly pure peroxide. The company has used the gathered knowledge and our results to improve its product.

Abstract

The European Chemical Agency is planning to ban the use of the currently most used space propellant, hydrazine, due to its high toxicity [31, 32]. As a response, the EU-funded GRASP research consortium nominated high concentration hydrogen peroxide (HP) as a suitable non-toxic replacement [5]. However, to date still several issues impede the implementation of HP as a space propellant, which have been addressed in this research. First of all, high concentration HP is either poorly available or only at high cost. SolvGE has invented a safe and user-friendly method to carry out purification of easily available low concentration to propellant-grade HP [54]. Even though this purification process already has an acceptable efficiency, the waste stream still contains HP. Since the efficiency of the concentration process itself is limited by Raoult's law, it is only possible to increase the overall process efficiency by recuperation of HP from the effluent flow. The company desired that the proposed solution would not affect the current process, and would add minimal complexity to the system. In addition, the solution should not affect neither the passive nature of the system nor the system's autonomy. It was found that subsequent cooling and condensation of the waste stream would be the optimum approach to achieve this goal. In order to gain fundamental understanding of this process, a theoretical model was set up that would predict the required condenser properties. Then, experiments were conducted that supplied evidence to validate both the key assumptions in the model and the model itself. Though, it was found that the model would considerably underestimate the required condenser size, which can be attributed to both the relatively low concentration of HP in the waste stream and the relatively low turbulence in the flow, as well as the large uncertainty in the actual flow rate. Ultimately, the research efforts did not culminate into a detailed design solution, yet they did provide SolvGE with further understanding of the problem and a starting point for further development.

Secondly, at this time no catalyst is available that can ignite HP - ethanol mixtures and withstand the environment (up to 2000°C and over 20 bar) in a rocket engine for prolonged periods of time. Current research efforts have focused on the synthesis of a HP decomposition catalyst: the hence liberated heat then serves to ignite ethanol. Generally, when manganese oxide (MnOx) catalysts would be operated under these conditions the active phase will rapidly deactivate. Yet, Serra Maia's group has shown that properly supported MnOx catalysts can be operated in decomposition for twenty-five minutes without noticeable degradation [7–9]. Though, these catalysts most likely cannot withstand the operation conditions of a HP - ethanol engine.

This research utilized drop-testing to investigate reactivity and deactivation behavior of MnOx catalysts on different supports. Drop-testing is a common method to investigate hypergolicity, as opposed to engine testing. It can also be employed to study decomposition behavior, for instance of HP. Even though the resemblance to decomposition chamber conditions is poor, this method allows for a fast screening of catalysts. In addition, it mimics repeated engine starts, and can thus simulate long-term deactivation behavior. In drop-testing a drop of HP is released from a set height onto the catalyst, and the subsequent reaction is monitored. Here the reactions were monitored using high speed imaging and a fast thermal data recorder. Ceramic catalyst pellets (cercaps) were prepared by mixing 1.5 wt.% MnO₂ with different metal oxides and subsequently firing at high temperature. Of the tested support materials (i.a. silica, titania, kaolin and magnesium spinel), only yttria-stabilized zirconia (YSZ) and γ -alumina (γ Al) showed measurable activity in drop-testing with 98% HP. The latter would still be sufficiently reactive with only 0.30 wt.% MnO₂. Based on the utilized characterization methods (Raman, total diffuse reflectance and energy-dispersive X-ray spectroscopy, and X-ray diffraction) it was found that the reactive manganese phase in γ Al is most likely Mn₃O₄; other cercaps do not allow identification of any MnOx. The formation of Mn₃O₄ in γ Al is both in line with literature ([11, 12, 17]) and the results of this research: all tested γ Al catalysts seemed to require an activation step (possibly to convert to more reactive MnO₂). Despite the comparatively low loading of γ Al, it showed both higher decomposition temperatures (sufficient to ignite ethanol) and longer catalytic lifetime than YSZ until (temporary) water poisoning would set in. After drying of the catalysts, their reactivity would be restored; no clear further deactivation effects were measured spectroscopically. Other experiments showed for both cercaps a total lifetime of over 300 decomposition events. Further, YSZ displayed higher mechanical rigidity and lower porosity (which can lead to higher stability in a combustion engine). To conclude, despite the relatively small number of experiments conducted on these cercaps, it is clear that they offer unsurpassed mechanical stability

in combination with good catalytic reactivity. The results obtained in this investigation will pave the way towards catalytically ignited HP rocket engines.

Lastly, in contrast to commonly used space propellants, HP has limited storage life, which reduces its applicability for long-duration space missions. Therefore stabilizers are added to HP, but these do not stabilize propellant-grade HP sufficiently or are incompatible with (catalytic) propulsion system elements. This research sought to physically support tin oxide stabilizers to mitigate these shortcomings. By dispersing varying amounts of colloidal tin oxide in 90 and 95% HP and monitoring the concentration over seven months, their stabilizing ability was shown. Similar loadings were deposited on hard anodized aluminum strips by dipcoating and subsequent calcination, which were tested equivalently. The results indicate that high loadings of tin oxide lead to enhanced stability with respect to low loadings, while still performing worse or equal than HP that is not additionally stabilized. Perhaps this effect is caused by an interaction of the tested stabilizers with stabilizers already present in the acquired HP. Characterization performed at the end of the research indicated that the aluminum was severely damaged by the HP, leading to both release of (decomposition inducing) metal contaminants into the solution and removal of the stabilizers. The deterioration was most likely originating from both the nature of the passivation process and the coating procedure. To conclude, these tin oxide stabilizer coatings are a promising method to stabilize HP.

Acknowledgments

Of all people I am most grateful to Matteo Monai, for his daily guidance during most of the project carried out at Utrecht University. Without his creative ideas most of this work could not have been realized. Further I am very thankful that Botchu Jyoti was able to supervise me from TU Delft, so I could benefit from her vast knowledge on propellant chemistry and testing and hydrogen peroxide in general. From SolvGE I would like to thank Jaime Quesada Mañas, who guided my project from the company side. He often surprised me with his intricate knowledge on hydrogen peroxide.

Further, I want to thank the entire SolvGE team, not only for the very enjoyable work environment during my stay, but also for conducting the laborious concentration measurements. Pranav Prashand, thank you for staying patient with me all the time and for all the hours you spent watching through the looking glass. It should not go unnoticed that without SolvGE's Hydrogen Peroxide Printer I would not have been able to conduct this research.

I would not want to forget the Inorganic Chemistry and Catalysis (ICC) department at Utrecht University. Here I have appreciated the friendly and cooperative atmosphere set out by all staff and students. Every new member is immediately accepted and treated equally in this close scientific community, independent of one's rank. Also I would like to express my gratitude towards the technical personnel; Jochem Wijten for setting up the calcination oven, Ramon van Oord for preparing the experimental setup and of course Jules van Leusden and Tim Prins for their often indispensable help in the lab. Further I would like to thank Peter Ngene for his valuable input on the catalyst-support effects and the preparation of washcoats. Additionally, I want to acknowledge the effort of Thomas Hartmann and Hongyu An for conducting Raman spectroscopy for me and supervising me during subsequent analyses. Finally I would like to thank Huygen Jöbsis for helping me to evaluate TDR spectra.

Contents

	Page
Preface	iii
Layman's abstract	v
Abstract	vi
Acknowledgments	ix
List of Figures	xiii
List of Tables	xv
List of abbreviations	xvii
List of symbols	xix
1 Introduction	1
1.1 State-of-the-art and challenges in space propulsion	2
1.2 Spacecraft propellant type comparison	3
1.2.1 Propellant evaluation criteria	4
1.2.2 Trade-off outcomes	8
1.3 Hydrogen peroxide as propellant	8
1.3.1 Inducing decomposition and hypergolicity in hydrogen peroxide	8
1.3.2 Hydrogen peroxide decomposition catalysts	9
1.4 Hydrogen peroxide procurement	13
1.5 Hydrogen peroxide storage	14
1.6 Research questions and objectives	15
1.6.1 Purification of propellant-grade H ₂ O ₂	15
1.6.2 Support effect on the decomposition of H ₂ O ₂ over MnOx catalysts	15
1.6.3 Stabilizing propellant-grade H ₂ O ₂	15
1.7 Outlook	16
2 Purification of propellant-grade H₂O₂	17
2.1 Recuperator design concept	17
2.2 Theoretical condensation model	18
2.2.1 Condensation-based recuperator model assumptions	19
2.2.2 Condensation model description	21
2.2.3 Condensation model results	22
2.3 Experimental setup	23
2.3.1 Calibration efforts	24
2.4 Recuperation experiments	25
2.4.1 Heatsink-based recuperators	25
2.4.2 Direct impact condenser	28
2.5 Conclusion	29
2.6 Recommendations	29
3 Support effect on the decomposition of H₂O₂ over MnOx catalysts	31
3.1 Background	32
3.1.1 Catalyst operation conditions	32
3.1.2 Decomposition delay	32
3.1.3 Requirements	33
3.1.4 Solid state synthesis of bulk catalysts	34
3.1.5 SSS of supported manganese oxide catalysts	34

3.2	Experimental	35
3.2.1	Catalyst preparation	36
3.2.2	Catalyst characterization.	36
3.2.3	Activity measurements.	36
3.2.4	Data analysis and calibration	38
3.3	Results and discussion	39
3.3.1	Thermodynamic characterization	39
3.3.2	Prereaction characterization of yAl and YSZ cercaps	40
3.3.3	Catalyst activity testing	46
3.3.4	Post-reaction characterization	58
3.4	Conclusion	59
3.5	Recommendations	60
3.5.1	General recommendations.	60
3.5.2	Reactor design	61
3.5.3	Recommendations with respect to instrumentation	61
4	Stabilizing propellant-grade H ₂ O ₂	63
4.1	Background	63
4.1.1	Decomposition mechanisms of H ₂ O ₂	63
4.1.2	Currently used stabilizers	64
4.1.3	Aluminum as stabilizer support	65
4.1.4	Immobilizing tin oxide stabilizers	66
4.1.5	Requirements	66
4.2	Experimental	67
4.2.1	Coating preparation	67
4.2.2	Stability testing	67
4.2.3	Instrument calibration.	68
4.3	Results and discussion	68
4.3.1	Deviations from setup	68
4.3.2	Data manipulation and analysis procedures	69
4.3.3	Area and concentration effects.	70
4.3.4	Diluting water compatibility	71
4.3.5	Aluminum compatibility.	71
4.3.6	Stabilizer effects on the stability of HP	73
4.4	Conclusion	80
4.5	Recommendations	80
4.5.1	General research improvements	80
4.5.2	Concentration uncertainties	80
4.5.3	Stabilizers	81
5	Conclusion	83
6	Recommendations	85
	Bibliography	87
	Appendices	95
A	Hydrogen peroxide properties	97
B	Rocket theory	99
C	Metal oxide perovskite catalysts	101
D	Materials and methods	103
D.1	Support effect on the decomposition of H ₂ O ₂ over MnOx catalysts	103
D.1.1	LCT(Pt) synthesis	103
D.1.2	Manganese dioxide on YSZ synthesis	103
D.1.3	Support development	104
D.1.4	Chemical list	105
D.1.5	Test checklists	106

D.1.6	Test flow representation	108
D.2	Calibration	111
D.2.1	Thermocouple calibration	111
D.2.2	Refractometer calibration	112
D.2.3	Anemometer calibration	112
D.2.4	Drop volume calibration	113
D.2.5	Bubble detection	115
E	Supporting information	117
E.1	Purification of propellant-grade H_2O_2	117
E.2	Support effect on the decomposition of H_2O_2 over MnOx catalysts	118
E.2.1	Regenerative LCT(Pt) perovskite	118
E.2.2	Mn/YSZ catalysts	118
E.2.3	MnOx cercaps	124
E.3	Stabilizing propellant-grade H_2O_2	136

List of Figures

	Page
1.1	Typical satellite thruster system, with relevant parts indicated 1
1.2	Different common propellant systems for space propulsion. 3
1.3	Typical catalyst support structures 13
1.4	SolvGE Research Grade Printer. 14
2.1	Input data as received from SolvGE, based on experiments with the RGP. 18
2.2	Representation of the chosen approach to extract HP from the SolvGE RGP outflow. 18
2.3	Concentration of H ₂ O ₂ vapor as a function of the liquid concentration. 21
2.4	Schematic representation of the condensation model. 23
2.5	Results of model calculations, both for the nominal case and sensitivity analysis. 23
2.6	Basic testing setup for the condensation experiments. 24
2.7	Individual parts as used in the test setup for the condensation experiments. 25
2.8	Refractometer used during all experiments in this research. 25
2.9	Setup and results of condenser experiments using a 100 x 100 mm heatsink. 26
2.10	Setup and results of the condenser experiments using effectively 200 x 100 mm heatsinks. 27
2.11	Heatsink discoloration due to hydrogen peroxide. 28
2.12	Direct impact condenser setup. Encircled are clearly visible condensate drops. 28
3.1	Simplified mechanism of the phase-mixing of Mn ₃ O ₄ and Al ₂ O ₃ 35
3.2	Schematic representation of the synthesis procedure of the cercaps. 36
3.3	Schematic and actual drop-testing setup as used during the experiments. 37
3.4	Cercaps after calcination. 40
3.5	Equilibrium concentration of MnOx at varying temperatures. 41
3.6	Equilibrium concentrations of mixed manganese oxides at varying temperatures. 41
3.7	Comparison of the surface topography of the YSZ-1.5 and γAl-0.30 cercaps. 42
3.8	XRD results for γAl cercaps with varying MnO ₂ loading. 43
3.10	Optical spectroscopy conducted on γAl cercaps with varying MnO ₂ loading. 44
3.11	Simplified mechanism of formation of solid solution of MnO in YSZ. 44
3.12	Temperature traces from experiments conducted on an unconstrained YSZ-1.5 cercap. 45
3.13	Temperature traces from experiments conducted on an unconstrained γAl-0.30 cercap. 46
3.14	Typical smoke development during a decomposition event for γAl-0.30 and YSZ-1.5. 47
3.15	Comparison of visual and thermal data for a prototypical decomposition event. 49
3.16	Representation of the thermal data analysis procedure for the drop-testing experiments. 50
3.17	Temporal evolution of decomposition peak temperatures for YSZ-1.5-1. 51
3.18	Peak temperature data for all tested cercaps. 52
3.19	Results from the video data showing the start and end of bubble formation. 54
3.20	Comparison of the thermal trace of every first two droplets for all tested cercaps. 55
3.21	Development of a black front on the γAl-1.5 catalysts. 57
3.22	Raman spectra comparing different γAl-0.30 samples. 58
3.23	XRD patterns of both pristine and spent γAl-0.30 catalyst. 59
4.1	PDC molecule. 65
4.2	Surface area effect in decomposition of hydrogen peroxide. 70
4.3	Comparison of samples containing DI water with control. 72
4.4	The effect of aluminum on the decomposition of HP. 72
4.5	PDC-O molecule. 73
4.6	SEM image of pristine stabilizer and stabilizer strip surface composition based on SEM-EDX. 74
4.7	Comparison of the effect of dispersed and supported tin oxide stabilizers to SA HP. 75

4.8	Comparison of the effect of dispersed and supported tin oxide stabilizers to Sy HP	76
4.9	Comparison of the effect of dissolved and supported tin chloride to HP.	77
4.10	Comparison of pristine and spent SA-90-S.	78
4.11	Electron micrographs of SA-90-S showing difference in topology.	79
C-1	Schematic representation of exsolution-dissolution process	102
D-1	Functional flow representation of safety precautions as taken during the experiments.	108
D-2	Functional flow representation of the testing.	110
D-3	Heat trace showing the decomposition of 87% HP using manganese acetate.	111
D-4	Thermocouple temperature recording measurement after calibration.	112
D-5	Cross-calibration data of the analog refractometer.	113
D-6	Spread of the drop volumes as measured with water.	114
D-7	Spread in drop timing and volume as determined from camera data.	114
D-8	Example of a typical drop evolution event, showing two subsequent frames.	115
E-1	Results of the model calculations for the nominal case and sensitivity analysis for $d > 5$ mm.	117
E-2	Results for the model calculations for parallel flow and the sensitivity analysis.	117
E-3	XRD patterns of $Ba_3Pt_2O_7$ and calcined and reduced LCT(Pt).	118
E-4	XRD patterns of calcined YSZ and calcined Mn/YSZ.	119
E-5	Characterization of Mn/YSZ, dropcasted on fused alumina.	120
E-6	Results from testing of silica washcoat.	121
E-7	TiO_2 washcoated samples prior to and after testing.	121
E-8	Thermal traces of experiments conducted with titania washcoats.	122
E-9	XRD patterns of the washcoated and dropcasted alumina slides.	123
E-10	Raman spectrum obtained of both precalcined and calcined YSZ-1.5 cercap.	124
E-11	Raman shifts as measured for the inactive cercaps.	125
E-12	Total diffuse reflectance spectrum of γ Al and YSZ-1.5 cercaps.	126
E-13	Total diffuse reflectance spectra of all inactive cercaps.	126
E-14	Powder X-ray diffraction data for all cercaps except for γ Al-1.5.	127
E-15	Typical decomposition event of 98% HP over γ Al-0.30.	128
E-16	Peak temperature development for γ Al-0.30-1 during drop-testing.	129
E-17	Peak temperature development for γ Al-0.30-2 during drop-testing.	130
E-18	Peak temperature development for γ Al-0.30-3 during drop-testing.	131
E-19	Peak temperature development for YSZ-1.5-1 during drop-testing.	132
E-20	Peak temperature development for YSZ-1.5-2 during drop-testing.	133
E-21	Peak temperature development for YSZ-1.5-3 during drop-testing.	134
E-22	Comparison of measurements with results from least-square fit for SA-90-S.	136
E-23	Comparison of measurements with results from least-square fit for SA-90-D.	137
E-24	Comparison of measurements with results from least-square fit for SA-95-S.	138
E-25	Comparison of measurements with results from least-square fit using Origin Pro 2016 for SA-95-D.	139

List of Tables

	Page
1.1 Trade-off between different types of propellant types.	6
1.2 Summary table with different propellant type characteristics.	7
1.3 Trade-off on ignition methods.	10
1.4 Trade-off to find the most promising active elements to use for the catalysts in this research.	11
3.2 Qualitative comparison of the physical and catalytic properties of the tested cercaps.	60
4.1 Sample library for stabilizer tests.	68
4.2 Equivalent concentration of the added stabilizer in mg Sn per kg HP solution.	69
4.3 Surface to volume ratios, including the area of the aluminum strip when applicable.	69
A-1 Hydrogen peroxide physical properties	97
D-1 Summary of all chemicals used during the catalytic synthesis.	105
D-2 Pre-testing procedures	106
D-3 Pre-testing precautionary procedures	106
D-4 Testing procedures	106
D-5 Post-testing analyses	107
E-1 Summary table with all tested catalysts comparing relevant aspects.	135
E-2 Fitting parameters for SA-90-S.	140
E-3 Fitting parameters for SA-90-D.	140
E-4 Fitting parameters for SA-95-S.	140
E-5 Fitting parameters for SA-95-D.	140

List of abbreviations

Cercap	Ceramic catalyst pellet	pp. 36, Sec. 3.2.1
COD	Crystallography open database	pp. 38, Sec. 3.2.4.1
DAQ	Data acquisition system	pp. 38, Sec. 3.2.4.1
DD	Decomposition delay	pp. 32, Sec. 3.1.2
DP	Deposition precipitation	pp. 39, Sec. 3.3
EBF	End of bubble formation	pp. 39, Sec. 3.2.4.2
EDX	Energy dispersive X-ray spectroscopy	pp. 36, Sec. 3.2.2
EtOH	Ethanol	pp. 2, Sec. 1.1
HP	Hydrogen peroxide	pp. 2, Sec. 1.1
HSC	High speed camera	pp. 38, Sec. 3.2.4.1
ID	Ignition delay	pp. 32, Sec. 3.1.2
LCT(Pt)	$\text{La}_{0.4}\text{Ca}_{0.3925}\text{Ba}_{0.0075}\text{Ti}_{0.995}\text{Pt}_{0.005}\text{O}_3$	pp. 101, chapter C
LH2	Liquid hydrogen	pp. 2, Sec. 1.1
LOX	Liquid oxygen	pp. 2, Sec. 1.1
MnOx	Manganese oxide	pp. 11, Sec. 1.3.2.2
MOP	Metal oxide perovskite	pp. 101, chapter C
mpp	Mass percent point	pp. 17, Sec. 2.1
NP	Nanoparticle	pp. 12, Sec. 1.3.2.3
NTO	Dinitrogen tetroxide	pp. 2, Sec. 1.1
PDC	Pyridine dicarboxylic acid	pp. 64, Sec. 4.1.2
PDCO	Pyridine dicarboxylic acid oxide	pp. 71, Sec. 4.3.5
ReMOP	Regenerative MOP	pp. 101, chapter C
RGP	Research grade printer	pp. 15, Sec. 1.6.1
SBF	Start of bubble formation	pp. 39, Sec. 3.2.4.2
SEM	Scanning electron microscopy	pp. 36, Sec. 3.2.2
SSS	Solid state synthesis	pp. 34, Sec. 3.1.4
TEM	Transmission electron microscopy	pp. 80, Sec. 4.5
TDR / TDRS	Total diffuse reflectance (spectroscopy)	pp. 36, Sec. 3.2.2
TOC	Tin oxide colloid	pp. 65, Sec. 4.1.2.2
XRD	X-ray powder diffraction	pp. 36, Sec. 3.2.2
YSZ	Yttrium-stabilized zirconia	pp. 11, Sec. 1.3.2.2

List of symbols

A	m^2	Contact area	pp. 21, Eq. 2.3
C_{p,H_2O_2}	$J/g \cdot K$	Hydrogen peroxide specific heat	pp. 21, Eq. 2.2
C_{p,N_2}	$J/g \cdot K$	Nitrogen specific heat	pp. 21, Eq. 2.2
d	m	Local hydrodynamic diameter	pp. 22, Eq. 2.7
D_h	m	Hydrodynamic diameter	pp. 19, Eq. 2.1
ΔEN	-	Electronegativity difference	pp. 54, Sec. 3.3.3.2
ζ	-	Friction coefficient	pp. 22, Eq. 2.12
$\Delta_v^0 H$	J/g	Standard vaporization enthalpy	pp. 21, Eq. 2.2
k	$W/m \cdot K$	Heat conductivity	pp. 21, Eq. 2.3
L	m	Length	pp. 22, Eq. 2.7
$\dot{m}_{H_2O_2}$	kg/s	Hydrogen peroxide mass flow rate	pp. 21, Eq. 2.2
\dot{m}_{N_2}	kg/s	Nitrogen mass flow rate	pp. 21, Eq. 2.2
μ	kg/s^2	Kinematic viscosity	pp. 19, Eq. 2.1
Nu	-	Nusselt number	pp. 21, Eq. 2.3
ΔP	Pa	Pressure drop	pp. 22, Eq. 2.12
Pr	-	Prandtl number	pp. 22, Eq. 2.7
\dot{q}	J/s	Heat flow	pp. 21, Eq. 2.2
Q	J	Total heat	pp. 21, Eq. 2.3
\dot{Q}	Power	pp. 21, Eq. 2.2	
Re	-	Reynolds number	pp. 19, Eq. 2.1
ρ	kg/m^3	Density	pp. 22, Eq. 2.12
ΔT	K	Temperature difference	pp. 21, Eq. 2.2
v	m/s	Flow velocity	pp. 22, Eq. 2.12
x	m	Position along length	pp. 22, Eq. 2.7

Introduction

Due to the success of commercial spaceflight enterprises, space itself continues to become more accessible. As an example, private companies are launching thousands of satellites to deliver worldwide high speed internet even in remote areas. Even though space appears vast and rather empty, there is quite some (parts of) decommissioned spacecraft orbiting Earth. Each of these debris can impact a working space system. In order to assure that the space mission will not be ended prematurely due to a collision with space debris, (almost) each spacecraft is equipped with a propulsion system to evade these¹. Other uses of the spacecraft's propulsion system are to change its position around Earth or to lose rotational momentum.

This research will focus on chemical rocket motors, also known as combusting rocket motors, because these engines are still widely used in industry and here the largest advancements in environmental impact can be made. In combusting rocket motors (see [Figure 1.1](#)), the energy required to propel a spacecraft is provided by the bond energy in the propellant or the combination of propellants. In the combustion chamber part of the energy contained in the propellant molecules is released when they fall apart into the most thermodynamically stable molecules (exothermy). This residual energy is manifested in a large increase of temperature (and accordingly, pressure), while the (usually) larger number of molecules result in an additional increase in gas pressure. This thermal and barometric potential is expanded and accelerated in the nozzle. The momentum of the exhaust flow adds to the spacecraft's original momentum, and hence propels the spacecraft.

Chemical propulsive systems can be subdivided by the nature of the propellants, which on itself has a large impact on the possible applications. If only one or a few high thrust burns are required, a solid propellant rocket (see [Figure 1.2a](#)) might be selected. Here, the propellant is cast into a predetermined shape, which largely determines the burning profile (and consequently the delivered thrust) of the rocket motor. Two considerable disadvantages of conventional solid rocket motors are that after ignition they cannot be extinguished and that they cannot be actively throttled. To that end, a lot of research has been put into hybrid systems where only either the fuel or the oxidizer is cast. This is believed to mitigate some of the disadvantages of conventional solid systems. The only known commercial application is in the (non-orbiting) rocket stage of Virgin Galactic's SpaceShipTwo [126].

Liquid propellant systems are used when throttling is required. For low thrust operations, such as the dumping of rotational momentum, and for maneuvers that require high reliability, often monopropellant systems (see [Figure 1.2b](#)) are employed. The thrust in these engines is generated by decomposition of the propellant, which is often brought about by passing the propellant over a catalyst bed (often consisting of physically immobilized porous pellets, which are coated with a catalytically active substance). It can be understood that the simple design of these systems results in high reliability. If both throttling and high(er) thrust are required, bipropellant systems can be selected in which a separate fuel and oxidizer are combined in the combustion chamber. Bipropellant systems can be subdivided based on their means of initiating combustion, as is illustrated in [Figure 1.2c](#): igniter-based,

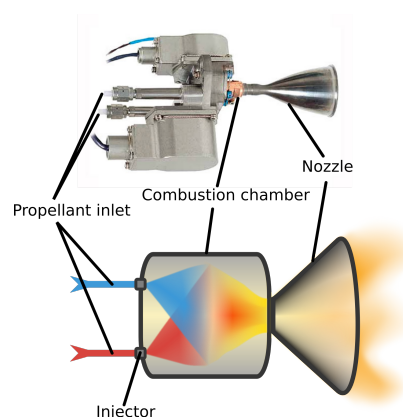


Figure 1.1: Typical satellite thruster system, with relevant parts indicated. Adapted from ArianeGroup [20].

¹Historically cubesats did not have a propulsion system, their popularity however led to the development of dedicated micropropulsion systems.

hypergolic or using a catalyst bed. Often used igniters are of pyrotechnic (explosion of a small charge) or electric nature (comparable to an automotive spark plug). More reliable are hypergollants, which are propellant combinations that display hypergolicity, that is they spontaneously combust upon contact. When the propellants do not degrade over time, this hypergolic ignition is also extremely reliable over long periods of time; this is important for e.g. deep-space missions and missiles. Because only a limited amount of propellant combinations display this hypergolicity, it can also be opted to *induce* this hypergolic behavior to ensure reliable ignition. In so-called quasi-hypergolic systems one of the propellants is decomposed over a catalytic bed, and its decomposition heat is used to heat the other propellant to its autoignition temperature, leading to combustion of the propellant mixture. Although a lot of research has been conducted on these induced hypergolic systems over the past decades, no working prototype of a catalytic ignition system can be found in current literature. This is most likely caused by the hostile conditions occurring in the combustion chamber, as will be elaborated upon later.

To conclude this section, the total propulsion system mass can sometimes be reduced if a mono- and bipropellant system are combined in one rocket motor. This system can then run merely on monopropellant for low thrust operations, whereas the second propellant can be injected if more performance is necessary. Such propulsion systems are commonly referred to as dual-mode rocket motors. Especially quasi-hypergolic systems are suited for this operation mode: any quasi-hypergolic system can be used in monopropellant mode by only emitting the decomposing propellant into the combustion chamber [34, 67, 117]. It can be understood that such a system is very attractive for weight-critical space missions.

1.1. State-of-the-art and challenges in space propulsion

Rocketry has been a field of rapid developments ever since the start in the early 20th century; Nazi Germany's development of the revolutionary V-2 rocket weapon was a true turning point. After the Second World War, the V-2 served as a solid foundation for the space programs of both the USA and USSR. During the early Cold War, performance of rocket propellants was considered more important than their toxicity or cost, because of which the hypergolic propellants hydrazine and dinitrogen tetroxide (NTO) became the standard. Another benefit of hydrazine, next to its hypergolicity, is that it can also be used as a monopropellant: hydrazine easily decomposes when it is brought in contact with e.g. iridium. This decomposition results in a mixture composed of i.a. highly flammable, but high impulse providing hydrogen [34, 67, 73, 117]. Yet, these conventional hypergollants also have serious disadvantages. Most prominently, both the propellants themselves and their combustion products (among other things nitrous oxides) are very toxic to humans and the environment [102, 124, 125]. Because of the high risks thus associated with assembly, storage and launch of spacecraft loaded with hydrazine and NTO, extensive safety measures are required, which result in high associated cost. As a result of the continuous tightening of regulations for the handling of hydrazine, NASA's costs associated with the procurement of hydrazine have increased tenfold from 1990 to 2006 [5]. More urgently, due to the displayed toxicity and suspected carcinogenicity, the European Commission is considering to ban the use of hydrazine on all its territory (including French Guyana, which hosts Guyana Space Center) [31, 32].

Space launchers, or commonly known as *rockets*, have mainly relied on more benign propellant combinations, such as kerosene or liquid hydrogen (LH₂) and liquid oxygen (LOX), that offer comparable performance. Yet, long-term storage of these cryogenic propellants is disadvantageous due to boil-off, resulting in considerable propellant loss over time, which makes them unsuited for use in satellites. Because of the high costs associated with the development and launch of a spacecraft, the choice for a novel and less-proven propellant induces extra risk and is thus unappealing. Therefore, without a creditworthy alternative, space contractors often still choose to incorporate hydrazine (and NTO) in satellites.

Due to the severe disadvantages associated with the use of hydrazine in space propulsion, there has been a search for benign alternatives. A large part of the research in literature has focused on high concentration (>87% m/m) hydrogen peroxide (HP), either as a monopropellant or as quasi-hypergollant in combination with for instance ethanol (EtOH). Bioethanol is often designated as a green propellant, not only due to its ease of (environmentally friendly) manufacturing using e.g. fermentation, but also due to its low toxicity and harmless reaction products [68]. Some prominent advantages of HP over hydrazine are its low toxicity and considerably higher liquid range (from -50°C to 150°C), which relaxes the requirements on the thermal control system [19, 22, 67, 85, 109]: temperatures in space can vary between -150°C in darkness and +150°C in full sunlight.

Unfortunately, several factors still impede its widespread implementation as a propellant in the space in-

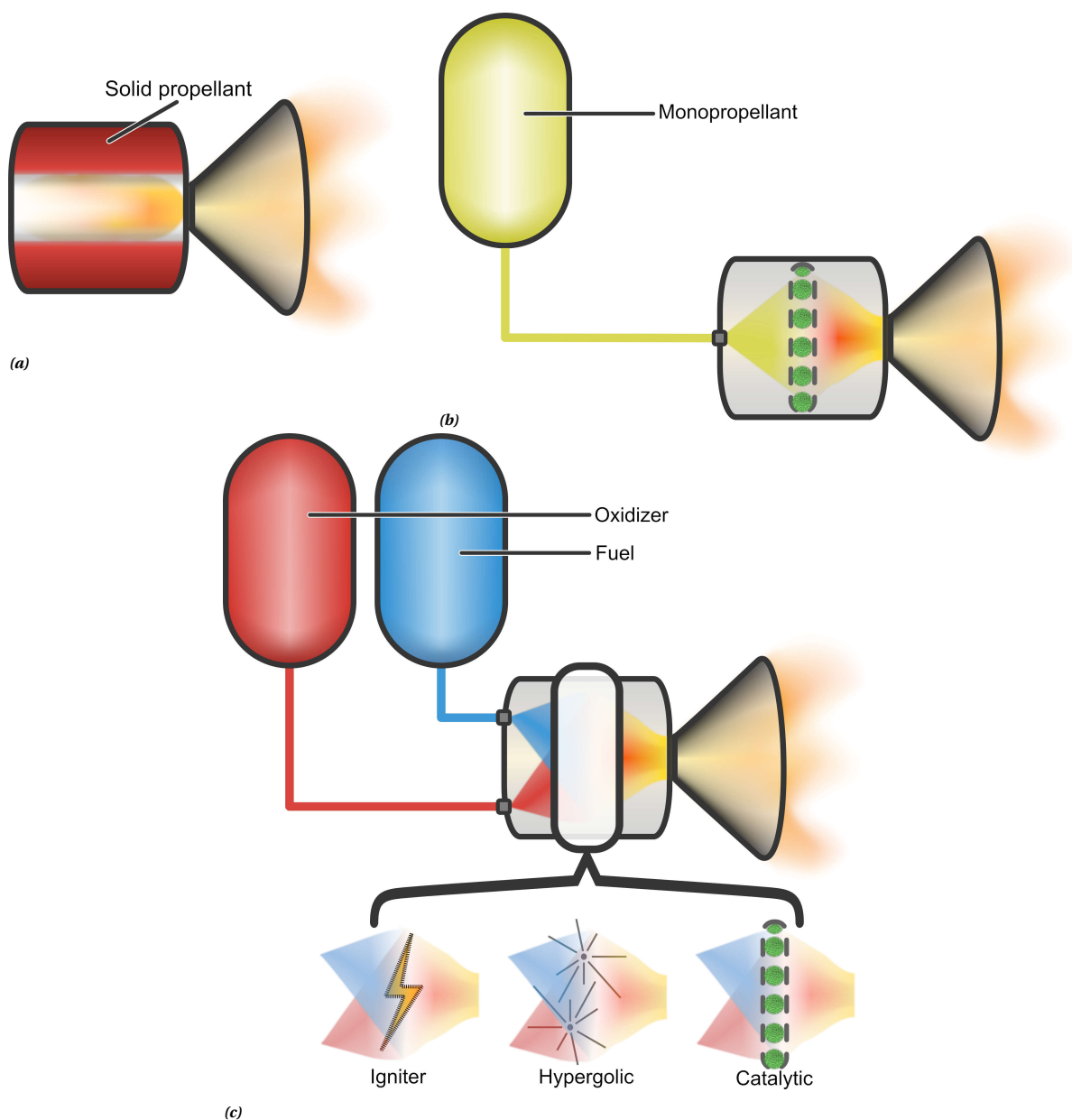


Figure 1.2: Different common propellant systems available for space propulsion, categorized on propellant type. *a)* Typical solid propellant rocket system. *b)* Typical monopropellant rocket system. These usually rely on decomposition of the monopropellant over a catalyst, as is shown. *c)* Typical bipropellant rocket system, with three possible ignition methods illustrated. Active ignition systems are widely used in space launchers, whereas hypergolic ignition is mostly found in satellites. Catalytic ignition systems have not been reported in literature.

dustry. The most prominent challenge is that HP does not show hypergolic behavior with ethanol and thus requires a catalytic ignition system. A second challenge is that the procurement of high concentration HP is difficult and expensive. Another major challenge is its autodegradation, which decreases its long-term performance. However, as will be shown in the next section, HP-based propellant systems show to be a promising alternative to current propellant systems if these challenges are overcome.

1.2. Spacecraft propellant type comparison

This section will qualitatively evaluate the differences between the earlier mentioned chemical rocket engine types and their propellants using a typical system engineering tool, a trade-off matrix. In a trade-off matrix all concepts are listed, together with several selection criteria on which these concepts are evaluated. This method tries to, as objectively as possible, judge these concepts on their ability to solve the problem as

outlined above, in the realm of this research project. Hence, each of these criteria has been attributed a specific weight factor to discern factors deemed more important from less influential ones. These weights have been awarded based on pairwise comparison of the criteria, e.g. cost is more important than handling safety, therefore cost is weighted as 2 and handling safety as 1. Scores are then given to each concept based on its performance with respect to the respective criteria, i.e. if a concept clearly does not satisfy a certain requirement, it is awarded a "-1". Similarly, if the concept fulfills a requirement or outperforms a requirement it will be attributed the score "0" or "+1", respectively. When these scores are combined with the weights a total score results, which identifies the best concepts in the trade-off. Since the trade-off can unjustly designate the best concept, here it was chosen to employ a more advanced trade-off method, the Pugh matrix [99]. In addition to the above, in a Pugh matrix also the sum of underperforming criteria ($\Sigma(-1)$) etc. are displayed; hence it can easily be seen that e.g. the highest scoring concept shows more weak points than the runner-up. Evaluation of these weak points may then lead to the final selection of the runner-up at expense of the original winning concept.

1.2.1. Propellant evaluation criteria

Several key criteria have been identified that can be used to score different propellants and propellant systems: reliability, performance, storage stability, cost, greenness and handling safety. From Table 1.1 it can be seen that reliability and performance are rated equally important. This has been done since these are often key requirements in propulsion system design [117]. Of medium importance are the storage stability of the propellant, the associated costs and the greenness. Greenness has not been awarded the highest weight factor: even though environmental impact is increasingly important in society, spaceflight represents only a minor fraction of all greenhouse gas emissions and environmental pollution. The handling safety was rated at the lowest importance, because propellant handling only represents a small fraction of the space mission life and impact.

Reliability Reliability is here defined as the inverse of the chance of long-term propellant ignition failure: ignition should be successful even for long-duration space missions, such as deep-space exploration missions. Since conventional hypergolic systems do not require an ignition system, as do both monopropellant and the green induced hypergolic bipropellant systems, these have been awarded the maximum score for reliability. Conventional solid propellant systems can not be extinguished after ignition. Since their ignition system thus only needs to function once, it can be designed with sufficient margin, due to which their reliability is considered nominal. Because non-hypergolic bipropellant and hybrid solid propellant systems require a separate ignition system, that has to be able to work several times, which introduces additional risk, these have been awarded lowest reliability.

Performance Performance has been evaluated using the mass specific impulse (I_{sp}), a short background on rocket performance can be found in chapter B. Hydrazine decomposition can deliver a specific impulse of 199 seconds, whereas HP can deliver only 165 seconds (at 87.5% concentration, both at 7 MPa chamber pressure) [34]. This difference decreases when the concentration is increased to 98%; then the mass specific impulse increases by at least 12 seconds to 177 seconds [42]. If HP is combined with ethanol, a mass-based specific impulse of around 325 seconds can be achieved [68]. When hydrazine is combined with NTO a slightly higher mass-based specific impulse results: 330 s [67]. It should be noted that although the mass-based specific impulse is lower for HP, the density-normalized impulse is higher, which means that for the same total delivered impulse less volume is required (which correlates to the tank mass) [42]; yet, the mass-normalized specific impulse will be used in this comparison due to its omnipresence in space engineering literature. Non-hypergolic propellant combinations such as kerosene with LOX can reach a mass specific impulse of around 350 s. Although their specific impulse is similar to hypergolic systems, these engines can deliver much more thrust (up to 7 MN) and are thus sometimes preferred. Solid rocket motors systems perform comparably to the former, but deliver even more thrust (up to 15 MN) [34, 67].

Storage stability Some propellants can be stored indefinitely, whereas other propellants degrade or evaporate over time; this is quantified in the storage stability. It also encapsulates additional requirements the propellants pose onto the storage system. Even though cryogenic propellants are intensely insulated, they still suffer from boil-off that causes a quick loss of propellant (on the order of % per day). In contrast, the quality of hydrazine and NTO does not decrease over time, but the limited liquid range of NTO (approximately -11 to 22°C [128]) stresses the need for proper thermal control of the oxidizer tanks. It should be noted

that hydrazine has a melting point of 2°C [128], but this can be easily mitigated by using alkylated hydrazines. Hydrogen peroxide on the other hand *does* degrade over time (on the order of % per year [33, 125]), although this has a limited impact on performance (please refer to the discussion on performance), but its large liquid range (up to -60°C [19, 109]) does not impose as high requirements on storage. Ethanol is stable over time and solidifies only below -117°C [128] and hence does not negatively influence the storage stability. Finally, solid propellant grains do not suffer from degradation over time. However, they have been penalized for the fact that they pose extreme danger in storage (conventional solid propellants cannot be extinguished after ignition).

Cost The cost of a propellant is not limited to its procurement, but also the loading into the spacecraft may induce considerable costs. For instance, due to the high toxicity of hydrazine and NTO, extensive safety measures are required, which lead to a strong increase in total propellant operation cost. Although this has been already accounted for, the associated costs for the safety measures are so large that they are taken into consideration for the cost criterion as well. In addition, procurement costs are high and rising for these propellants. Cryogenics are generally not considered expensive, but pose specific demands on storage, and can only be loaded shortly before launch. Hydrogen peroxide and ethanol can be purchased at low cost; yet, propellant-grade (high concentration) HP is currently as expensive as hydrazine. However, with the use of SolvGE's patented HP purification technique (see [section 1.4](#)) propellant costs promise to decrease drastically. Further, both ethanol and HP can be handled relatively safely, stored under atmospheric condition and loaded well ahead of launch. Single grain propellant systems can traditionally be made at low cost, since they are rather uncomplicated systems, whereas hybrid systems need additional systems for handling of the liquid oxidizer. As was already indicated, the conventional solid propellant systems demand elaborate safety precautions, but this has already been accounted for under the criterion storage stability.

Greenness Another aspect that gains importance in the space industry is the ill-defined concept of greenness. In this context it is interpreted as the environmental impact of the propellants and their combustion products. As was discussed above, conventional hypergolic propellants and their combustion products are both extremely toxic and have a large impact on the environment. Conventional (non-hypergolic) bipropellants, such as kerosene with LOX, can be partially green (due to the low toxicity) or fully green if kerosene is replaced with (green) LH2. HP and ethanol possess low toxicity and can nowadays be produced via sustainable production processes; upon reaction they form a mixture of water, oxygen and carbon dioxide. Additionally, their intrinsic environmental impact is negligible too, due to their fast decomposition under UV irradiation. Finally, due to the wide range of compositions of solid rocket propellants, no unambiguous judgment can be given. Nevertheless, it can be said that the combustion products are most often not environmentally benign, which is caused by incomplete combustion or (metallic) additives.

Handling safety The final criterion considered in this trade-off is the handling safety of the propellants. This does not include the impact the propellants have on the environment, it merely represents the dangers that occur during transportation and loading of the propellants. Since hydrazine is both very toxic and spills can lead to explosion risks, it is given the lowest score; the same applies for the hypergolic combination with NTO. Because of the mentioned factors loading of these propellants is always postponed to the last possible time before launch, which induces programmatic risk. HP on the other hand is not toxic. As with hydrazine spills can cause danger, but due to the low vapor pressure of HP explosive risks are significantly lower, and therefore is awarded a nominal score. Since ethanol does not cause any major dangers, the combination with HP is awarded a higher score. This is justified when the handling safety is compared with that of (partly) cryogenic propellants: not only can the cryogenic liquids cause embrittlement of materials and human skin damage, liquid oxygen spills are extremely dangerous because they can cause spontaneous ignition. Yet, toxicity of these propellants is low. Hybrid solid propellant systems are rather safe to handle, since fuel and oxidizer are handled separately; though hazard may arise depending on the oxidizer used. In contrast, in conventional solid propellants fuel and oxidizer are mixed and hence must be handled with extreme care. Though, since this has been penalized earlier this has not been accounted for twice.

Table 1.1: Trade-off between different types of propellant types both mono- and bipropellants, and solid propellants.

Criterion	Monopropellant		Bipropellant		Solid		
	Conventional Hydrazine	Green HP	Conventional NTO/hydrazine	Hypergols Green, induced HP/EOH	Conventional LOX/kerosene	Single grain NH ₄ NO ₃ -Al	Hybrid NO _x /rubber
Example propellants							
Reliability	+1	+1	+1	+1	-1	0	0
Performance	+1	0	0	0	+1	0	0
Storage stability	+1	0	0	0	-1	-1	+1
Cost	-1	+1	-1	+1	0	+1	0
Greenness	-1	+1	-1	+1	0	-1	-1
Handling safety	-1	0	-1	+1	0	0	+1
$\Sigma(+)$	3	3	1	4	1	1	2
$\Sigma(0)$	0	3	2	2	3	3	3
$\Sigma(-)$	3	0	3	0	2	2	1
Total	3	7	-2	8	-2	-2	1

Table 1.2: Summary table with different propellant type characteristics.

Example propellants	Conventional		Hypergolic		Quasi-hypergolic
	LH2/LOX	Low	Hydrazine/NTO	High and increasing	
Cost per kg	Established infrastructure	Low	Increasingly difficult due to safety hazards	High and increasing	Increasingly available due to green production process
Procurement	Low for LH2/LOX, usually low for other common combinations	Low	High, especially for hydrazine	High, especially for hydrazine	Barely
Toxicity	LOX: spills explosive; LH2 extremely flammable	Low	High due to high vapor pressure and hypergolicity	High due to high vapor pressure and hypergolicity	Low vapor pressure, but catalytic ignition on most surfaces
Explosion risk	Cryogenics: frostburn, H ₂ embrittlement	Low	Corrosive, carcinogenic	Corrosive, carcinogenic	Corrosive
Other hazards	Cryogenics: low, requires severe thermal control	Low	NTO: -11 to 21°C; hydrazine: 2 to 114°C	NTO: -11 to 21°C; hydrazine: 2 to 114°C	EtOH: -114 to 78°C; HP: 0 to 150°C, -60°C achievable due to supercooling
Temperature range	Boil-off; storage limited to days	Low	High vapor pressure; almost infinite storage age	High vapor pressure; almost infinite storage age	Decomposition; multiple year storage with ample performance decrease, stabilizer development further enhances storage life
Storage losses	Active ignition system	Low	Spontaneous upon contact, thus highly reliable	Spontaneous upon contact, thus highly reliable	Decomposition using a catalyst, thus highly reliable
Ignition	450 s, but large volume needed due to low density of LH2	Low	330 s	330 s	325 s
Max. specific impulse		Low			

1.2.2. Trade-off outcomes

When all these factors are taken into account in a trade-off, as visualized in [Table 1.1](#), it is clear that HP promises the best overall compliance, both when it is used as a monopropellant and when it is operated in a bipropellant system. For monopropellant systems, this is mainly because it does not feature hydrazine's high toxicity (which induces high costs). Though, it should be noted that HP does not offer the same storage life. Further, the decomposition of HP offers slightly lower performance when compared to hydrazine; this can only be resolved with higher combustion chamber pressures or more efficient nozzles, which can increase system mass and cost.

If bipropellant systems are considered, the HP-EtOH system does not present deficiencies in this trade-off table. Besides, not considered in above trade-off are the comparatively low vapor pressures of HP (0.66 kPa) and ethanol (6.1 kPa) when compared to hydrazine (1 kPa) and NTO (96 kPa) [128]. Storage tanks need to be vented to prevent pressure buildup, thus high vapor pressures thus result in higher vapor losses, especially in bipropellant systems [53, 85, 112]. Additionally, these high vapor pressures pose additional explosion and toxicity risk while handling these propellants on Earth, hence further strengthening the argument for HP. Yet, a very prominent disadvantage is that at the present time no commercial HP-EtOH engines are available. Further, as was elaborated above, performance is lower for (quasi-)hypergolic systems when compared to non-hypergolic systems. Conversely, these hypergolic systems offer improved long-term storage and (ignition) reliability. Hybrid solid propellant systems do not exhibit many uncorrectible deficiencies either, but are not further considered in this research. Not only because these often need an ignition system (which decreases reliability), but also because, due to the quasi-random nature of grain burning, their thrust behavior is difficult to predict. Finally, sensitivity analysis of this trade-off shows that altering the weights or the complete removal of one or two criteria will not result in a different conclusion.

All things considered, it is imperative that more research should be carried out to aid the development of HP-based rocket engines, not only to make space more accessible and economical, but also to decrease the environmental impact of spaceflight. This research hopes to make a (minor) contribution in achieving this goal.

1.3. Hydrogen peroxide as propellant

As was shown in the previous section, HP-based propellant systems display some remarkable advantages when compared to the current state-of-the-art. In addition, the challenges that withhold their implementation have been introduced shortly. This section will evaluate several methods that can be used to decompose HP and subsequently induce hypergolicity in HP-ethanol mixtures.

1.3.1. Inducing decomposition and hypergolicity in hydrogen peroxide

Because HP does not form hypergolic combinations, the combustion with ethanol must be triggered either using an (electric) ignition system or catalytically. The relatively low onset temperature of H_2O_2 autodecomposition (400°C at atmospheric conditions [49]) means that little energy is required for starting its thermal decomposition to oxygen, water and heat. This heat could facily be supplied by e.g. an electric discharge [14]. When ethanol is injected accordingly, the decomposition heat from HP (-2884.5 kJ/kg for anhydrous HP [94]) can easily raise the mixture temperature to above the fuel's autoignition temperature (369°C at atmospheric conditions [16]). Though, it should be noted that at this time no records can be found in literature on electric ignition systems for HP.

Further, two concepts are researched to passively ignite HP - ethanol mixtures. The first method aims to mimic true hypergollants by dispersing a compound in the fuel that intensely reacts with HP and hence causes ignition of the ethanol; this can be either a strongly oxidizing or reducing compound or a catalytically active material. Examples of the former are organic manganese(III) salts [50, 112] and sodium borohydride [56]; an example of the latter are dispersed copper(II) salts [50, 86, 112]. Even though tests with these compounds show very good ignition behavior, their use poses significant downsides. First of all, gravity causes these compounds, even though properly dispersed, to settle out over time, hence losing ignition capability. These compounds thus need to be properly dispersed to allow extended storage on Earth (the effect of space and its reduced gravity environment on the stability of dispersions is still an active field of research). Another intrinsic factor that leads to degradation of ignition behavior especially for redox-active compounds is their reactivity. This causes the additives to react slowly with the ethanol fuel, hence reducing the concentration of the active compound and thus making successful ignition increasingly difficult over time [23, 50, 55, 56, 91]. It can be understood that this method does not function in absence of the fuel; this method is thus only suit-

able for single-mode bipropellant systems. Though, this concept will still be considered in this trade-off due to the amount of research conducted.

The second concept aims to decompose HP over a supported catalyst in the combustion chamber and use this decomposition heat to ignite the fuel. A direct consequence hereof is that the catalytic material is exposed to high temperatures and pressures (over 2000°C and 40 bar [83]). Mostly because of these hostile conditions, extensive research efforts over the past decades have not produced a stable decomposition catalyst. Nevertheless, some spacecraft have incorporated HP decomposition catalysts (based on MnO₂ pellets or platinum gauzes [67, 117, 124]), yet these catalysts degrade quickly due to the experienced reaction conditions, and hence are not suitable for long-term space missions.

1.3.1.1. Comparison of ignition methods for HP-EtOH mixtures

Several ignition mechanisms for inducing hypergolicity in HP-EtOH mixtures have been described above. Using the same system engineering method as in section 1.2, a trade-off matrix, these methods are compared for their compliance on four criteria: reliability, performance stability, their ability to operate in pulsed mode and in monopropellant mode. The weights have again been determined based on pair-wise comparison of these criteria, resulting in the weights as given in Table 1.3.

Reliability Most important for an ignition system is its reliability, that is, does it operate as it should at the time required. To exclude degradation effects from this criterion, only the reliability at the start of the mission will be analyzed. Electric igniters generally have a low reliability and therefore induce high operation risk. Both fuel additives and supported catalysts initially show excellent performance.

Performance stability The decrease in ignition reliability over the lifetime of the mission is captured in the performance stability. As elaborately discussed above, dispersed fuel additives tend to settle out of the solution or react with the fuel, hence losing ignition ability. Electric ignition systems, even though they have overall low reliability, suffer from performance degradation to a much lesser extent than fuel additives [117]. Properly designed catalytic beds barely suffer from deactivation effects over time, or the degradation can easily be accounted for by design, without affecting propellant properties.

Pulsed operation Not discussed above is the ability of an ignition system to support pulsed operation. During pulsed operation (>10 Hz) short thrust bursts are generated to execute precise maneuvers without mass flow controllers. Electric ignition systems in rocket engines usually cannot cope with the associated precise timing requirements, due to which normally decomposing or hypergolic propellants are used [42, 117]. Due to the absence of additional mechanisms, both passive ignition methods perform rather well in pulsed operation mode.

Monopropellant mode Above it was mentioned that dual-mode operation of a thruster is often an advantage. Since all these ignition methods are mainly intended for bipropellant operation, this criterion evaluates how well an ignition system can induce decomposition of pure HP, in absence of ethanol. A rocket motor dependent on ignition from the fuel additives can simply not operate in absence of the fuel. As mentioned above, electric ignition systems could be used to trigger HP decomposition. The supported catalyst however is designed to catalyze H₂O₂ decomposition and thus will perform fully conform specification in monopropellant mode.

1.3.1.2. Trade-off outcomes

When above considerations are taken into account and put in the trade-off matrix (Table 1.3), it is clear that a supported catalyst would be the best option to induce hypergolicity in HP-EtOH mixtures. Removal of any of the criteria does not lead to another concept performing better in the trade-off. From the above discussion is clear that the settling of fuel additives is an uncorrectable deficiency, whereas the reliability leads to exclusion of electric ignition systems. Therefore this research aimed to develop a supported catalyst to decompose HP that has the potential to ignite HP-based propellant mixtures for space propulsion.

1.3.2. Hydrogen peroxide decomposition catalysts

Many catalytic materials have been researched for their reactivity with HP, but none of the currently tested catalysts can withstand the harsh conditions as present in the combustion chamber for prolonged time

Table 1.3: Trade-off on ignition methods.

Criterion	Weight	Electric ignition	Fuel additive e.g. NaBH ₄	Supported catalyst
Reliability	3	-1	+1	+1
Performance stability	2	+1	-1	+1
Pulsed operation	1	0	+1	+1
Monopropellant mode	1	0	-1	+1
$\Sigma(+)$		1	1	4
$\Sigma(0)$		2	1	0
$\Sigma(-)$		1	2	0
Total		-1	1	7

(please refer to the excellent review by Guseinov and coworkers [42]). The best results have been obtained with manganese oxides and metallic platinum; therefore these metals have found sparse applications over the past decades as decomposition catalysts.

1.3.2.1. Active catalytic metal trade-off

The choice of the active element in a catalyst is essential for its proper functioning. Some elements are catalytically active, but will remain so only for very short times. Therefore, in order to increase the chances that this research will produce a properly functioning catalyst, different chemical elements were compared based on i.a. their reactivity with HP. Since little research has been conducted up to now into achieving hypergolicity with supported catalysts, this trade-off will compare these catalytically active metals solely on their performance in HP decomposition. Other criteria are the lifetime such a catalyst would display in the combustion environment, the (relative) exhibited technological readiness level, costs associated with fabrication of the catalyst, and the amount of research conducted so far. As before, the weights have been determined based on pair-wise comparison of these criteria. Table 1.4 displays several metallic elements that have been researched at least two times in the past, i.e. silver, gold, iridium, manganese, ruthenium, palladium and platinum.

Reactivity The most important criterion to evaluate different catalytic metals is their reactivity. Even though no single research has compared all of the evaluated metals simultaneously, the results obtained in these investigations can be globally combined to give a fair comparison of the reactivity of all of the here listed elements [2, 5, 15, 27, 42, 57, 63, 71, 97, 105, 106, 108, 116]. It is evident that expensive materials as silver, ruthenium and platinum seem to offer the highest catalytic performance. Iridium on the other hand, which is commercially used in hydrazine decomposition engines, has only low reactivity with HP. Gold, manganese and palladium all are rather reactive, but less than the aforementioned metals.

Expected lifetime Almost equally important as the catalytic reactivity is the lifetime of the catalyst. Up until now, only little research has been conducted in a representative environment, that is, in a (small scale) rocket motor. Therefore, due to the importance of an extended lifetime of the catalyst, it is tried to compare the candidates based on results obtained in HP decomposition research, and basic physicochemical information. For instance, it is known that both iridium and ruthenium are very resistant to oxidative environments, even at elevated temperatures, which is why iridium has found such widespread use in hydrazine rocket motors. Further, it is known that silver, manganese and platinum have been used for HP decomposition in spaceflight [85, 124]. Yet, due to either swift sintering, evaporation or oxidation their catalytic lifetime is limited; because of their flight heritage this is deemed acceptable performance. The largely similar properties of palladium when compared to platinum result in palladium being awarded the same score. Lastly, it has been shown that gold catalysts only show very low stability due to poor adhesion to common catalyst support materials [15].

Cost The aim of these research efforts is the development of a combustion catalyst that should be operated in space. Yet, the space industry is becoming more and more competitive. To increase the attractiveness of the developed catalyst for industry, it is important to focus on cost already early in the development. The platinum group metals (Pt, Pd, Ru) and the noble metals gold and silver are known to be very expensive, with

the same applying to iridium. The price of these metals is expected to increase steeply in the coming decades due to the increased demand because of their use in green energy solutions [46]. Of the considered materials manganese is (and most probably will remain) readily available in large quantities due to its abundance on Earth.

Technological readiness Less important at this stage than the costs associated with the catalytic metal is the technological readiness of the active metals under scrutiny. As has been stated earlier, only silver, manganese and platinum have found prior use in HP decomposition engines. In addition, iridium has been awarded with acceptable performance due to its heritage in hydrazine engines. The remaining elements have no recorded use in spaceflight.

Amount of research conducted The final evaluation criterion is the amount of research that has been conducted in the past on these elements with respect to HP decomposition. This aspect has been included, since prior knowledge can serve as an easy starting point for further catalyst development. Most research efforts have focused on the development of platinum- and manganese-based catalysts, while less have focused on incorporating palladium. The other here reported catalytic metals have received only little attention in the past.

Table 1.4: Trade-off to find the most promising active elements to use for the catalysts in this research.

Criterion	Weight	Active element						
		Ag	Au	Ir	Mn	Ru	Pd	Pt
Reactivity	3	+1	0	-1	0	+1	0	+1
Expected lifetime	2	0	-1	+1	0	+1	0	0
Cost	2	-1	-1	-1	+1	-1	-1	-1
TRL	1	-1	-1	0	+1	-1	-1	+1
Amount of research conducted	1	-1	-1	-1	+1	-1	0	+1
$\Sigma(+)$		1	0	1	3	2	0	3
$\Sigma(0)$		1	1	1	2	0	3	1
$\Sigma(-1)$		3	4	3	0	3	2	1
Total		-1	-6	-4	4	1	-3	3

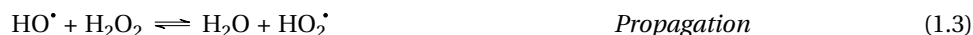
Trade-off outcomes

The results of the trade-off can be found in Table 1.4; it is evident that both manganese and platinum are the most promising metals to investigate. The costs associated to the incorporation of platinum appear to form an intractable deficiency. Yet, when this catalytic material is dispersed on a nanoscopic scale, the total costs can be seriously reduced without severely influencing the overall reactivity. It might be argued that this would then also be applicable to other catalytic metals that display this same deficiency. Though, due to the even higher predicted increase in demand for these material the costs associated to manufacturing of the catalyst would increase even more than for platinum. The trade-off further shows that, based on its score, ruthenium could be considered as well in this research. Beside the disadvantageous costs associated with ruthenium, it has not been used before in spaceflight, nor has received much attention in literature. Hence it will not be further considered here. Finally, a sensitivity analysis performed on this trade-off and its criteria shows that only removal of the cost aspect from the comparison results in a different conclusion, i.e. ruthenium and platinum would be most promising. Yet, as has been mentioned above, the competitiveness of space industry impedes a strong focus on cost minimization, hence justifying the original outcomes of the trade-off.

1.3.2.2. Manganese oxide catalysts

Manganese oxide (MnOx) catalysts do not only display good reactivity in the reduction of H₂O₂, they are also rather economical. Their catalytic behavior is believed to function in a cycle between the +4 and the +3 oxidation state (see Equation 1.1 – 1.5 [49]). An intrinsic problem with these MnOx catalysts however is the is that the metal ion undergoes a sequential phase transition from Mn(IV) to inactive Mn(II) at elevated

temperatures, starting above 525°C [42, 49].



It is thus fundamental to stabilize the +4 and +3 oxidation states to retain the catalytic performance at the operating conditions; this can be achieved by a meticulously chosen catalyst support material. To illustrate, Russo Sorge's research group has been investigating supported MnOx catalysts for HP decomposition for some time [5, 7–9, 84, 108]. They have managed to postpone the undesired mentioned phase transition to higher temperatures by means of a proper catalyst support material: yttria-stabilized zirconia (YSZ; zirconia with 10 wt.% yttria). No catalyst degradation was noticed after multiple cold starts nor after more than twenty-five minutes of HP decomposition above 650°C. Yet, even though the catalyst shows excellent stability behavior at 650°C, at the earlier mentioned combustion conditions the catalyst will most likely completely transform into the inactive Mn(II) phase. To conclude, MnOx catalysts are suited for use in HP decomposition engines, but a better support is necessary for their successful implementation in quasi-hypergolic engines. In [subsubsection 1.3.2.4](#) more information will be supplied on support materials and their preparation.

1.3.2.3. Platinum catalysts

Platinum has been used in spaceflight to decompose HP in the form of metallic gauzes; unfortunately these sinter rapidly due to the occurring temperatures in the decomposition chamber. More sustainable and economical than these gauzes is the application of a fine dispersion of nano-scaled platinum particles, or nanoparticles (NPs) [80, 81]. Unfortunately, NPs suffer from additional deactivation phenomena, such as Oswald ripening. This requires extensive anchoring in or to the support material. These deactivation effects are less prominent for larger NPs, which also show a higher activity in H₂O₂ decomposition [110]. It must be considered though that the use of larger NPs often implies a higher catalyst weight loading, and thus higher cost.

A group of support materials that has a very strong interaction with platinum NPs is formed by so-called metal oxide perovskites, as is elaborated upon in [chapter C](#). Research has shown that these supports almost completely impede the deactivation of the platinum phase (see e.g. [62]). Consequently, the use of metal oxide perovskitic supports can potentially enable the use of platinum catalysts in HP decomposition or even quasi-hypergolic engines. Nevertheless, both due to the complexity associated with the synthesis of such materials and the high cost of platinum catalysts, this research will merely discuss MnOx catalysts for HP decomposition.

1.3.2.4. Catalyst support materials and synthesis

The discovery of a well-performing catalytic phase is merely the start of a long process before a catalyst can be put into practice. Among the most prominent causes is the choice of a proper catalyst support material. As was already illustrated above, the right catalyst-support combination is essential for maintaining integrity of the active catalytic phase. Other important motives in the development of a support are cost, stability (e.g. when a compound has a low transition temperature to another inactive oxidation state, such as MnO₂), or activity (most often a pure catalytic compound is too reactive). Metal oxides are commonly utilized support materials, for instance alumina (Al₂O₃) and titania (TiO₂). Each metal oxide has different interactions with the catalytic phase, due to their intrinsically differing electronic properties. These properties can be further altered by doping or mixing with different metal oxides. In this manner, the behavior of both the catalytically active phase and the support can be adjusted for each application. Unfortunately, despite extensive research, prediction of the right catalyst-support combination is still difficult: the optimal support composition for a certain catalytic phase still needs to be found by elaborate research.

Parallel to the choice of the metal oxide is the selection of the support class of the catalyst. Namely, two general classes of supported catalysts can be discerned: bulk catalysts, in which the catalytic phase is homogeneously mixed with the support material, and impregnated catalysts, where (a precursor of) the catalytic phase is impregnated into a porous support material. In bulk catalysts, the mechanical properties of the carrier are influenced by the presence of the catalytic phase, for instance it can lead to sintering of the support material. Further, the full embedding of the catalytic phase will often result in different interactions with the



Figure 1.3: Typical catalyst support structures; monoliths (back) and a wide range of catalyst pellets [24].

support when compared to impregnated catalysts. Thus, a well-performing support material in a bulk catalyst does not necessarily perform equally well when the active phase is loaded by impregnation. A distinct advantage of the homogeneous dispersion of the active phase, is that erosion of the bulk catalyst surface does not immediately lead to loss of catalytic performance. On the other hand, because of this dispersion, the effective use of catalytic material is low. Therefore bulk catalysts are often only used for inexpensive catalytic metals, such as iron or nickel. Another distinct disadvantage is that during the preparation of such catalysts often undesired crystalline compounds are formed, by reaction of the active phase with the support material [25, 107].

Impregnation is commonly used for the loading of precious metals or unstable materials [107], of which platinum and manganese oxide, respectively, are adequate examples. The active catalytic phase is applied by exposure of the support to a solution containing the catalyst precursor. The adsorption of the catalytic compounds occurs spontaneously or is brought about by a change in solubility. This step is followed by calcination, during which intricate bonds are formed between the catalytic compound and the support material. Almost without exception, this changes the electronic energy levels of the catalytic phase, which on its turn influences the binding interaction with the reactants and products, which influences the catalytic performance. Since all chemical elements possess different electronic properties, it can be understood that some support materials may have a positive effect on the catalytic performance whereas others could totally nullify catalytic activity. Further, in contrast to bulk catalysts the mechanical properties of impregnated catalysts are only marginally affected by the application of the active phase. This allows an ab-initio focus on the support properties, such as thermal operation limits, whereas for bulk catalysts these properties can change considerably during their preparation. From the above discussion it is clear that a support can have profound

influence on the catalytic properties. This investigation will thus mainly focus on the effects of the support material on the catalytic properties of manganese oxide.

1.4. Hydrogen peroxide procurement

Generally available solutions of HP are between 30 to 50% concentration, whereas for propulsion purposes >98% is desired. Due to the increased explosion risk associated with high purity HP, these concentrations are often only available on special demand, which increases cost and induces long waiting periods associated with its acquisition. In addition, these risks also lead to high transportation cost. Furthermore, national and international regulations on the shipment of propellant-grade HP may even prohibit procurement from spe-

cific supplier [22, 30]. These disadvantages associated with the acquisition of high concentration HP could make purification of easily available HP on-site attractive. Typical processes that are used in industry to remove water from peroxide solutions are water sorbents, membrane separation, vacuum distillation et cetera [33]. Unfortunately these methods are either too inefficient, time consuming, costly or complicated to be carried out on-site by the space contractor itself, which up to now necessitates procurement of expensive propellant-grade HP.

Recently, SolvGE has developed a process that has the potential to allow safe and on-site purification of low concentration HP. Additionally, this process does not require additional chemicals. This technique promises to largely decrease the cost and waiting time associated with the procurement of HP for space propulsion. Pivotal in this process is a fundamental difference in physical properties between water and H_2O_2 . SolvGE has exploited this physical phenomenon by thermodynamically stimulating the continuation of water removal, which consequently leads to an increase of the HP concentration in the residue [54]. Since this process is carried out at atmospheric conditions and with only a source of inert gas, process costs and complexity are low. Also, because there is no additional contact with foreign substances (such as condensers or adsorbents) introduction of pollutants is minimal: the purity grade of the final product is dependent on the initial solution quality. Implementation of this method can greatly decrease cost and delays associated to HP procurement for spacecraft manufacturers.



Figure 1.4: SolvGE Research Grade Printer.

Until recently the purification equipment developed by SolvGE was only available at laboratory scale, as can be seen in Figure 1.4. At this scale it was already clear that the efficiency of the process is limited by thermodynamics: as the purification process progresses, the contribution of HP to the gas phase increases, which is consequently vented off. Thus, in order to increase the economics of an industrial sized setup, HP must be recovered from the waste stream. Based on the results of this work, the company has recently launched a product that can generate up to 1 kg of high concentration HP, and is suitable for chemical process development.

1.5. Hydrogen peroxide storage

Hydrogen peroxide is commonly believed to be an unstable chemical. This is however only conditionally true, as very pure and concentrated HP is almost infinitely storable, but highly expensive [22, 125]; less pure (and thus more economical) high concentration HP typically decays with several % per year [109]. The accelerated decomposition is triggered by metal ions and organic contaminations that have been introduced during manufacturing and storage; current manufacturing techniques can limit the concentrations of these contaminants to the ppm-level. For the implementation in space, this still does not offer sufficient long-term stability, which raises the need for additional stabilizers. Several types of stabilizers are used in industry, based on different approaches. For instance, with a decrease of pH the concentration of the reactive OOH^- ion is reduced, which has been shown to increase the lifetime of HP [33, 70, 109]. Yet, in this realm it must be considered that a more stable H_2O_2 molecule requires a more active catalyst. On top of that, acidic solutions can have a corrosive effect on the propulsion system and the catalyst itself, and are therefore not preferred. Chelating compounds are another type of stabilizers; examples are phosphates and multidentate organic phosphorus complexes. These compounds strongly bind reactive metal ions and hence increase the storage life of HP. Yet, because most phosphorus compounds have a poisoning effect on catalysts, they are not suitable for stabilizing HP for space propulsion [30, 47, 97, 100]. The last group of stabilizers used for HP are dispersed metal oxides, tin oxide being used most often for the stabilization of propellant-grade HP [19, 51, 70, 109]. It has been posed that upon dissolution of stannate ($Sn(OH)_6^{2-}$), tin oxide colloids are formed [109]. These tin oxide colloids present a negatively charged surface to the solution and hence bind the positively charged metal ion

impurities. As all colloids, these tin oxide colloids will settle over time, thereby not only reducing stabilizing performance, but also possibly causing propulsion system blockage. Hypothetically, it is possible to prevent settling of these colloids by mechanically fastening, for instance to aluminum tank walls. This supporting of tin oxide colloids has been researched for use in battery electrodes [61, 75]; yet, no report can be found in literature on the use of supported SnO₂ for HP stabilization.

1.6. Research questions and objectives

The rest of this thesis report will explore the current difficulties that impede incorporation of HP as a space propellant, that is its availability, instability and the lack of a hypergolicity inducing catalyst. In order to reach that goal, the main research question around which this research revolves was formulated as:

How can the implementation of HP as a space propellant be promoted, i.e. by increasing its availability, the development of a catalytic ignition system and improvement of its stability?

As indicated above, the problem will be divided in three different research directions; the first being the increase of efficiency of the SolvGE HP production process, as can be found in [subsection 1.6.1](#). The second topic is the development of a suitable supported catalyst that can decompose HP with enough vigor to potentially induce hypergolicity in HP-EtOH mixtures, as will be discussed shortly in [subsection 1.6.2](#). The research into the stability of stored HP will be outlined in [subsection 1.6.3](#).

1.6.1. Purification of propellant-grade H₂O₂

The first aspect this research will focus on is the procurement of propellant-grade HP. SolvGE has devised a technique to carry out purification of low concentration HP to concentrations above 90%, i.e. suitable for space propulsion. Since this technology is relatively new, large improvements in efficiency can still be made. The goal of this part of the thesis, as elaborated on in [chapter 2](#), was to increase the efficiency of the purification process of propellant-grade HP with the company's Research Grade Printer (RGP) setup without affecting the quality of the HP. The research question that aided in the development was formulated as follows:

RQ-CND *How can HP be recovered from the waste stream of SolvGE's purification process, without affecting its purity?*

1.6.2. Support effect on the decomposition of H₂O₂ over MnOx catalysts

Up until now, all research into inducing hypergolicity in HP-based propellant mixtures has focused on catalysts (or related compounds) that are dispersed in the fuel. Yet, these additives will either settle over time or slowly react with the fuel and thus lose their hypergolicity. In the above it was shown that supported MnOx catalysts are an affordable candidate for use in HP decomposition engines. Therefore, the main focus of this work was to find a MnOx-support combination that would decompose HP vigorously enough to potentially induce hypergolicity and simultaneously possess high mechanical strength. The results of these research efforts can be found in [chapter 3](#). As a guidance, below the research questions formulated for this part of the thesis research can be found, which will be shortly introduced and answered in aforementioned chapter.

- RQ-CAT-1** *What is the effect of the support on activity and stability of MnOx for H₂O₂ decomposition in drop-testing?*
- RQ-CAT-1-1** *What is the nature of the active site of the catalyst?*
- RQ-CAT-1-2** *What is the influence of the support material on the transition temperature of MnOx?*
- RQ-CAT-1-3** *What phenomena cause deactivation of the MnOx catalyst during drop-testing?*
- RQ-CAT-2** *How can drop-testing be used for decomposition testing of HP over a supported catalyst?*
- RQ-CAT-3** *Is the decomposition of HP over the catalyst vigorous enough to induce hypergolicity?*

1.6.3. Stabilizing propellant-grade H₂O₂

As introduced above, long-term storage of HP is one of the major hurdles that inhibit its use in space. Thereto, as described in [chapter 4](#), several stabilizing methods were compared and the concentration of the exposed HP was monitored over several months. To aid the research, the below research questions had been posed, which are introduced and answered in [chapter 4](#).

- RQ-STA-1** *How does the concentration of HP affect its stability?*
- RQ-STA-2** *What is the influence of the surface-to-volume ratio of stored HP on its stability?*
- RQ-STA-3** *How can aluminum be treated such that it is suitable as a stabilizer support?*
- RQ-STA-4** *What effect does immobilization have on the stabilizing action of the colloids?*
- RQ-STA-5** *How do different types of stabilizers interfere with each other?*

1.7. Outlook

To conclude, this thesis report will set out to investigate the most pressing issues currently impeding the implementation of HP in spaceflight. Thereto it hopes to contribute to the availability of propellant-grade HP by further improving the efficiency of the SolvGE HP purification process. Further, this work will attempt to develop a catalyst that can decompose HP so efficiently that the resultant heat can potentially be used to ignite ethanol and hence induce hypergolicity. Additionally, the developed catalyst should remain active for a considerable amount of time. Finally, this thesis will investigate the stability of HP and whether it can be stabilized without negatively affecting its propulsion characteristics.

Purification of propellant-grade H_2O_2

SolvGE's current hydrogen peroxide purification setup is limited in efficiency by physics, not by design: the vapor pressure of a component is linearly dependent on its concentration in the liquid phase (Raoult's law). That is, with increasing HP concentration the vapor will accommodate higher amounts of HP and lower amounts of water. This means that when the vapor above the fluid is replenished, more and more HP is lost over the course of the purification process. In order to counter this physical barrier that limits the process efficiency, the HP must be captured from the concentrator outflow. Several methods can be used to perform this extraction: absorption, membrane separation, high pressure gas distillation or condensation. The first two methods suffer especially from low selectivity for H_2O_2 over H_2O , due to the large similarities between both molecules. An additional difficulty with absorption is the extra step required to regenerate the absorbant and hence release the HP and water. High pressure gas distillation is used on an industrial scale to separate air in its constituents, but this process is rather complicated and only viable on such a large scale. Thus the only remaining option is condensation [54, 121]. The objective of this part of the research was to investigate if propellant-grade >90% HP can be recuperated from the waste stream of the SolvGE RGP without negatively affecting the efficiency and simplicity of the process. The following research question was used as a support in the design:

RQ-CND *How can HP be recovered from the waste stream of SolvGE's purification process, without affecting its purity?*

Motivation: For the implementation in space industry it is of utmost importance that no contaminants are introduced into the HP, since this may negatively effect its storage life or combustion performance. In addition, regulations put a limit on the allowable concentration of stabilizers for its use as propellant.

The contents of this chapter have been based on several standard works on heat exchanger design [74, 95, 111, 120, 121]. This chapter will first describe the design concept and its background, followed by the theory behind condensation and a description of the model used to predict the required properties for the recuperator. Afterwards, the results obtained with different recuperator designs will be presented and discussed.

2.1. Recuperator design concept

Two main requirements were posed to the HP recuperation system design by SolvGE. The first requirement (REQ-CND-1) demands that the designed recuperator will separately produce pure HP and pure water. The second requirement (REQ-CND-2) puts a threshold on the efficiency of the recuperator system. Based on the data as supplied by the company (Table 2.1a), Figure 2.1b was constructed, which shows the efficiency of a typical concentration experiment with the RGP. When this data is combined with REQ-CND-2 it shows that the cumulative HP loss must be decreased to below 10%. Concretely this means that the designed recuperation system should produce over 30 mL of pure HP.

REQ-CND-1 The designed recuperation system shall selectively remove HP and water from the SolvGE RGO outflow.

REQ-CND-2 The designed recuperation system shall recover over 80% of all evaporated HP when starting from an initial volume of 300 mL HP of 30% concentration with the SolvGE RGP.

From Figure 2.1b it can be clearly deduced that the purification follows an exponential trend towards 100% concentration. Further, when taking into account the cumulative loss (defined as percentage loss of the originally present amount of HP), it can be seen that most losses occur during the purification from 60 to

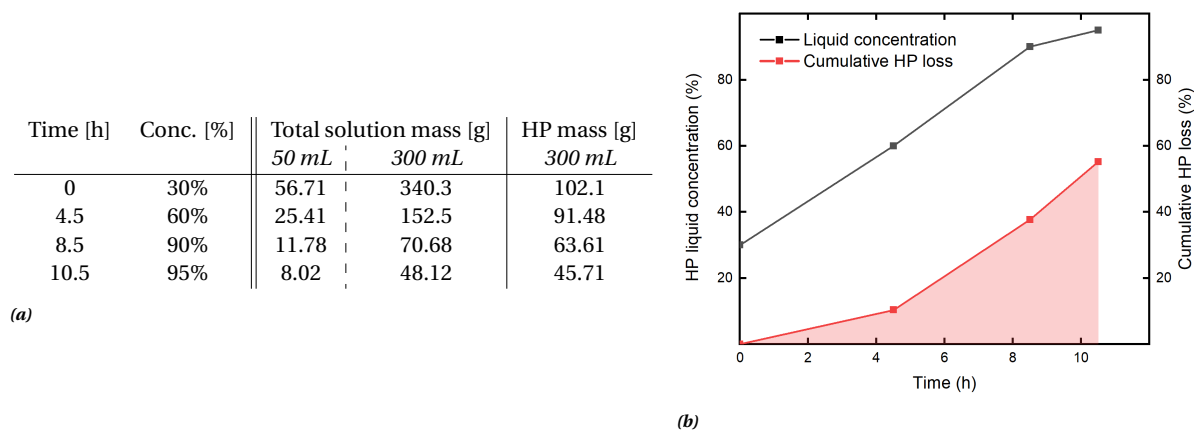


Figure 2.1: Input data as received from SolvGE, based on experiments with the RGP.

a) Experimental data used as input for model; the first three columns were supplied by SolvGE. They consist of time, initial concentration and total solution mass at the start of that step for a concentration procedure of approximately 50 mL. The last two columns are an extrapolation of this to the intended 300 mL volume and the total mass of present HP.

b) Variation of HP concentration during a typical purification experiment with the RGP. Also indicated is the cumulative HP loss during this experiment.

90%. Furthermore, the efficiency of the final purification stage is low as well, while the residue only increases with 5 mass percent point (mpp). The largest increase in overall process efficiency can thus be obtained in these two stages.

Since the purification is carried out under atmospheric conditions, the purification gas (nitrogen) can only contain relatively small amounts of both water and HP (up to 2 wt.% of water and 0.2 wt.% of HP at 20°C). However, at lower temperatures these amounts become even smaller [127]. Note that one kilogram of atmospheric air constitutes 816 liters; this indicates that large volumes are necessary to carry off the water and HP. This phenomenon is the key to the here proposed design: when the mixture is cooled, the surplus molecules in the gas phase are inclined to condense to restore equilibrium in the vapor phase.

The cooling can be brought about by a liquid cooling loop (such as in a refrigerator) or with a solid state cooling system (Peltier elements). The former offers higher efficiency, but at expense of higher complexity, increased maintenance frequency and risks (such as leakage). As the entire HP recuperator should be kept as simple and reliable as possible, it is therefore chosen to employ solid state cooling, specifically using Peltier elements. Because the efficiency of Peltier elements is very strongly dependent on the applied current and potential, a (switching) temperature controller is essential to maintain a decent power efficiency. A direct consequence hereof is that the entire condenser will be forced to be at the same temperature. In the case that the condenser will be fabricated of aluminum (due to ease of manufacturing and HP compatibility), the heat distribution over the condenser will be further equalized due to its high heat conductivity.

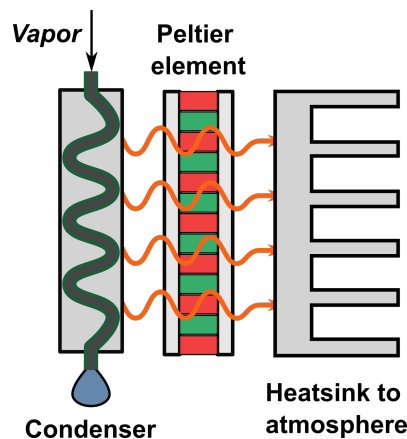


Figure 2.2: Schematic representation of the chosen approach to extract HP from the SolvGE RGP outflow.

2.2. Theoretical condensation model

This section will give a description of the fluid dynamics that underlie the predictive model that was set up. For the reader with less experience in fluid dynamics, first some important concepts are explained that are fundamental for proper understanding of the following.

A boundary layer is the shear layer between free flow and the stagnant wall of the fluid. That means that there is a velocity gradient from zero to the flow velocity, parallel to the flow. With increasing flow velocity, the thickness of the boundary layer increases, as well as the friction it imposes on the flow. At some point this friction becomes so high that the boundary layer detaches from the wall. This is the onset of turbulent flow.

The simple velocity gradient then disappears and is replaced by a random velocity field.

A key parameter in fluid dynamics is the Reynolds number of the flow, which describes the ratio of inertial forces to viscous forces, given by Equation 2.1, where \dot{m} is the mass flow [kg/s], μ is the kinematic viscosity [kg/s²] and D_h is the hydrodynamic diameter in [m], which is the diameter of a circular duct with equal cross sectional area as the tube under consideration.

$$Re = \frac{\dot{m}}{4\pi\mu D_h} \quad (2.1)$$

For low Reynolds numbers, the flow remains laminar. In laminar flow, heat transfer to the condenser wall is minimal due to limited mixing between bulk gas and gas present in the boundary layer, thus resulting in a longer required condenser length. For high Reynolds numbers, the flow is turbulent which results in increased mixing between the bulk fluid and the boundary layer; this on its turn causes heat transfer to be more efficient. It is thus opted to induce turbulent flow.

In between these two regimes a transition regime (often referred to as transient flow) exists in which behavior is very difficult to predict. Transitions between laminar and turbulent flow can be brought about by increasing the Reynolds number; ergo, by increasing the mass flow or decreasing the channel diameter. This transition can also be triggered by (im)properly produced inlet manifolds, rough edges, sharp kinks in flow ducts et cetera. Since the mass flow is a given parameter for the system at hand, the only variable is the channel diameter. As explained further below, there is a lower limit to this channel diameter to prevent (partial) fluid obstruction of the tube, which results in large pressure drops.

2.2.1. Condensation-based recuperator model assumptions

In order to allow computational modeling of complex phenomena as fluid and heat flow, some simplifications have to be made to the problem laid down above. These have been divided in assumptions with regard to the flow behavior (subsubsection 2.2.1.1) and vapor characteristics (subsubsection 2.2.1.2), and the boundary conditions necessary for solving the equations in subsubsection 2.2.1.3.

2.2.1.1. Flow behavior assumptions

As already introduced above, the assumption of transient flow (ASP-CND-FLO-1) has far-reaching consequences with respect to heat transfer. Because of the setup of the process and experiment (see section 2.3), it is safe to assume that the flow leaving the purification vessel is not anymore laminar, and thus is at least partly turbulent.

Further, all condensers used in the experiments (see section 2.4) were either extruded aluminum profiles or hot rolled metal sheets, which therefore exhibited extremely smooth surfaces (ASP-CND-FLO-2). One could argue that it would be beneficial to have rough condenser walls (introducing more turbulence, hence resulting in higher heat transfer). Yet it must be considered that a higher roughness will on its turn lead to a larger pressure drop over the condenser, which then leads to higher pump power. Therefore both in the model and in the experiments it was chosen to maintain the current wall smoothness.

In the conducted experiments, as described in section 2.4, the smooth-corner assumption (ASP-CND-FLO-3) is heavily violated. This will lead to increased flow turbulence, thus increasing condenser efficiency, and reducing condenser size and hence reducing cost. Yet, since this property is very difficult to parameterize, the effects of the violation of the assumption will not be considered directly.

The last two assumptions have a similar outcome, although they are not physically related. When a flow is developing through a channel, the boundary layer thickness increases to a steady-state value. The boundary layer decreases the available space for the flow, leading to a higher flow speed, which increases the boundary layer thickness up until equilibrium is established. It can be understood that this negatively influences flow characteristics such as the pressure drop. Assumption ASP-CND-FLO-4 is applied to the model, since in the transient flow regime fluid behavior is difficult to predict.

A similar reasoning applies to the last assumption (ASP-CND-FLO-5). The presence of condensate, either in the form of droplets or a film, decreases the effective diameter of the channel. It can be understood that the presence of the condensate reduces the effective diameter of the flow, which on its turn causes a higher pressure drop. Further, it is not improbable that, at some point, the condensate might fully block the condenser channels and hence impede operation of the entire system. Therefore a minimum diameter of 5 mm is chosen, so that the size of drops becomes relatively small with respect to the channel diameter.

ASP-CND-FLO-1 The incoming flow is in or above the transient regime.

- ASP-CND-FLO-2** The condenser walls are smooth.
ASP-CND-FLO-3 Bends and curves in condenser have no effect on flow behavior.
ASP-CND-FLO-4 The boundary layer does not cause choking of the flow.
ASP-CND-FLO-5 The condenser inner hydrodynamic diameter is larger than 5 mm.

2.2.1.2. Vapor characteristics assumptions

This section will explain the assumption made on the thermodynamic properties of the fluids involved, which can be found below.

- ASP-CND-VAP-1** The condensation is a two-phase process (first HP condenses, then water).
ASP-CND-VAP-2 The system is assumed to be in continuous equilibrium, hence the mass flow of HP and water are constant.
ASP-CND-VAP-3 The mass flows of HP and water are negligible compared to that of N₂.

Since HP is a more valuable chemical than water, this design will merely focus on the recuperation of HP. Also, since the vapor pressure of HP is roughly one-fifth of that of water (see [chapter A](#)), HP will be much more inclined to condense out of the vapor phase. These two considerations lead to the two-stage condensation assumption (ASP-CND-VAP-1). Effectively this means that the heat contribution from condensing water can be ignored. Yet, it is theoretically impossible to achieve a two-stage condenser design, since water and HP will, due to their high affinity, always condense partially together: no 100% HP can be achieved by single-step distillation (note that repeated distillation is used in industry for HP purification). Concretely this means that it is impossible to satisfy requirements REQ-CND-01 and REQ-CND-02 simultaneously. A fundamental design decision is thus necessary: the process will either recover only part of all HP and achieve a high concentration, or the majority of HP will be removed from the flow, but at a low concentration. Of course, both approaches have an influence on the required cooling power and thus the length of the condenser. Due to the exploratory nature of this research project, it was chosen by SolvGE to postpone this design decision, and base the predictive model on two-stage condensation. Note that in later design iterations the recuperated HP concentration can be easily adjusted by changing the temperature difference between flow and condenser wall to give the desired concentration.

Even though recent SolvGE experimental evidence clearly shows that the gas phase composition changes over time (as can be deduced from [Figure 2.3](#)), for a first order estimate it was assumed that the mass flow of HP and water are constant and in equilibrium during the considered purification phase (ASP-CND-VAP-2). Because of this, the resulting heat flow to the condenser will be constant over time. This assumption will most likely lead to an underestimation of the required condenser size. However, due to the limited knowledge about the process at this point, no more data are available to quantify this error. Note that when the condenser would be operated with constant heat dissipation (taking into account the increasing HP concentration over time), at the start of the purification process primarily water would condense from the vapor.

From [Table 2.1a](#) the mass flow of HP and water can be calculated. When these mass flows ($2.5 \cdot 10^{-3}$ g/s and $6.5 \cdot 10^{-3}$ g/s, for HP and water, respectively) are then compared to the nitrogen flow (1.56 g/s), it is clear that there is a difference of approximately three orders of magnitude. For a first order estimate this justifies neglecting of the former two mass flows (ASP-CND-VAP-3).

2.2.1.3. Boundary conditions

This section describes some further conditions that are necessary for solving the flow equations in the model, which are formulated below.

- ASP-CND-BC-1** The condenser inlet and outlet are 20°C and 0°C, respectively, leading to a ΔT of 20°C.
ASP-CND-BC-2 The condenser wall has a constant temperature along its length, viz. 0°C.
ASP-CND-BC-3 The condenser wall temperature is constant over time.

Since the SolvGE concentration setup is operated under standard atmospheric conditions, it was chosen to let the inlet temperature of the system equate to normal room temperature (ASP-CND-BC-1). The outlet temperature is kept fixed at 0°C as a first estimate, since at that temperature HP has a vapor pressure of only a few pascal [[109](#)], whereas water still has a considerable vapor pressure.

The second boundary condition (ASP-CND-BC-2) requires further explanation. In condenser design generally two different condensation situations are discerned: constant temperature and constant heat dissipation. As explained above, the condenser will consist of a single piece of aluminum, to which Peltier elements

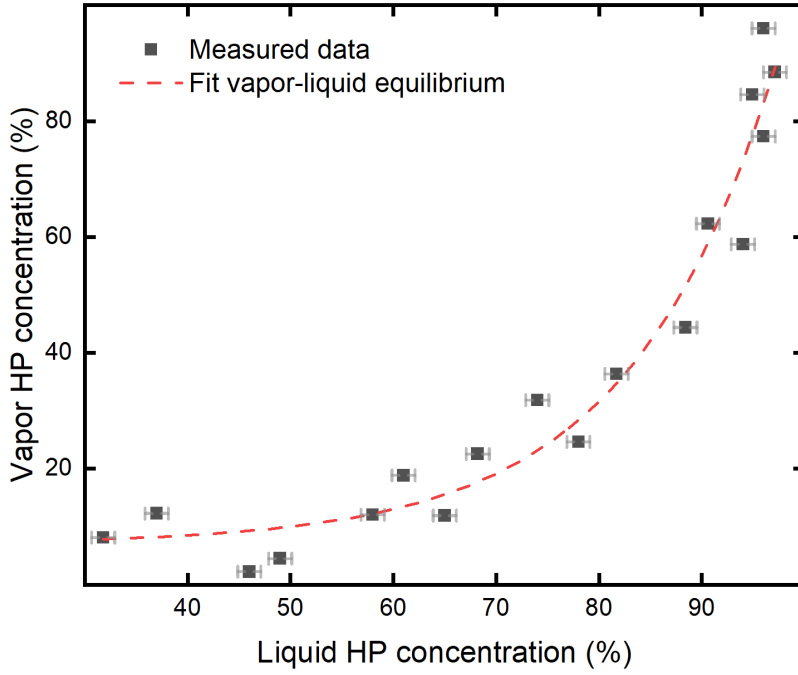


Figure 2.3: Concentration of vapor over HP as a function of solution concentration as measured by SolvGE. The liquid concentration has an error of 1.13%; the errors in the vapor concentration is indicated by the dimensions of the data-points ($\sigma = 1.6\%$). The dashed line indicates a clear exponential trend with function $y = 7.054 + 0.08593e^{7.069x}$, $r^2 = 0.954$

are attached. When combined with a thermal controller, this gives a constant temperature over the entire condenser due to the high heat conductivity of aluminum. As all channel walls are in direct contact with each other, constant heat dissipation might be difficult to realize, also since heat may flow from one channel to another. As a consequence, it has been decided to assume a constant wall temperature along the condenser. At this stage of development, it has been opted to let the wall temperature remain constant over time as well (ASP-CND-BC-3). This not only eases the computational efforts, but also the operation of the power supply for the Peltier elements. Yet, a well-defined condenser temperature profile not only aids in optimizing both the quantity and concentration of the recuperated HP, it also can lead to higher power efficiency of the recuperator. The implementation hereof is left for a future design iteration.

2.2.2. Condensation model description

This section will supply the equations required to calculate the thermodynamic and fluid dynamic properties of the condenser flow. A schematic illustration of the model can be found in Figure 2.4. In order to find the heat that needs to be removed from the gas flow, taking into account above assumptions, only the heat is considered that is released by cooling of nitrogen, condensation of HP, and cooling of liquid HP from 20°C to 0°C. The required power \dot{Q} [W] can be calculated using Equation 2.2, where $\Delta_v^0 H$ is the standard vaporization enthalpy [J/g], \dot{m} the mass flow in [g/s], C_p the specific heat at constant pressure [J/g·K] and ΔT the temperature difference between wall and flow [K]. When required heat is calculated for condensation between 60 and 90% (5.8 W) and 90 and 95% (6.5 W), it shows that the latter stage has a higher power requirement. Thus, the design will be sized for the recuperation of HP during the purification from 90 to 95%.

$$\dot{Q} = \dot{m}_{N_2} C_{p,N_2} \Delta T + \dot{m}_{H_2O_2} (\Delta_v^0 H + C_{p,H_2O_2} \Delta T) \quad (2.2)$$

The power absorption from a gas stream is given by Equation 2.3. Here A is the contact area in [m²], Nu is the Nusselt number, which is the ratio of convective over conductive heat transfer in a boundary layer, k is the heat conductivity of the fluid in [W/m·K], and D_h and ΔT are again the hydrodynamic diameter and the temperature difference, respectively.

$$\dot{Q} = ANu \frac{k}{D_h} \Delta T \quad (2.3)$$

It is immediately clear that the heat transfer is highly dependent on the value of Nu : a larger convective heat transfer will lead to a lower required contact area and thus a smaller condenser. Over the years there have

been significant improvements in flow behavior predictions. Nevertheless, most equations to predict flow behavior are still based on empirical relations, which is also true for calculation of the Nusselt number. Using Equation 2.7, the Nusselt number in the laminar regime ($Re < 2300$) can be calculated for varying (relative) location along the flow path x in [m], normalized by the local hydrodynamic diameter d in [m]. In order to have an average Nusselt number for the entire flow path, it is normalized by integration. From this equation it can be seen that Nu itself is dependent on the dimensionless Prandtl number (Pr), which is a measure for how easily heat is transported by the movement of mass elements compared to heat diffusion between mass elements. Further it can be noted that the condenser length occurs implicitly, which necessitates incremental solving.

$$Nu_{x,1} = 3.66 \quad (2.4)$$

$$Nu_{x,2} = 1.077 \left(RePr \frac{d}{x} \right)^{\frac{1}{3}} \quad (2.5)$$

$$Nu_{x,3} = 0.5 \left(\frac{2}{1 + 22Pr} \right)^{\frac{1}{6}} \sqrt{RePr \frac{d}{x}} \quad (2.6)$$

$$Nu_x = \left(Nu_{x,1}^3 + 0.7^3 + (Nu_{x,2} - 0.7)^3 + Nu_{x,3}^3 \right)^{\frac{1}{3}} \quad (2.7)$$

Similarly, the average Nusselt number in the turbulent regime ($Re > 4000$) is given by Equation 2.9; here ξ is an intermediate factor with no physical meaning. Since flow behavior in the transition regime is still a very active field of investigation, and currently little is known about the flow behavior in this regime, Gnielinski advises to interpolate between the boundaries of the laminar and turbulent regime [95]. As was mentioned in subsection 2.2.1.1, in this design the incoming flow is assumed to be at least transient.

$$\xi = (1.8 + \log(Re) - 1.5)^{-2} \quad (2.8)$$

$$Nu_{avg} = \frac{\frac{\xi}{8}(Re - 1000)Pr}{1 + 12.7\sqrt{\frac{\xi}{8}}(Pr^{\frac{2}{3}} - 1)} \left(1 + \left(\frac{d}{L} \right)^{\frac{2}{3}} \right) \quad (2.9)$$

As was stated above, the flow channels are assumed to be smooth. Following Gnielinski, the total pressure drop is found by integrating Equation 2.12 over the entire condenser [95, Ch. G1]. Here, ζ is the dimensionless friction coefficient, ρ is the average density of the gas flow [kg/m^3] and v is the flow velocity [m/s].

$$\Delta P = \zeta \frac{L}{d} \frac{1}{2} \rho v^2 \quad (2.10)$$

$$Re < 2300 \quad \zeta = \frac{64}{Re} \quad (2.11)$$

$$Re > 2300 \quad \zeta = \frac{0.3164}{Re^{\frac{1}{4}}} \quad (2.12)$$

The next section will present and discuss the results from the model calculations, based on the above discussed relations.

2.2.3. Condensation model results

The solution of the model as described in the previous section can be found in Figure 2.5, based on the process conditions of the RGP. It is immediately visible that at small diameters the required condenser length (L_{req} , for "nom", the nominal case) decreases but the pressure drop (ΔP) increases largely. This large pressure drop is caused by the implausible flow speeds occurring in the channel (~ 160 m/s, see Figure 2.5b). At the earlier assumed 5 mm minimum diameter the predicted flow speed is circa 6 m/s. With increasing channel diameter the effective flow velocity decreases and hence also the Reynolds number. The sudden change around 13.5 mm is caused by the change from turbulent to transient flow; similarly, the drop around 24 mm is caused by the transition from transient to laminar flow. Both these phenomena are caused by the step-wise implementation of Equation 2.7 and Equation 2.9. To substantiate: at 24 mm channel diameter the flow reaches a (transition) Reynolds number of 2300, whereas at 13.5 mm the flow reaches a (transition) Reynolds number of 4000.

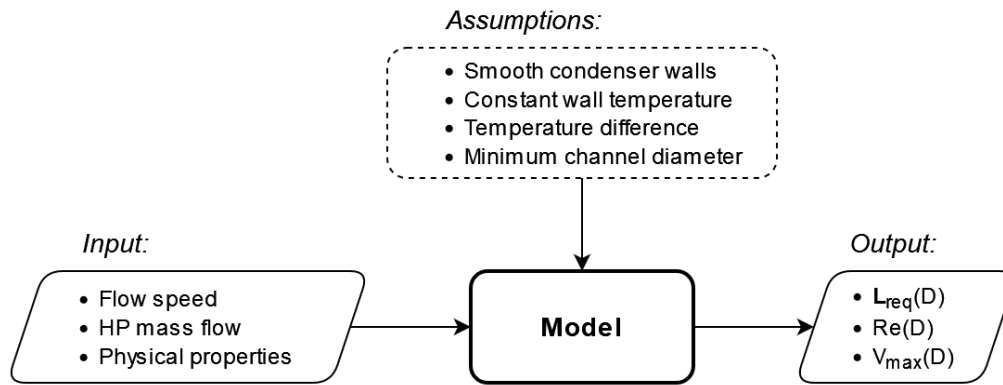


Figure 2.4: Schematic representation of the condensation model, indicating the inputs, outputs and assumptions.

As a sensitivity analysis, also included are the results given the situation that the flow rate is five times higher ("5x") than initially assumed, corresponding to a 2.2 times higher flow velocity. The transition from turbulent to transient is then postponed to large duct diameters (not shown here), which is in line with reality: since the flow speed is higher, the duct must be larger to reduce the speed and thus bring the flow in the transition regime. Furthermore, from the sensitivity analysis it can be deduced that the pressure drop behaves as expected: for a higher flow rate, the pressure surge with decreasing channel diameter starts at a larger channel diameter, thus showing behavior according to Equation 2.12. Yet, although Gnielinski does not state limits on the valid Reynolds numbers [95], it can be assumed that his relations for the turbulent regime are not valid at the large Reynolds numbers shown here. Therefore the actual pressure drop at small diameters and high flow rates may be different in reality. However, since other factors are more influential in determining the minimum channel diameter, no further efforts were spent in refining the pressure drop results for small diameters and high flow rates. More detailed plots omitting the behavior below 5 mm can be found in Figure E-1.

From the here presented results and the earlier discussion it is clear that the final design diameter should be chosen as small as possible, i.e. 5 mm; the associated pressure drop and required condenser length are 70 Pa and 0.51 m, respectively.

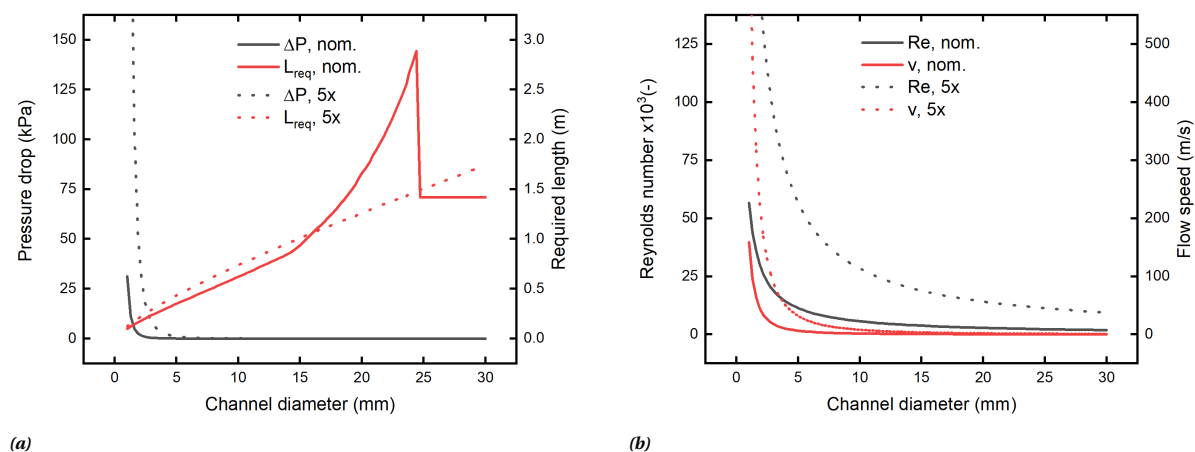
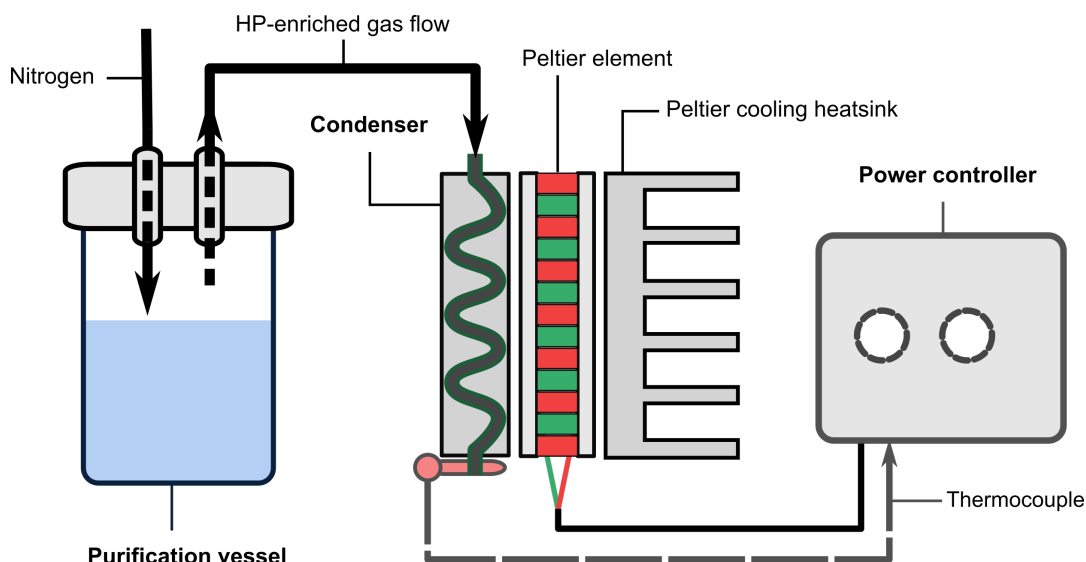


Figure 2.5: Results of model calculations for both the nominal case ("nom") and the sensitivity analysis, with a five times higher flow rate ("5x"). a) Figure showing the predicted pressure drop (ΔP) over the condenser and minimally required condenser length (L_{req}). b) Figure showing the predicted Reynolds number (Re) and occurring flow speed (v) in the condenser.

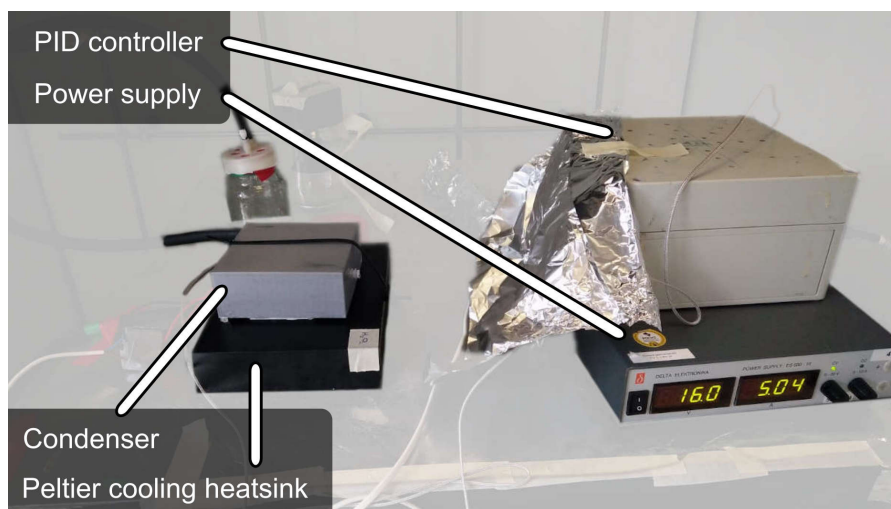
2.3. Experimental setup

The section shortly describes the setup (see Figure 2.6) of the experiments used to investigate different recuperator concepts. The HP-enriched vapor was produced in a glass vessel containing HP, by impinging a nitrogen flow perpendicularly on the fluid surface, as can be seen in Figure 2.7a. The emanating flow, containing gaseous HP and water, was then fed into the tested condenser. The diameter of the transport tube was

chosen such that the gas flow would be less than 25% of that in the nitrogen supply line to minimize gas leakage. As has already been introduced above, during these experiments, primarily due to the exploratory nature of this research, use has been made of extruded heatsinks to serve as condensers. An example of a heatsink as used in these experiments can be seen in Figure 2.7b. These heatsinks were closed off with 3D-printed caps, placed on top to guide the flow along all individual cooling blades. The heat would be removed from the condenser using Peltier elements, connected to a PID power controller, which measured the temperature inside the condenser using a thermocouple. The heat was discharged from the Peltier elements through large aluminum heatsinks that were submerged in ice to maximize cooling efficiency. After the experiments the condensers would be disassembled and the concentration of the condensate would be determined using a refractometer, as can be seen in Figure 2.8.



(a)



(b)

Figure 2.6: Basic testing setup for the condensation experiments. a) Schematic representation indicating all elements. The flow leaves the purification vessel and is fed into the heatsink condenser. The Peltier elements are controlled based on the temperature in the condenser, which is measured using a thermocouple. b) Test setup with relevant parts indicated. Visible behind the condenser is the purification vessel. Clearly noticeable is the aluminum foil used to protect sensitive surfaces.

2.3.1. Calibration efforts

In this research three main instruments have been used: thermometers, a refractometer (to determine the HP concentration) and a scale. As is clearly visible in Figure 2.10a, two thermometers have been used. One thermocouple was attached to the power controller, while the other was attached to a handheld digital ther-

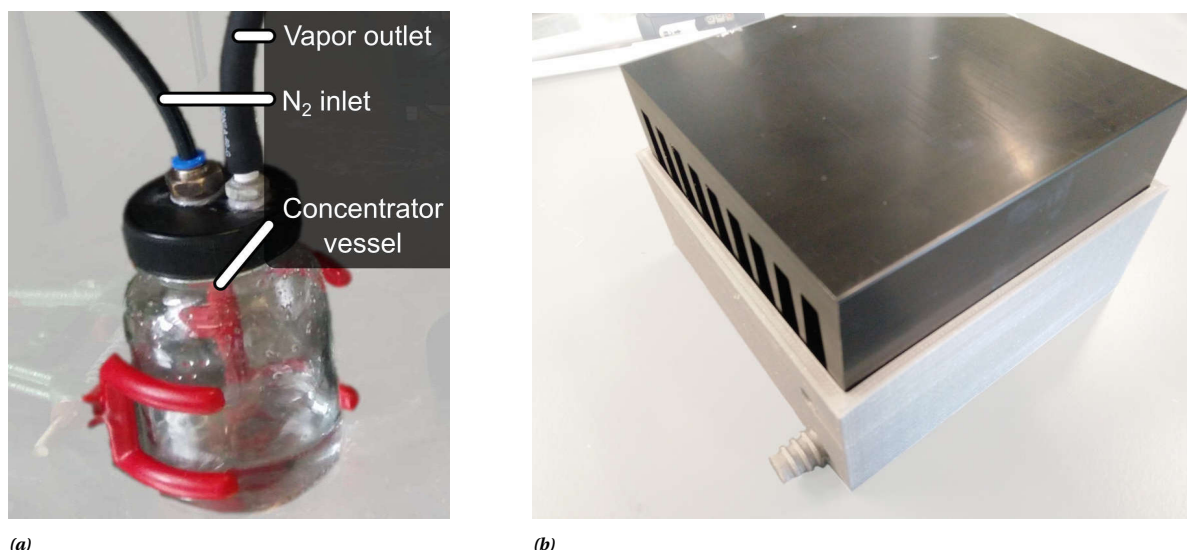


Figure 2.7: Individual parts as used in the test setup for the condensation experiments. a) Condenser heatsink as used during the experiments. The outflow location can be clearly seen (bottom left). b) Simulative purification vessel as used during the experiments, based on the design of the RGP.



Figure 2.8: Refractometer used during all experiments in this research. The inset shows a typical reading in brix-%.

momometer unit. The description of the calibration efforts of all these instruments can be found in [section D.2](#).

After the research had been completed, a calibrated mass flow controller was purchased; this controller showed that the flow rates as determined with the anemometer were in fact five times higher. This large factor can be explained considering that the gas would emanate from a small tube (3.5 mm inner diameter), while the anemometer is merely intended for undisturbed air flows, e.g. in a wind tunnel.

2.4. Recuperation experiments

As mentioned earlier, due to the high manufacturing cost of a custom made aluminum condenser, most experiments were conducted with aluminum heatsinks, with different flow patterns. Since the geometry of these here tested condensers is substantially different from a simple tube condenser, from which most theoretical equations are deduced, these experiments did not provide enough evidence to verify the model itself. Yet, evidence was supplied in favor of both the assumption of constant wall temperature (ASP-CND-BC-2) and two-stage condensation (ASP-CND-VAP-1).

2.4.1. Heatsink-based recuperators

For the first set of experiments, the flow guides were designed such that the flow would travel in a zigzag motion through the whole condenser (serial flow, [subsection 2.4.1.1](#)). Later experiments were set up such that the flow would be divided between the heatsink channels, as described in [subsection 2.4.1.2](#).

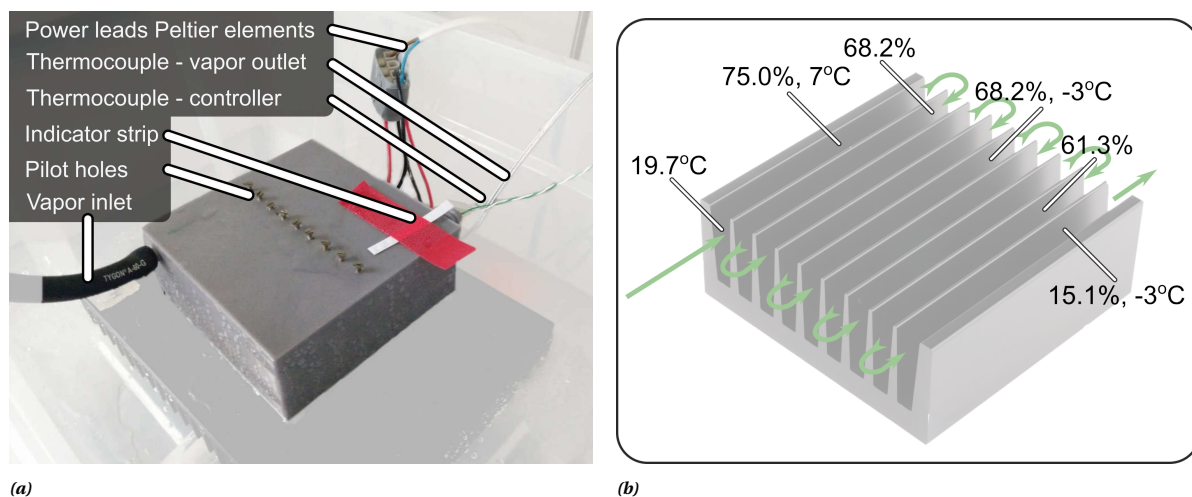


Figure 2.9: Setup and results of condenser experiments using a 100 x 100 mm heatsinks. a) The heatsink used in the experiments, featuring pilot holes. All relevant parts have been indicated. The indicator strip is sensitive to HP and hence can detect its presence in the condenser outflow. b) Results from condensation using a 100 x 100 mm heatsink. The green arrows indicate the flow direction through the heatsink. At various locations the flow temperature was measured. At spots where sufficient fluid had condensed, concentrations could be determined. The results clearly show that the concentration of the condensed HP decreases towards the exit and that the second half of the condenser is at the same temperature.

2.4.1.1. Serial flow condenser

Several design iterations were performed before a working recuperator could be tested; early iterations suffered from i.a. limited sealing capability due to manufacturing tolerances.

The third major iteration was based on a 100 x 100 mm heatsink, which featured channels with a hydrodynamic diameter of 30 mm and total channel length of 0.9 m. When this is compared to Figure 2.5a, it is clear that this setup gives a total condenser length more than one third lower than required for this channel diameter (1.42 m); it was thus expected that condensation would be suboptimal. Further, this iteration included improved tube fittings, so that the pressure drop over the recuperator entrance would be less and gas leakage was largely eliminated. This design was further improved by sealing of the recuperator with silicone sealant, and the placement of a thermocouple (attached to the PID controller) near the gas flow condenser exit. With the PID controller the flow could now be kept at an almost constant temperature. Initial testing only utilized two Peltier cooling elements, but it quickly appeared that more cooling power was required, due to the slow equilibration time of the system around the set value. Also a large temperature difference ($\pm 7^\circ\text{C}$) was visible between the gas outlet and the location of the thermocouple, despite their small separation. This difference might be explained by the location of the thermocouple (on the top, instead of near the base of the condenser); atmospheric heat may thus have influenced the thermal readings. Unfortunately the location of the thermocouple could not be changed due to physical limitations. Another major issue was that the condensed phase could not be accessed inside the condenser. Thereto pilot holes were drilled in the top casing and closed off with bolts, as can be seen in Figure 2.9a.

In the experiment 60 g of HP was concentrated from 79.5 to 87.2% and the emanating vapors were condensed inside the discussed condenser. After the experiment concentrations of the condensate were determined as visible in Figure 2.9b. Unfortunately not all channels could be sampled due to the limited amount of condensed liquid, but still a clear trend can be seen in Figure 2.9b: the concentrations of HP decrease towards the end of the condenser. The first channel showed a lower HP concentration (75%) when compared to the bulk liquid, whereas the channels towards the end of the condenser showed even lower concentrations.

Counter-intuitively, the relatively low concentrations in the condensed liquid (as compared to those in the purification vessel) can be explained as proper functioning of the recuperator. Namely, it should be considered that the vapor concentration above the liquid is not equal to the liquid concentration itself (as displayed in Figure 2.3). In this case (with a concentration in the purification vessel increasing from 79.5 to 87.2%), the emanating vapor increases in HP concentration from 34.0% to 48.5%. The fact that the concentrations as measured in the condenser are much higher indicates that the HP in the exhaust vapor is more inclined to condense than the water. The lower concentrations towards the end of the recuperator then indicate that most HP had been condensed out of the vapor. Though, as was mentioned above, the actual length of the

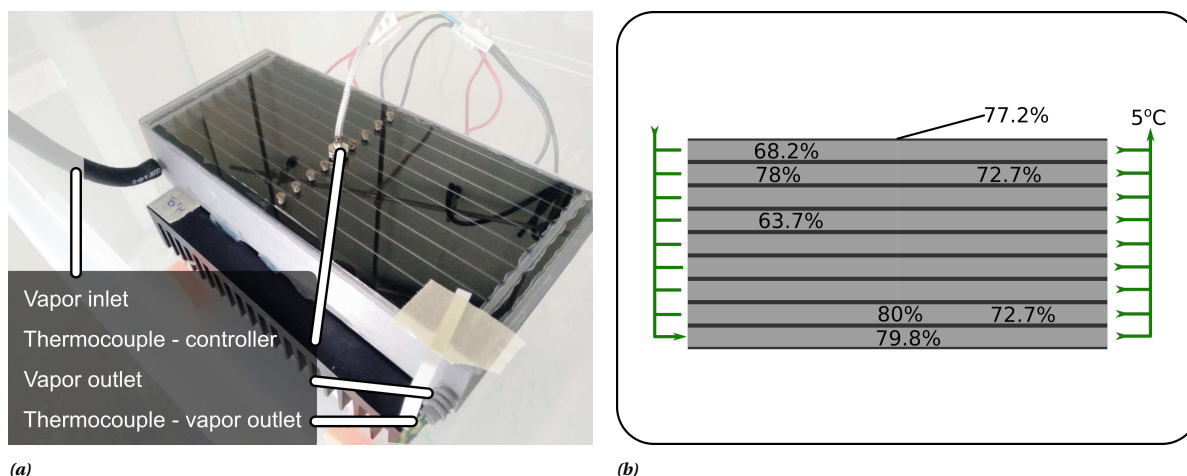


Figure 2.10: Setup and results of the condenser experiments using two 100 x 100 mm heatsinks, thus effectively having nine parallel 200 mm long channels. a) Condenser setup with transparent cap. b) Schematic top view of the parallel condenser setup; the arrows indicate the flow direction. At spots where sufficient fluid had condensed, concentrations could be determined as indicated in the figure. The temperature was determined at the outlet to be 5°C.

condenser was lower than predicted by the theoretical model, thus it was expected that condensation would be suboptimal. In that light it is remarkable that in the last compartment only low concentration HP (15.1%, σ_s 6.2%, $n = 4$) had condensed, whereas one would expect higher concentration HP. Alternatively, the low concentrations at the end might be the result of inflow of cooling water from the Peltier cooling side. It should be considered here that only a small part of all evaporated HP was recovered; this is attributed to gas leakage at tube connections and in the condenser.

Furthermore, Figure 2.9b also shows the temperature distribution over the recuperator, which due to insufficient means had not been measured at all locations. It is clear that the assumption of constant temperature is not strictly true, although the temperature rapidly decreases from around 20°C to 7°C (within 50 mm in the first channel), after which the temperature remains constant over the last half of the condenser.

2.4.1.2. Parallel flow condenser

The former test clearly showed that the highest concentration of HP was collected in the first segment of the condenser. In order to investigate whether this phenomenon could be exploited to enable recuperation of merely high concentration HP, it was chosen to utilize a parallel flow setup. Because of the distribution of the flow over nine channels, the flow rate per channel decreased with 89%. According to the model (see Figure E-2) the required length for each channel would still be 0.87 m, whereas the actual length of each channel is only 0.2 m. Because of this, it was expected that only a small amount of high concentration HP would condense. Further, it was chosen to glue a transparent top onto the plastic flow guides. This would enable visual monitoring of the condensation process, and additionally aid in recovery of trapped HP by simply removing the top cap, as can be seen in Figure 2.10a.

The parallel condenser setup was tested while concentrating 165 g of 81.7% HP to 87%. The experiment resulted in the collection of less than 1 mL of condensate; because of this, not enough liquid could be sampled inside the recuperator to draw definite conclusions with respect to its performance. The available data can be found in Figure 2.10b, which show that the majority of the sparse data seems to be in line with the expectations. Firstly, the measured concentrations seem to suggest that the vapor emanating from the purification vessel behaves as it should: HP condenses sooner than water, giving higher concentrations at the condenser entrance and lower concentrations near the exit. This experiment further adds to the earlier given evidence in favor of the two-stage condensation assumption (ASP-CND-VAP-1). Namely, when the concentrations measured in the recuperator (see Figure 2.10b) are compared with those in the vapor (38 to 41%), it is clear that the concentration of all condensate has a higher concentration (>60%). Remarkably, the data further show that most vapor condenses at the first two and last two channels, and almost nothing in the center. Perhaps this is caused by flow phenomena related to the inlet design; flow dynamics simulations need to be performed to elucidate these matters and result in an optimal design.

Secondly, as was predicted by the earlier discussed model results, it is clear that the condenser is too short to extract all HP from the waste stream. Conversely, this means that this condenser length only recovers high concentration HP. N.B. as was discussed in [subsection 2.2.1.2](#), it was chosen to postpone the design decision with regard to the extent of the two-stage condensation. Nevertheless, the here obtained results clearly indicate the effects of this design choice. A direct consequence of the relatively short condenser channel length is that the temperature had not reached the required exit value ($\Delta T = 20^\circ\text{C}$). That means that assumption ASP-CND-BC-2 is violated, and that results obtained from the model cannot be directly translated to this setup. For a further design stage it is thus recommended to either increase the cooling power or alter the model taking into account this discrepancy.

The limited amount of HP that was collected was predominantly caused by leakage, even though the recuperator had been properly tested for leakage before operation. An initial indication of this leakage was given by strong discoloration of the Peltier cooling heatsink. The liquid present on top of this cooling heatsink had a HP concentration below 30%, which was lower than could be expected based on the earlier presented results. This might have been caused by dilution with water surrounding the cooling heatsink. Alternatively, the paint of the heatsink had reacted with the HP, causing discoloration and a drop in concentration of the HP. This reactivity of the paint with HP was proven by application of a small amount of concentrated HP onto a pristine heatsink, as can be seen in [Figure 2.11](#). Immediately following the application bubbles started to form, indicating the decomposition of HP. After a few minutes, the entire exposed area was totally discolored.

A replication of the experiment did not result in larger amounts of condensate. During this experiment it was noticed that large amounts of vapor had condensed on the side of the enclosing plastic container: only little vapor had condensed inside the heatsink. Contrarily, the location where the exit flow impinged on the enclosing container featured high concentration (>65%) HP. This led to the development and testing of the setup as elaborated upon in the following section.

2.4.2. Direct impact condenser

Based on the aforementioned findings a new setup was constructed, where the flow impinged perpendicularly on a (one Peltier) cooled flat plate (see [Figure 2.12](#)), hence inducing high flow turbulence at the condenser surface. The concentrating of 120 g 84.9% HP to 90.6% (vapor: 44 to 55%) resulted in collection of several milliliters of 54.5% HP; drops on the condenser itself varied between 54.5 and 61.3%. These concentrations are lower than obtained with the heatsink-based setups, but are still slightly higher than the concentrations in the vapor phase. The difference with respect to earlier conducted experiments might be explained by almost complete condensation of the vapor due to the induced high turbulence, hence giving concentrations in the condensate similar to that in the vapor. The comparably low concentrations and large amounts might also be explained by the lack of atmospheric sealing, thus leading to atmospheric water condensation. To conclude, even though still only part of the HP from the waste stream is recuperated, the total amount of condensate is considerably higher than collected with the previous experiments. In order to strengthen these interesting findings more experiments should be conducted.

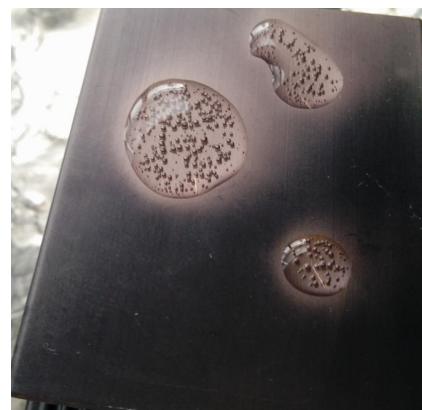


Figure 2.11: After application of concentrated HP onto a pristine heatsink, it immediately started to react, as can be seen from the bubble formation. The surfaces that had been in contact with HP have been permanently discolored.

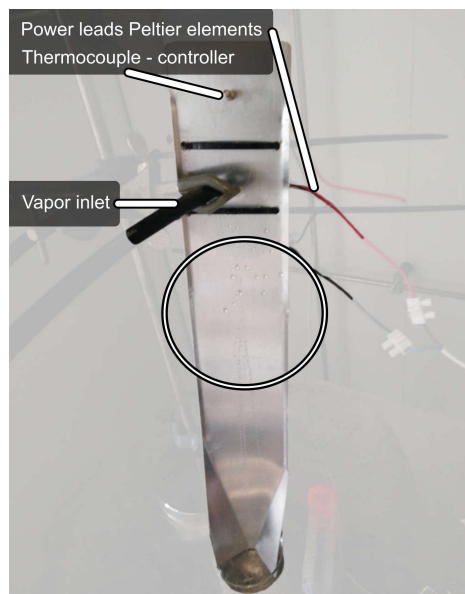


Figure 2.12: Direct impact condenser setup. Encircled are clearly visible condensate drops.

2.5. Conclusion

This chapter set out to increase the efficiency of the SolvGE HP purification process by recovering HP from the process' waste stream. The developed theoretical model relied heavily on the assumptions of constant temperature along the condenser and two-stage separation of water and HP. Experiments supplied evidence for validity of these assumptions in the case of serial flow. More research is necessary to fully prove these key model assumptions. Further, the model should be adapted for the use of parallel condensers that recover only high concentration HP, since it was proven that the constant wall temperature assumption is violated in this setup.

Since the design problem was more difficult than initially assumed, this work has not resulted in a final design solution. However, the experiments have proven the viability of using a solid state condenser to remove HP from the RGP outflow. Combined with the theoretical knowledge acquired in this work, the conducted research will aid SolvGE in the further development of their HP purification products.

Requirement REQ-CND-01 turned out to be too strictly formulated. Although HP and water can be separated to a large extent from the waste stream, recovered HP concentrations never reached 100%. Also the second requirement (REQ-CDN-02) cannot be fulfilled. Even though HP was condensed, this was only in small amounts: drops instead of tens of milliliters. Yet, this research showed that the direct impact condenser proved to be more efficient than the heatsink condenser; though, more research is required to substantiate these observations.

2.6. Recommendations

Further research is required to validate all assumptions that underlie the theoretical model. At this time, only a little evidence was collected that would support the validity of these assumptions. For later design stages, the model should be adapted to better model different flow phenomena that are related to condenser geometry. Especially the flow behavior at the inlets seems to play a vital role. In addition, the model should take into account the temperature gradient along the condenser, up until the point that the temperature remains constant. Furthermore, the model should allow the distinction between recuperating all HP and recuperating high concentration HP; as was shown, the latter requires a shorter condenser (or equivalently a lower heat dissipation).

Further, the optimal position for the power controller's thermocouple should be investigated. Here it was either placed at the outlet, leading to too severe cooling, or half-way in the condenser, which appeared to result in too little cooling. Additionally, the optimal operation conditions of the Peltier elements should be investigated, such that they dissipate the maximum amount of heat, while producing as little heat as possible.

More importantly, it is fundamental for future design iterations to decide whether all HP in the RGP outflow should be condensed, or that it is desired to recuperate HP at an as high as possible concentration. As was shown here, this decision has a large influence on the design of the condenser.

To conclude, the direct impact condenser concept should be further investigated. Even though the HP concentration of the condensate is not as high as with the heatsink-based condensers, the total volume is much higher and could be collected with lower power consumption. Here it was postulated that the lack of atmospheric sealing might have lead to dilution of the recuperated HP. Unfortunately, due to the lack of appropriate manufacturing equipment no closed direct impact recuperator could be fabricated at this time. Though, it is believed that a properly designed and manufactured direct impact condenser will result in the most efficient and economical condenser design.

3

Support effect on the decomposition of H_2O_2 over MnOx catalysts

This chapter will present the results of the research efforts directed at the development of a supported catalyst that can decompose high concentration hydrogen peroxide, and has the potential to induce hypergolicity in HP - ethanol mixtures. Supported decomposition catalysts for HP have been widely investigated, for instance in relation to the EU-wide GRASP project which investigated i.a. HP decomposition for space propulsion [5]. Catalytically induced hypergolicity has also been reported in literature, however only with dispersed catalysts which degrade over time. Due to the complexity of developing such a catalyst, this work merely focused on achieving decomposition of HP. The here presented combination of experimental research with extensive literature survey and elaborate spectroscopic measurements aims at answering the research questions as formulated below.

RQ-CAT-1 *What is the effect of the support on activity and stability of MnOx for H_2O_2 decomposition in drop-testing?*

RQ-CAT-1-1 *What is the nature of the active site of the catalyst?*

Motivation: As already introduced in [subsubsection 1.3.2.2](#), manganese-based catalysts are believed to operate via a catalytic cycle involving the IV and III oxidation state.

RQ-CAT-1-2 *What is the influence of the support material on the transition temperature of MnOx?*

Motivation: Can a proper selection of support material postpone the deactivation of MnOx into MnO? And does this also apply during drop-testing?

RQ-CAT-1-3 *What phenomena cause deactivation of the MnOx catalyst during drop-testing??*

Motivation: Knowledge of the deactivation phenomena can be utilized to enhance the catalyst.

RQ-CAT-2 *How can drop-testing be used for decomposition testing of HP over a supported catalyst?*

Motivation: Drop-testing has found wide use in the investigation of hypergolic propellants, and has been used to investigate induced hypergolicity for HP. Yet, no records in literature can be found that have used drop-testing for either decomposition testing or the evaluation of supported catalysts. It is important to investigate whether the catalyst body can withstand the repeated fast heating-cooling cycles.

RQ-CAT-3 *Is the decomposition of HP over the catalyst vigorous enough to induce hypergolicity?*

Motivation: The objective of this research is to develop a catalyst that can induce hypergolicity. Thereto a highly reactive catalyst is required that releases enough energy from HP decomposition to ignite ethanol.

The starting point of this investigation was formed by the manganese oxide on yttrium-doped zirconia catalyst as developed by Russo Sorge's research group [7–9]. Its poor stability during drop-testing led to the preparation of several MnOx bulk catalysts, based on the work by Wu and coworkers [129]. Hence, different support materials were successfully tested for their ability to stabilize and promote the reactivity of MnOx with concentrated HP in drop-testing. This chapter will first supply a short background on several concepts fundamental in this investigation. This is followed by a description of the experimental setup, and an elaborate discussion of the obtained results.

3.1. Background

This section will supply an extensive background on some of the key aspects in the development of a decomposition catalyst for HP, in addition to the concise theory that has been supplied earlier. First, [subsection 3.1.1](#) will shortly touch upon the harsh environment to which the catalyst is exposed, and what effects this could have on the catalyst. Then, [subsection 3.1.2](#) will elaborate on one of the key requirements of catalytic decomposition systems, the decomposition delay. Since directed design iterations require a thorough knowledge of the used catalyst preparation processes, [subsection 3.1.4](#) and [subsection 3.1.5](#) will scrutinize the synthesis methods used in this realm of this research. Finally, the requirements that serve to aid in selection of a proper catalyst will be posed and briefly discussed.

3.1.1. Catalyst operation conditions

Since the catalyst as designed here should ultimately induce hypergolicity, the related operating conditions should be considered already at this stage of the development. The first challenge in the design of this catalyst is the thermal environment as manifested in the combustion chamber. Namely, temperatures during decomposition of HP can reach 954°C (for 98% HP [27]), whereas during combustion with ethanol temperatures can reach over 2000°C (under stoichiometric conditions [83]; under lean operation temperatures will drop while performance only slightly decreases). Further, it is important to note that this gas environment is mainly composed of oxygen and ethanol: a mixture that is both strongly reducing and oxidizing simultaneously. Obviously, this will put high stress on the catalyst materials; most catalysts will be rapidly deactivated in such an atmosphere. The catalyst as is the subject of this research should not degrade noticeably under these circumstances. This represents a large challenge from a chemical perspective: very few catalysts are used in temperatures above 800°C , and thus little knowledge is available of catalysts exposed to such conditions.

The large temperature fluctuations form another major challenge: virtually all catalysts that operate at such high temperatures are operated under constant conditions to prevent the disastrous effects of temperature shocks. The relevance of these thermal shocks becomes clear when the operation of the engine is considered. Namely, many rocket motors (especially when intended for orbit corrections et cetera) are often operated in pulsed mode; this enables simpler engine design as throttling is carried out by varying the amount of pulses instead of throttling the flow [1, 117]. Consequently, multiple times per second both the temperature and pressure sharply increase, resulting in heating rates within the combustion chamber (and thus also within the catalyst) of 200 to $300^\circ\text{C}/\text{s}$ [42, 108].

3.1.2. Decomposition delay

A very important parameter in the design of a combustion system is the ignition delay (ID). The ID is measured as the delay between contact of fuel and oxidizer until the moment of ignition or the attainment of combustion [73, 86]. Equivalently, for engines relying on propellant decomposition a decomposition delay (DD) can be defined. In the current discussion, the DD is defined as the period from the moment of contact between propellant and catalyst up until attainment of steady-state decomposition. It should be noted that little investigations in propellant decomposition have been published that focus on the evaluation of such operational parameters. Even more, the term ID is often erroneously used to indicate the DD [1]. The following discussion is therefore based on the literature available on hypergolicity, and thus on the ID. Though, the same concepts apply to the design of decomposition catalysts.

Unfortunately, prediction of DD values is difficult, due to the large number of parameters involved, ranging from ambient temperature to viscosities (both of the liquid and gas phase, which are also dependent on temperature). In addition, the introduction of a supported catalyst further complicates prediction of the DD values [52]. Aspects known to have a decreasing effect on the DD of HP decomposition are e.g. the concentration of HP and the dispersion of the catalytic phase [55, 73]. Dismally, due to the large number of factors involved, DD values still have to be determined experimentally. This also applies to the ID in hypergollants; these ID values are still commonly determined using drop-testing (please refer to [subsection 3.2.3](#)), even though the obtained results are not representative of real-world performance [23]. Due to the widespread use of drop-testing in hypergolicity research, it will be used here to determine DD values for supported catalysts. Though, it should be noted that no record in literature can be found on the usage of drop-testing to test the decomposition behavior of supported catalysts.

Knowledge of these delay values is fundamental in engine design. Namely, for rocket motors the DD determines to a large extent the dimensions (especially the length) of the combustion chamber [117]. A larger combustion chamber results in a higher total system mass which is undesired; thereto it is aimed to decrease

the DD as much as possible. Furthermore, accurate knowledge of the DD (and its spread) is essential for safe operation of the engine: if the DD is larger than the motor is designed for, reactive gasses will accumulate in the combustion chamber, which can lead to catastrophic failure by a sudden pressure spike [35]. Conversely, a too short DD results in cooling down of the exhaust gasses in the aft part of the combustion chamber (before the nozzle), thereby wasting part of the propellant's energy. Lastly, the DD is also important from an operational point of view. Since the future application of a HP-ethanol motor is primarily in orbital maneuvers and maintenance, a short DD (and corresponding ID) is important to ensure high precision in the delivered impulse [1]. To illustrate, a commonly used guideline is a maximum *ignition delay* of 100 ms. This is believed to satisfy most requirements in rocket motor design [6, 42, 108].

The total decomposition delay can be divided in two parts: a physical delay and a chemical delay. The physical delay comprises injection, atomization, evaporation, spreading of the propellant over the catalyst and heating of the propellant to the activation temperature, if applicable. It should be noted that the definition as will be used in this experimental context slightly differs from the generally used definition; in the experiments conducted here no closed reactor was used. Instead, here the physical delay is defined as the time between droplet impact on the catalyst up until the moment that evaporation is completed. The chemical delay is then defined as the delay from the attainment of the conditions required for the decomposition reaction until the overall attainment of decomposition. That is, the chemical decomposition delay can be used to assess how fast the heat liberated by the reaction of the first few molecules can be absorbed by the remaining propellant to escalate into full decomposition [36, 52, 86]. Hence, it can be understood that the physical delay is usually longer than the chemical delay [36], especially at engine start-up when the system is relatively cold. In that situation, more energy needs to be supplied to heat and evaporate the propellants. To reduce the start-up time of the engine (and thus the DD), the liquid phase reactivity of the catalyst with HP should be high. It is worth noting that for evaporation and heating of the propellants energy is required, so that strictly speaking the physical and chemical delay are convoluted. Stated in the realm of this research: decomposition heat is necessary to start decomposition, while decomposition heat is required to sustain decomposition. Therefore precise determination of either of these is ambiguous; only the overall decomposition delay can be determined with certainty.

3.1.3. Requirements

In order to judge the scientific and practical value of the developed catalyst, several requirements on its performance were formulated, which can be found below.

- REQ-CAT-1** The catalyst shall induce decomposition in 87% HP in the liquid phase during drop-testing.
- REQ-CAT-2** The measured maximum catalytic decomposition temperature of 98% HP during drop-testing shall be above 369°C.
- REQ-CAT-3** The catalyst shall endure at least 200 decomposition cycles before the maximum measured decomposition temperature drops below 50°C during drop-testing with 87% HP.
- REQ-CAT-4** The measured decomposition delay shall be below 200 ms in drop-testing with 87% HP.

It is easily understood that the reactivity of a catalyst is higher when the reactants are in the vapor phase, where the molecules are finely dispersed and no additional energy is required for evaporation. Yet, as has been mentioned in the proceedings, the developed catalyst should also function well under cold-start conditions, where the reactants are in the liquid phase and at relatively low temperature. More energy, or a more efficient catalyst, is required under these circumstances to initiate decomposition. Hence, the cold-start phase is the main design driver in HP decomposition catalyst development. Drop-testing then replicates this cold-start behavior when the delay between incoming drops is chosen, so that the catalyst has sufficient time to cool down to the initial temperature. Further, the catalyst should perform well with the required concentration of HP; a lower concentration will result in a less intense reaction due to the higher water content (which needs to evaporate during the decomposition). These considerations are all captured in requirement REQ-CAT-1.

The ultimate aim of this research is to produce a catalyst that can induce hypergolicity in HP - ethanol mixtures. Therefore, the decomposition catalyst should be able to decompose HP with such vigor, that the released heat is sufficient to evaporate and ignite ethanol (REQ-CAT-2). A simple criterion to judge whether this is possible, is if the temperature during decomposition reaches the autoignition temperature of ethanol (369°C [16]). Even though this does not prove that the catalyst is able to induce hypergolicity, it can at least serve as a preliminary assessment of this ability. In this early stage it is merely desired to prove that the catalyst

itself is able to deliver this performance. It is therefore chosen to evaluate this criterion using 98% HP; later design stages may show that lower concentration HP can also suffice.

The third catalyst demand (REQ-CAT-3) puts a minimum on the lifetime before deactivation occurs. Especially in a space environment where no maintenance is possible, the lifetime of the catalyst should be high enough to operate during an entire mission. Drop-testing can give an indication of this lifetime by replicating repetitive cold-starts, which usually put large stress on the catalyst. The maximum temperature attained during decomposition is used as a criterion to evaluate the extent of catalyst deactivation. At this point, the threshold value is considered too lenient for future practical applications, even more so since deactivation is an advancing process. Thus, already before the required number of cycles is achieved, the catalyst will most likely have deteriorated too much to still induce hypergolicity. Nevertheless, concerning the early stage of development this limiting value is deemed appropriate.

Finally, a requirement is put on the time from the moment of contact between catalyst and propellant, and the attainment of steady-state decomposition. Requirement REQ-CAT-4 sets a maximum acceptable delay for this phenomenon. As was elaborately discussed above, this value is a pivotal parameter in rocket motor design. It should be noted that the threshold value here is considerably larger than is deemed acceptable for a functioning attitude control thruster. Yet, this value can be justified by considering the large discrepancies between the testing setup and an actual rocket motor.

3.1.4. Solid state synthesis of bulk catalysts

Bulk catalysts are commonly synthesized using wet synthesis methods, such as co-precipitation or sol-gel synthesis. In co-precipitation the precursors are dissolved in water and by changing their solubility (e.g. by pH increase) they precipitate out of the solution, as used by e.g. Bulavchenko et al. for the preparation of manganese oxide catalysts [12]. An excellent overview of sol-gel synthesis is given by Danks et al. [21]. A prominent advantage of wet synthesis methods is that the precursors are mixed on an atomic level, which results in high dispersion of the active phase and intimate contact with the support material. A direct consequence hereof is that the interaction of the active phase precursor with the support material is often brought about relatively facile (i.e. already at a low calcination temperature). Yet, the simplicity of this process is deceiving: many factors have an influence on the final product, such as choice of precursor, gelling agents (for sol-gel), level of cleanliness et cetera. A successful synthesis is thus not guaranteed, and the adaption of process conditions to change the properties of the catalyst is often not straightforward [21]. Furthermore, often metal nitrates (e.g. [12]) or alkoxides (e.g. [4, 114]) are used, which are not only toxic and dangerous, but often also expensive.

In solid state synthesis (SSS) the precursors are usually metal oxides which are neither toxic nor expensive. Yet, due to the stability of the oxides their reactivity is low. In addition, the precursors are separated in large clusters (crystals). And, since the reactants are in the solid state throughout the reaction, diffusion is very limited, which hampers the establishment of their mutual interactions. Therefore often high temperatures are required to increase the mobility of the ions in the reaction mixture and hence facilitate the reaction between the precursors. These high temperatures do not only induce high costs related to synthesis, but also can result in the formation of inactive compounds or crystal phases [25].

There are several solutions to this problem. A first possibility is to use pretreat the precursors with highly energetic impacts to enforce solid-state diffusion in a small volume. These impacts can be brought about under atmospheric conditions for instance by using a ball mill [29, 72, 90]. This leads to a prominent decrease in the calcination temperature [3, 40], which mitigates the major disadvantage of conventional SSS. Yet, as stressed by Dulian, proper choice of milling parameters is difficult, but essential to achieve success [29].

Less involved is the addition of a dispersant, which acts as a shielding cocoon around a small cluster of precursors. Hence sintering is hampered and the interaction between different precursors is promoted [62, 129]. This can be carried out by mixing the precursors and a proper dispersant with an inert solvent. Ultrasonication can then be used to break up larger clusters into smaller ones, which causes the desired intimate contact between the reactants. It can be understood that similarly as for ball milling this has a beneficial effect on the final synthesis temperature.

3.1.5. SSS of supported manganese oxide catalysts

For MnOx catalysts that rely on the Mn(IV) or Mn(III) oxidation state, it is counter-intuitive to utilize SSS, because of their (commonly believed) relatively low transition temperature to MnO. Yet, by proper choice of the supporting oxide material, this oxidation state change can be postponed to considerably higher temperatures (see e.g. [11]). Though, as was mentioned above, the preparation of a bulk catalyst can result in the formation

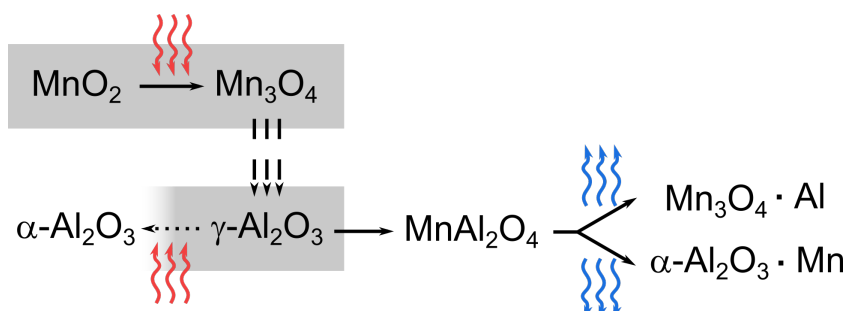


Figure 3.1: Simplified mechanism of the phase-mixing of Mn_3O_4 and Al_2O_3 . The boxes separate the different species. Three dashed arrows indicate migration of atoms. Dotted arrows indicate unfavorable transitions.

of (undesired) compounds. For instance, when calcining a mixture of MnO_2 and γ -alumina a mixed phase arises; it turns out that these display excellent catalytic performance, a.o. in CO oxidation [12, 119] and peroxysulfate decomposition, a chemical analog of H_2O_2 [129]. In addition, these mixed-phase catalysts display high mechanical rigidity. The high thermal stability of this mixed phase would make it attractive to use in a HP-based rocket motor.

These alumina-manganese mixed-phase compounds have attracted interest over the years, with researchers studying the effect of calcination temperature on reactivity [12] and on the occurring phase transformations [11, 17, 122, 122]. It turns out that the transition of MnO_2 into Mn_3O_4 (hausmannite, a mixed valence compound, with average charge $2\frac{2}{3}^+$) is essential for the formation of this mixed compound. Normally, hausmannite forms when manganese dioxide is heated to temperatures above $400^\circ C$. The formation of the mixed phase, as illustrated in Figure 3.1, is thought to be dependent on the both isomorphous and isothermal phase transitions of γ - Al_2O_3 and Mn_3O_4 . During these phase transitions, atoms from both oxides are moving around and can end up in the "wrong" crystal, ultimately forming only one mixed equilibrium phase. Yet, presumably due to the difference in average charge between the aluminum and manganese ions, the mixed oxide disintegrates upon cooling in air, forming one phase consisting predominantly of alumina (>85%, depending on the Mn-content) and one which is mainly composed of Mn_3O_4 . The presence of a small amount of the other metal leads to an "incorrect" average valency, which results in loosely bound oxygen atoms that are believed to be responsible for the measured enhanced catalytic activity. Besides, the addition of a fraction of manganese oxide also results in a lowering of the phase transition temperature of several metal oxides, for instance for the transition of γ - to α -alumina [17, 129].

This phase-mixing behavior also occurs for other support materials, such as titania [114] and zirconia [10]. Similarly as for γ - Al_2O_3 , the presence of $MnOx$ here leads to a decreased phase transition temperature. In addition, the resulting mixed oxides show enhanced catalytic activity. It is important to note that in the here presented research yttria-stabilized zirconia was used. The addition of yttria is known to prevent the phase transition of zirconia, thus, no simultaneous phase transition of $MnOx$ and YSZ takes place. This may have an effect on the incorporation of manganese in the zirconia lattice.

Since the phase transitions in these materials have been shown to occur already at lower temperatures, it is not certain how this phase-mixing effect will apply to the catalysts synthesized in this research due to the here used calcination conditions. Furthermore, assuming that this phase-mixing takes place, it is unknown how stable the resulting phases will be at the operation temperatures of a HP engine. To the best knowledge of the authors, no previous research has been performed on the catalytic activity in HP decomposition of these manganese-based catalysts. This research thus hopes to add to the body of science by investigating these catalysts in the decomposition of HP.

3.2. Experimental

This section will start by elaborating upon the synthesis of the catalysts in this research, which is followed by a short description of the employed characterization techniques. Then, the experimental setup as used during the activity measurements is introduced. Lastly, the calibration and data analysis efforts will be shortly touched upon.

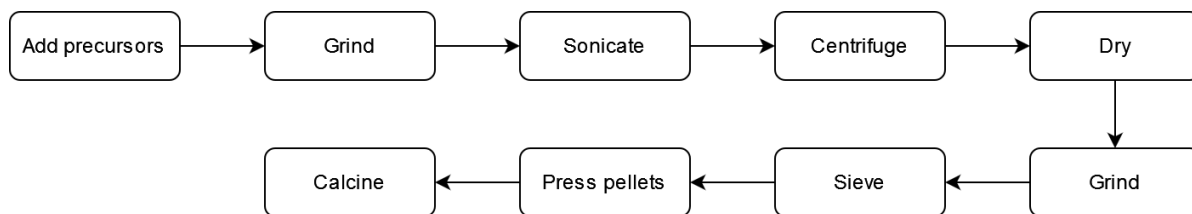


Figure 3.2: Schematic representation of the synthesis procedure of the cercaps.

3.2.1. Catalyst preparation

The manganese-based ceramic catalyst pellets (cercaps) in this research have been synthesized based on the work by Wu and coworkers [129]. Accordingly, cercaps based on different metal oxides were synthesized as illustrated in Figure 3.2, i.e. titania (TiO_2), γ -alumina ($\gamma\text{-Al}_2\text{O}_3$), magnesium spinel (MgAl_2O_4), silica (SiO_2), kaolin ($\text{Al}_2\text{Si}_2\text{O}_5(\text{OH})_4$, known as porcelain clay), and YSZ. Appropriate amounts of these materials were mixed with 1.5 wt.% MnO_2 , 1.5 wt.% glycerol and 1.0 wt.% PVA (all Sigma Aldrich, 99%). For the alumina-based cercaps, also 0.30 wt.% MnO_2 samples were prepared in a similar fashion. All the precursors were first ground in a mortar, after which to each an equal mass of water was added; subsequently the samples were sonicated for 30 minutes and dried overnight at 80°C . Then, the undissolved PVA was sieved out and the samples were all ground to a fine powder using a mortar, and pressed into pellets with 620 MPa pressure. Release of the pellets was troublesome and was achieved using carefully applied mechanic shocks. Afterwards the pellets were first dried at 80°C for two hours prior to firing at 1050°C for 6 hours, with heating and cooling rates of 5°C per minute.

3.2.2. Catalyst characterization

Both the origins of the catalysts' activity and possible deactivation effects were scrutinized using different non-destructive analysis techniques. Heavily was relied on X-ray diffraction (XRD, Bruker D8 phaser, using $\text{CuK}\alpha$ radiation, operated at 40mA, 40kV) to characterize crystal phases. All catalysts were scanned from 15 to $90^\circ 2\theta$ in 0.025° intervals with 0.4 s integration time. Further, scanning electron microscopy (SEM, Thermo Fisher Phenom ProX, 15 kV) was conducted to observe topological variations. The integrated energy-dispersive X-ray spectrometer (EDX) was used to show the elemental dispersion on the catalyst surface. Raman spectra were recorded at 785 nm (unless noted otherwise) using a Renishaw inVia confocal Raman microscope, with a 50x Leica objective. Raman shifts were recorded from 120 to 2000 cm^{-1} with 90 s total acquisition time at 5% laser power. Total diffuse reflectance spectra (TDR spectra, or TDRS) were recorded with a Perkin Elmer Lambda 950S spectrophotometer, equipped with InGaAs integrating sphere. This was used to capture all reflected light, i.e. both diffuse and specular, to maximize signal intensity. TDR spectra were recorded from 320 to 1200 nm with 2 nm resolution (0.2 s integration time).

3.2.3. Activity measurements

Drop-testing is an established method to determine whether certain propellant combinations display hypergolicity. As mentioned earlier, it is also often used to measure ID values; however, due to the large number of variables (e.g. drop volume, impact speed, temperature) these values only offer limited practical value in engine design [56]. One of the most prominent causes is that in drop-testing the propellants exist most of the time in the liquid phase, which limits diffusion speeds and thus impedes propellant mixing and hence hampers ignition [18, 23, 52]. Thus, IDs measured using drop-testing will most likely be noticeably larger than in a real engine. Besides investigation of hypergolicity, drop-testing can potentially be used to investigate the decomposition of HP over heterogeneous catalysts, as was done in this research. Drop-testing can hence serve as a quick tool to determine the activity and deactivation of a catalyst in a controlled environment. In addition with accurate temperature measurements a prediction can be given of a catalyst's potential to induce hypergolicity. Since the activity of the catalyst is correlated to the decomposition temperature, monitoring of the temperature evolution during the drop-testing can give an indication of catalyst lifetime.

3.2.3.1. Safety precautions

Strict precautions were required, since strongly oxidizing chemicals (H_2O_2) pose high risk of undesired decomposition or even ignition. Decomposition can be triggered with catalytic metal contaminants and catalysts. This necessitated working exclusively with compatible materials, such as aluminum, stainless steel,

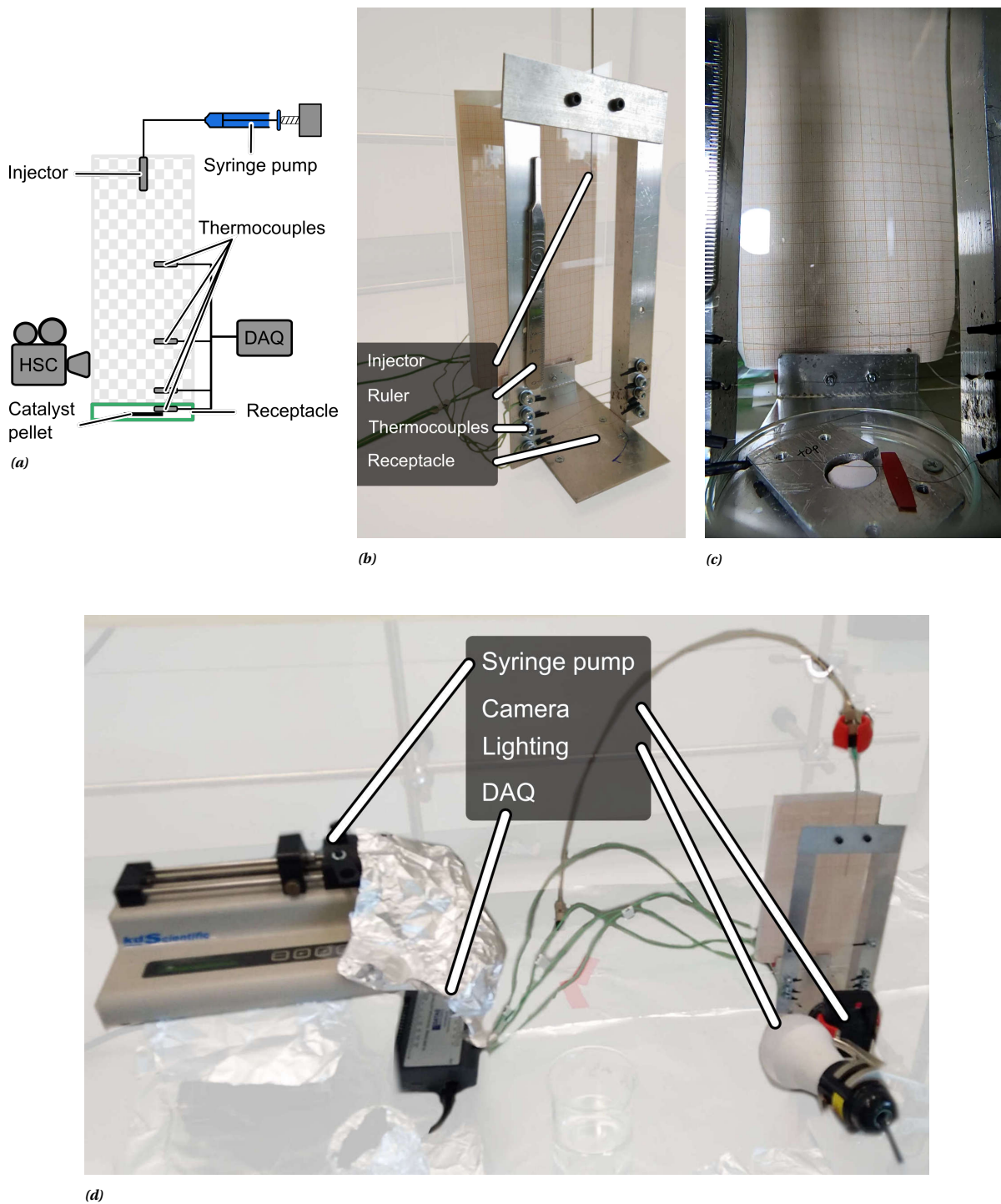


Figure 3.3: a) Schematic representation of the drop-testing setup. b) Close-up of test setup as used during the experiments. c) Test setup during the testing phase; clearly visible is the bracket constraining the lateral movements of the cercap. d) Complete overview of the drop-testing, including the syringe pump, DAQ, lighting equipment and HSC.

silicone and borosilicate glass. Both before and after use all materials were meticulously cleaned with DI water to remove trace metal impurities. When organic solvents were used for cleaning, the respective objects were subsequently rinsed rigorously with DI water. In order to avoid build-up of HP fumes, the experiments were conducted in a well-ventilated fumehood. To ensure a clean workspace and to prevent damage thereto, a large part of the fumehood was covered in aluminum foil. HP that would be left after the experiments was diluted to 3% before disposal.

3.2.3.2. Test setup and testing procedure

This section will elaborate on the procedures used during the testing phase. Schematic representations can be found in [subsection D.1.6](#) and checklists can be found in [subsection D.1.5](#). For each sample, the procedure described below was repeated three times, as can be found schematically in [subsection D.1.6](#).

In these decomposition experiments, low concentration HP (Sigma Aldrich Perhydrol 30%) was used, which had been concentrated to the desired concentration using SolvGE's RGP. The concentrations were determined using a calibrated refractometer, which was shown in [Figure 2.8](#). Before the testing, the drop-testing setup was flushed with HP into a thoroughly cleaned receptacle. In a typical decomposition experiment (as is visualized in [Figure 3.3](#)), a predetermined amount of HP (approximately 100 μ L) was released using a syringe pump from 158 mm height; the pump would ensure an approximately constant flow rate (i.e. 2.40 mL/h), and thus drop rate (once per 11 seconds). The drops were generated using a 21G (0.50 mm inner diameter) syringe needle. Following their release, they would impact the catalyst in the receptacle and start decomposing. Simultaneously with starting of the pump, data acquisition was started, which consisted of both thermal and visual data. The high speed camera (HSC) footage was used to determine i.a. the moment of impact of the drop on the catalyst; this video footage was recorded using a GoPro Hero 8 camera (240 frames per second). Thermal data was gathered using a set of four thermocouples (Omega CHAL-003 K, 0.075 mm diameter, thermal range: -180 to 1360°C). They were positioned at 2, 15, 23 and 33 mm (h_0 to h_3) from the catalyst surface, and were sampled at 40 kHz and read out at 50 Hz average using a digital data acquisition system (DAQ, DataQ DI-2008). As discussed above, the maximum temperature achieved during decomposition could be used to assess the decrease of the catalytic power, or equivalently catalyst degradation. The hence determined decomposition temperatures are not absolute values due to the physical limitations of the thermocouples: their intrinsic thermal capacity causes both temporal and thermal peak smoothing in the measurements. In addition, the DAQ has only a limited time resolution. Nonetheless, these peak temperatures can be used to compare the performance of different catalysts in a semi-quantitative manner.

The administering of HP would continue up to the moment that the observed bubble formation would be almost diminished and the catalyst pellet would remain wet. When sufficient liquid was present, its concentration was determined using the refractometer. The sample was allowed to cool down and dry before it was stored in an non-airtight container (to prevent gas build-up from unreacted HP). Additionally, the concentration of the HP in the syringe was determined to check for degradation effects during the testing.

By monitoring the thermal and visual behavior of the catalyst during the addition of series of drops, degradation effects could be noticed by a decrease in maximum temperature. All catalysts were first screened in this manner using a few drops of HP. If their performance clearly did not satisfy the requirements already in this short test (especially the DD, REQ-CAT-4), it was not expected that behavior would improve with extended testing, and hence testing of these samples was discontinued.

3.2.4. Data analysis and calibration

This section is dedicated to elaborate on the manipulations performed on the measurement data, and the subsequent analyses conducted thereon. First, a short summary will be supplied on the calibration efforts.

3.2.4.1. Calibration

All used laboratory equipment is yearly calibrated by external parties. This includes standard laboratory equipment, e.g. scales, but also analysis equipment. Additionally, these apparatuses, such as the X-ray diffractometer and Raman spectrometers, are inspected regularly by qualified technicians. Further, the results obtained from the analyses were validated with reference data from the Crystallography Open Database (COD) [41] or from the RRUFF Project [64].

Much effort was put into calibration of all equipment used during the reactivity testing, which is elaborately described in [section D.2](#). During the experiments it was noticed that the pump speed would fluctuate over time, resulting in a standard deviation of 5% in the drop delays. The drop volume had been determined using deionized water instead of concentrated HP, due to the similar viscosity and surface tension as HP,

yielding a standard deviation of 3.7%. Validation of the drop size during the experiments based on visual data gave a 50 times higher volume, which can be attributed to both the properties of the camera and the lensing effect caused by the droplets. Yet, the spread in the thus measured drop size was only 2%. Further, the thermocouples would have a typical standard deviation of 0.18°C. They were calibrated against both 0 and 100°C water and a calibrated handheld thermometer (with an error of 0.1°C). Additionally, to validate the test setup itself, decomposition experiments were conducted with manganese(II) acetate, resulting in similar readings as the decomposition experiments with the developed catalysts. Further, to validate the compatibility of syringe, tubing and syringe needle that would come in direct contact with concentrated HP, these were left filled overnight with 98% HP without showing a decrease in concentration.

3.2.4.2. Data analysis

From the video data, only every two other drops were analyzed. This was done to limit analysis efforts, while limiting the effect on the data quality: logically, two subsequent decomposition events should behave similarly; outliers should be more easily detectable in this manner. Even though 120 drops were administered in each experiment, only the first 70 drops were analyzed as such, due to the early onset of complete surface wetting of the cercaps. Part of the analysis tried to find the start of bubble formation (SBF), since this could correlate to the start of the HP decomposition. Since the size of the bubbles was approximately equal to one pixel, it was decided to classify one such pixel as a bubble when it would remain for more than three subsequent frames (or 13 ms); otherwise it was classified as noise. An example hereof can be found in [Figure D-8](#). The image analysis was further hampered by the anti-aliasing algorithm of the camera, which sometimes would change the sampling area in between frames. The time from the moment of drop impact up until the last bubble would disappear (end of bubble formation, EBF) was determined similarly in order to find a simple measure for the reaction duration. The presence of smoke caused an additional challenge to observe the possible bubbles.

3.3. Results and discussion

The high exothermic nature of the decomposition reaction combined with the gas development (volume expansion) and the mechanic force of the drop impact put high demands on the mechanical integrity of a catalyst body. Therefore several design iterations were performed before a suitable support method was found for manganese oxide. Among the tested support methods are deposition precipitation (DP) on powdered YSZ (giving Mn/YSZ), dropcasting of Mn/YSZ and DP on fused alumina, silica and YSZ and on washcoated alumina. For details and results please see [subsection E.2.2](#).

Since the Mn/YSZ powder could not be stabilized on top of another support, it was chosen to prepare an intimate *mixture* of MnO₂ and the respective metal oxide support material and calcine this at a high temperature. With the proper choice of metal oxides this could lead to extensive sintering between the manganese oxide and the metal oxide support, as described in [subsection 3.1.5](#). Besides, it was hypothesized that if the cercap would still be active after calcination, it should also be able to withstand the typical conditions in a HP decomposition engine.

Cercaps based on kaolin, titania, silica, magnesium spinel, (gamma-)alumina (further referred to as γ Al) and YSZ were successfully prepared. All originally white metal oxide precursors turned gray upon addition of black MnO₂; as is clear from [Figure 3.4](#), calcination lead to notable color changes for spinel, kaolin and γ Al. Following calcination, the mentioned cercaps were tested for their activity with 87% HP. Of these cercaps only YSZ (YSZ-1.5) and γ Al (γ Al-1.5) showed observable reactivity. Even more, for the γ -alumina-based cercap the MnO₂ concentration had to be decreased to 0.30 wt.% to maintain mechanical integrity during drop-testing. As a control, a Mn/YSZ pellet was calcined under the same conditions. Even though the MnO₂ loading was 10 wt.%, its decomposition behavior was much less than that of the YSZ-1.5 cercap. It appears that the high dispersion as obtained by deposition precipitation negatively influences the thermal stability of the active catalytic phase. The cause of inactivity of the inactive cercaps could not be found using the available spectroscopic techniques; please refer to [subsubsection E.2.3.1](#) for spectroscopic details of these cercaps. The high reactivity of the YSZ-1.5 and γ Al-0.30 lead to a more in-depth investigation as will be laid down in the following sections.

3.3.1. Thermodynamic characterization

In order to investigate the oxidation state changes of MnO₂, which is generally reported to be the oxidation state that is reactive with HP, thermodynamic equilibrium calculations were performed using HSC Chemistry

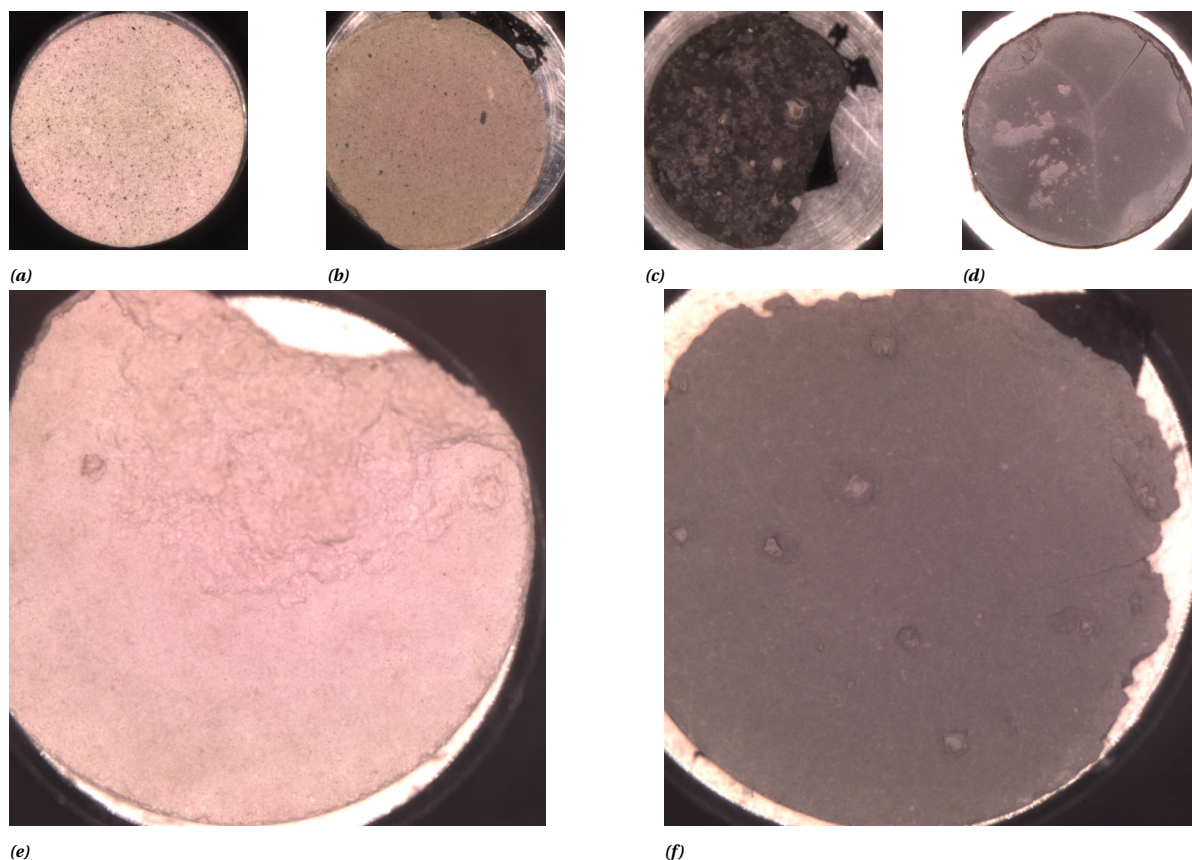


Figure 3.4: Cercaps after calcination. *N.B. the large irregularities had been caused by undissolved PVA; therefore this was later sieved out.* a) Kaolin; b) Magnesium spinel; c) Silica; d) Titania; e) $\gamma\text{Al-1.5}$; f) YSZ-1.5.

6.0. Here, manganese dioxide (1.5 wt.%) was mixed with various metal oxides (viz. alumina, titania, silica and YSZ) and the equilibrium phase content up to 1200°C in air was evaluated as can be seen in [Figure 3.5](#) and [Figure 3.6](#). As a control, pure manganese dioxide was evaluated as well. Care must be taken not to overinterpret these results: these calculations merely show the equilibrium concentrations, and do not take into account the time required for the associated transformations. Thus, it might as well be that the shown compounds do not occur in practice, or only under very special synthesis conditions. Additionally, compounds that form during calcination may transform into another (more stable) form upon cooling.

Nevertheless, the thermodynamic analysis yielded several remarkable results. First of all, the believed transformation of (pure) manganese dioxide to (catalytically inactive) monoxide only takes place to limited extent. Though, this transformation seems to be favored by the presence of particular metal oxides; especially YSZ appears to favor this phase transition. When manganese dioxide is instead mixed with aluminum oxide and subsequently heated in air, it will not transform in MnO, but instead it will form a mixed oxide with the alumina, $\text{MnO} \cdot \text{Al}_2\text{O}_3$, as has been reported in literature (see [subsection 3.1.5](#)). The same applies to titania and silica, forming MnTiO_2 and $\text{MnO} \cdot \text{TiO}_2$, and MnSiO_2 and Mn_2SiO_4 , respectively. Similar mixed-oxide compounds are formed if for instance kaolin ($\text{Al}_2(\text{OH})_4\text{Si}_2\text{O}_5$) is used as a precursor. If one would merely look at the oxidation state of manganese in each of these mixed-oxide compounds, it would seem that these show low to no reactivity with HP. Yet, as was explained above, these mixed oxides decompose during cooling into i.a. hausmannite. Further, drop-testing experiments proved the high reactivity of YSZ and γAl .

3.3.2. Prereaction characterization of γAl and YSZ cercaps

Prior to conducting extensive reactivity testing, both $\gamma\text{Al-0.30}$ and YSZ-1.5 were thoroughly analyzed with diverse analytical techniques. The results will be presented in this section. As was already clear from visual inspection, both cercaps have a rather homogeneous surface composition when compared to the other cercaps (see [Figure 3.4](#)). Additionally, it appeared that the $\gamma\text{Al-0.30}$ cercap has a more rough surface than YSZ-1.5; close inspection of these cercaps with SEM substantiates this observation (representative images can be

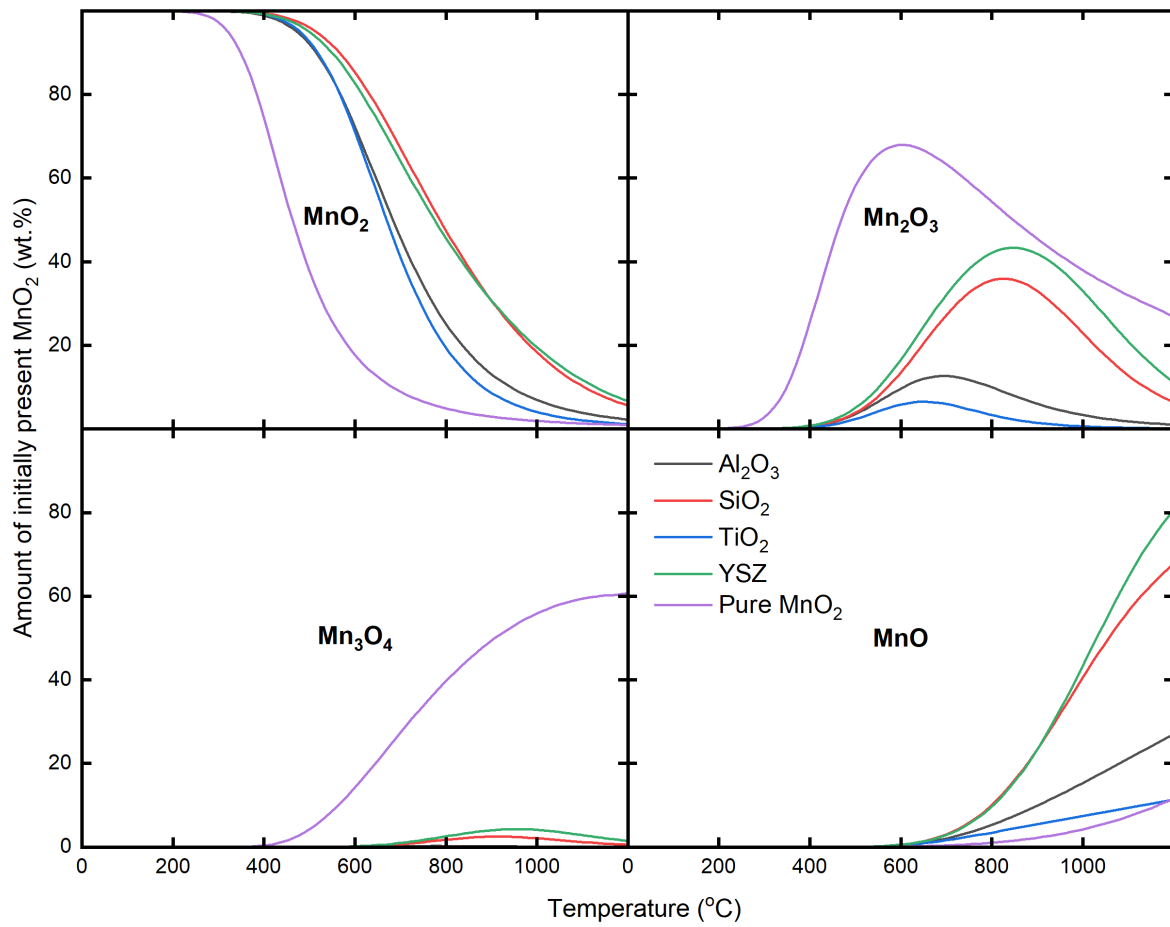


Figure 3.5: Equilibrium concentration of MnOx at different temperatures, as calculated with HSC Chemistry 6.0.

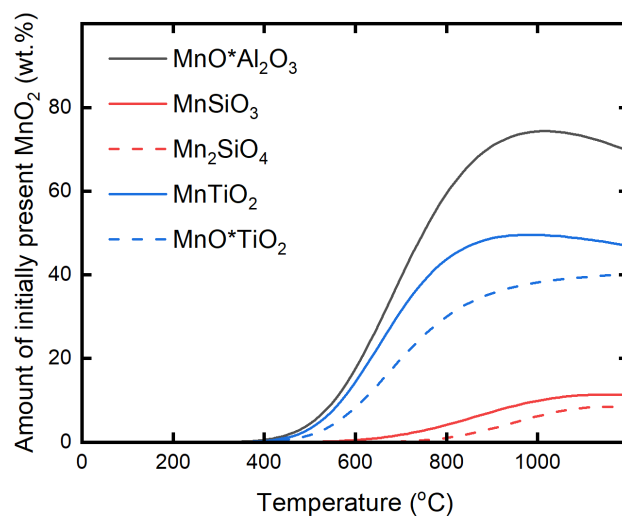


Figure 3.6: Equilibrium concentrations of different mixed oxides at varying temperatures, as calculated with HSC Chemistry 6.0.

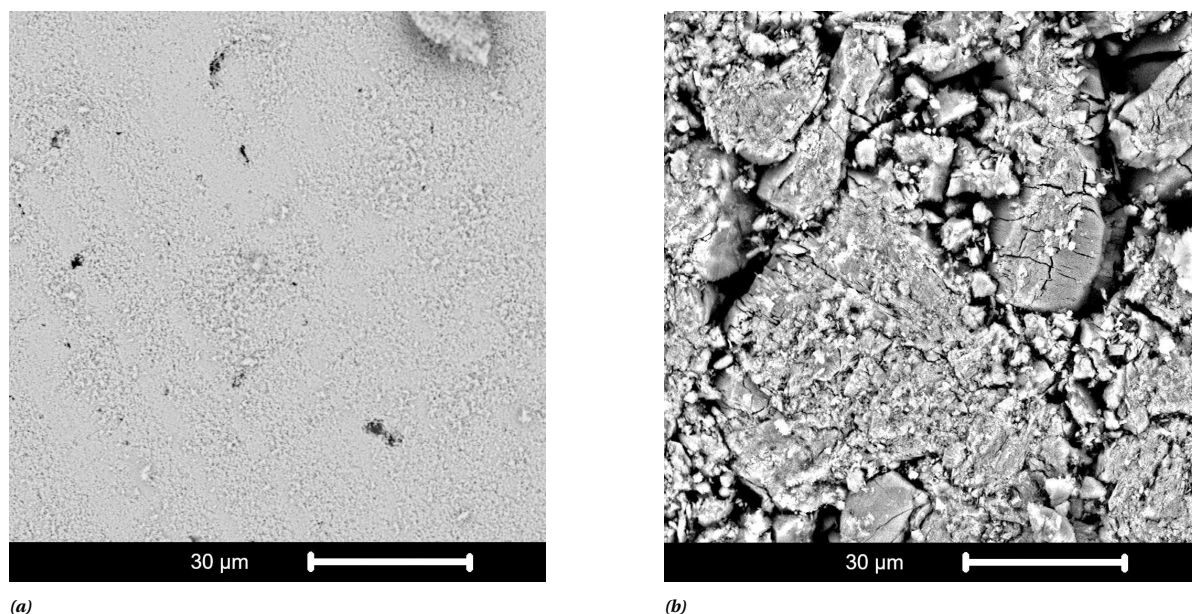


Figure 3.7: Comparison of the surface topography of the YSZ-1.5 (a) and γAl -0.30 (b) cercaps. These electron micrographs show the higher surface roughness of γAl -0.30.

found in Figure 3.7). Even more, these micrographs seem to indicate that the γAl -0.30 cercap has a higher porosity than the YSZ-1.5. This is relevant for future application of the catalyst, since high porosity may be disadvantageous when the catalyst is operated in a rocket engine. Namely, highly reactive gaseous H_2O_2 may then penetrate into the bulk of the cercap and react there, leading to explosive decomposition and most likely deterioration of the catalyst body. To substantiate the presumed porosity, a γAl -0.30 cercap was placed on a paper tissue, and a drop of water was put on the cercap's surface: the tissue immediately became moist. The YSZ-1.5 cercap would behave similarly, yet this can be attributed to the severe surface cracks present on all YSZ-1.5 samples. Unfortunately no further porosity data could be gathered at this time.

3.3.2.1. γAl cercaps

As was already mentioned above, the γAl cercaps turned pink during calcination, with the color intensity increasing with higher manganese concentration. This is also evident from the TDR spectra (Figure 3.10a): the adsorption increases with increasing manganese loading. Note that this material is also used as dye material, known as Pigment Red 231. Close examination of the surface shows the presence of dark spots (spaced ca. $500\ \mu\text{m}$ apart, see Figure 3.9 for γAl -0.30), which is most prominent for the γAl cercaps. These could have been caused by the size of the manganese precursors; presumably to aid elemental dispersion, most authors resort to wet chemical methods for the synthesis of these manganese-alumina catalysts (e.g. [12, 129]). Analysis of these spots and the surrounding material with Raman spectroscopy substantiates this hypothesis: while the spots give a strong Mn_3O_4 signal, the lighter surrounding material almost exclusively gives intense fluorescence from $\alpha\text{-Al}_2\text{O}_3$, with no sign of MnOx. Though, the overall pink shade of the cercaps indicates that manganese is spread over the entire volume, but apparently not evenly. The global presence of hausmannite is confirmed by XRD.

Further investigation of the γAl cercaps shows that the MnOx serves as a sintering or phase-transformation aid for the γ -alumina precursor: with increasing manganese concentration, the $\gamma\text{-Al}_2\text{O}_3$ intensity clearly decreases in XRD, Raman and TDR, see Figure 3.8 and Figure 3.10. Additionally, the total Raman intensity decreases with increasing manganese loading; this can be explained by the transformation to α -alumina, which gives a much lower Raman intensity. This is confirmed by the XRD data, which show an increase in the maximum peak intensity of $\alpha\text{-Al}_2\text{O}_3$ of approximately 5 times when comparing γAl -0.30 with



Figure 3.9: Magnified image of pristine γAl -0.30 cercap showing dark spots on its surface.

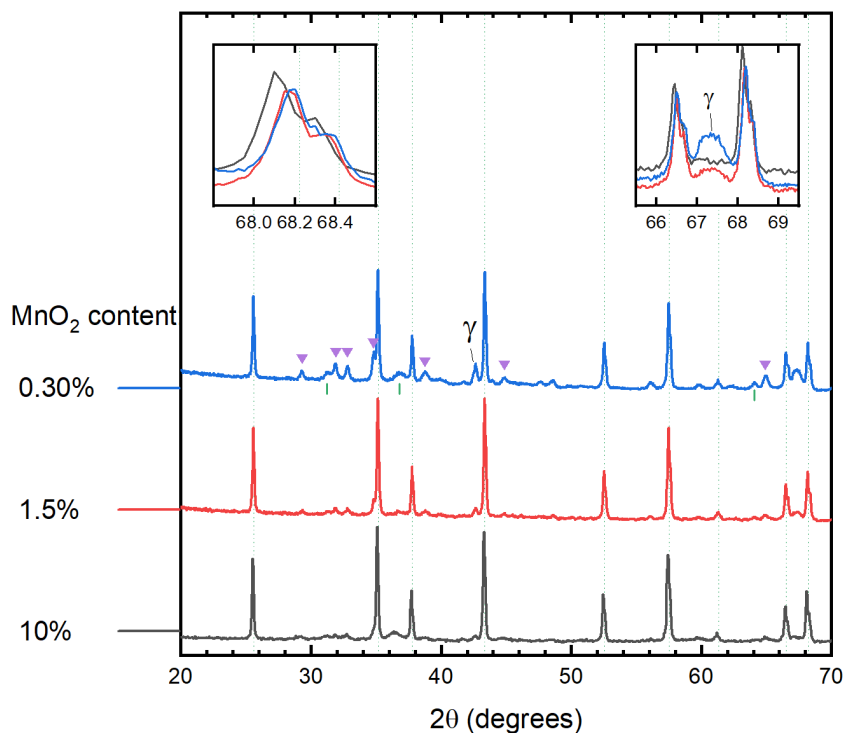


Figure 3.8: Comparison of CuK α X-ray diffraction data for γ Al cercaps with increasing MnO $_2$ loading; all signals have been scaled to the maximum peak intensity. The vertically dashed lines indicate the location of α -alumina according to COD 96-230-0449. (▼) indicates the hausmannite phase which is shifted with respect to the reference (COD 96-151-4116 [41]). (▲) indicates the locations of the supposed Mn-Al mixed phase, according to [12]. The left inset shows the shift to lower 2θ of the α -alumina signals with increasing manganese loading. The right inset shows the decrease in γ -alumina content with increasing manganese loading.

yAl-10. Thus, a higher concentration of MnOx leads to more crystalline α -alumina. In addition, the observed Raman intensity is further decreased by the (predicted) formation of a mixed manganese-aluminum oxide phase (Mn $_x$ Al $_{2-x}$ O $_4$, known as galaxite) and its subsequent decomposition into hausmannite upon cooling. Namely, variations in elemental content of the galaxite (and thus the resulting hausmannite), caused by i.a. a non-uniform MnO $_2$ dispersion during calcination, will cause broadening of Raman signal and thus a lower observed intensity.

Surprisingly, Figure 3.10b hints at the presence of galaxite in yAl-0.30 and most notably in yAl-10 [133] (its presence could not be detected with Raman in yAl-1.5, which could depend on the investigated area), while its formation is reported in literature only when the compounds are cooled in an inert atmosphere. XRD cannot directly prove this formation of galaxite, not even in yAl-10, even though the baseline signal increases (with an intensity comparable to the noise level) at the predicted peak positions [43]. Perhaps this is caused by the fact that XRD measures the composition of the entire cercap, in combination with the probably localized nature of the galaxite and its varying composition. Additionally, the formed crystallite phase is reported to possess low crystallinity [12], which would even further decrease the signal intensity in both Raman and XRD. Nevertheless, when the here observed XRD patterns are compared to those obtained by Bulavchenko and coworkers [12], some peaks in the here presented XRD patterns appear to indicate the formation of galaxite at low Mn-loadings. Though, those reported peak positions are notably different from galaxite spectra reported elsewhere (e.g. COD 96-900-0877). The agreement to the XRD patterns as reported by Bulavchenko et al. is surprising, both because they used 12 wt.% MnO $_2$ loadings and since they calcined the catalysts in an inert atmosphere. Perhaps then the formation of galaxite is favored at low Mn-loadings due to the excess of alumina. Further analysis should be performed to confirm the formation of galaxite.

Next, evident from XRD is that the peak positions shift to lower 2θ angles with increasing manganese loading, as can be seen in the left inset in Figure 3.8. While this shift is not prominent for yAl-0.30, it increases to -0.125° (at $68.2^\circ 2\theta$) for yAl-10. This implies that Mn ions are being incorporated in the octahedral α -alumina lattice: due to the larger size of a Mn ion in an octahedral position the crystal unit cell expands, leading to diffraction at lower angles. Conversely, the hausmannite phase is shifted with $+0.3^\circ$ (at $64.9^\circ 2\theta$), indicating a shrinkage of the unit cell, hinting at the incorporation of the smaller aluminum ions, as was

shown by Bulavchenko et al. [12].

To conclude, the thermodynamic analysis predicted the formation of some 20% MnO, which should give a very prominent signal in both Raman spectroscopy and XRD; yet, no traces of MnO could be detected. This might mean that the phase-mixing phenomenon takes place faster than does the reduction to MnO. It could again also indicate the high dispersion and low crystallinity of this phase.

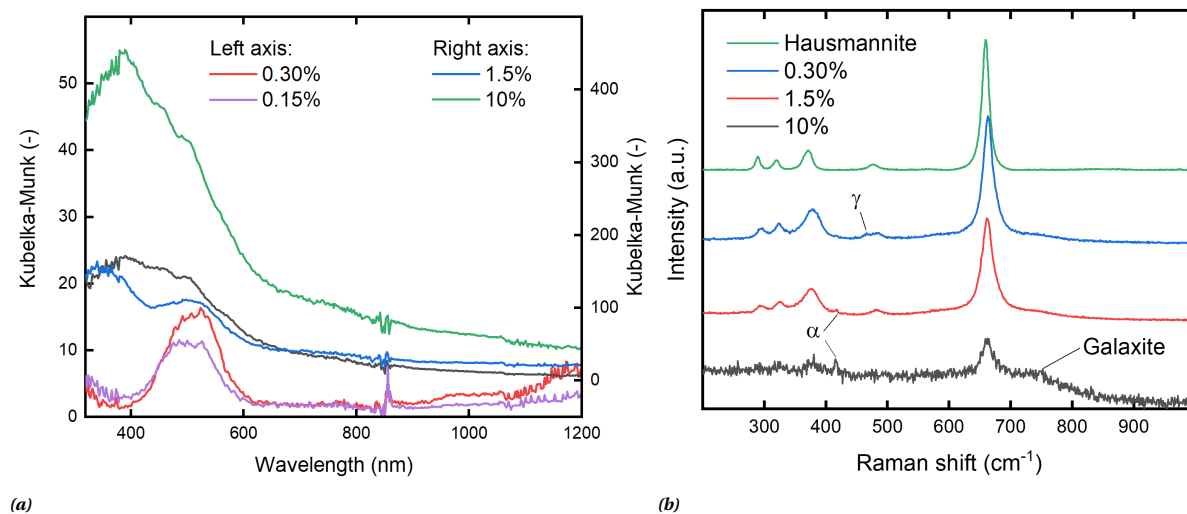


Figure 3.10: Optical spectroscopy conducted on γAl cercaps with varying MnO_2 loading. a) TDR spectra for γAl cercaps with varying MnO_2 loading. The increasing manganese content has a strong effect on the $\alpha\text{-Al}_2\text{O}_3$ peak at 390 nm, and on the overall reflectance. b) Raman (785 nm) shifts originating from the different γAl cercaps. Clearly visible is the increasing α - and decreasing γ -alumina content (indicated by α and γ , respectively). The peak at 750 cm^{-1} hints at the formation of galaxite. The hausmannite spectrum is taken from RRUFF R110179 [64].

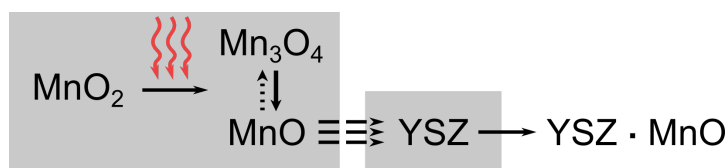


Figure 3.11: Simplified mechanism of formation of solid solution of MnO in YSZ. The boxes separate the different species. Three dashed arrows indicate migration of atoms. Dotted arrows indicate unfavorable transitions.

3.3.2.2. YSZ cercaps

Examination of the XRD data of the YSZ-1.5 cercaps (see Figure E-14) learns that not any manganese oxide phase can be discerned. Though, the thermodynamic analysis above showed that approximately 1/3 of the MnOx should be present as Mn_2O_3 , whereas the majority of the MnO_2 should have been converted to MnO in the vicinity of YSZ. Perhaps this phenomenon can be explained by the nature of the YSZ. It is known that the addition of yttria to zirconia results in increased stability of the cubic zirconia phase, which is ordinarily only stable at high temperatures. This stabilization is probably induced by the comparatively large atomic radius of Y(III) ions (104 pm) when compared to Zr(IV) (86 pm) in the cubic lattice, which prohibits the phase transformation back to the stable phase at atmospheric conditions [128]. It can be understood that the addition of a considerable fraction of these larger yttrium ions leads to the formation of interstitial positions in the YSZ lattice. Further, it is known that MnO can already easily migrate into ZrO_2 , which can lead to a Mn content of 25 at.% [10, 28, 37, 38]; this favorable migration can be explained by the similar size of Mn^{2+} and Zr^{4+} ions [128]. It could then be assumed that in the presence of YSZ, with its interstitial positions, this migration is even more favorable. Perhaps the thus occurring removal of MnO from the reaction mixture during calcination leads to an equilibrium shift, due to which the remaining MnOx will be again partially converted to MnO, which on its turn migrates again into the YSZ et cetera, as is schematically illustrated in Figure 3.11. If this proposed migration would take place, the YSZ-1.5 cercap should be inert for the decomposition of HP, assuming no other (electronic) effects arise. Besides, the fact that the host lattice does not need to accommo-

date for the presence of manganese ions can explain why no peak shifts are noticeable in the XRD patterns for YSZ-1.5.

Further, SEM-EDX shows that the manganese ions have a high degree of dispersion on the cercep's surface. This dispersion would cause large peak broadening of the already weak signals from MnOx (applicable to both XRD and Raman), and hence decreases the signal intensity below the noise level. Note that this observed dispersion does not necessarily substantiate the oxide-mixing theory as described; prove for this theory should be given by spectroscopic methods that are sensitive to the oxidation state (and electronic levels) of manganese, such as XPS. Neither Raman (see Figure E-10) nor TDR spectroscopy (see Figure E-12b) were able to detect any MnOx. In addition to the possible spectral broadening of the manganese signals, the former also suffered from high fluorescence by the YSZ, whereas the latter merely indicated the same two (unidentified) peaks as are found in all cerceps but γ Al. Further spectroscopy should be conducted to elucidate the oxidation state of manganese in the YSZ-1.5 cerceps.

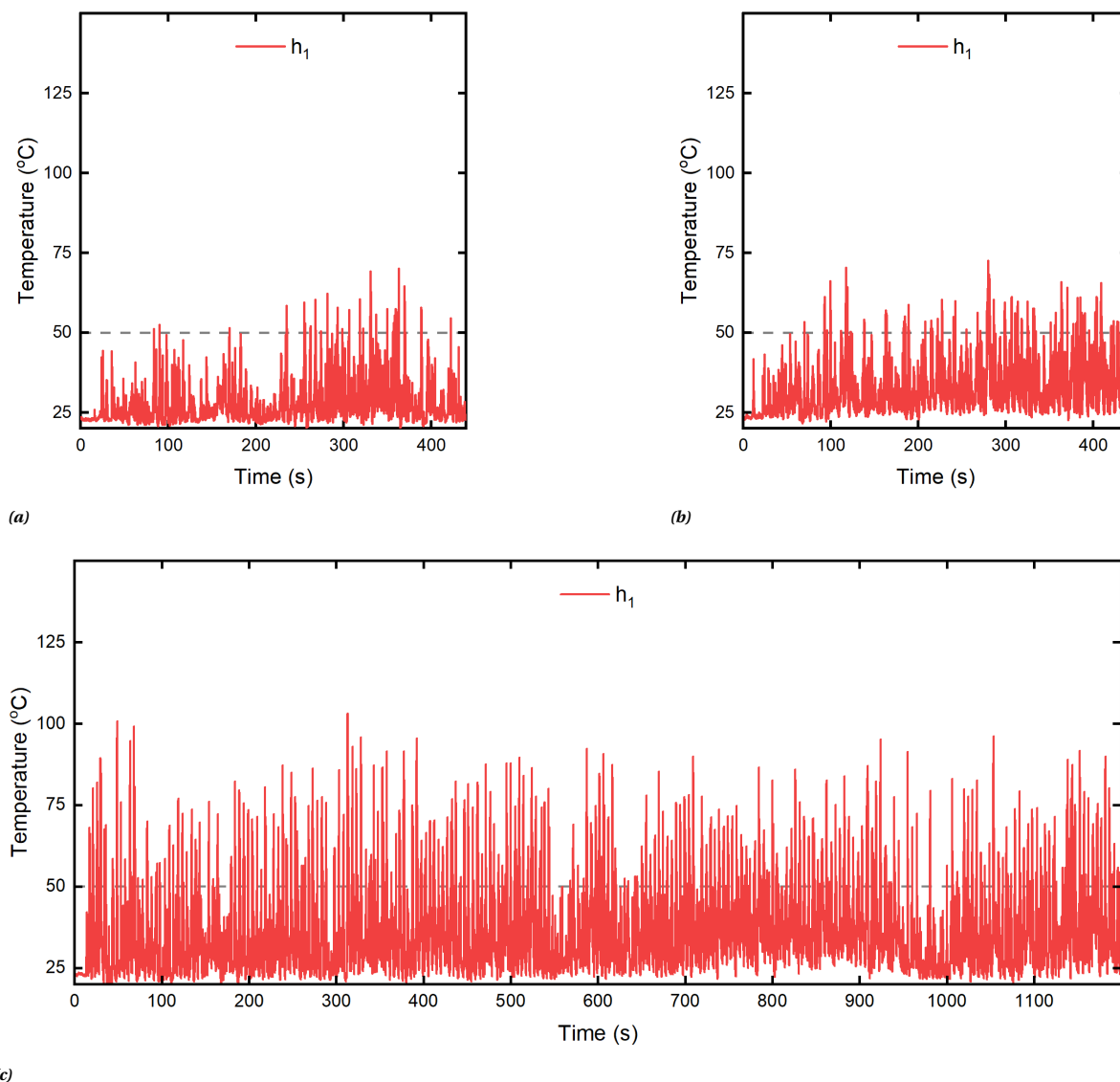


Figure 3.12: Temperature traces from experiments with an unconstrained YSZ-1.5 cercep with 87% HP. Note that thermocouple h_0 was not mounted in these experiments due to physical constraints; only h_1 is plotted for clarity. Further a dashed line indicates the deactivation temperature threshold set by REQ-CAT-3. Experiment a) and b) were conducted seven days apart, during which the catalyst was stored in a closed vial. b) and c) were conducted two hours apart, during which the cercep was allowed to dry in open atmosphere. Hence, these figures demonstrate the both good restartability and excellent endurance of the YSZ-1.5 catalyst when no reactants and products are allowed to accumulate. Clearly visible in all figures is the temperature variation attributed to the constantly varying position of the cercep with respect to the thermocouples, and the results of improved alignment in c).

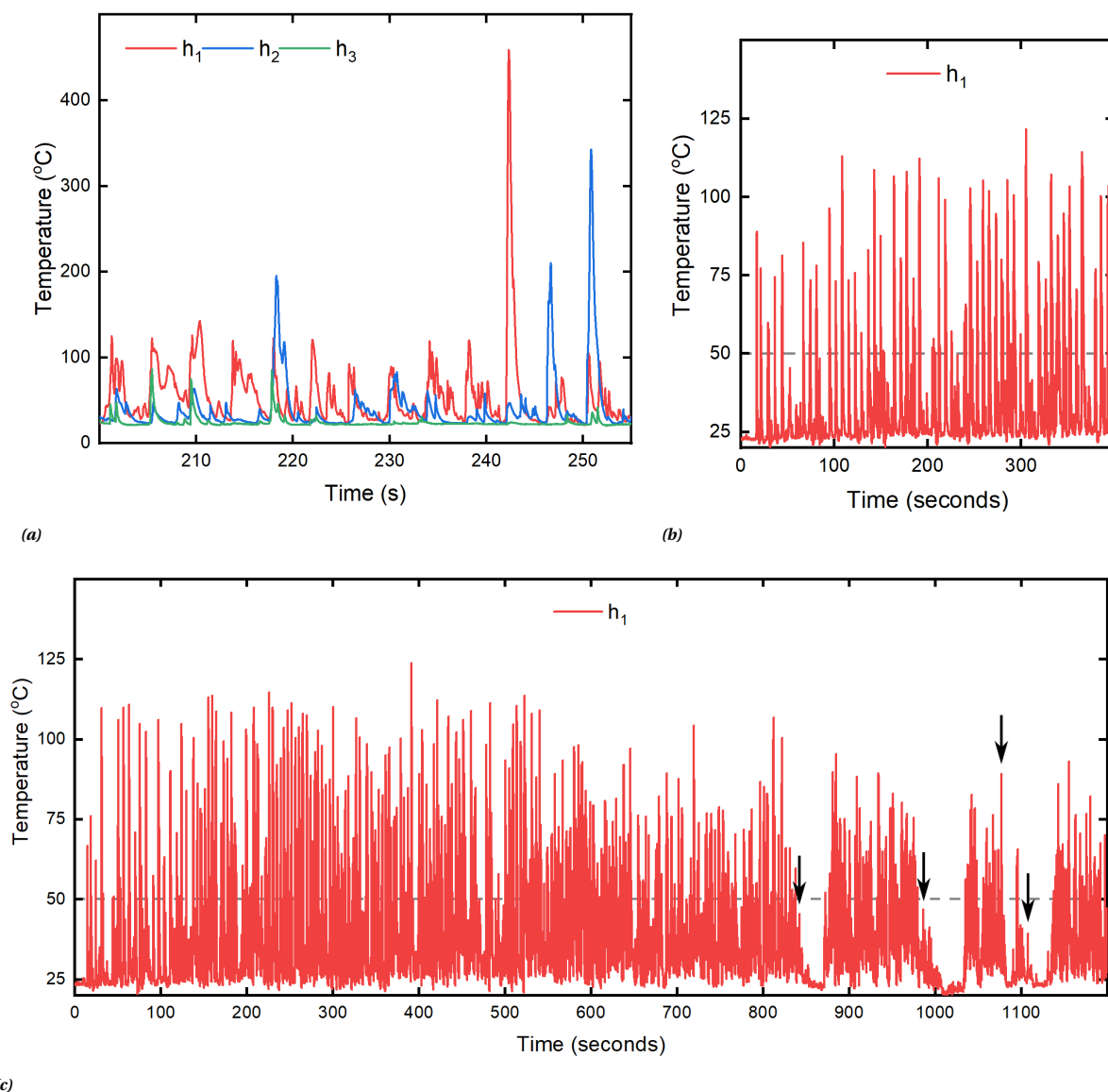


Figure 3.13: Temperature traces from experiments with an unconstrained $\gamma\text{Al-0.30}$ cercap. Note that thermocouple h_0 was not mounted in these experiments due to physical constraints.

a) The once occurring high temperature peak during testing with 98% HP. Evident is the low correlation in temperature between the different heights.

b) and c) show the thermal traces of two experiments conducted one hour apart with 87% HP, during which the catalyst was allowed to dry in open atmosphere. Here only the lowest available thermal trace (h_1) is plotted for clarity; in addition a dashed line indicates the deactivation temperature threshold set by REQ-CAT-3. During the comparably longer experiment in c), the drop-testing was halted at several instants (indicated with the arrows) to investigate restarting behavior. This clearly shows that the $\gamma\text{Al-0.30}$ cercap displays both good restartability and excellent endurance when no reactants and products are allowed to accumulate. Additionally, both b) and c) clearly exhibit the temperature variations attributed to the constantly varying position of the cercap with respect to the thermocouples.

3.3.3. Catalyst activity testing

The catalysts were tested for HP decomposition in the setup described in subsection 3.2.3. Since the decomposition reaction is highly exothermic, the activity was evaluated by measuring the temperature rise during subsequent decomposition events. During the experiments it was found that the cercaps would move around in the receptacle, which caused large fluctuations in the measured temperatures. Typical temperature traces can be found in Figure 3.12 and Figure 3.13 for YSZ-1.5 and $\gamma\text{Al-0.30}$, respectively. Despite the large uncertainties in the temperature, these figures show the excellent lifetime of both catalysts: both were able to convert over 300 drops of 87% HP without losing their reactivity. In addition, in contrast to other tested catalysts (see subsection E.2.2.1), no deactivation was noticed upon halting the addition of HP. Afterwards though,

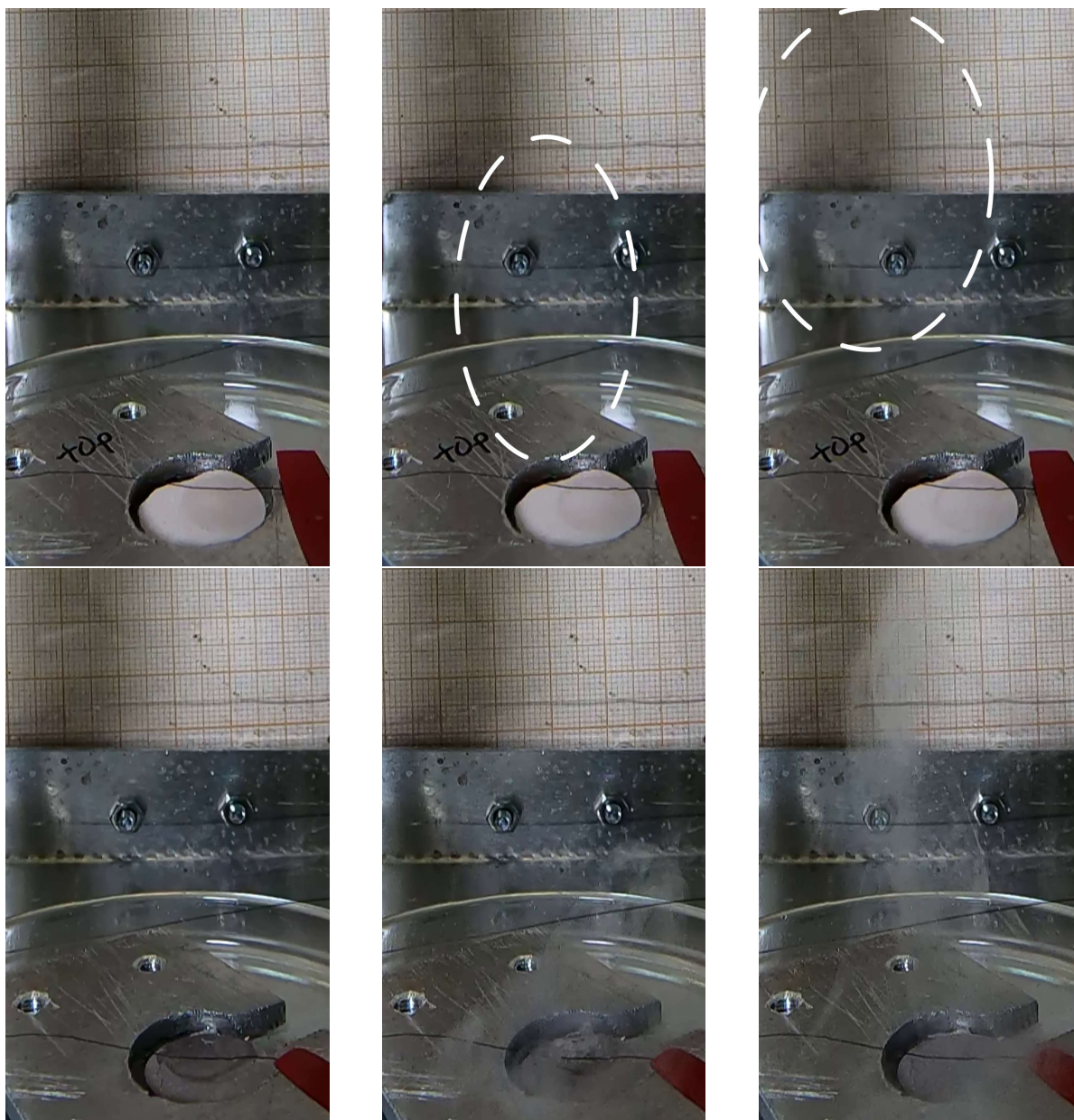


Figure 3.14: Typical smoke development during a decomposition event for γ Al-0.30 (top) and YSZ-1.5 (bottom); for the former circles have been included to indicate the areas where smoke is visible. A comparison of the smoke generation by both cercaps clearly shows that the reaction over YSZ-1.5 leads to a larger amount of darker smoke.

the two tested YSZ-1.5 cercaps had decreased in mass by 0.4%, which might explain the formation of comparably dark smoke (see [Figure 3.14](#)). No change in mass could be found for the γ Al-0.30 cercaps due to minute crumbling of the edges, but since the smoke was much less intense, it could be assumed that the γ Al-0.30 cercap is more resistant to the decomposition conditions.

Then, in an attempt to increase the maximum temperatures attained during the reaction, and hence speed up and better simulate catalyst degradation, the concentration of HP was increased to 98%. During one experiment on a γ Al-0.30 catalyst, a peak temperature of 460°C was measured at h_1 , as can be seen in [Figure 3.13a](#). This shows that the temperatures attained during decomposition can be high enough to potentially induce ignition of ethanol fuel.

Subsequently, the cercaps were constrained in an aluminum bracket in order to limit their lateral movement; this also allowed to measure the temperature at 2 mm from the catalyst surface (h_0). Unfortunately, the immobilization in the bracket lead the cercap to rapidly accumulate both reactant water and unreacted

HP, which consequentially lead to quick deactivation. This deactivation can be explained by both the known competing adsorption of water and HP on MnOx [65] and flooding of the active sites. Therefore the bracket was equipped with a drainage channel (please refer to Figure 3.3c), which enabled part of the reactants to spread into the receptacle. Yet, this only increased the time until complete flooding and subsequent loss of activity to an average of 47 drops for $\gamma\text{Al-0.30}$ and 28 for YSZ-1.5 (as can be derived from Figure 3.17). Though, this flooding merely resulted in temporary deactivation of the catalyst: when the cercaps were left to dry, either at atmospheric conditions or at 80°C , no decrease in reaction vigor was noticed. Unfortunately not enough time was available to conduct further experiments with a more advanced reactor that would not suffer from reactant and product accumulation. However, since the cercaps did not show signs of degradation, either physically (by spectroscopy) or in reactivity, and based on the earlier experiments, it can be assumed that extended testing with an adapted setup will not lead to different overall conclusions.

3.3.3.1. Thermal analysis of sequential HP decomposition events

Representative pictures of a single decomposition reaction of 98% HP over YSZ-1.5 can be found in Figure 3.15. Only very few drop impacts (viz. Figure 3.15a) are discernible in the thermal data, which can be understood from Figure 3.15f: here the temperature decrease at the drop impact corresponds to only 2.7 standard deviations of the noise intensity (i.e. the chance is lower than 0.5% that this decrease originates from thermal noise). From this point on, the first H_2O_2 molecules start to react, which leads to a release of heat, which speeds up decomposition of other H_2O_2 molecules. This can be seen as a rapid increase in temperature at h_0 (Figure 3.15b). Then, due to the spreading of the reaction heat, more and more molecules start absorbing the generated heat, which is visible as a short dip. Consecutively, the main decomposition event occurs (Figure 3.15c), soon followed by dissipation of heat to the environment, reaching a maximum at Figure 3.15d. The spatial separation of the thermocouples is reflected in the temporal spacing of the maxima; one might notice that the required time for heat transport decreases with height. This is partially caused by the gas development on the catalytic surface, propelling the above smoke further upwards, but most likely also by the high air circulation in the fumehood. Finally, the decomposition comes to an end (approximately at Figure 3.15e) and all heat is further dissipated, visible as steam (possibly incorporating solid catalyst matter, hence forming smoke).

Because with increased surface wetting not all present HP would decompose at once, secondary peaks could occur after the main decomposition event had already taken place. Therefore the peak data from the several heights could not be simply overlaid, but some data manipulation was required. The peak temperatures were found as illustrated in Figure 3.16 for $\gamma\text{Al-1.5}$. First, the maxima were found in the raw temperature dataset at h_0 using Matlab's 'findpeak' algorithm (minimum peak prominence: 0.7, minimum peak distance: 8 seconds). Based on the location of the peak at base height, a search window was constructed, from -1.00 to + 3.00 seconds after occurrence from the base (i.e. at h_0) peak. Then, based on these search windows, the higher located datasets were evaluated for the maximum occurring temperature. As is visible in Figure 3.16, near the end of the experiment the peak intensities would become more or less equal to the baseline or noise, impeding detection of the remaining decomposition events. This effect was present for all cercaps quickly after the full wetting of the surface occurred. Therefore, and since from the video data only the first 70 drops were analyzed, the dataset was confined to the first 70 decomposition events.

Clear from Figure 3.17 is that all measurements show an increasing base temperature and decreasing peak intensities with the number of administered drops. This is most likely related to the increased wetting of the catalyst, and the associated deactivation with product water. In addition, the increasing baseline seems to suggest that the cercap is slowly heating over time. Further, the attained peak temperatures at h_0 are lower than at higher locations, indicating a persistent thermocouple alignment error. Additionally, these figures clearly show that the temporal delay of the peak at higher distances from the catalyst is not constant with time for all tested samples. For the catalyst shown here, YSZ-1.5-1, the peaks at h_1 and h_2 seem to gradually proceed the temporal location of the base peak, that is, the decomposition heat is measured earlier at larger distances from the catalyst. Perhaps this is caused by the low intensity and the signal broadening of the base temperature, so that the highest occurring temperature at h_0 is falsely attributed to the main decomposition event. For the other tested cercaps (as can be found in subsection E.2.3.3) this behavior is present but not as consistent.

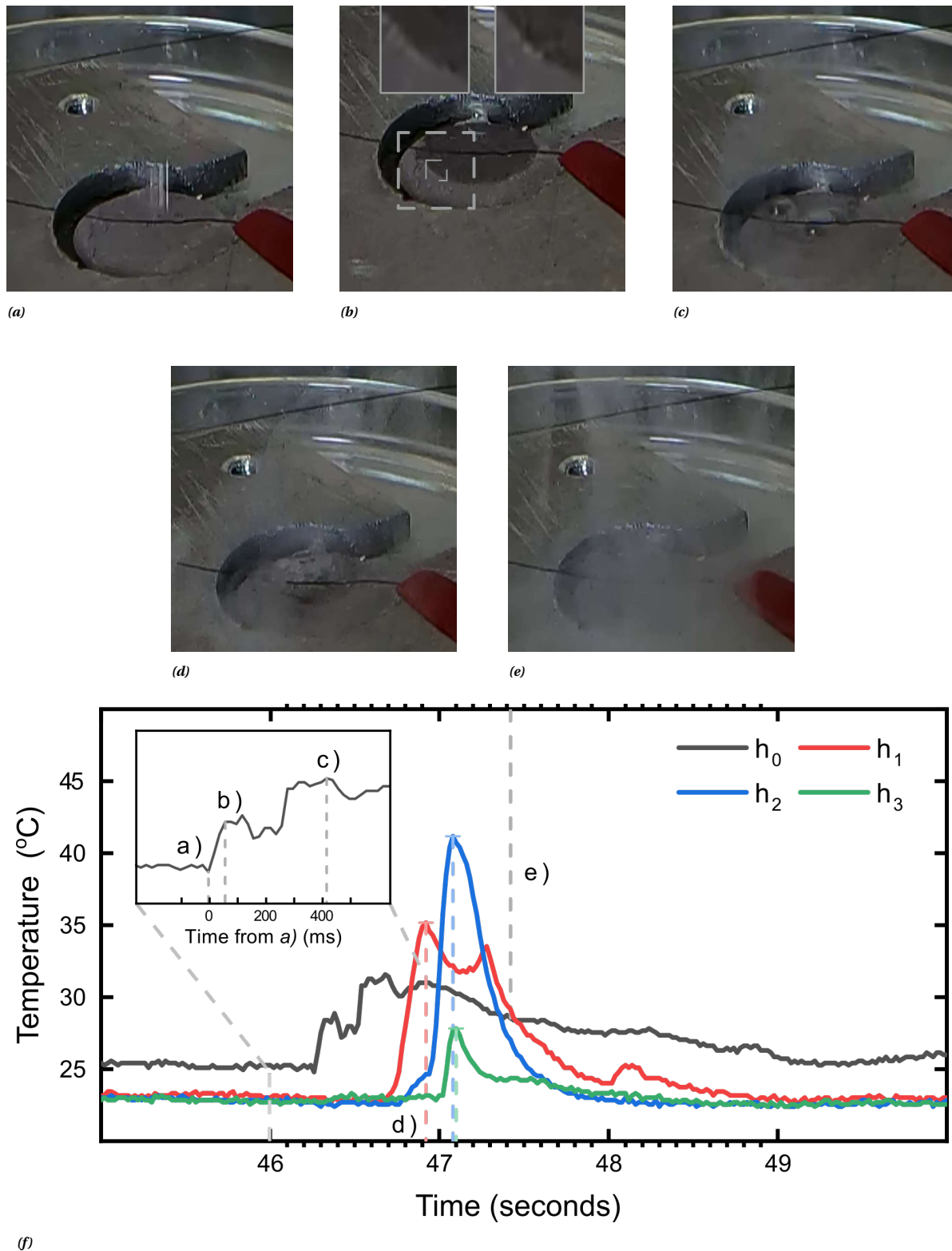


Figure 3.15: Comparison of visual and thermal data for a prototypical decomposition event of 98% HP over YSZ-1.5, for the fourth administered drop. Illustrated on the temperature trace (f) are the drop impact (a), the onset of decomposition (b, the retraction of the fluid layer is visible in the inset), the maximum vigor of decomposition (c), the approximate moment of maximum heat dissipation (d) and the approximate end of the reaction (e). Further, the thermal trace (f) shows the delay between the maximum heat dissipation at increasing height, indicated by the colored dashed lines.

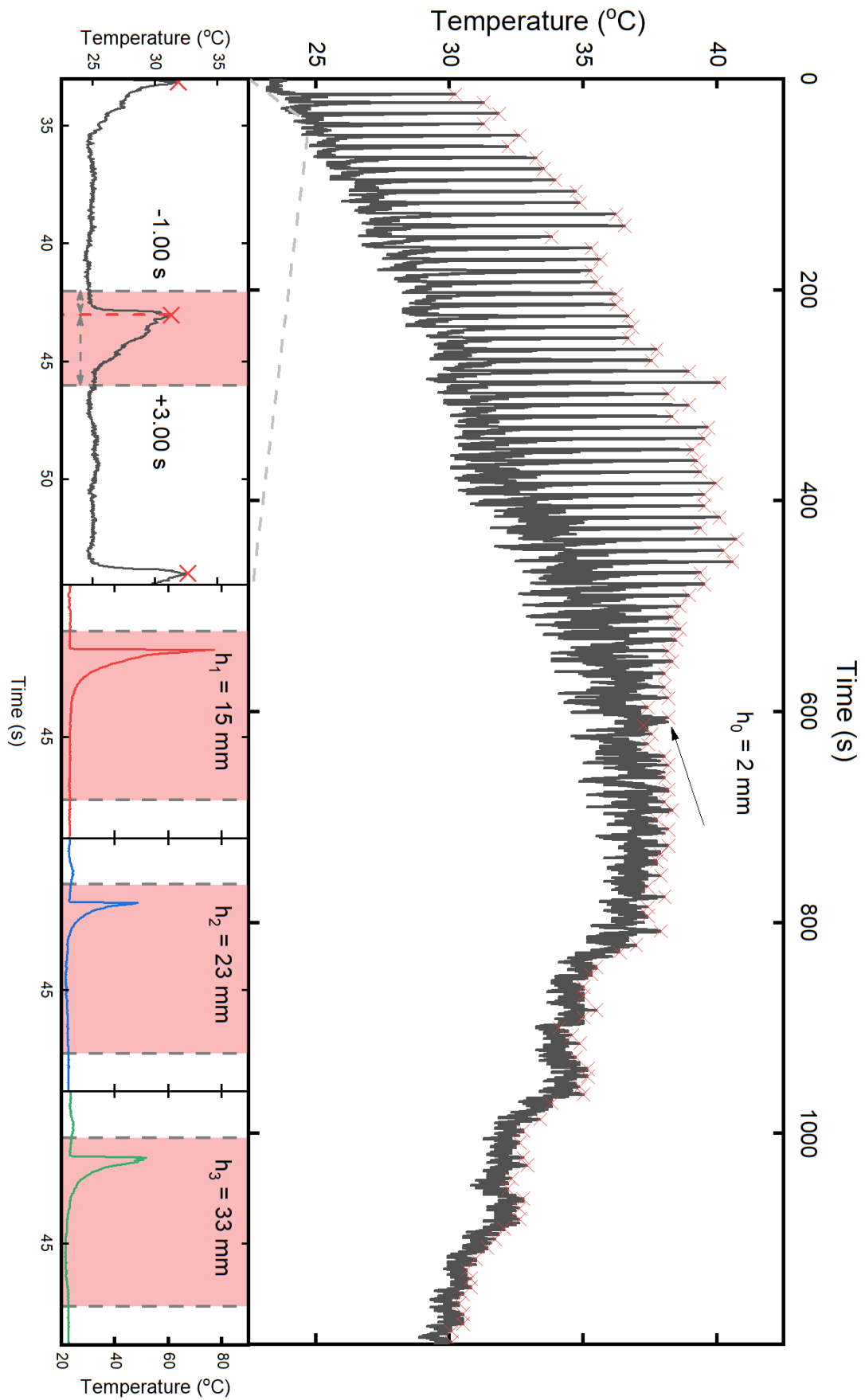


Figure 3.16: Schematic representation of the thermal data analysis for the drop-testing experiments. First the peak positions at the lowest point were found in the raw data (top). Search intervals were created with these peak positions (bottom, left) to find the matching thermal peaks at 15, 23 and 33 mm (FLTR), h_1 to h_3 , respectively. The arrow indicates the 70th drop. Note the different scale on the temperature axis for h_0 compared to h_1 to h_3 .

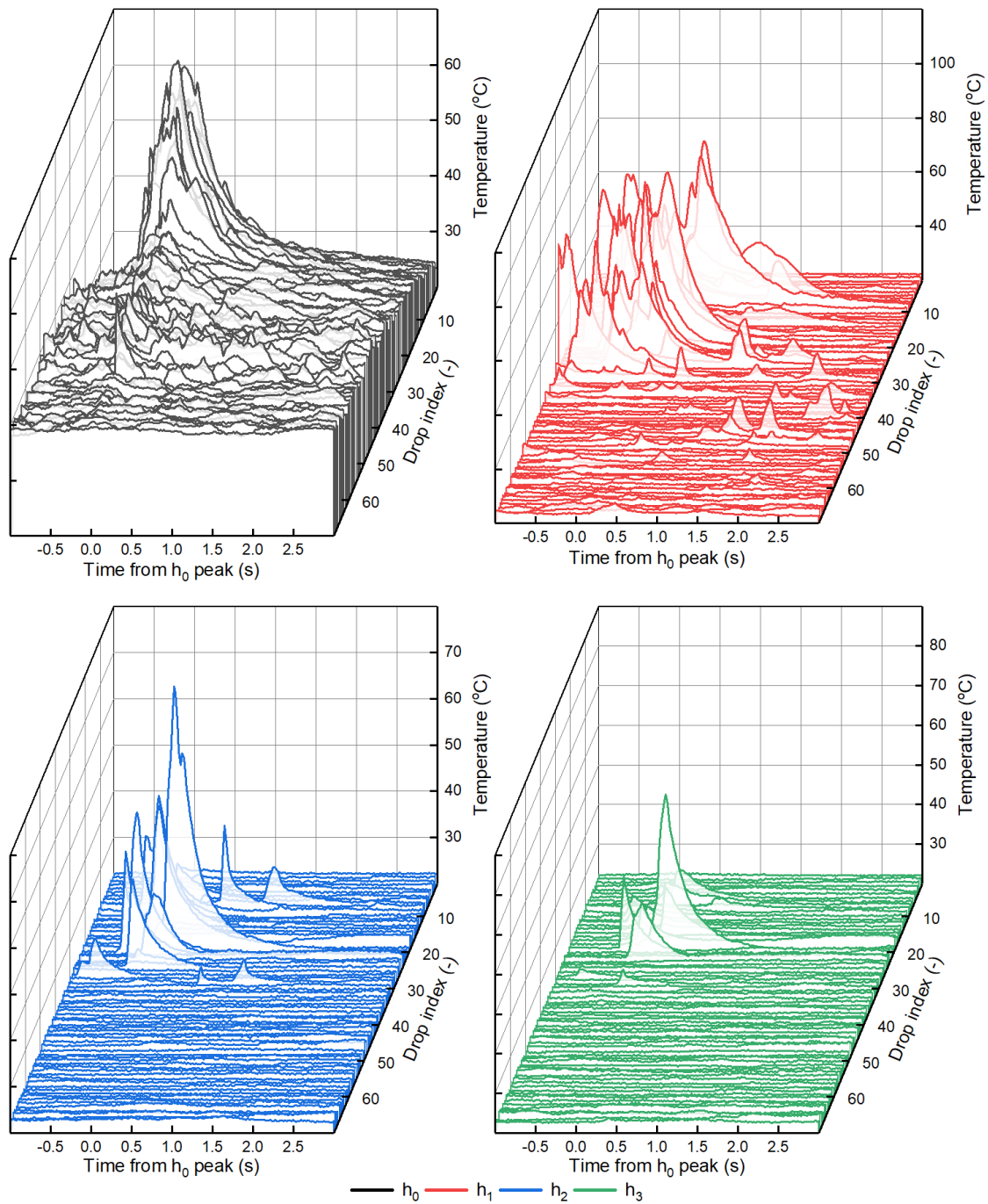


Figure 3.17: Temporal evolution of decomposition peak temperatures for YSZ-1.5-1 at the four measured heights. The temperatures are plotted with respect to the time of occurrence of the peak at h_0 . It is evident that after some 30 drops the peak temperatures at h_1 to h_3 swiftly decrease.

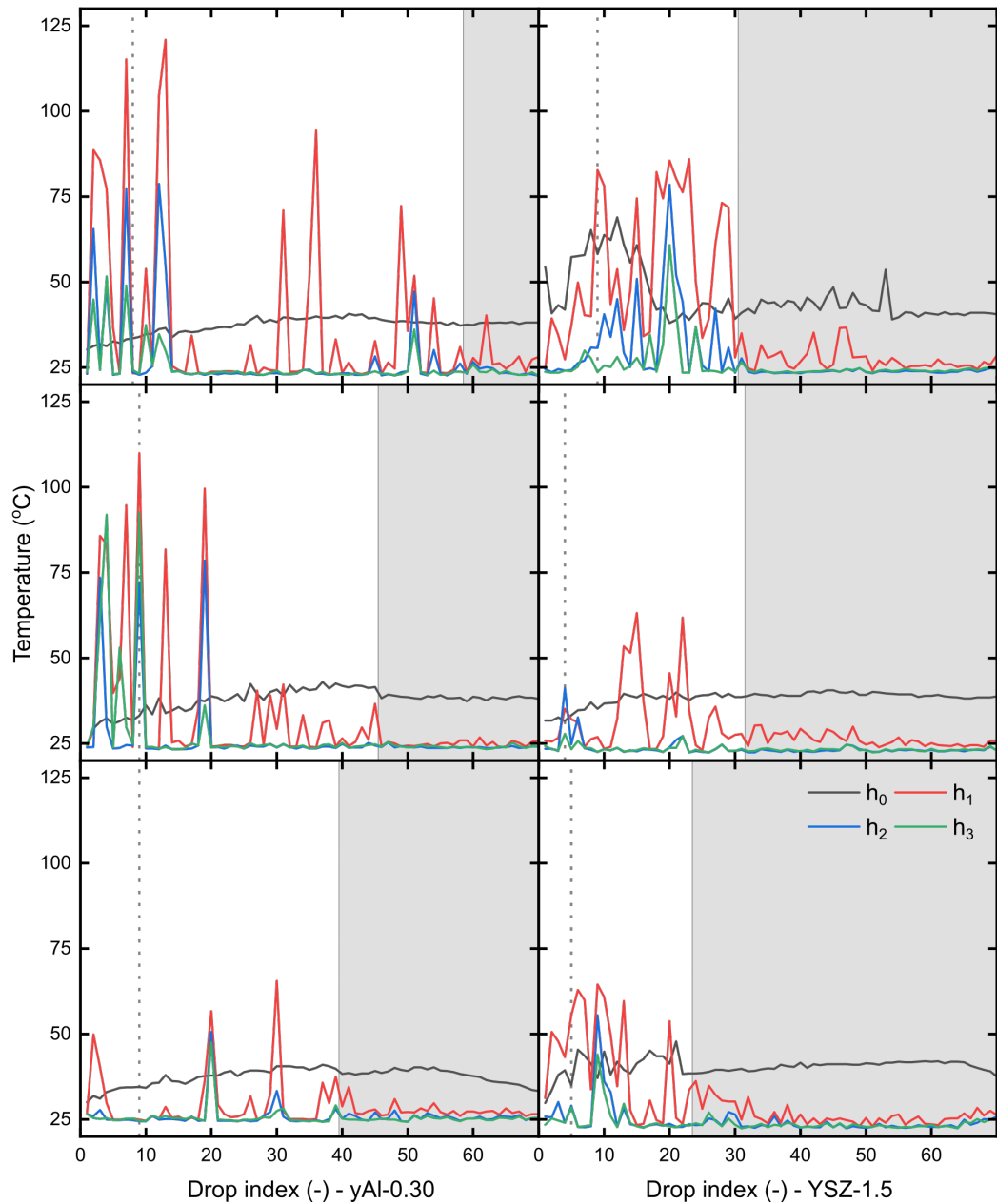


Figure 3.18: Peak temperature data for yAl-0.30 (left) and YSZ-1.5 (right). The onset of wetting is indicated by the vertically dotted line, whereas the fully wetted state is indicated by the shaded area. It can be seen that around the moment of full wetting all peak temperatures decrease.

Peak temperatures Figure 3.18 is a simplified representation of Figure 3.17 for all tested catalysts, showing the maximum attained temperatures at all heights, hence allowing an easy comparison. Immediately visible from Figure 3.18 are the (on average) higher attained and longer sustained (with respect to the number of decomposition events) temperatures for γ Al-0.30. Also evident is a large spread in behavior between equivalent samples, refer to e.g. γ Al-0.30-3. Further, the thermal data for γ Al-0.30 can be easily discerned from those for YSZ-1.5: the latter have a higher maximum base temperature (all above 40°C), but overall achieve a lower temperature at h_1 to h_3 . In addition, the peak temperatures fluctuate less at these higher points for YSZ-1.5. Since the YSZ-1.5 cercaps had a higher density, and thus were thinner, aluminum foil (pressed flat with 500 MPa) was placed underneath these cercaps to compensate for the height difference. It might be that, even though the piece was pressed flat, slight warping may have caused the YSZ cercaps to be located a little higher than the γ Al-0.30 cercaps. This on its turn decreased the distance to the base thermocouple, hence decreasing the effect of dissipation on the measured heat. Further, the consistently higher achieved base temperatures of YSZ-1.5-1 may be caused by a coincidental better alignment to the sensitive area of the base thermocouple.

Further, while all base temperatures appear to peak around the moment of full surface wetting, the maxima at h_1 to h_3 have all decreased considerably already before that. Even more, the latter all quickly go to zero after the onset of full wetting. Three fundamentally different phenomena might be responsible for this observed behavior. First of all, the present water effectively decreases the concentration of HP as experienced by the catalyst, thus leading to lower heat generation. This lower heat generation on its turn hampers the evaporation of product water, which further decreases the catalyst's activity. Secondly, the presence of water in the catalyst changes the transport mechanism of the reactant to the slower diffusion. Thus, less H_2O_2 molecules will be present at the active site and the replenishment takes longer, due to which less heat is generated. Lastly, the concurrent adsorption of water and H_2O_2 at the active sites might explain the decreasing heat generation: with increased wetting, more water is present, and less sites are available to decompose HP. If this would be the case, it can be posed that the interaction strength with the active site is similar for water and H_2O_2 : if water would block the active sites, the catalyst activity should already decrease after the first signs of wetting (as indicated in Figure 3.18 by the dotted line). Instead, the base temperatures of all samples continue to increase after the first signs of wetting; no such trend can be spotted in the effect of wetting initiation on the temperatures measured at h_1 to h_3 . Yet, it can be seen that the higher water content in the sample has a (temporary) deactivating effect on the cercap, hinting at a similar interaction strength with the active site for water and HP.

Bubble formation Figure 3.19 shows the spread in SBF and EBF. Next to that, the average moment of full wetting is indicated. Most likely because determining the end of the bubbling became ambiguous at some point, due to the limited video quality, the average time until full wetting (marked area) and the EBF do not coincide. In addition, the large SBF for one of the YSZ-1.5 cercaps (almost 600% higher than for the other two YSZ-1.5) is probably caused by the same video quality. When the data are inspected more closely, it is evident that the moment of total flooding of the cercap does not have a distinct effect on the SBF. One would expect that when the cercap is continuously exposed to (deactivating and diluting) water, the time required for the reaction to start would increase, and thus the time required for the formation of the first reactant gasses, and consequentially the first bubble. On the one hand this could mean that the triggering of decomposition (Figure 3.15b) is not dependent on the number of available active sites or the concentration of HP; this could be proven by repeated testing with different HP concentrations and cercaps with varying manganese loadings. More likely though, these results seem to indicate that the SBF is merely a measure for bubble formation kinetics, not so much for reaction kinetics. The slight downward trend in SBF for γ Al-0.30 seems to support this hypothesis: bubble formation is easier when liquid is already present. So, when a larger fraction of the surface is already wet, the time to bubble formation should decrease, which is exactly what is shown by γ Al-0.30. This effect is not as much present in YSZ-1.5; only after some 55 drops this effect seems to take place. This is presumably caused by the presence of cracks in the YSZ-1.5 cercaps, which can serve as seeding points for bubble formation already at the start.

Further, the aforementioned differences in vertical alignment do not explain the smaller fluctuation in peak temperature at h_1 to h_3 for YSZ-1.5. A correlation between the EBF (see Figure 3.19) and the reaction length might explain these fluctuations. Namely, when the the time it takes to convert one drop of HP increases, so will the time of heat generation. The cercap thus will stay warm for a longer time, which on its term leads to a higher heat release on the next decomposition event (since less heat has to be used to warm up the entire cercap to the required activation temperature), and thus the measured temperatures will be

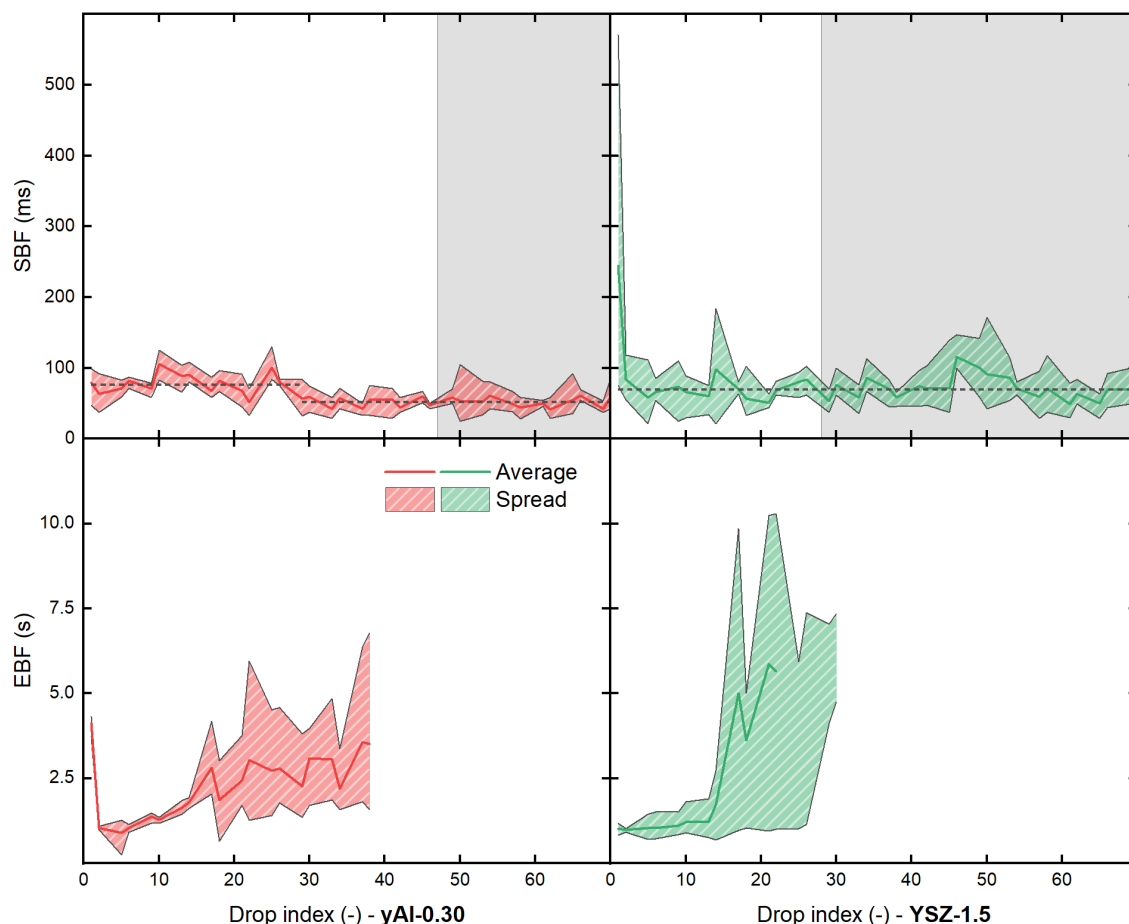


Figure 3.19: Results from the video data showing the start of bubble formation (SBF, top) and the end of bubble formation (EBF, bottom), both for $\gamma\text{Al-0.30}$ (left) and YSZ-1.5 (right). The shaded area indicates the fully wetted state of the cercaps. The dashed lines are intended as a guide for the eye.

higher. Though, when the individual EBFs are directly compared to the temperature traces of YSZ-1.5, there is clearly no such correlation. Nevertheless, even though there does not seem to be a correlation between the (visually observed) EBF and the observed phenomenon, this does not necessarily mean that the extended reaction length cannot explain the increasing base temperature. Namely, the YSZ-1.5 cercaps appear to possess a much lower porosity. While the $\gamma\text{Al-0.30}$ cercaps seem to absorb the entire drop, for the YSZ-1.5 cercaps it was obvious that part of the HP would end up next to the cercap. This barely visible "reservoir" of HP could then allow the cercap to continue decomposition and hence remain warm until the next drop of HP arrives. The presence of this reservoir might also explain the lower peak temperatures as found for YSZ-1.5: when less HP is converted, less heat is generated and thus a larger fraction is dissipated in surroundings, which leads to a lower detected peak temperature at larger distances from the catalyst.

3.3.3.2. Activation effects

Close inspection of the first two decomposition events, as is displayed in Figure 3.20, shows that the second decomposition event for $\gamma\text{Al-0.30}$ consistently results in a higher heat dissipation; while this is not so much visible for YSZ-1.5. These observations indicate that the $\gamma\text{Al-0.30}$ cercaps seem to require activation to liberate their full catalytic potential. This section will investigate this phenomenon in more detail and try to explain it based on the samples' composition.

$\gamma\text{Al-0.30}$ activation effects First of all, based on the present manganese phase in $\gamma\text{Al-0.30}$, Mn_3O_4 , it is surprising that the catalysts show such high reactivity: authors usually report that this manganese oxide is only slightly more active than the rather inert MnO with concentrated HP, see e.g. Guseinov [42]. The reactivity might be explained by the charge deficiency in the mixed (II)-(III) valence manganese phase, which is caused

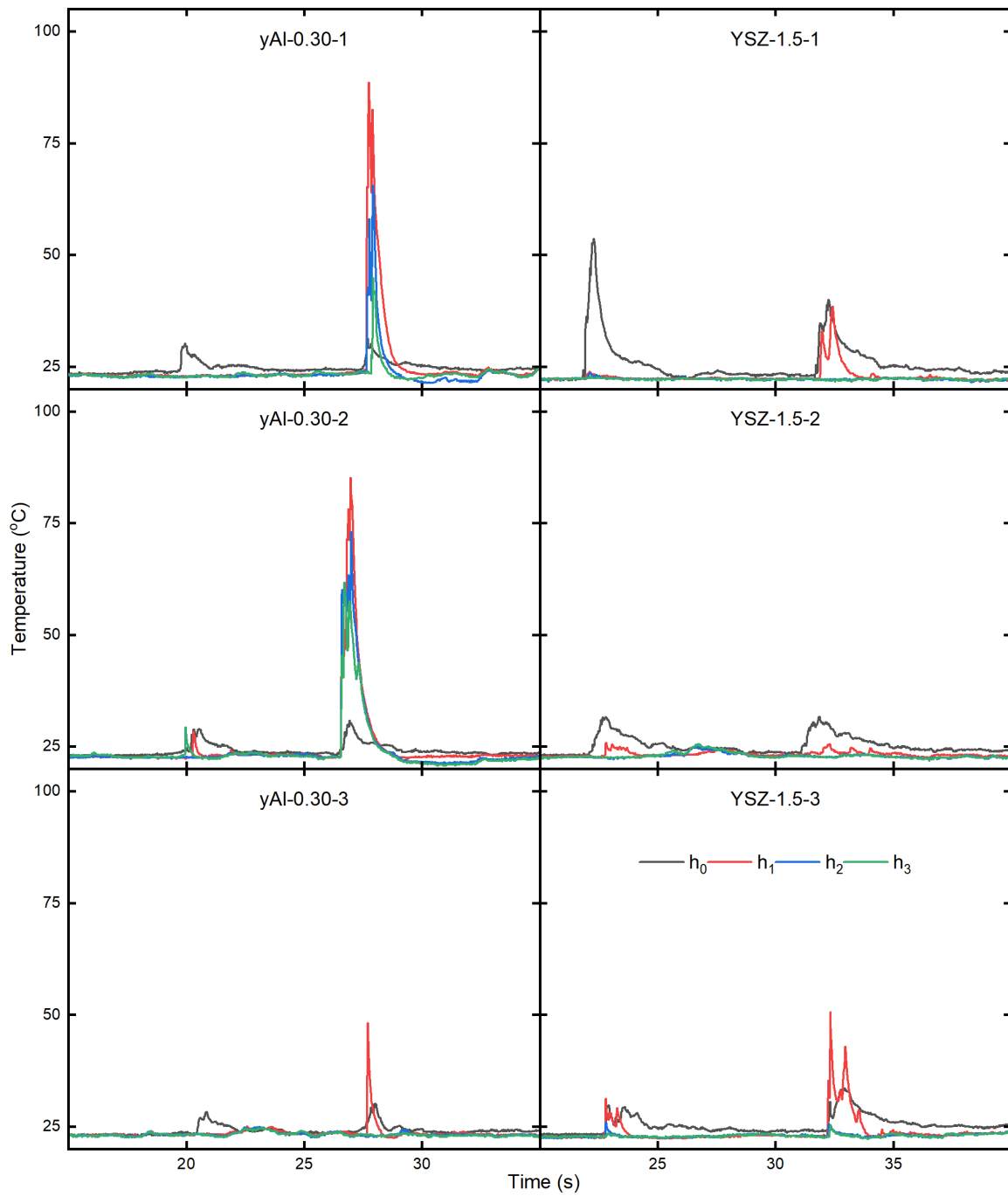


Figure 3.20: Comparison of the thermal trace of every first two droplets for all tested (constrained) cerccaps. For yAl-0.30 it is evident that the heat released to the surroundings is higher for the second drop; this hints at a possible activation effect.

by doping with Al^{3+} ions, as is discussed in [subsection 3.1.5](#) and shown by Wu and coworkers [130]. Concretely, this charge deficiency will lead to a partial oxidation of the Mn^{2+} ions, and may also divert some charge away from the Mn(III) ions (the latter effect will not be intense though, due to the almost equal electronegativity of aluminum and manganese: $\Delta\text{EN} = 0.06$). This means that the doped Mn_3O_4 probably behaves similarly as Mn_2O_3 , which is known to be more reactive with HP (although less than MnO_2). If it is assumed that the catalytic cycle given in [subsubsection 1.3.2.2](#) is correct, this could explain the peculiar behavior as is visible in [Figure 3.20](#). Namely, this figure seems to show that the $\gamma\text{Al-0.30}$ cercaps require an activation step, i.e. the present MnOx phase first needs to be converted into a (more) reactive phase. It is thus possible that the first drop with HP leads to a true oxidation of hausmannite to the more reactive Mn_2O_3 or even MnO_2 . The large EBF at the first decomposition event as displayed by all three $\gamma\text{Al-0.30}$ samples seems to be in favor of this hypothesis.

As was already mentioned above, the proposed conversion is not persistent: after the reaction both XRD and Raman spectroscopy show that still only hausmannite is present. If the mentioned oxidation *does* take place, it would mean that during or after drop-testing, the back-reduction to hausmannite has to occur. Perhaps hausmannite (or a in-situ formed derivative) is not even involved with the observed reactivity. Rather, the reactivity is caused by an undetected compound, of which only a relatively small amount is present. This compound could go unnoticed due to the qualitative nature of the available characterization techniques. Hence, further characterization of the γAl cercaps is essential to find the active manganese phase.

Further, during the experiments conducted on $\gamma\text{Al-0.30}$, a clear black line would appear at the fluid front after 16 to 39 drops, as can be seen in [Figure 3.21](#). The emergence of the black front does not seem to correlate with the onset of wetting. This black area would move together with the fluid front to the other edge of the cercap where it would disappear. The presence of this black line did not seem to influence the thermal data, nor the EBF and SBF. Its movement along with the fluid front suggests that the species responsible for the dark color is poorly soluble in water. In addition, [Figure 3.21](#) suggests that the concentration of this compound increases with time (or surface wetting). Since this phenomenon would disappear during the testing, no spectroscopy could be conducted on this specific area. Additionally, its occurrence did not reflect in the chemical characterization performed after the experiments. Several explanations can be supplied to elucidate this phenomenon. Either this chemical is soluble in HP, but not in water, which explains why it is only visible after HP has reacted. Alternatively, the reaction heat may have converted a soluble into an insoluble species. The movement of the fluid front might then have gradually removed it from the cercap. It could also be that some species had washed out of the cercap itself during the reaction. This could be carbonized PVA or glycerol (as are claimed to be present by Wu et al. [129]); yet, pre-reaction characterization did not show *detectable* amounts of carbon. Another explanation of this phenomenon might be the formation of a different phase of MnOx at the water-air interface. This conversion might be permanent, but then only a small amount of the hausmannite had been converted, since no changes in composition could be found. Conversely, the hausmannite is reformed upon drying of the cercap. Further testing and (in-situ) spectroscopy should thus be conducted to explain this observation.

YSZ-1.5 activation effects While the YSZ-1.5 cercaps contain five times more manganese than the $\gamma\text{Al-0.30}$ samples, their catalytic activity appears comparable. A physical factor contributing to this observation may be the observed lower porosity, due to which not only less active sites are exposed, but also transportation of reactants to the active sites can be influenced. Alternatively, this observation can indicate that the catalytic phase is simply less active, or that only part of the added MnO_2 is converted into an active species. Due to the lack of knowledge on porosity and on the present oxidation states of manganese in YSZ-1.5, no definite conclusions can be tied to the observations. A similar activity enhancing electronic effect as described above for $\gamma\text{Al-0.30}$ is most likely not present for YSZ-1.5: manganese has a higher electronegativity than both yttrium ($\Delta\text{EN} = 0.33$) and zirconium ($\Delta\text{EN} = 0.22$). This would put a higher electronic charge on manganese, hence stabilizing lower (less reactive) oxidation states.

Even though in the above it was postulated that most manganese would be present as the inactive MnO, drop-testing clearly proved the catalytic activity of the YSZ-1.5 cercaps. This could be caused by the presence of a certain amount of Mn_2O_3 , as was predicted by the thermodynamic calculations. When compared to hausmannite, Mn_2O_3 should already be more active initially. While the first EBF values for YSZ-1.5 seem to be in favor of this hypothesis, this is not unambiguously evident from [Figure 3.20](#). This may indicate that the mechanism as posed in [subsubsection 3.3.2.2](#) is correct, i.e. most manganese is present in a finely dispersed MnO phase. The YSZ-1.5 cercaps would then either require more HP to be oxidized into an active catalytic phase or remain less reactive (which is compensated for by the relatively high weight loading).

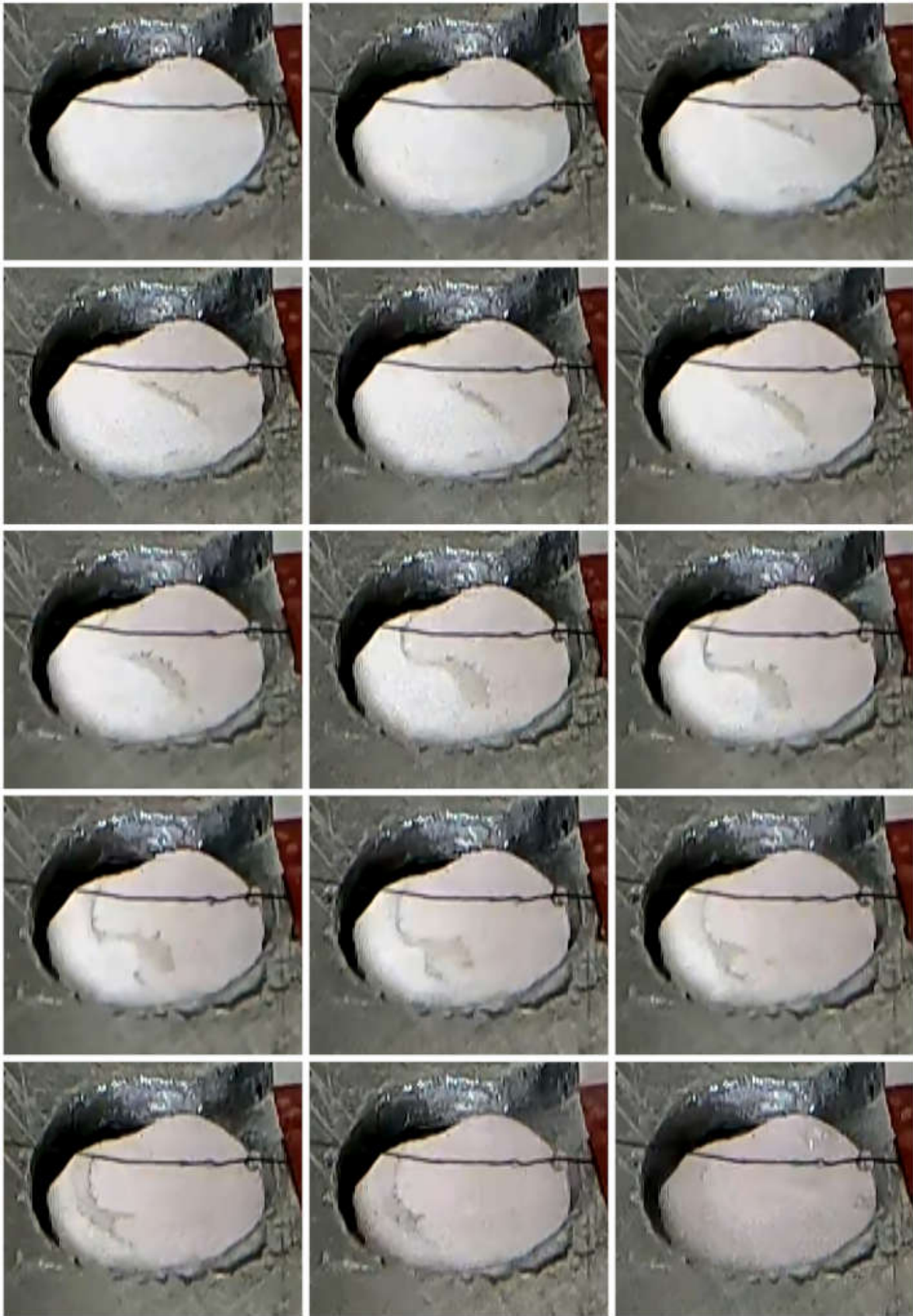


Figure 3.21: Development of a black front on the γ Al-1.5 cercaps, here shown for γ Al-0.30-3.

To conclude this section, in order to elucidate the origins of the reactivity of both ceriap materials, more advanced spectroscopy is required; for $\gamma\text{Al-0.30}$ to determine the effects of doping on the electronic properties of manganese ions and correlate this to the observed catalytic activity, for YSZ-1.5 to determine the present oxidation state of manganese.

3.3.4. Post-reaction characterization

As has been mentioned above, the inadequate sensitivity of the available analysis equipment severely hampered the identification of MnOx phases. This is also true for the spent cercaps. Due to the high background signal of the YSZ, XRD and Raman spectroscopy could not be used for the identification of manganese in YSZ-1.5. Further, the Raman spectra taken of a spent $\gamma\text{Al-0.30}$ sample (Figure 3.22) showed some remarkable features. No hausmannite can be detected in the first probed (comparatively dark) location, whereas earlier it was found that these dark spots were enriched with hausmannite. The dark shade is most likely caused by the presence of carbon deposits, as can be concluded from the typical carbon peaks at 1310 and 1600 cm^{-1} . As was reported above, these carbon species most likely originate from carbonization of PVA and glycerol. The highly localized nature of Raman measurements might explain why no carbon could be found in the pristine cercaps. The second probed (dark) location seems to show a rather disturbed hausmannite spectrum. It is known that the orientation of a crystal with respect to the laser source has a large effect on the observed spectrum [98]. Perhaps then the here observed location features highly crystalline hausmannite in a single orientation. This hypothesis is supported by the XRD data (see Figure 3.23) that show the post-reaction presence of hausmannite in $\gamma\text{Al-0.30}$. Comparison with reference Raman spectra for other manganese phases does not result in further identification of the clearly present compound in this location.

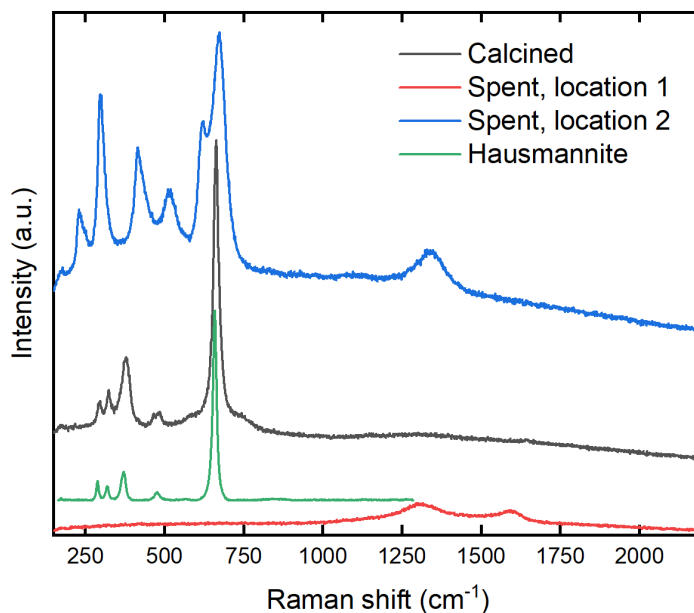


Figure 3.22: Raman spectra showing a comparison between fresh $\gamma\text{Al-0.30}$, and two different locations of a spent $\gamma\text{Al-0.30}$ ceriap. Included for reference is a hausmannite signal recorded from a large number of randomly oriented crystal grains (RRUFF R110179).

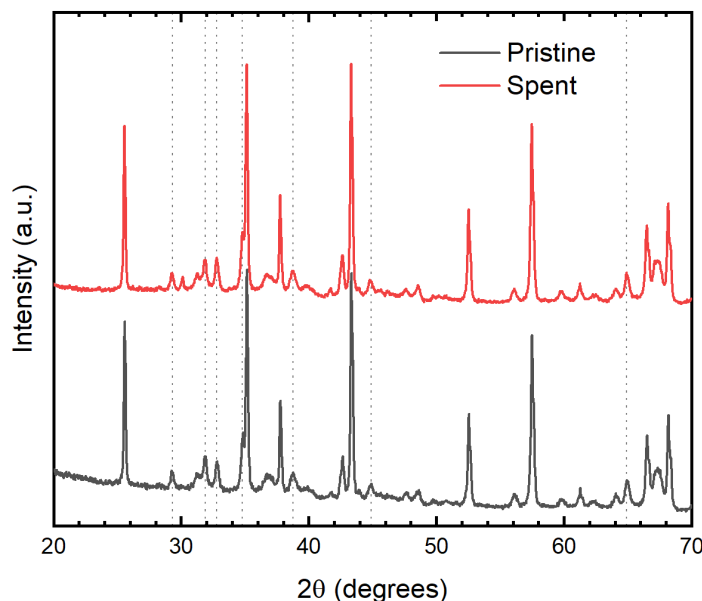


Figure 3.23: XRD patterns of both pristine and spent γ Al-0.30 catalyst. The vertically dashed lines indicate the position of hausmannite. Comparison of the diffraction patterns shows that the hausmannite has remained unchanged.

3.4. Conclusion

First of all, the here used solid state synthesis method produced mechanically rigid catalyst bodies. In contrast to what is commonly accepted [42, 49], the exposure of manganese oxide catalysts to high temperatures, such as used here for calcination, does not necessarily lead to permanent deactivation of the catalyst. It was shown here that this thermal deactivation can be avoided with a properly selected support material. Of the here tested metal oxides, only γ -alumina and YSZ displayed satisfactory catalytic activity with 87% HP during drop-testing (REQ-CAT-1). Spectroscopic information indicated that the dominant manganese phase in γ Al-0.30 is Mn_3O_4 , as is reported elsewhere [11, 12, 17]. The manganese phases present in YSZ-1.5 could not be determined using the carried out characterization efforts. Based on thermodynamic calculations, it is proposed to consist primarily of (supposedly inactive) MnO and Mn_2O_3 .

Further, this research has successfully demonstrated that drop-testing with concentrated HP can be used to probe the catalytic activity of heterogeneous catalysts. The carried out investigations showed that both γ Al-0.30 and YSZ-1.5 are active for a prolonged time. During experiments in which the catalysts were allowed to move laterally, it was shown that even after 300 decomposition cycles with 87% HP, the decomposition temperatures would not drop below 50°C for both catalysts (REQ-CAT-3). When the catalyst bodies were constrained, deactivation due to flooding occurred already after an average of 28 (YSZ-1.5) or 47 (γ Al-0.30) decomposition reactions. It was also shown that this deactivation by product water was temporary and the catalyst could be easily regenerated by simply drying to the atmosphere (this should occur readily in the vacuum atmosphere as present in space). These findings indicate that an improved reactor design will mitigate most experienced problems.

During testing of γ Al-0.30 it was noticed that the catalytic reactivity would not be maximal already at the first decomposition event. Instead it would require one or two drops of 98% HP to considerably increase the measured decomposition temperatures. This behavior hints at the in-situ formation of an active phase. Yet, post-reaction characterization merely showed the presence of Mn_3O_4 ; thus, the active phase is either not stable and converts back to Mn_3O_4 or is present in too low quantities. In contrast, the YSZ-1.5 catalysts did not exhibit such behavior, moreover these showed consistently lower catalytic performance. This was attributed to both the nature of the active phase and its supposedly lower porosity (causing reactant transport limitations).

Additionally, it was shown that decomposition of 98% HP over the γ Al-0.30 catalyst can potentially induce hypergolicity with ethanol: the maximum reached temperature was 460°C (REQ-CAT-2; threshold: 369°C). For YSZ-1.5 such a peak temperature was not observed; further research should serve to validate REQ-CAT-2 for both catalysts. Unfortunately the equipment used for reaction monitoring was not sensitive enough to investigate the decomposition delay accurately. Requirement REQ-CAT-4 can thus not be validated at this

time.

Further, to enable successful implementation in rocket engines, more practical aspects must be considered as well. From an economic point of view, a lower loading of active phase would be more beneficial, especially if this does not influence the catalyst's reactivity. It is clear that the γ Al-0.30 cercap offers an advantage here. It must also be considered that when a catalyst must operate in a very harsh environment, physical durability and low porosity are important. Even though both materials displayed surprisingly high mechanical strength, the γ Al-0.30 catalyst exhibited a higher brittleness. In addition, visual observations indicate that this cercap possesses notable porosity, which could lead to accelerated physical degradation in a representative combustion environment. Due to its brittleness, it was not possible to quantify the physical degradation of the γ Al-0.30 cercap, which hinders a direct comparison with YSZ-1.5. The relevant physical and experimentally probed catalytic properties of the γ Al-0.30 and YSZ-1.5 cercaps are summarized in Table 3.2.

Table 3.2: Qualitative comparison of the physical and catalytic properties of the tested cercaps. A higher performance has been marked with a (+) whereas lower performance has been marked with a (-). Deficiencies in the research have been indicated with a (?).

	γ Al-0.30	YSZ-1.5
Manganese loading	+	-
Mechanical strength	-	+
Observed porosity	-	+
Active phase deactivation	+	?
Peak temperatures	+	-
Lifetime	+	+
Hypergolicity potential	+	?

3.5. Recommendations

This chapter will conclude by supplying recommendations for further research. These will be split into recommendations with respect to testing equipment and to the materials. As many researches, this investigation suffered large delays due to the COVID-19 pandemic. This not only reflected in delayed delivery of materials, but also absence of personnel. The long-term absence of knowledgeable technicians required the author to construct the drop-testing setup from scratch, contributing to the misalignment errors.

3.5.1. General recommendations

First and foremost, due to time constraints this research was only able to focus on the decomposition of HP. The here presented results indicate that the decomposition heat is high enough to induce hypergolicity with ethanol. Future experiments should be aimed at proving this important feature.

At this time, the catalyst loading was too low to evaluate with the available spectroscopic tools. This led to the inability to determine the catalytic phases that are responsible for the catalysts' reactivity for all samples. Thus, more sensitive analysis equipment should be employed to clarify this matter. Namely, it is essential to know what is causing the reactivity in order to improve the overall catalyst behavior. Further, in-situ testing (e.g. in-situ TEM) could not only elucidate activation phenomena, but also show early signs of deactivation.

Because drop-testing in this form does not continuously expose the catalyst to high temperatures, and the use of a test engine is most often too involved, it is imperative to test the catalysts in a controlled environment (a flow cell) at high temperatures in order to monitor long-term deactivation phenomena. To exclude the dangers associated with handling gaseous high temperature HP, it should be considered to employ chemicals with a comparable effect on the catalyst, such as nitrous oxide.

Lastly, according to Bulavchenko et al., the best catalytic results are obtained with impregnated alumina and even more so for coprecipitated manganese oxide and alumina [12]. It is not sure to what extent this is also applicable to the decomposition of HP. Though, in this research it was shown that a YSZ cercap loaded by by deposition precipitation (10 wt.% MnO₂) showed low reactivity when compared to the SSS cercaps.

Parallel to the investigation of the MnOx catalysts, a platinum catalyst supported on a metal oxide perovskitic matrix was synthesized. As is elaborated upon in chapter C, this catalyst - support combination promises high suitability for use in HP-ethanol engines. The results of this investigation can be found in sub-section D.1.1. In the available time-frame, this platinum-based catalyst could not be sufficiently reduced into the active form, and hence it did not display catalytic activity with HP. Yet, the promising results as have been shown in literature necessitate more research of this ReMOP.

3.5.2. Reactor design

As is clear from the above, the current test setup showed severe shortcomings. First and foremost, the activity measurements could only be run for short periods due to the rapid wetting and consequential deactivation of the cercaps. Additionally, the high air circulation speed in the fumehood quickly carried away the hot decomposition gasses, due to which the measured temperatures were low. In addition, this may have contributed to the inadequate alignment of the thermocouples. Further, as was mentioned in [subsection 3.2.3](#), current drop-testing setups suffer from both poor reproducibility and poor resemblance to the combustor environment. This could be resolved by proper design of a closed drop-testing setup, while simultaneously allowing drainage of reactant water and surplus HP. Alternatively, standardized laboratory analysis equipment could be used to simulate the effects of decomposition or combustion on the catalysts.

Other factors that increase the applicability of drop-testing to rocket engine design are:

- Decreasing the drop size (propellant atomization). This would remove part from the measured ignition delay which is caused by spreading of the HP over the catalyst surface. Additionally, finer droplets would spread the reaction over the catalyst, which would also occur in a gaseous environment.
- A hollow shaped catalyst body would be more representative of the actual combustion environment. Additionally, this would help in preventing the wetting of the catalyst.
- When the catalyst would be kept at a constant temperature, the reproducibility of the experiments will increase. Gradual heating of the cercap, due to decomposition events, should be avoided. In addition, keeping the catalyst at an elevated temperature would aid in the evaporation of both hydrogen peroxide and produced water. In addition, heating of the catalyst will aid in achieving hypergolicity.

3.5.3. Recommendations with respect to instrumentation

The quality of the results can be considerably improved. As was noticed during the experiments, the time between drop impacts would deviate, even though the same flow rate was used, indicating the need for a more precise syringe pump. The fluctuating drop delay most likely has an influence on the equilibrium temperature of the catalyst, which on its turn affects its decomposition behavior. Further, this decomposition behavior could be monitored in more detail when a more sensitive camera is used that also has a higher time resolution, which also applies to the data recorder: with the current time resolution the different phases in a decomposition event can barely be distinguished. With increased temporal resolution of the instruments also the DD could be determined; for yAl it will probably remain troublesome to determine the DD from visual data due to its porosity.

Stabilizing propellant-grade H₂O₂

As has been elaborately discussed in [section 1.5](#), the storage life of hydrogen peroxide is limited: over time the molecules will fall apart into water and oxygen. When HP is used as a space propellant, this degeneration effectively reduces the amount of propellant and thus the lifetime of the spacecraft. Of course, this decrease in concentration can be accounted for by increasing the amount of HP stored in the spacecraft. Yet, since only the launch costs of one additional kilogram can already easily add over 10,000\$ to the project cost [104], it is always aimed to minimize spacecraft weight. To be able to present HP as a suitable alternative to current toxic fuels (such as hydrazine) its stability must be improved. In this research it was aimed to develop a new stabilizer that does not degrade over time and does not negatively influence the combustion system. To support the research effort, the following research questions were formulated.

RQ-STA-1 *How does the concentration of HP affect its stability?*

Motivation: Theoretically, higher concentrations of HP are more stable. Can this be reproduced here? Also, do the stabilizers work better or worse with higher concentrations of HP?

RQ-STA-2 *What is the influence of the surface-to-volume ratio of stored HP on its stability?*

Motivation: Since decomposition of HP mainly occurs on surfaces [109], more relative surface area would result in a higher decomposition rate. Also, does the addition of an anodized aluminum strip, ergo extra surface area, accelerate the decomposition?

RQ-STA-3 *How can aluminum be treated such that it is suitable as a stabilizer support?*

Motivation: Aluminum is compatible with HP; aluminum oxide is a often used support material. Anodizing produces such a layer on top of the aluminum. Does the presence of the oxide layer influence the compatibility of the aluminum with HP? Does the hard anodized aluminum interact sufficiently with the tin oxide colloids, or are they removed over time?

RQ-STA-4 *What effect does immobilization have on the stabilizing action of the colloids?*

Motivation: Is the mobility of the stabilizers fundamental for their stabilizing action, or does the calcination affect the stabilizing performance in any other way?

RQ-STA-5 *How do different types of stabilizers interfere with each other?*

Motivation: Already a small amount of stabilizers is often present in HP; some manufacturer supply a product with more stabilizer (e.g. Sigma Aldrich), whereas e.g. Solvay barely stabilizes their product. Do these added stabilizers interfere with the tested stabilizer strips?

First a concise background of H₂O₂ decomposition mechanisms and the state-of-the-art of stabilizers will be presented. This will be followed by the experimental description, and a discussion of the results. Some concluding remarks will be given in [section 4.4](#); recommendations for future research will be supplied afterwards.

4.1. Background

This section will first provide a short summary of the decomposition mechanisms of H₂O₂, since knowledge of the process enables rational design of a novel stabilizer. This is followed by a description of the currently used stabilizers for HP in [subsection 4.1.2](#). Then [subsection 4.1.3](#) explains how the TOCs will be supported, and afterwards the used immobilization process will be touched upon.

4.1.1. Decomposition mechanisms of H₂O₂

The instability of HP is caused by two degradation mechanisms that both result from the weak peroxide (O–O) bond: autodecomposition and catalytic decomposition. Both forms have a different behavior over time, which can be explained by the reaction taking place. Whereas the autodecomposition reaction requires

two H₂O₂ molecules to commence, catalytic decomposition requires only one [49, 110]. One can imagine that when the concentration of HP molecules decreases, it is increasingly more difficult for a H₂O₂ molecule to encounter a catalytic particle. Yet, it turns out that it is even more difficult to encounter and interact with another H₂O₂ molecule. It can thus easily be understood that the prominence of the autodecomposition reaction is less and decreases faster over time or concentration than that of the catalytic decomposition.

4.1.1.1. Autodecomposition

The degree of autodecomposition, which is generally several factors lower in intensity than catalytic decomposition, is dependent on several factors, of which most prominent are temperature, acidity and concentration. Temperature is a measure for the average thermal energy of a molecule. Thus, when the temperature is increased, more molecules will be able to overcome the activation energy barrier, or: more molecules will react. Conversely, if the temperature is decreased, fewer molecules will react: the chemicals can be considered more stable. While on Earth temperature fluctuations are generally relatively small and can be easily managed, in space temperatures fluctuate between -150 and +150°C: at such high temperatures thermally enhanced autodecomposition becomes more prominent.

Acidity also has an influence on the decomposition rate. The perhydroxide anion (HOO⁻), which is thought to be the reactive phase [33], increases in concentration at higher pH. To that extent many manufacturers choose to decrease the pH of the HP. It can be understood however that a too low acidity will negatively effect metallic propulsion system components, thus limiting the extent to which the acidity can be employed to enhance the stability of HP.

Lastly, whereas decomposition rates of chemicals generally increase with increasing concentration, the opposite is true for HP, which is most stable in its anhydrous form [109]. This behavior may be caused by the inherently lower concentration of water molecules at high concentrations: water molecules can easier deprotonate a H₂O₂ molecule than another H₂O₂ molecule can (see chapter A), and hence convert it into the reactive ion. Unfortunatley, this characteristic can only be exploited to a certain extent to improve HP lifetime, since the used concentration is often determined by the propellant system specifications.

4.1.1.2. Catalytic decomposition

Catalytic decomposition is induced by trace metal impurities (the ions of e.g. Cu, Fe, Mn), inevitably introduced during the production process. Current production processes have been optimized to reduce these contaminants into the ppm or ppb level, yet decomposition in storage drums can still be around a few % a year [33]. A well-known effect in the storage of HP is that larger drums result in a lower decomposition rate. It is plausible that this effect is caused by adsorption of these trace metal impurities on the storage vessel surface. This adsorption could make the interaction with a H₂O₂ molecule easier due to the reduced mobility of the metal ion, and hence increase decomposition. A lower relative surface area (i.e. larger storage vessels) would thus result in a lower decomposition rate, as is widely observed [22, 33, 109, 125].

In order to increase the storage life of HP, it is thus essential to either further decrease the introduction of these metals during production or storage, or to counteract the effects of these metal ions. Further optimization of manufacturing processes is rather tedious, since the concentrations of metal contaminants are already very small and difficult to detect by many analysis techniques. Introduction of contaminants during storage can be minimized by use of compatible materials, such as high purity aluminum or fluorinated polyethylene [22]; yet, these materials offer low structural performance. HP-compatible propellant tanks based on these inert materials would thus need to be additionally stiffened, either by increase of the tank wall thickness, the application of stiffener structures or a load-bearing shell. All these solutions result in an increase in storage tank mass which, for space missions, would result in a higher space mission cost. Alternatively, the impact of these impurities can be mitigated by the addition of stabilizers, as will be elaborated upon in the next section.

4.1.2. Currently used stabilizers

A more economical approach than further reduction of contaminants is the addition of stabilizers to the HP solutions, as has already been done for over seventy years [109]. These stabilizers can be separated in two categories: chelators and metal oxide colloids.

4.1.2.1. Chelator stabilizers

The first group of stabilizers is often composed of nitrogen- or phosphorus-based compounds, such as inorganic oxides (e.g. nitrates) or organic complexes (e.g. organophosphorus compounds). These (reversibly) immobilize the metal ions by the strong interaction between the stabilizer's reactive group and the metal ion, and hence decrease its ability to react with HP. However, this passivation effect also works with the catalysts that are used to convert the HP into thrust: phosphorus-based chelators poison the catalyst, hence deactivate it, and thus render the propulsion system inoperative [30, 47, 97, 100]. Merck (or formerly known as Sigma Aldrich) supplies HP with a nitrogen-based stabilizer, 2,6-pyridinedicarboxylic acid (PDC, as is visualized in Figure 4.1), which should have very limited (negative) interaction with catalysts.

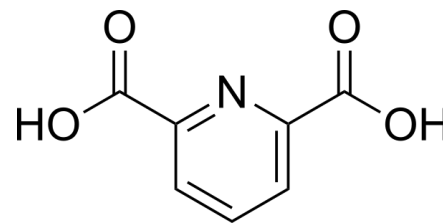


Figure 4.1: PDC molecule.

4.1.2.2. Tin oxide stabilizers

The other commonly used stabilization method is the dissolution of sodium stannate, $\text{Na}_2(\text{Sn}(\text{OH})_6)$. As hypothesized by Schumb already in 1954, the dissolution of this stannate will result in the formation of nanometer-sized metal oxide particles [109]; yet, to date no proof has been given in literature for this hypothesis. These dispersed nanoparticles (or colloids, with size between 1 and 1000 nm) can reversibly immobilize metal ions in an apparently similar manner to the chelators, however the underlying mechanism is fundamentally different. In short, the colloids present a negatively charged surface to the solution, which attracts and binds the positively charged metal ions. Even though this behavior can be observed for multiple metal oxides, for the stabilization of HP mostly sodium stannate is used [33], the precursor of the supposedly forming tin oxide colloids (TOCs). The kinetics of both the TOCs and the metal ions are essential in order to immobilize the latter: a higher concentration of stabilizer should lead to a higher chance of collision between them and thus lead to a decreased HP decomposition rate. Further, in contrast to many chelators, these stannate colloids do not have a similar poisoning effect on catalysts [97]. Unfortunately though, their stabilizing performance decreases over time, which is presumably caused by sedimentation of the colloids. This sediment could cause clogging of the propellant system and thus ultimately lead to complete propulsion system failure. Hence, it is of utmost importance to understand and mitigate the effects of the sedimentation.

Two size-dependent mechanisms can cause particle growth or ultimately settling of colloids. Gravitational settling is most prominent for large colloids. This process is most likely absent when the spacecraft is in space due to the experienced net zero gravity, not only by the spacecraft itself, but also by the individual colloids in the HP propellant¹. Though, it should be taken into account that spacecraft are not always immediately launched after the propellants have been loaded, especially when these propellants possess low toxicity or other handling risks.

The second sedimentation mechanism is that of Brownian encounters. Colloids move with high velocities in random directions through the fluid, with the magnitude of the velocity being inversely proportional to their size: smaller particles collide with higher momentum and thus have higher probability of fusing [96]. Further, each colloid is surrounded by a charged double layer whose size is independent of the size of the colloid. This double layer inhibits sufficiently close encounters of other colloids. However, the presence of dissolved ions, such as aluminum ions etched from the tank wall, decreases the extent of this double layer and hence increases the probability of particle fusion. For larger particles, the relative repulsion effect of the double layer is less, which means that a less energetic impact may already result in particle fusion. When the average particle size increases, this also means that the total surface area of the stabilizer decreases, and thus the total stabilizing capacity decreases.

4.1.3. Aluminum as stabilizer support

As was discussed above, the goal of this research is to immobilize TOC stabilizers. The performance of the support material is of great importance, not only since it is responsible for the anchoring of the colloids, but also because of the mutual electronic effects between them: a poorly chosen support can decrease the (negative) charge on the tin oxide, decreasing the stabilizing activity. In catalysis, metal oxides are a very important group of support materials, of which aluminum oxide (also known as alumina) is among the most

¹The extent of colloidal sedimentation in low gravity environments is still unclear and remains an active field of research.

used ones. Further, it is known that metallic aluminum forms a strongly adhering and passivating oxide layer when exposed to air. Theoretically, metallic aluminum construction materials, for instance tank walls, could thus serve as a supporting layer for the stabilizing colloids. Application of a stabilizing coating for HP on tank walls would lead to an increase in tank manufacturing cost, but with a negligible increase in weight, while simultaneously leading to an increased storage life of HP.

Unfortunately, the alloying elements present in most aluminum alloys accelerate decomposition of H_2O_2 . However, aluminum from the ASTM 1000 series can be considered inert with respect to concentrated HP due to the low concentration of reactive alloying elements (aluminum content >99%) [22, 33, 109]. Because of the near absence of alloying elements these alloys have low mechanical strength, due to which these pure alloys are of low interest in traditional tank design. Nowadays propellant tanks are increasingly manufactured of composite materials, which suffer from porosity and thus are often provided with a low load bearing metallic liner [117]: a pure aluminum alloy could be suitable for this purpose.

The naturally forming oxide layer on aluminum is rather thin and not necessarily uniform, which might lead to etching by or leaching of HP at crevices or thin spots; this can be easily resolved by (hard) anodizing the aluminum. Anodizing aluminum is an established technique to increase the thickness of this oxide layer and hence increase its corrosion resistance. It is carried out by forced electrolytic oxidation in a concentrated acid solution to form a thick and atomically flat Al_2O_3 -layer [13, 39, 89, 115]. In the realm of HP tank storage materials, anodizing would result not only in lower release of aluminum ions, but simultaneously in a suitable anchoring site for the tin oxide stabilizers. N.B. Ono et al. report that during this anodizing alloying elements are removed from the forming oxide layer [89]. This might imply that hard anodized aluminum construction alloys become compatible with HP, thereby significantly reducing traditional metallic tank mass and cost. Nevertheless, it is not known what effect this would have on the anchoring properties of the oxide layer.

All above considerations led to the selection of hard anodized ASTM 1000 series aluminum as a supporting material for the tin oxide stabilizer in these experiments.

4.1.4. Immobilizing tin oxide stabilizers

High surface area tin oxide is widely investigated for use in battery electrode materials, starting both from TOCs or tin chloride (for example [92]). Several routes are in use to anchor tin oxide to e.g. aluminum oxide, among other things spray pyrolysis and drip- or dipcoating on metal oxide surfaces, followed by calcination [58, 82, 101]. In this research, it was chosen to employ dip-coating followed by calcination to reach intimate contact between the supporting aluminum oxide and the colloids. This had several prominent advantages when compared to spray pyrolysis. Most importantly, since the starting product is uniform there is less uncertainty in the final surface area. Secondly, spray pyrolysis is a complex process, due to which the product properties are difficult to predict. Intimately related is that dipcoating can be more easily incorporated in current propellant tank manufacturing procedures, whereas spray pyrolysis would require the purchase of necessary equipment. A detailed experimental procedure of the synthesis can be found in [section 4.2](#).

4.1.5. Requirements

As is clear from the above discussion, no currently used stabilizer fully satisfies all the needs: either the stabilizer negatively influences the decomposition catalyst or the rest of the propulsion system, or it deactivates over time. A possible solution would be to immobilize the colloidal stabilizers, since that would mitigate their only disadvantage. Several requirements were formulated to guide the design and testing of the stabilizer and to be able to compare it to the currently applied stabilizer methods.

- REQ-STA-1** The designed stabilizer shall lead to a decay at least 2 mpp less than unstabilized >90% HP over the course of 6 months.
- REQ-STA-2** The designed stabilizer shall not react with stabilizers already present in the HP.
- REQ-STA-3** Use of the designed stabilizer shall not negatively impact the performance of the propulsion system.
- REQ-STA-04** Incorporation of the designed stabilizer shall not impact the design of other propulsion system parts except for the storage tank.

The first requirement posed on the designed stabilizer (REQ-STA-1) puts a threshold of the minimum stabilization capacity. The value as given here corresponds to the minimum difference observable with the equipment as available for this investigation. In addition, only such a small improvement in stability would already lead to an increase in lifetime of HP-based spacecraft, based on the storage life of the propellant.

Further, it is imperative that the here developed stabilizer does not react with stabilizers that are already present in the supplied HP (REQ-STA-2). Such a negative interaction would not only negate the addition of the stabilizer, but also possibly lead to additional degradation of the HP. Similarly, the designed stabilizer should not negatively influence propulsion system components, by effects as settling or etching (REQ-STA-3). The last requirement (REQ-STA-4) demands that no changes or additional components are necessary in the propulsion system, such as particulate filters, which would increase its commercial appeal.

4.2. Experimental

This section will shortly introduce the preparation of the stabilizers, after which a description of the stability monitoring experiment will be supplied.

4.2.1. Coating preparation

The coating solutions were prepared from a colloidal SnO₂ dispersion (Alfa Aesar 15%) in water (reported particle size: 10-15 nm; average 12.5 nm). According to manufacturer specification, no compounds incompatible with HP were present in this dispersion. The military specification MIL-PRF-16005F for the contents of propellant-grade HP [123] was used as a guideline to compare the stabilizing action of the TOCs to the maximum allowable concentration of tin (4 mg metallic tin equivalent per kg of 98% propellant-grade HP). It has been assumed that, in lieu of any reported information on particle size, dissolved sodium stannate will form colloids with an average diameter of 12.5 nm. Additionally it has been assumed that the TOCs lose half of their surface area upon immobilizing.

Further, a small test (n=10) showed that between 50 to 60 μL of water adsorbs to the aluminum strips. Using this information three coating solutions had been made. For the nominal case ("medium", "M"), the coating concentration was chosen such that the equivalent tin loading during immersion in HP would be equal to 4 mg/kg. Similarly, two coatings were prepared to give half the nominal concentration ("low", "L", 2 mg/kg) and six times the nominal concentration ("high", "H", 24 mg/kg). Additionally, one solution was prepared by dissolving 10.0 g SnCl₂ in 75 mL water (corresponding to 89.5 mg Sn per mL solution) and stirring overnight to convert the Sn(II) to Sn(IV) ("SnCl₂", 183 mg Sn per kg of HP). Finally, one coating solution was composed entirely of deionized water ("DI").

Then, hard anodized 1050 aluminum strips (10x40 mm) as supplied by the DEMO workshop of TU Delft, were prepared for coating. These strips were subsequently sonicated in acetone, ethanol and water for 10 minutes and afterwards dried using compressed air. Then, groups of four aluminum strips were glued to glass slides. It was verified beforehand that during calcination the glue would decompose, so as to not introduce further contaminations into the HP. Each of these sets was then fully submerged in the solutions for 10 seconds, after which they were left to dry in a fumehood. Afterwards, the strips were gently removed from the glass slides and calcined at 350°C for 5 hours with 5°C/min heating rate.

4.2.2. Stability testing

The objective of this research was to verify whether stabilizers currently used in the dissolved form can also be immobilized. To that end, each tested stabilizer was both present in dissolved form (D) and supported form (S). The former were prepared by dispersing appropriate amounts of the colloidal solution to give tin concentrations equal to those for the supported specimens. Due to limited availability of HP, the dissolved stabilizers were tested with a lower amount of HP (4 mL) and in smaller 5 mL glass vessels, while the supported stabilizers were tested in larger 20 mL glass vessels, containing 15 mL HP.

Two different blanks were prepared for each series. One blank ("DI") served to validate both the compatibility of the deionized water (DI-D) as available at the Delft Aerospace Materials Laboratory (DASML) and the compatibility of the hard anodized aluminum strips (DI-S). The other blank ("HP") served to investigate the decomposition behavior of HP without additional stabilizers, and to validate the surface effect in HP decomposition.

The effect of relative surface area is inevitably present in these experiments. Thus, in order to eliminate this surface effect from the stabilizer research, all samples should have an equal surface to volume ratio (SVR). Though, the introduction of the aluminum stabilizer strips increases the SVR. To find the prominence of this surface effect, the HP control samples can be studied. It should be taken into account that even though the aluminum strips are very pure (>99.5%), alloying elements are still present. Release of these during the experiments leads to an increased decomposition rate which convolutes with the SVR effect.

Further, since the stabilizers already present in the acquired HP may interact with the tested stabiliz-

Table 4.1: Sample library for stabilizer tests.

Supplier	Unstabilized HP Solvay		Stabilized HP Sigma Aldrich	
	90%	95%	90%	95%
Low	Sy-90-L	Sy-95-L	SA-90-L	SA-95-L
Medium	Sy-90-M	Sy-95-M	SA-90-M	SA-95-M
High	Sy-90-H	Sy-95-H	SA-90-H	SA-95-H
SnCl ₂	Sy-90-Cl	Sy-95-Cl	SA-90-Cl	SA-95-Cl
Blank DI	Sy-90-DI	Sy-95-DI	SA-90-DI	SA-95-DI
Blank HP	Sy-90-HP	Sy-95-HP	SA-90-HP	SA-95-HP

ers, two different suppliers of HP were tested: Sigma Aldrich ("SA", currently known as Merck) and Solvay ("Sy"). According to manufacturer specification, Sigma Aldrich HP (Perhydrol 30%) as supplied contains 25 to 30 ppm of PDC stabilizer, on top of many other (undisclosed) stabilizing compounds. Yet, when the HP is concentrated using the SolvGE RGP to >90%, the PDC concentration increases to over 100 ppm. If this is compared to the added amounts of Sn (see Table 4.2), it can be clearly seen that it might be difficult to distinguish a possible interaction due to the large surplus of PDC in the solution. Solvay HP (Interox 35%) on the other hand, only contains a limited amount of stabilizers. This HP can thus be used to monitor the possible interaction between different stabilizers. An overview of the samples can be found in Table 4.1.

4.2.3. Instrument calibration

The lab equipment used is calibrated yearly by an external party and checked regularly by the responsible technicians. Further, all concentration measurements were determined by a third party with the same analog refractometer as in section 2.3. The calibration efforts can be found in section D.2. It is important to note here that this instrument has a read-out uncertainty of 1.1 mpp and a constant error of 1.5 mpp, determined by cross-calibration with a calibrated digital refractometer.

4.3. Results and discussion

This section will present and discuss the findings with respect to the stabilization of HP. Thereto first the deviations from the setup as described above will be given and a short background on the manipulations performed on the concentration data. This is followed by a discussion of the area effect, the compatibility of the deionized water used for diluting, and the compatibility of the aluminum strips with HP, respectively. Afterwards, the effect of dissolved and supported stabilizers on the stability of HP will be presented.

4.3.1. Deviations from setup

In this research deviations have been caused by the then ongoing COVID-19 pandemic, which caused poor availability of chemicals, including HP: the unstabilized Solvay HP was delivered only after a six-month delay, due to which only limited decomposition data are available.

Further, at the end of this investigation, more stabilizer strips were prepared for reference. It was then noticed that after calcination the surface of the strips showed signs of cracking, which was also noticed in the spent stabilizer strips (see Figure 4.10). Most likely, the observed cracks in the oxide layer had formed due to thermal expansion coefficient mismatch with the aluminum substrate. In addition to cracking, at some places the oxide layer had completely separated, as was found by microscopic investigations of the spent stabilizer strips. On its turn, this cracking and detachment of the passivating oxide layer lead to exposure of the unprotected aluminum, presumably causing the introduction of incompatible metal ions during the experiments, which increased the decomposition rate.

An additional source of error was introduced by the remote nature of this experiment: both the addition of HP to the samples and the concentration measurements were conducted by a third party. This lead to inadequate filling: some SA samples received an amount different from initially planned. All SA-D samples contained 20% less HP than planned, which caused the stabilizer concentration to increase by 25%. In addition, the supported SA-S specimens had received too little HP as well. Yet, since the fluid height in the vials would decrease accordingly, this had little effect on the effective stabilizer concentration. Further, because no record was kept of the initial amount of HP added, at the end of the experiment the masses from the Solvay

samples were determined. It was found that at that time deviations of up to 78% in volume were present with respect to the intended volume. Beside being introduced during the filling, these deviations could also have arisen during the decomposition experiment itself. Unfortunately, due to the physical separation of the author from the experiment, no single cause can be pointed out. Therefore, the Solvay data can only be used with great care.

The incorrect filling of the samples has several consequences. First of all, the changes in the volume of HP added to the different samples results in a change in the actual stabilizer concentration. The resulting stabilizer concentrations can be found in Table 4.2; note that for the Solvay samples these concentrations are only approximate and based on the HP amount after 84 days.

Secondly, the incorrect filling caused a change in the relative surface areas, and thus in the SVR. However, due to the close relation of surface area with volume, this effect is not strongly visible in the actual SVR values, which can be found in Table 4.3. It should be noted that with the current SVRs the surface effect is almost excluded from the stability measurements, assuming that an anodized aluminum surface behaves similarly to a glass one. Dismally, due to the lower SVR of the pure HP control compared to the DI control, inertness of the aluminum and overall surface effects remain convoluted.

Table 4.2: Equivalent concentration of the added stabilizer in mg Sn per kg HP solution. N.B. for Solvay (Sy) the concentrations are approximate, due to the large error in H_2O_2 volume. *For DI the decrease factor is used, since for the dissolved case only water is added, which decreases not only the actual HP concentration, but also the effective stabilizer concentration.

			Low	Medium	High	Cl	DI*	HP
SA	90	S	1.85	3.70	14.8	168	-	-
		D	2.50	5.00	30.0	228	0.997	-
	95	S	1.35	2.70	16.2	112	-	-
		D	2.50	5.00	30.0	251	0.997	-
Sy	90	S	0.58	1.26	9.05	69.9	-	-
		D	3.23	6.89	39.8	361	0.995	-
	95	S	1.68	3.55	21.4	165	-	-
		D	2.66	5.42	31.7	248	0.995	-

Table 4.3: Surface to volume ratios, including the area of the aluminum strip when applicable. All values have been corrected for the actual inserted amount of HP.

			Low	Medium	High	Cl	DI*	HP
SA	90	S	2.7			1.9		
		D	3.0					
	95	S	2.8			2.1		
		D	3.0					
Sy	90	S	3.4	3.3	3.1	3.1	3.1	3.7
		D	3.2	3.2	3.2	3.3	3.2	3.1
	95	S	2.7	2.7	2.7	2.7	2.7	2.8
		D	3.0	3.1	3.0	3.1	3.1	3.1

4.3.2. Data manipulation and analysis procedures

From theory it is expected that unstabilized HP should decompose exponentially (in the presence of contaminants), whereas its stabilization should lead to a more gradual decay and not necessarily an exponential trend. Nevertheless, the data have been fitted with several functions in order to find the optimal fit, among which are linear, quadratic and cubic functions and the already mentioned exponential decay. In the process it was aimed to minimize the number of fitting parameters to avoid overfitting. In the end the exponential decay function $y = y_0 + Ae^{-k*t}$ proved to be the best fit ($R^2 > 0.92$, see section E.3) for the SA dataset. Because initially all samples had the same concentration, either 90 or 95%, this concentration value was given a double weight compared to the other values in order to force all trends through the same starting point. Additionally, the measurement points around 65 days were given a lower weight (0.25), since for a large part of the dataset this point showed a considerable increase in concentration with respect to either the previous measurement or the overall trend (up to 3 mpp). These errors might have been introduced due to a series of erroneous

measurements, or due to insufficient tightening of the sample tubes: due to the relatively higher vapor pressure of water, the contained HP might have concentrated over time. Since the errors were not too large to consider these datapoints as outliers, and to avoid bias, all relative weights were adjusted accordingly for this measurement point. Due to the limited amount of datapoints for Solvay HP, no trends could be discerned at this stage. Instead, only the concentrations will be plotted connected by lines as guide for the eye.

4.3.3. Area and concentration effects

Two questions this research set out to answer are whether an increasing concentration of HP results in increased stability (RQ-STA-1) and whether the relative surface area has an effect on the stability of HP (RQ-STA-2). To that end we will solely compare the stability data for the pure HP control samples, both with large (HP-D, SVR ~ 2) and small (HP-S, SVR ~ 3) SVR. The following reasoning will mainly revolve around the SA dataset, due to the both the large uncertainties associated with the initial SVR values for and the limited size of the Sy dataset. The development of the concentrations of these samples is plotted in Figure 4.2. For the Solvay dataset an increase in concentration can be seen for the HP-S sample, as has been touched upon above.

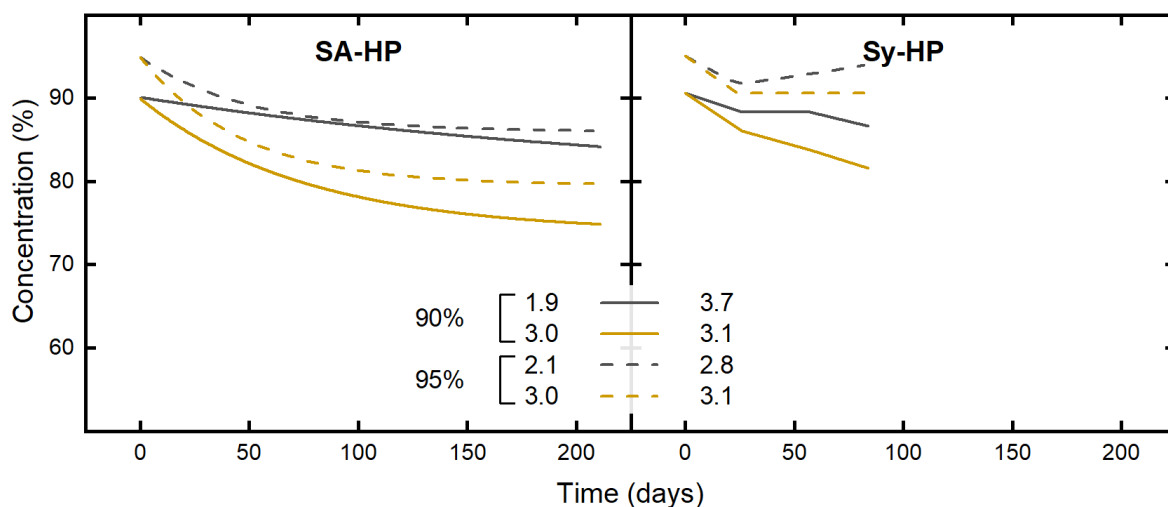


Figure 4.2: The effect of the SVR in the decomposition of HP. Please note the deviating legend; for clarity black is used for Supported and yellow for Dissolved samples. In the legend the respective SVR values have been indicated to allow easy comparison.

4.3.3.1. Concentration effect

First of all, no clear concentration effect can be distinguished based on these data in Figure 4.2. When both SA-HP samples with SVR=3 are compared, the difference after 210 days is still 5 mpp. The low-SVR data display an inverted concentration effect: the 90% sample has decayed less and is only 2 mpp lower in concentration than the 95% sample after 210 days. For Sy-HP, in the case of both SVR=3.1 samples, the initially 95% concentration sample has decreased 4.5 mpp, whereas the 90% sample has degraded 8.5 mpp. Due to the increasing concentration of the 95-HP-S sample no further conclusions can be drawn from the Solvay data. Perhaps the effect of a higher concentration does manifest in all samples, but goes unnoticed due to the large measurement uncertainty present.

4.3.3.2. Area effect

Further, the SA data clearly show an increase in decomposition rate with an increase in relative surface area. For both SVR 3.0 samples, the initial difference in concentration is maintained at the end, whereas the low-SVR samples have not decomposed to an equal extent and finally differ only 2 mpp in concentration. It is thus clear that a higher relative (glass) surface area leads to an increased decomposition rate. This effect is not visible from the current Solvay data: the effect even appears to be reversed. Though, no definite conclusions can be drawn from these sparse and erroneous data.

Another factor might explain the supposedly observed area effect: a prominent difference between the large and small SVR datasets is the glass vessel. Even though they are supposed to be composed of exactly the same glass, there might be changes in between batches or production methods for the large and small

vessels. These changes then may lead to e.g. a higher surface smoothness or a higher amount of hydroxylated surface sites, onto which catalytic contaminations may adsorb (either during manufacturing or during the experiment). More research should be conducted into this matter to further clarify this issue and its influence on the results. Yet, at this moment it will be assumed that these manufacturing effects are not noticeable in the conducted experiment.

Additionally, the trend as visible in [Figure 4.2](#) seems to indicate that the low-SVR 90% sample decomposes in a different manner compared to the other samples. Yet, there is no reason to expect a different decomposition mechanism; further research should be conducted to verify these results.

4.3.4. Diluting water compatibility

Since all coating solutions were diluted with deionized water, its compatibility with HP needed to be validated: small amounts of metal contaminants will inevitably remain after deionization of the water. [Figure 4.3](#) shows a comparison in decomposition behavior between SA-90-HP-D and SA-90-DI-D, and SA-95-HP-D and SA-95-DI-D (all with an SVR equal to 3.0). For SA-90-DI-D, there does not seem to be a negative effect caused by the addition of 0.4% deionized water, even more, the results seem to indicate that there is a slight positive effect. Yet, since the difference is both very small (2 mpp) and there is no physical reason for the increased stability, this difference is considered as measurement error. The addition of deionized water to 95% HP appears to have a severe effect on its stability: the stability shows a quick initial drop after which its concentrations stabilizes below that of 90%. This behavior appears more peculiar when the decomposition data are compared with that of the equivalent Solvay samples: these all seem to follow the same decomposition trend as SA-90-DI-D. Although this experiment does not show such an effect (as was discussed earlier), theoretically higher concentration HP should be more stable, which is displayed here by the sparse Solvay data.

An observation made near the end of the research may explain the apparent enhanced decomposition by the SA-95-DI-D sample: DASML lab users would put (cleaned) used sample vials in between the new ones. That could mean that the increased decomposition rate is caused by contaminants introduced by a previously used sample vial. Another factor that points to a contamination of the sample vial is that the concentration drop occurs primarily at the start of the experiment. The presence of organic compounds, such as solvents, would result in a concentration drop at the start of the experiment, caused by reaction with H_2O_2 . Supporting evidence for this hypothesis is supplied by shifting the SA-95-DI-D data points upwards by 7.5 mpp (see the inset in [Figure 4.3](#)). The resulting points then lie very closely to the those of SA-95-HP-S: only when time passes they fall below that curve.

This latter observation might mean that another or additional effect is at play. Perhaps this effect can be explained by a metal contamination. Namely, if a catalytic metal ion would be present at the start, it would require some time for the PDC stabilizer to neutralize it, despite the high concentration of PDC. This would demonstrate as an initial concentration drop. Further, it must be considered that the metal ion - PDC interaction, even though it is very strong, is reversible, i.e. the ions can be released at some point in time, allowing them to react with HP. Hence, when catalytic metal contaminants are present from the start, they have a destabilizing effect over the entire lifetime, despite the presence of stabilizers. This phenomenon is most likely occurring in all specimens, yet it might only become noticeable when the contaminant concentration increases, as is supposedly the case for SA-95-DI-D. When the PDC concentration is high with respect to the metal contaminants, it can be imagined that when an ion is released it will quickly bind to another PDC molecule, due to which it can barely catalyze HP decomposition. Conversely, when these concentrations are comparable, the chance of a PDC and contaminant ion randomly meeting is decreased and hence the ion spends more time freely moving through the solution and decomposing HP.

4.3.5. Aluminum compatibility

Another goal of this research was to investigate the suitability of anodized aluminum as a support for the TOCs (RQ-STA-3). Thereto [Figure 4.4](#) compares the decomposition behavior of the SA-DI-S samples with the SA-HP-D samples, which have approximately equal SVRs. It is intriguing that at the end of the experiment SA-90-DI-S and SA-90-HP-D have approximately equal concentrations, but the temporal trend to these points is inverted; the same is true for SA-95. Apparently the hard oxidized aluminum strip has a destabilizing effect on the HP, even though the hard anodizing should have removed virtually all catalytically present elements from the surface. Even more, where the decomposition of the reference samples stabilizes over time, it accelerates for HP in contact with passivated aluminum. Three physical phenomena could explain this behavior.

Firstly, inevitably cracks and crevices are present in the Al_2O_3 -layer, through which HP can slowly leach and reach the base metal, which causes oxidation of metallic aluminum atoms. Oxidizing slightly increases

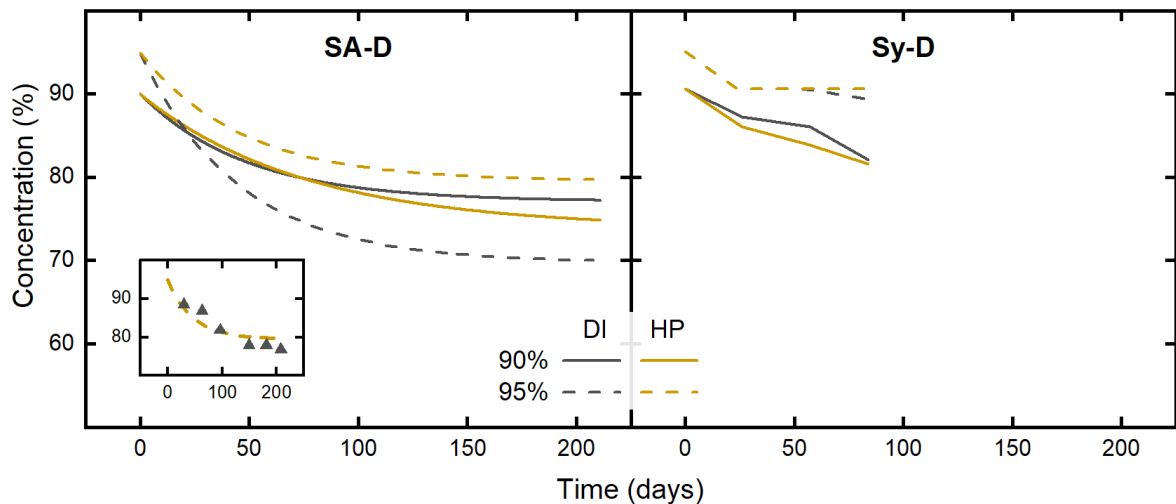


Figure 4.3: Comparison of samples containing DI water with control (HP) with comparable SVR, being 3.0 for SA and ~ 3.1 for Sy, respectively. For SA-95-DI-D the presence of deionized water seems to negatively influence the stability of HP; this effect is not visible for the SA-90 or Solvay samples. The inset shows the effect of an upwards translation by 7.5 mpp of the SA-95-DI-D data.

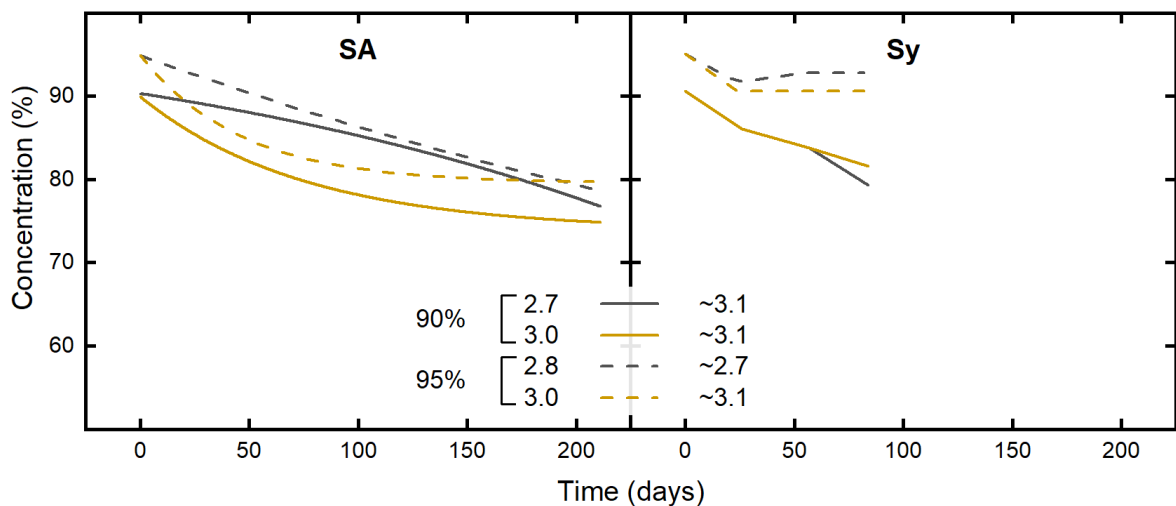


Figure 4.4: Comparison of decomposition behavior between HP-D (yellow) and DI-S (black) samples with comparable SVR. Especially for SA the presence of the aluminum strip seems to have a negative effect. In the legend the relevant SVR values have been indicated.

the size of an aluminum atom: this volume growth will induce stress in the superior oxide layer, which will ultimately lead to it cracking and flaking off. This is a self-reinforcing effect: because of the flaking off of the protective oxide layer, more pristine aluminum atoms emerge. Beside removal of the protective layer, this leaching has another effect. Even though the aluminum consists for $>99.5\%$ of aluminum, still 0.5% consists of metals (mostly iron) that are incompatible with HP. When the base metal is exposed, these alloying elements can react and dissolve in the bulk solution. Evidence in favor of this theorem is supplied by SEM, as visible in [Figure 4.6a](#). Instead of forming a flat and uniformly closed layer, an unexposed and untreated anodized aluminum strip already shows crack initiation points, in addition to, albeit limited, surface roughness. It should be recalled that validation experiments conducted after this research showed that crack formation would take place already during calcination. The effects of prolonged exposure to HP seems to support above theorem (refer to [Figure 4.11](#)): the fault lines become more pronounced and locally the original oxide layer is largely removed. Unfortunately the used SEM does not allow for height measurements, nor does the sensitivity of the EDX spectrometer suffice to distinguish the low concentrations of the alloying elements on the exposed surface.

Further, EDX shows measurable fractions of both sulfur and phosphorus on the seemingly unaffected surface, whereas heavily affected areas only show the presence of sulfur (see [Figure 4.6](#) for representative

electron micrographs with elemental composition data). The presence of these two compounds can only be explained by the nature of the hard anodizing process; it is not uncommon to use a combination of sulfuric and phosphoric acid for anodizing [115], and it is known that these electrolytes are captured in the oxide layer [13]. Unfortunately the responsible company did not want to share details of their hard anodizing process, due to which this hypothesis cannot be proven. Additionally, it is commonly known that when either concentrated sulfuric acid or phosphoric acid is combined with H_2O_2 this results in strong etching solutions, which are commonly used in the semiconductor industry. It might thus be possible that the remnants of the (theoretically protecting) hard anodizing process are (partly) responsible for the severe damage to the stabilizer strip surface. In addition, it must be noted that release of these phosphorus compounds from the oxide layer is highly undesired, due to their catalyst-poisoning ability.

An alternative explanation for the enhanced decomposition rate of HP when brought in contact with hard anodized aluminum might be that the Al_2O_3 serves as a stabilizing layer for the metal contaminants, effectively working as an ion exchanger for the solution. An important prerequisite for this explanation is that interaction strength to the metal ions by PDC and alumina is similar. Namely, if the interaction with PDC would be much stronger, the contaminants would be more stabilized by the PDC over time, and thus their destabilizing effect should decrease over time. It might then be that the nature of the interaction of PDC and alumina is different: the former decreases the energy levels of the metal ion to such an extent that it is not able to catalyze HP decomposition. It might as well be that the interaction with the Al_2O_3 is of a different nature, so that it does bind strongly, but does not lower the ion's energy levels, due to which the metal ion would remain catalytically active. Dismally, the available analysis equipment does not offer high enough sensitivity to measure both the presence and the energy levels of metal ions on top of the alumina surface. Another explanation for the differing decomposition trends might be the nature of the PDC molecule. The (pyridine-group) nitrogen in PDC is slowly oxidized in concentrated HP [59], which turns the metal ion coordinating group into an almost ionically charged oxygen, which can be seen in Figure 4.5. In absence of the aluminum oxide, this is beneficial for the stability of HP due to the much stronger interaction with the contaminant metal ions. This phenomenon is possibly responsible for the decrease in decomposition rate of HP, as is observed for SA-HP-S.

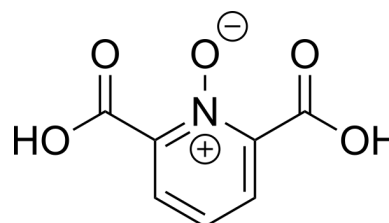


Figure 4.5: PDC-O molecule. Note that the apparent ionic charge on the pyridine oxygen is partially stabilized by resonance.

In presence of aluminum oxide, another counterproductive effect may occur. Pyridine, a molecule with physicochemical properties similar to PDC, is often used in catalyst research to probe surface properties. It is known to strongly bind to alumina surfaces already at room temperature. PDC, due to its larger conjugated π -system, has a higher electron density on the coordinating nitrogen than pyridine. Analogously, PDC should bind even stronger to Al_2O_3 than pyridine, or concretely: aluminum oxide might (gradually) remove the PDC stabilizer from the solution, allowing the unstabilized metal ions to decompose H_2O_2 molecules. Furthermore, the oxidized PDC (PDC oxide, or PDCO) should also bind more strongly to aluminum oxide than both pyridine and PDC, completely removing the (oxidized) PDC stabilizer from the HP solution, effectively leaving the HP solution unstabilized. SEM-EDX did show definite amounts of carbon present on all exposed stabilizer strips, both on unaffected and heavily affected areas as is shown in representative images Figure 4.6b and Figure 4.6d. Unfortunately, neither Raman nor UV-Vis TDR spectroscopy possessed a sufficiently high sensitivity to identify the nature of the carbon compound. Therefore it cannot be concluded that this carbon-based surface deposit is formed by either PDC or PDCO.

4.3.6. Stabilizer effects on the stability of HP

In order to find and compare the stabilizing performance of both the dispersed and the supported TOC stabilizers, three different loadings were tested in this experiment. For the SA samples, their performance is compared to both uncoated anodized strips (DI-S) and HP-D in Figure 4.7, to exclude surface effects. All samples in this figure show an increasing stability with an increasing stabilizer loading; for SA-95-S the difference between the medium and high loading is considerably less prominent, likewise for SA-90-L-D and SA-90-M-D. Yet, when the decomposition behavior of the stabilized samples is compared with that of the reference, all series show different behavior. As reference, Figure 4.8 shows the stability data for the Solvay experiment.

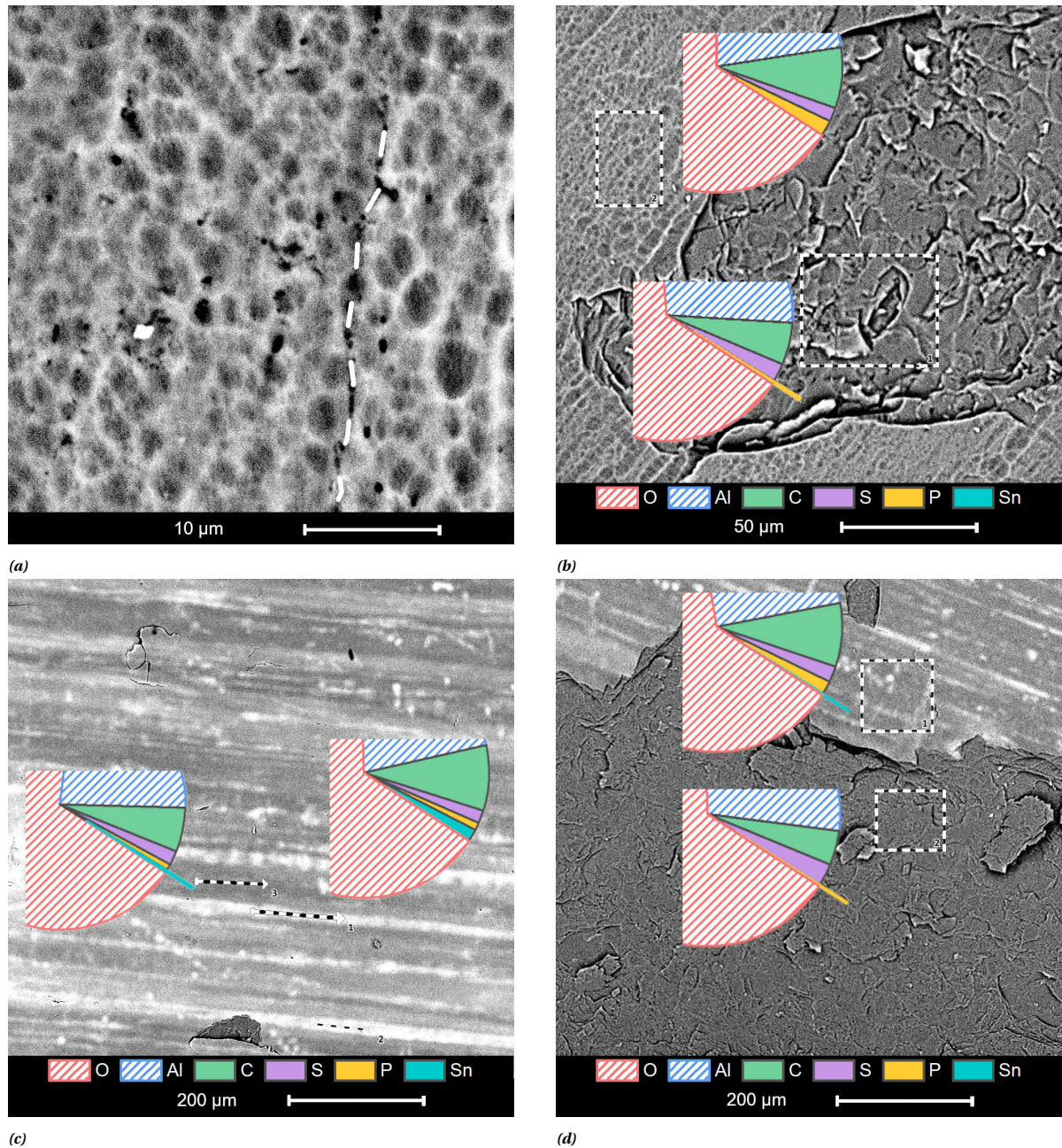


Figure 4.6: Representative electron micrographs of different stabilizer strips. *a*) SEM image of an untreated anodized aluminum strip. Clearly visible is the surface roughness, and the crack initiation points (dashed line). *Figure b) - d)* show the elemental composition of different places on the surface of treated strips determined by SEM-EDX. The unaffected areas show presence of sulfur, carbon, nitrogen and tin, while heavily affected areas show comparable quantities of carbon and sulfur. *N.B.* for clarity the areas of aluminum and oxygen have been largely omitted. *b*) A spent strip without coating (SA-95-DI-S) showing the presence of carbon, sulfur and nitrogen at the unaffected surface, and the absence of nitrogen at the heavily affected area. *c*) Electron micrograph of SA-95-H-S showing the higher signal intensity at regions with higher tin content. *d*) Electron micrograph of SA-90-M-S shows the presence of tin at unaffected surface and absence at overturned area.

4.3.6.1. Dissolved stabilizers

This section will describe the effect of dissolved stabilizers on the decomposition stability of HP. First, the effect of the addition of TOCs will be described. This will be followed by an analysis of the effect that the addition of tin chloride has on the stability of HP.

Dispersed TOC stabilizers For SA-90-D, an increase in TOC concentration leads to a clear increase in stability over time when compared to the baseline as is shown in Figure 4.7. Already the addition of the lowest amount of stabilizers leads to an increase of stability, which over time becomes comparable to that of the maximum allowed amount of tin oxide (SA-90-M-D). By increasing the concentration of TOCs considerably (SA-90-H-D), the decomposition is limited to only 5 mpp in over 200 days. Even though this does not prove that the addition of sodium stannate produces TOCs, these results indicate that TOCs display a clear stabilizing effect for HP.

The SA-95-D data show a similar trend with respect to stabilizer concentration, but here the difference between low and medium concentration is more pronounced. Furthermore, the addition of TOCs appears to negatively influence the HP stability: both low and medium concentration display a higher decomposition rate than the baseline. When it is considered that more pure HP should be more stable, the comparison between the former two series is striking: decomposition in all SA-95-D samples is higher than in SA-90-D, except for SA-90-HP-D and SA-95-HP-D, which both show a 15 mpp decrease over the length of the experiment. When the data are inspected more closely, it can be observed that the largest decrease is over the first time instant. This leads to think that this initial period is essential to settle the stabilizing performance of the TOCs. Perhaps the higher water content in the 90% HP is beneficial for proper dispersion of the tin oxide particles. Alternatively, the higher water content may facilitate in removal of the surfactants present on the colloid surface that otherwise may inhibit their stabilizing function. Nevertheless, these data show that, in the presence of these dispersed TOCs, 90% HP is more stable than 95%.

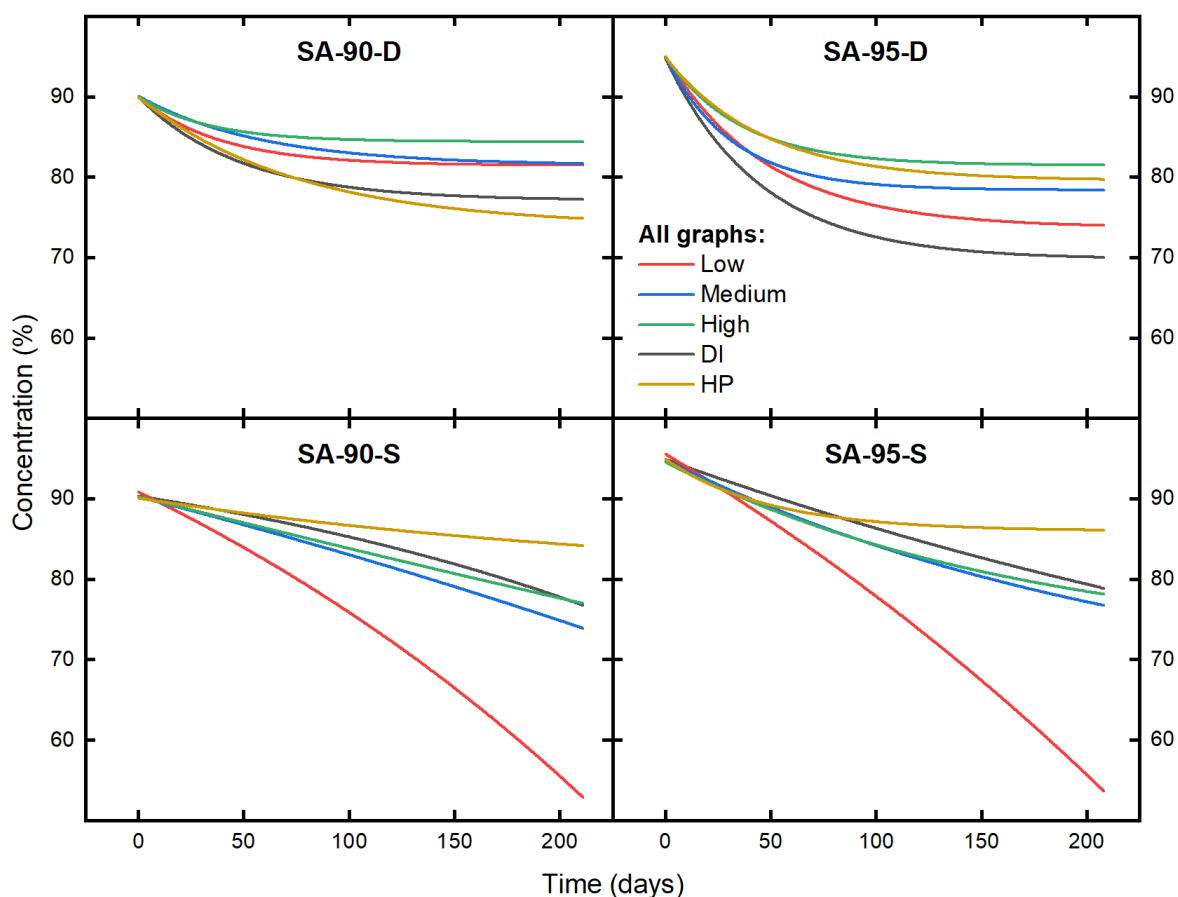


Figure 4.7: Comparison of the effect of the addition of dispersed (top) and supported (bottom) tin oxide stabilizers to Sigma Aldrich HP of 90 and 95%.

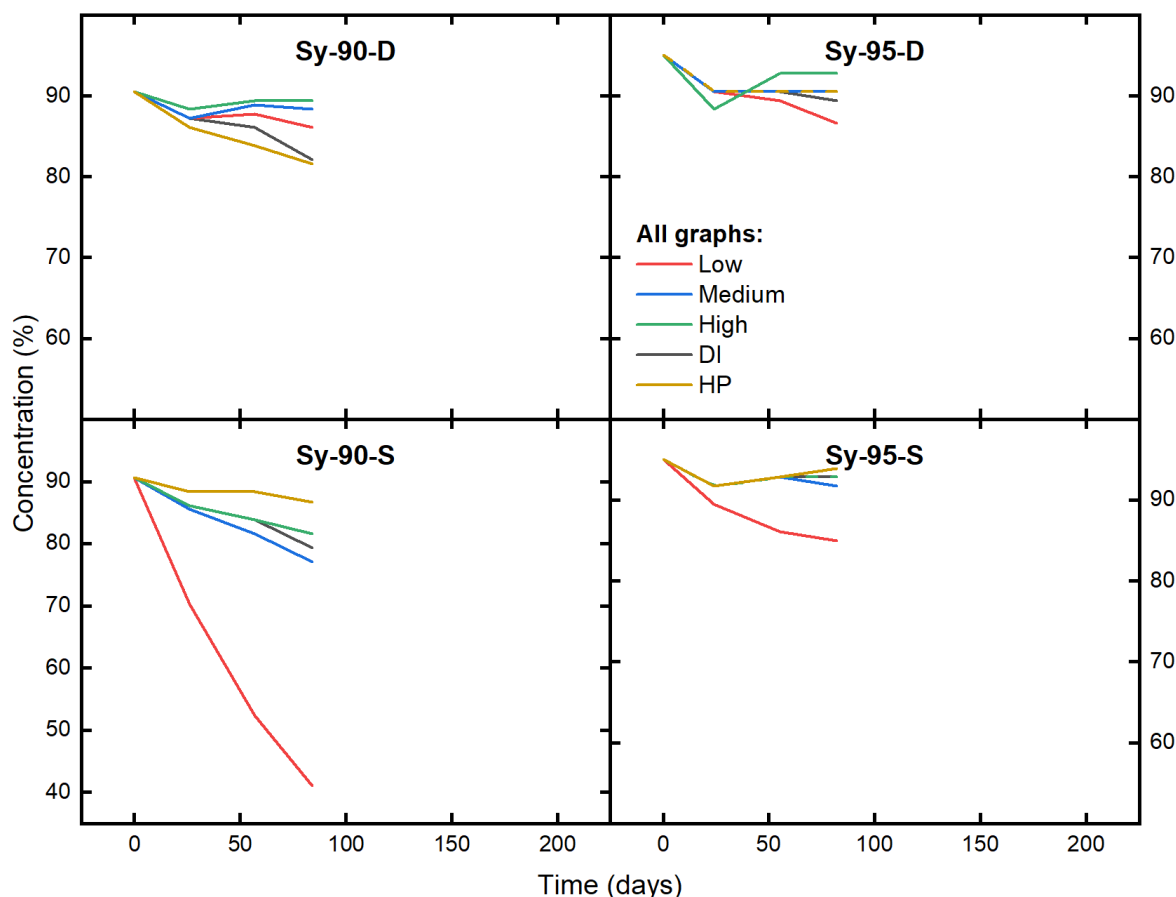


Figure 4.8: Comparison of the effect of the addition of dispersed (top) and supported (bottom) tin oxide stabilizers to Solvay HP of 90 and 95%. Note: for Sy-95-D, medium and HP coincide; similarly for Sy-95-S, DI and High coincide. Also note the different y-scale for Sy-90-S compared to other graphs.

Dissolved tin chloride stabilizers Already at the start it was noticed that immediately after addition of HP to the vessels containing SnCl₂ gelling would occur. This gelling was expected and can be explained by the formation of colloidal SnO₂. The addition of HP would lead to oxidation of the Sn(II) to Sn(IV); this reaction consumes H₂O₂ molecules and thus causes a concentration drop, predominantly in the first time interval. Yet, if this reaction would form the stabilizing TOCs, these samples should display superior stability over time compared to the other samples, due to the high initial concentration of SnCl₂ (see Table 4.2). The absence of this effect as displayed in Figure 4.9 might be caused by contaminants present in the SnCl₂ precursor. These contaminants constitute up to 2% of the total weight of the precursor; common contaminants in tin chloride are iron and silver, which both show high catalytic activity for HP. Unfortunately, the contaminant concentrations are too low to detect using the available measurement equipment. It might also be that the enhanced decomposition is caused by still unconverted tin chloride. It is well known that tin chlorides have a strong interaction with H₂O₂, among other things they catalyze the polymerization of HP with acetone [48]. Perhaps in absence of such an organic molecule, the unoxidized tin chloride still interacts with HP. The comparably large decomposition of the SA-95-Cl-D sample might again be due to involuntary introduction of contaminants due to the use of a contaminated glass vial.

4.3.6.2. Supported stabilizers

This section will elaborate on the effect of the addition of supported stabilizers to concentrated HP. First the addition of TOC coated strips will be discussed; this will be followed by a discussion of the stabilizing properties of tin chloride-coated strips.

TOC coated strips For both 90 and 95% HP, the presence of a stabilizer strip seems to have a clear negative effect, which is much more pronounced for low stabilizer loadings (please refer to Figure 4.7 and Figure 4.8).

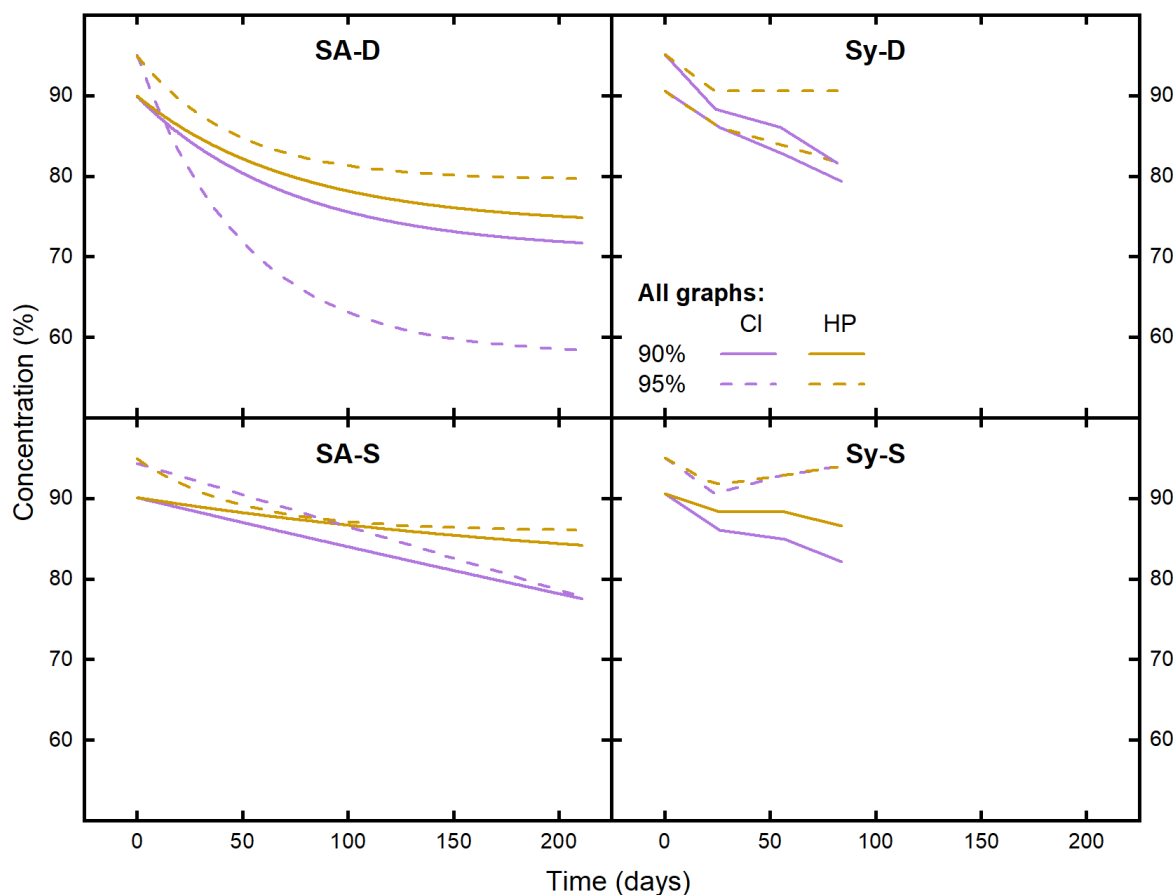


Figure 4.9: Comparison of the effect of the addition of dissolved (top) and supported (bottom) tin chloride stabilizers to HP.

Furthermore, where the dissolved stabilizers overall display a stabilizing trend, decomposition appears unimpeded or even increasing in the presence of the supported stabilizers. In fact, when the decomposition trend of the supported stabilizers is compared to that of DI-S (untreated strip; without taking into account the higher SVR for the dissolved stabilizers), it seems that the presence of the TOCs on the aluminum strip has a destabilizing effect; only the highest concentration of TOCs appears to nullify the effects of their presence. Perhaps the earlier posed theory of adsorption of PDC and PDCO can explain this behavior, taking into account the high surface area of the colloids (in the order of 250 cm^2 per strip for high stabilizer loading, assuming 50% area loss on calcination). It is known that pyridine also adsorbs well onto tin oxide surfaces, which most likely applies to PDC and PDCO too. Then, the lowest loading of TOCs might just be sufficient to immobilize all PDC(O), leaving the solution effectively unstabilized, which would be the case for the low stabilizer loading. The additional tin oxide sites in the medium and high loadings would then be responsible for capturing metal contaminants from the solution. This reasoning might suffice when the aluminum strips were not so heavily affected by HP as shown in Figure 4.10. It is most likely that this surface damage has resulted in additional decomposition. Though, this is only apparent from the stability data for the low stabilizer loading. Perhaps the remaining intact stabilizer surface on the medium and high loading strips is sufficient to remove the released alloying ions from the solution again and hence counteract this additional decay. It might also be that the immobilized TOCs are released back in the solution, where they show the same stabilizing behavior as demonstrated for the dispersed TOCs above.

Due to the large amount of noise introduced by the damaging of the aluminum oxide layer, no direct comparison can be made in stabilizing performance between the dissolved and supported stabilizers. Further, due to the small size of the TOCs (10 - 15 nm) they are not directly visible to the SEM available for this research. Inspection of the strips with EDX shows that, at least on the unaffected areas of the spent stabilizer strips, tin is still present, as shown in Figure 4.6. Thus, despite the destructive effect of the HP, the tin oxide still adheres to the surface of the aluminum strips. Consequently, it can be concluded that the used calcination temperature and duration are sufficient to immobilize the here used TOCs. Though, overall it is clear



Figure 4.10: Comparison of pristine and spent SA-90-S stabilizer strips; evident is the high degree of surface cracking. a) Pristine and uncoated strip. b) Spent SA-90-DI-S. c) Spent SA-90-L-S. d) Spent SA-90-M-S. e) Spent SA-90-H-S. f) Spent SA-90-Cl-S.

from the electron micrographs that the used anodized aluminum strips are not compatible with the currently applied calcination process. Most likely, a lower heating and cooling rate will already have a beneficial effect on the integrity of the oxide layer. Further, considering the fact that the uncalcined anodized strips already possessed many surface defects, part of the incompatibility may be found in the anodizing process itself.

Tin chloride-coated strips The tin chloride-covered strips show a behavior in between that of the uncoated strip and that with high TOC loading, as can be deduced from Figure 4.9 and Figure 4.7. At first glance this may be considered as good stabilizing performance. Though, it should be considered that the Cl-S specimens have not degraded as much as any of the other stabilizer strips, as is evident from Figure 4.10 and Figure 4.11. That means that the Cl-S measurements suffer comparatively less from the effects of aluminum deterioration and its accompanying effect on decomposition. Ergo, these measurements are (presumably) primarily showing the effect of increased SVR, the (possible) stabilizing effect of tin oxide, and the compatibility of the $SnCl_2$ precursor. This phenomenon can be explained by the unusual case that the tin chloride coating solution has remained almost completely dispersed during drying: small holes and cracks in the Al_2O_3 would hence be mostly filled with a thin layer of tin salt, which after calcination has been converted to tin oxide. During exposure to HP, H_2O_2 molecules might still leach into the few remaining holes and initiate cracking, though at a comparatively smaller pace. If this was the only factor of influence on HP decomposition, the Cl-S samples should display superior stability, at least in comparison with the uncoated strips. The higher decomposition rate with respect to DI-S is perhaps caused by contaminations in the $SnCl_2$ precursor, as was the case for the case for the dissolved tin chloride samples. Another explanation might be that the calcination temperature was not high enough to fully convert the precursor to SnO_2 . And, as was already mentioned earlier, unconverted tin chloride might accelerate decomposition. Possibly therefore other researchers that use tin chloride precursors to synthesize porous tin oxide structures calcine at a higher temperature (e.g. $600^\circ C$ [92]). In this research a lower calcination temperature was chosen, because these high temperatures not only are approaching the melting point of aluminum, but also may cause even more elaborate rupture of the surface oxide layer. One final justification for the behavior might be that all tin chloride is converted to tin oxide, but that the electronic properties of the tin ions are modified due to the close interaction with Al_2O_3 . This could then have lead to such interaction with dissolved metal contaminants that these are bonded stronger to the tin oxide than to the PDC, while not negatively influencing the catalytic behavior of these metals, leaving them unhindered to decompose HP.

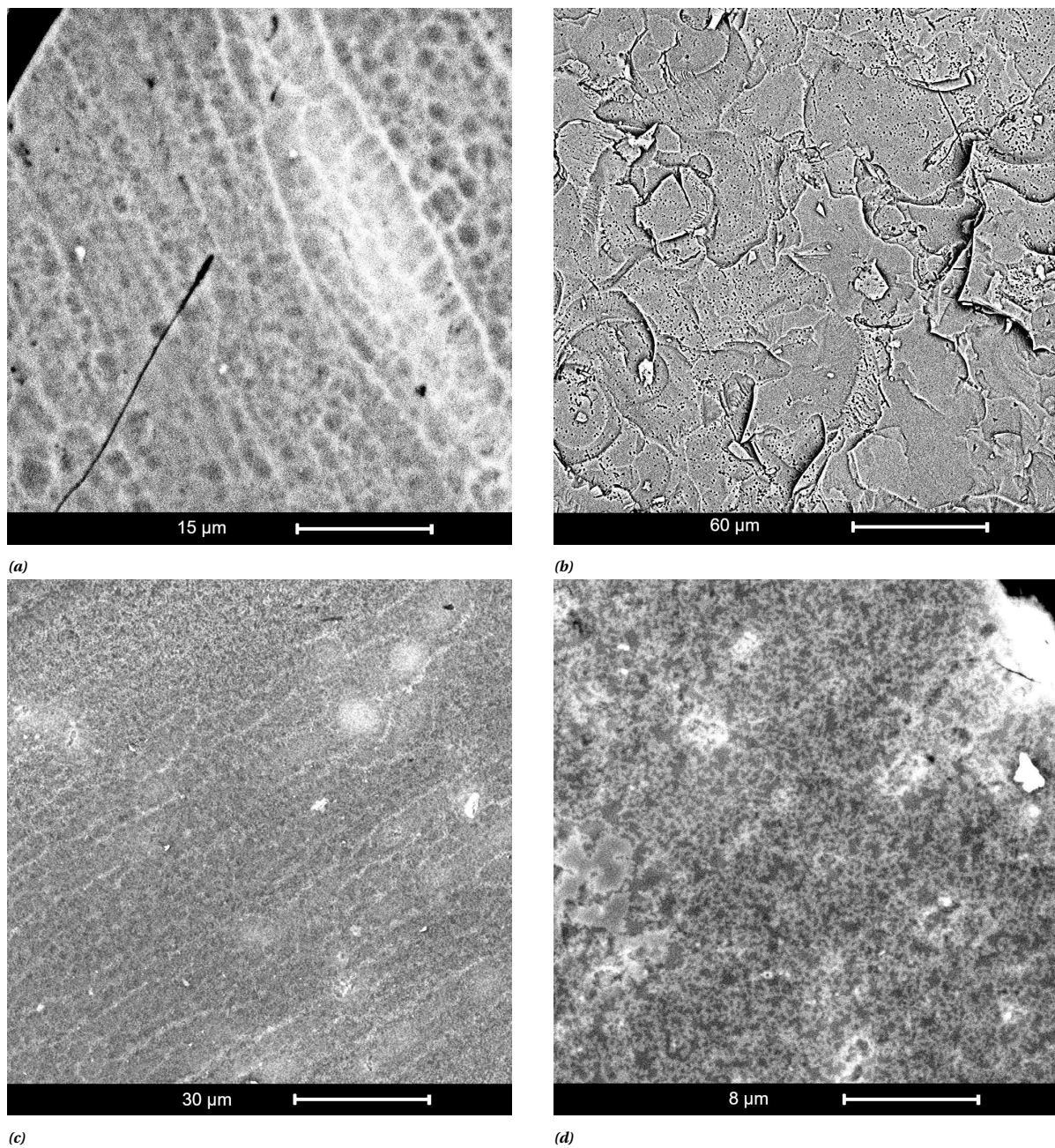


Figure 4.11: Representative electron micrographs of spent SA-90-S. *a)* Relatively unaffected area of spent SA-90-L-S. *b)* Heavily affected area of spent SA-90-L-S. *c), d)* Typical topography of spent SA-90-CI-S. Clearly visible is the difference in topology between low colloidal surface loading and tin chloride.

4.4. Conclusion

In the above it was shown that a higher surface-to-volume ratio correlates with a higher HP decomposition rate. Though, more evidence should be gathered to separate the possible surface properties of the used vessels from the surface effect. Additionally, it was demonstrated that the available DI water does not influence the stability of HP. From the current data, the concentration effect in HP stability cannot be proven. Even more, when all data are considered, a higher concentration of HP seems to result in an enhanced decomposition rate.

Further, it was shown that the addition of dispersed TOCs positively increases the stability of HP; though, relatively large amounts are required. Conversely, adding SnCl₂ does not inhibit the decomposition of HP. This is attributed to the present contaminants in the SnCl₂ precursor, which presumably cause enhanced decomposition.

Further, it was shown that the here tested stabilizers may be a viable means to stabilize HP. Firstly, the used calcination conditions proved sufficient for anchoring the TOCs. Secondly, immobilizing the TOCs did not remove their stabilizing capacity. Additionally, it was shown that the stability of HP increases with the TOC loading of the stabilizer strips. Unfortunately, all used hard anodized aluminum 1050 strips experienced severe degradation over time, which resulted in accelerated HP decomposition. This incompatibility is presumably caused by the anodizing process, while it was intensified by the calcination process. The application of a layer of SnCl₂ decreased the extent of this degradation. In this realm it was hypothesized that one of the stabilizers present in Sigma Aldrich HP (PDC, and its derivative PDCO) is at least partially responsible for the relatively poor performance of the supported stabilizers, due to removal from the solution by both aluminum and tin oxide.

To conclude this section, at this time none of the requirements posed on this research can be verified. Specifically, REQ-STA-1 cannot be fulfilled, due to the higher relative decomposition as shown by all mechanically stabilized samples. On the hand hand, the validation of REQ-STA-2 is impeded by the sparsely available knowledge on the stabilizers present in both tested types of HP, in addition to the earlier mentioned factors. On the other hand, the validation is hindered by the little and erratic data resulting from the Solvay stability tests. REQ-STA-3 cannot be verified either. Exposure of the stabilizer strips to HP resulted in clear surface degradation, which consequently lead to release of catalyst-poisoning phosphorus compounds, which have been introduced during the anodizing process. The additional release of aluminum oxide and tin oxide is equally undesired, since these compounds can potentially clog e.g. injection systems. Lastly, REQ-STA-4 can only be validated at a later development stage of these stabilizers; though, it can be assumed that the proposed design will not affect other propulsion system elements.

4.5. Recommendations

This section will supply the reader with possible improvements and recommendations for future research. These recommendations have been split into different categories as can be found below.

4.5.1. General research improvements

A large deficit in this research is the fact that all samples are available for testing only once. Individual deviations hence severely affect the reliability of the results and thus this entire research. Each sample should be prepared at least in triplo, due to the many potential sources of error.

As discussed above, at this time the surface effect in HP decomposition cannot be proven with certainty, due to the different glass vessels used. This influence of the different vials and the area effect can be investigated by submersion of a glass slide with known composition and dimensions in both vessels. In this manner, the size effect should arise in both the large and small vessels.

One of the goals of this research was to find whether different types of stabilizers would interact with each other. Solvay HP (containing little stabilizer) was essential to achieve this goal. Unfortunately, not only did the COVID-19 pandemic lead to significant delay in its delivery, improper filling (and no ab initio knowledge hereof) lead to a small and erroneous dataset.

4.5.2. Concentration uncertainties

The many present sources of error give rise to large uncertainties, which can not be quantified at this stage. As had already been discussed above, concentrations of HP sometimes (seem to) increase over time. This may be caused by inaccurate measurements: cross-correlation with a calibrated digital refractometer (see [section D.2](#)) showed that the error induced by the analog refractometer is larger than that of the digital one.

Future research would benefit from the increased accuracy of the latter. Inconsistently closed storage vessels might be another source of error: due to the relatively low vapor pressure of HP the solutions concentrate naturally over time. Future research can exclude this from the test by using (tightly closed) lids with a venting membrane or replacing the lids with appropriate rubber stoppers. Explosion risks would hence be eliminated, while all samples would be vented comparably, and thus not experience natural concentration increase over time. A second measure to eliminate the effects of evaporation from the research is by also monitoring the weight of each sample over time, together with that of comparable vials filled with deionized water as a reference. Further, as was noticed at a late stage of this research, lab habits as displayed in the Delft AeroSpace Materials Laboratory are poor. Previously used vessels are cleaned and put back in the storage cabinet indistinctively in between the new vessels. Hence, some of the testing tubes may have contained previously introduced contaminants, influencing the acquired stability results. Additionally, trace metals could remain in the vessels as a result of manufacturing processes. Both processes could be resolved simultaneously by sequentially pre-exposing the storage vessels with high concentration stabilizer (to adsorb metal ions) and ultra pure HP solutions (to oxidize organic impurities), preferably multiple times and for extended periods of time. In this manner both trace metal and organic contaminants would be removed from the vessels, while not introducing new contaminants.

4.5.3. Stabilizers

Since this research cannot provide evidence for the formation of colloidal tin oxide upon dissolution of sodium stannate, future research should look further into this matter. A solution of aforementioned stannate in concentrated HP could be analyzed with transmission electron microscopy (TEM) not only to verify the presence of these colloids, but also to determine their size and crystal structure. These data could validate the comparison with the here used colloidal tin oxides. Further, TEM could also be used to monitor the changes occurring upon calcination of TOCs when these are suspended on an anodized aluminum TEM grid.

Unfortunately no exact information with respect to the mass loading of the supported stabilizers could be gathered. This had to do with several reasons, of which the most important one is the lack of appropriate laboratory equipment: no accurate enough scale was present to measure the mass difference on the strips. This was further hampered by the fact that the highest concentration of colloids was only 2.5 wt.%, which on its turn means that with 50 μL deposited solution only 1.25 mg colloids would have been deposited. Yet, for future applications these mass loadings are important, not only for predictive purposes but also from an economic point of view.

Further, after the stability experiments had been conducted, it was found that the pristine oxide layer already displayed measurable defects, while one of the goals of hard anodizing was to create a thick and impenetrable oxide layer. Future research should further investigate surface finishing techniques in order to create an almost perfect aluminum oxide layer, and hence prevent the considerable damage to both the oxide layer and the underlying aluminum. Perhaps extensive surface etching or polishing prior to hard anodizing could already improve these shortcomings. In addition, the anodizing should be carried out without phosphoric acid to increase the compatibility of the stabilizer strips with a potential catalytic ignition system.

Furthermore, future research should monitor the surface topography of the supported stabilizer strips at more stages during the research with SEM, instead of merely afterwards. In addition, the research would benefit from a SEM (and accompanying EDX spectrograph) with higher sensitivity and resolution. The used SEM could only clearly distinguish features with a minimum resolution of around 100 nm, whereas the deposited colloids are about one order smaller. Hence, at this moment it cannot be verified that the tin oxide has remained finely dispersed during all stages of the experiment.

More practical though, when the dispersion of the deposited TOCs can be observed, it is advisable to investigate the effect of both higher coating concentrations and multiple coating applications. In addition the effect of calcination conditions should be investigated. This would show how many coating applications would be necessary to fully cover the aluminum surface with the tin oxide stabilizer. Finally, the difference in stabilizing performance between SnCl_2 and SnCl_4 should be looked into, since the oxidation may not be carried out to completion. As was postulated above, this conversion may have an influence on the stability of the HP or the aluminum.

Conclusion

This research has taken important steps to take away the barriers that currently hinder the implementation of hydrogen peroxide (HP) in space propulsion.

Purification of propellant-grade H_2O_2

The first part of this thesis research set out to improve the production process as is being developed by SolvGE. Even though the conducted investigations have not resulted in a final design solution, much knowledge was gathered that contributed and contributes to the improvement of their HP purification process. Concretely, this research has successfully recovered elevated concentration HP from the waste stream of SolvGE's RGP; due to the limited amounts of recuperated HP no analyses could be conducted on the contaminant concentrations. It was clear that the recuperation process conditions influenced the concentration of the obtained HP (RQ-CND-1).

Support effect on the decomposition of H_2O_2 over MnOx catalysts

First of all, this research has successfully shown that drop-testing is a suitable method to characterize catalytic performance of supported catalysts, as was demonstrated here with concentrated HP (RQ-CAT-2). Furthermore, several sintered MnOx-based catalysts were prepared and tested. Activity testing showed that only the catalysts based on γ -alumina (γ Al) and YSZ possessed sufficient reactivity with >87% HP. Further, based on thermodynamic calculations and chemical characterization, the active site of the alumina-based catalyst was shown to consist of Mn_3O_4 . For YSZ, the former predicted the formation of catalytically inactive MnO, while the latter was not able to discern any MnOx. Though, the formation of MnO in YSZ is not likely, judging by the displayed catalytic performance (RQ-CAT-1-1). Further, it was demonstrated that the presence of MnOx during calcination led to a decrease of the phase transition temperature for γ Al, whereas no phase transition could be observed for YSZ (RQ-CAT-1-2). Open reactor testing showed that neither of these two catalysts would be deactivated, not even after the addition of over 300 drops of 87% HP. Yet, the YSZ catalyst showed slight physical degradation, which was merely manifested in a mass decrease of 0.4%; this could not be determined for the γ Al catalysts due to their higher brittleness. During semi-open reactor testing both catalysts were quickly (but temporarily) deactivated by flooding with product water (RQ-CAT-1-3). A more advanced reactor can prevent the accumulation of reaction products, and increase the practical relevance of drop-testing experiments (RQ-CAT-2). Furthermore, from open reactor testing with 98% HP it can be concluded that the γ Al catalyst is sufficiently reactive to potentially induce hypergolicity with ethanol (RQ-CAT-3).

Stabilizing propellant-grade H_2O_2

The research into the stabilizing of HP provided interesting conclusions. First of all, no explicit difference in stability was found between 90 and 95% HP (RQ-STA-1). Another effect that is known to influence the stability of HP, the surface-to-volume ratio, was noticed and shown to have a negative effect on the stability of HP (RQ-STA-2). Further, it was shown that the tin oxide stabilizers had adhered to the aluminum throughout the exposure to concentrated HP. Hence it was shown that hard anodizing is a suitable process to enable supporting of tin oxide stabilizers on aluminum (RQ-STA-3). Though, the combination of anodizing and calcination conditions used here resulted in severe deterioration of the oxide layer; this can presumably be mitigated by optimizing of the process conditions. Additionally, the results indicate that increased loadings of *immobilized* colloidal tin oxide improve the stability of HP, although this effect is much less than for *dispersed* colloidal tin oxide (RQ-STA-4): higher loadings are thus required. Finally, it was hypothesized that the (only disclosed) stabilizer present in Sigma Aldrich HP is removed from the solution by the colloidal tin oxide, both in its dispersed and immobilized form (RQ-STA-5). Though, this cannot be confirmed due to the lack of sensitive (chemical) analysis equipment and suitable reference stability data.

Recommendations

Unfortunately the available time for this research is restricted. Therefore only a selected number of aspects could be tested. This chapter will supply the reader with concrete directions for further research.

Purification of propellant-grade H_2O_2

The research as presented here produced a predictive model for condenser design. This model should be adapted to include i.a. more advanced flow phenomena and geometries to increase the predictive value of the model. Additionally, based on promising early results obtained with the direct impact condenser, this should be subject to further research. Since the carried out investigation was not able to measure the impurity content in HP, further research should also investigate the effect of evaporation and condensation on the product purity.

Support effect on the decomposition of H_2O_2 over MnO_x catalysts

First of all, because of time limitations this research could not produce a functional platinum catalyst, embedded in a so-called metal oxide perovskite matrix (see [chapter C](#)). Due to its promising reported high temperature catalytic behavior (e.g. [62]), and thus its possibly high suitability for use in HP rocket engines, more research effort should be dedicated to its development.

Further, the catalysts that are the main topic of discussion should be subjected to extensive spectroscopic investigation in order to determine the nature of their active phase. This will not only allow targeted improvements in the catalyst design, but also add important knowledge to the body of science in this amply explored field of high temperature catalysis.

And, as has been pointed out earlier, results from drop-testing as implemented in this research have low correlation to real life performance, but will still be vital for a basic understanding of the catalytic system at hand. Beside testing in a small scale engine, it is also possible to adapt the drop-testing reactor to i.a. accompany for the outflow of reaction products and reduce environmental heat dissipation. This would not only improve the quality and reproducibility of the results, but additionally increase the correspondence with combustion chamber performance. In addition, an improved reactor design would enable extended lifetime testing, and hence show currently invisible deactivation effects. The adapted setup could ultimately result in the establishment of a novel technique to reliably predict real-world performance of combustion catalysts based on relatively simple laboratory testing.

In addition, due to time constraints, this research was not able to investigate the induced hypergolicity of HP with ethanol. As this topic is of high relevance for industry, further research should aim to achieve this hypergolicity. It is expected that the proposed changes to the drop-test setup would enhance the probability of hypergolic ignition.

Stabilizing propellant-grade H_2O_2

Further investigations should look into the optimal anodizing process parameters in order to generate a perfectly flat and continuous oxide layer, without the use of phosphoric acid. Namely, it has been explained that the anodizing and calcination process conditions have most likely resulted in the observed deterioration of the aluminum strips. In addition, the calcination conditions should be chosen such that no cracking will occur; most likely this can be brought about by decreasing the heating and cooling rate of the calcination process.

Additionally, the effect of further increasing tin oxide surface loadings should be investigated, due to the associated shown higher stability of HP with respect to absence of these coatings. It is very well possible that even higher loadings of tin oxide will have a distinct positive effect on the stability of HP, and thus result in

a "solid-state" stabilizer. When these future experiments would also be coupled with sensitive spectroscopic methods, the physicochemical degradation of the stabilizers can be monitored over time, on its turn easing further improvements.

Bibliography

- [1] S. An, R. Brahmi, C. Kappenstein, and S. Kwon. Transient behavior of H₂O₂ thruster: Effect of injector type and ullage volume. *Journal of Propulsion and Power*, 25(6):1357–1360, 2009.
- [2] S. An, J. Lee, R. Brahmi, and C. Kappenstein. Comparison of Catalyst Support Between Monolith and Pellet in Hydrogen Peroxide Thrusters. *Journal of Propulsion and Power*, 26(3):439–445, 2010.
- [3] F. Apaydin, T. Tunç Parlak, and K. Yıldız. Low temperature formation of barium titanate in solid state reaction by mechanical activation of BaCO₃ and TiO₂. *Materials Research Express*, 6(12):126330, 1 2020.
- [4] M. Baldi, F. Milella, J. M. Gallardo-Amores, and G. Busca. A study of Mn-Ti oxide powders and their behaviour in propane oxidation catalysis. *Journal of Materials Chemistry*, 8(11):2525–2531, 1998.
- [5] Y. Batonneau, R. Brahmi, B. Cartoixa, K. Farhat, C. Kappenstein, S. Keav, G. Kharchafi-Farhat, L. Pirault-Roy, M. Saouabé, and C. Scharlemann. Green propulsion: Catalysts for the European FP7 project GRASP. *Topics in Catalysis*, 57:656–667, 2014.
- [6] J. Blevins, R. Gostowski, and S. Chianese. An Experimental Investigation of Hypergolic Ignition Delay of Hydrogen Peroxide with Fuel Mixtures. In *42nd AIAA Aerospace Sciences Meeting and Exhibit*, Reston, Virginia, 1 2004. American Institute of Aeronautics and Astronautics.
- [7] S. Bonifacio, G. Festa, and A. Russo Sorge. Catalytic Ignition in Hydrogen Peroxide-Based Space Propulsion Systems. In *48th AIAA/ASME/SAE/ASEE Joint Propulsion Conference & Exhibit*, Atlanta, 8 2012. AIAA.
- [8] S. Bonifacio, G. Festa, and A. R. Sorge. Novel Structured Catalysts for Hydrogen Peroxide Decomposition in Monopropellant and Hybrid Rockets. *Journal of Propulsion and Power*, 29(5):1130–1137, 2013.
- [9] S. Bonifacio, A. R. Sorge, D. Krejci, A. Woschnak, and C. Scharlemann. Novel manufacturing method for hydrogen peroxide catalysts: A performance verification. *Journal of Propulsion and Power*, 30(2): 299–308, 3 2014.
- [10] O. Bulavchenko, Z. Vinokurov, T. Afonasenko, E. Gerasimov, and V. Konovalova. The activation of MnOx-ZrO₂ catalyst in CO oxidation: Operando XRD study. *Materials Letters*, 315:131961, 5 2022.
- [11] O. A. Bulavchenko, S. V. Tsybulya, P. G. Tsyryls'nikov, T. N. Afonasenko, S. V. Cherepanova, and E. Y. Gerasimov. Chemical and structural transformations in manganese aluminum spinel of the composition Mn_{1.5}Al_{1.5}O₄ during heating and cooling in air. *Journal of Structural Chemistry*, 51(3):500–506, 2010.
- [12] O. A. Bulavchenko, T. N. Afonasenko, P. G. Tsyryl'nikov, and S. V. Tsybulya. Effect of heat treatment conditions on the structure and catalytic properties of MnOx/Al₂O₃ in the reaction of CO oxidation. *Applied Catalysis A: General*, 459:73–80, 5 2013.
- [13] N. Burgos, M. Paulis, and M. Montes. Preparation of Al₂O₃/Al monoliths by anodisation of aluminium as structured catalytic supports. *Journal of Materials Chemistry*, 13(6):1458–1467, 6 2003.
- [14] G. A. Campbell and P. V. Rutledge. Detonation of hydrogen peroxide vapour. In *Symposium series No. 33*, pages 37–43, London, 1972. Institute of Chemical Engineers.
- [15] A. Cervone, L. Torre, A. SpA, A. J. Musker, G. T. Roberts, C. Bramanti, and G. Saccoccia. Development of Hydrogen Peroxide Monopropellant Rockets. In *42nd AIAA/ASME/SAE/ASEE Joint Propulsion Conference & Exhibit*, Sacramento, 2006. AIAA.
- [16] C. C. Chen, H. J. Liaw, C. M. Shu, and Y. C. Hsieh. Autoignition temperature data for methanol, ethanol, propanol, 2-butanol, 1-butanol, and 2-methyl-2,4-pentanediol. *Journal of Chemical and Engineering Data*, 55(11):5059–5064, 11 2010.

- [17] S. V. Cherepanova, O. A. Bulavchenko, E. Y. Gerasimov, and S. V. Tsybulya. Low- and high-temperature oxidation of $\text{Mn}_{1.5}\text{Al}_{1.5}\text{O}_4$ in relation to decomposition mechanism and microstructure. *CrystEngComm*, 18(19):3411–3421, 2016.
- [18] A. Chowdhury, S. T. Thynell, and S. Wang. Ignition Behavior of Novel Hypergolic Materials. In *45th AIAA/ASME/SAE/ASEE Joint Propulsion Conference & Exhibit*, Denver, 8 2009. AIAA.
- [19] K. A. Cooper and J. G. Watkinson. The supercooling of aqueous hydrogen peroxide. *Transactions of the Faraday Society*, 53:635–641, 1 1957.
- [20] S. Cortès Borgmeyer. Chemical bi-propellant thruster family, 2021. URL <https://www.space-propulsion.com/brochures/bipropellant-thrusters/bipropellant-thrusters.pdf>.
- [21] A. E. Danks, S. R. Hall, and Z. Schnepf. The evolution of 'sol-gel' chemistry as a technique for materials synthesis. *Materials Horizons*, 3(2):91–112, 3 2016.
- [22] D. D. Davis, L. A. Dee, B. Greene, S. D. Hornung, M. B. McClure, and K. A. Rathgeber. Fire, Explosion, Compatibility and Safety Hazards of Hydrogen Peroxide. Technical report, NASA, Las Cruces, 2005.
- [23] S. M. Davis and N. Yilmaz. Advances in Hypergolic Propellants: Ignition, Hydrazine, and Hydrogen Peroxide Research. *Advances in Aerospace Engineering*, 2014:1–9, 9 2014.
- [24] G. De Faveri. Strategies in organocatalysts immobilisation, 2011.
- [25] K. P. De Jong, editor. *Synthesis of Solid Catalysts*. Wiley-VCH, 1 edition, 10 2009.
- [26] C. Deng, M. McAllister, M. R. De Guire, and A. H. Heuer. Effects of Operating Conditions on LSM-Based SOFC Cathodes: EIS Analysis. In *21st Annual Solid Oxide Fuel Cell (SOFC) Project Review Meeting*, Virtual Event, 7 2020. National Energy Technology Laboratory.
- [27] S. Dolci, D. Belli Dell'Amico, A. Pasini, L. Torre, G. Pace, and D. Valentini. Platinum catalysts development for 98% hydrogen peroxide decomposition in pulsed monopropellant thrusters. *Journal of Propulsion and Power*, 31(4):1204–1216, 4 2015.
- [28] V. P. Dravid, V. Ravikumar, M. R. Notis, C. E. Lyman, G. Dhalenne, and A. Revcolevschi. Stabilization of Cubic Zirconia with Manganese Oxide. *Journal of the American Ceramic Society*, 77(10):2758–2762, 10 1994.
- [29] P. Dulian. Solid-State Mechanochemical Syntheses of Perovskites. In *Perovskite Materials - Synthesis, Characterisation, Properties, and Applications*, chapter 1. IntechOpen, 2 2016.
- [30] W. Ebelke, editor. *Hydrogen peroxide handbook*. Rocketdyne, 1967.
- [31] ESA. Considering hydrazine-free satellite propulsion, 11 2013. URL https://www.esa.int/Safety_Security/Clean_Space/Considering_hydrazine-free_satellite_propulsion.
- [32] ESA. ESA responding to EU's REACH chemical law, 5 2019. URL https://www.esa.int/Enabling_Support/Space_Engineering_Technology/ESA_responding_to_EU_s_REACH_chemical_law.
- [33] W. Eul, A. Moeller, and N. Steiner. Hydrogen Peroxide. In A. Seidel, editor, *Kirk-Othmer encyclopedia of chemical technology*, volume 14, chapter 2, pages 35–78. John Wiley & Sons, Inc., Hoboken, 4 edition, 2004.
- [34] P. Fortescue, J. Stark, and G. Swinerd, editors. *Spacecraft systems engineering*. John Wiley & Sons, Ltd., Chichester, third edition, 2003.
- [35] J. E. Funk and S. I. Heister. Development Testing Of Non-Toxic, Storable Hypergolic Liquid Propellants. In *35th Joint Propulsion Conference and Exhibit*, Los Angeles, 6 1999. AIAA.
- [36] V. Ganesan. *Internal combustion engines*. McGraw-Hill, 4 edition, 8 1995.

- [37] L. Gao, L. Zhou, C. Li, J. Feng, and Y. Lu. Kinetics of stabilized cubic zirconia formation from $\text{MnO}_2\text{-ZrO}_2$ diffusion couple. *Journal of Materials Science*, 48(2):974–977, 1 2013.
- [38] L. Gao, R. Guan, S. Zhang, H. Zhi, C. Jin, L. Jin, Y. Wei, and J. Wang. As-Sintered Manganese-Stabilized Zirconia Ceramics with Excellent Electrical Conductivity. *Crystals*, 12(5):620, 4 2022.
- [39] F. A. Garcés-Pineda, J. González-Cobos, M. Torrens, and J. R. Galán-Mascarós. Fluorine-Doped Tin Oxide/Alumina as Long-Term Robust Conducting Support for Earth-Abundant Water Oxidation Electrocatalysts. *ChemElectroChem*, 6(8):2282–2289, 4 2019.
- [40] C. Gomez-Yañez, C. Benitez, and H. Balmori-Ramirez. Mechanical activation of the synthesis reaction of BaTiO_3 from a mixture of BaCO_3 and TiO_2 powders. *Ceramics International*, 26(3):271–277, 4 2000.
- [41] S. Gražulis, D. Chateigner, R. T. Downs, A. F. T. Yokochi, M. Quirós, L. Lutterotti, E. Manakova, J. Butkus, P. Moeck, and A. Le Bail. Crystallography Open Database – an open-access collection of crystal structures. *Journal of Applied Crystallography*, 42(4):726–729, 8 2009.
- [42] S. L. Guseinov, S. G. Fedorov, V. A. Kosykh, and P. A. Storozhenko. Hydrogen Peroxide Decomposition Catalysts Used in Rocket Engines. *Russian Journal of Applied Chemistry*, 93(4):467–487, 2020.
- [43] U. Halenius, F. Bosi, and H. Skogby. Galaxite, MnAl_2O_4 , a spectroscopic standard for tetrahedrally coordinated Mn^{2+} in oxygen-based mineral structures. *American Mineralogist*, 92(7):1225–1231, 7 2007.
- [44] Y. Hemberger, N. Wichtner, C. Berthold, and K. G. Nickel. Quantification of Ytria in Stabilized Zirconia by Raman Spectroscopy. *International Journal of Applied Ceramic Technology*, 13(1):116–124, 1 2016.
- [45] K. Huang. An emerging platform for electrocatalysis: perovskite exsolution. *Science Bulletin*, 61(23):1783–1784, 12 2016.
- [46] IEA. The Role of Critical Minerals in Clean Energy Transitions. Technical report, IEA, Paris, 2021.
- [47] D. Jang, S. Kwon, and S. Jo. Effect of phosphate stabilizers in hydrogen peroxide decomposition on manganese-based catalysts. *Journal of Propulsion and Power*, 31(3):904–911, 1 2015.
- [48] H. Jiang, G. Chu, H. Gong, and Q. Qiao. Tin Chloride Catalysed Oxidation of Acetone with Hydrogen Peroxide to Tetrameric Acetone Peroxide. *Journal of Chemical Research*, 23(4):288–289, 4 1999.
- [49] Z. B. Jildeh, J. Oberländer, P. Kirchner, P. H. Wagner, and M. J. Schöning. Thermocatalytic behavior of manganese (IV) oxide as nanoporous material on the dissociation of a gas mixture containing hydrogen peroxide. *Nanomaterials*, 8(4), 4 2018.
- [50] J. John, P. Nandagopalan, S. W. Baek, and S. J. Cho. Hypergolic ignition delay studies of solidified ethanol fuel with hydrogen peroxide for hybrid rockets. *Combustion and Flame*, 212:205–215, 2 2020.
- [51] P. Jones, M. L. Tobe, and W. Wynne-Jones. Hydrogen peroxide + water mixtures - Part 5 - Stabilization against the iron perchlorate catalyzed decomposition of hydrogen peroxide. *Transactions of the Faraday Society*, 55:91–97, 1959.
- [52] B. V. Jyoti, M. S. Naseem, and S. W. Baek. Hypergolicity and ignition delay study of pure and energized ethanol gel fuel with hydrogen peroxide. *Combustion and Flame*, 176:318–325, 2 2017.
- [53] B. V. S. Jyoti, M. S. Naseem, S. W. Baek, H. J. Lee, and S. J. Cho. Hypergolicity and ignition delay study of gelled ethanamine fuel. *Combustion and Flame*, 183:102–112, 2017.
- [54] B. V. S. Jyoti, J. Quesada Mañas, and P. G. Prasad. Process and apparatus for concentrating hydrogen peroxide to 95 wt.% or more, 2021.
- [55] H. Kang and S. Kwon. Experiment and speculations on nontoxic hypergolic propulsion with hydrogen peroxide. *Journal of Spacecraft and Rockets*, 55(5):1230–1234, 5 2018.
- [56] H. Kang, S. Park, Y. Park, and J. Lee. Ignition-delay measurement for drop test with hypergolic propellants: Reactive fuels and hydrogen peroxide. *Combustion and Flame*, 217:306–313, 2020.

- [57] C. Kappenstein, L. Pirault-Roy, M. Guérin, T. Wahdan, A. A. Ali, F. A. Al-Sagheer, and M. I. Zaki. Monopropellant decomposition catalysts: V. Thermal decomposition and reduction of permanganates as models for the preparation of supported MnO_x catalysts. *Applied Catalysis A: General*, 234(1-2):145–153, 8 2002.
- [58] G. Kelp, T. Tätte, S. Pikker, H. Mändar, A. G. Rozhin, P. Rauwel, A. S. Vanetsev, A. Gerst, M. Merisalu, U. Mäeorg, M. Natali, I. Persson, and V. G. Kessler. Self-assembled SnO_2 micro- and nanosphere-based gas sensor thick films from an alkoxide-derived high purity aqueous colloid precursor. *Nanoscale*, 8(13):7056–7067, 4 2016.
- [59] A. Kerekes and S. Esposito. 2,6-Pyridinedicarboxylic Acid, 1-Oxide. In *Encyclopedia of Reagents for Organic Synthesis*. John Wiley & Sons, Ltd, Chichester, UK, 9 2009.
- [60] W. S. Kijlstra, E. K. Poels, A. Bliet, B. M. Weckhuysen, and R. A. Schoonheydt. Characterization of Al_2O_3 -Supported Manganese Oxides by Electron Spin Resonance and Diffuse Reflectance Spectroscopy. *Journal of Physical Chemistry B*, 101(3):309–316, 1997.
- [61] J. U. Kim, J. K. Kim, J. W. Choi, Y. H. Kim, J. H. Ahn, G.-T. Kim, D. K. Jun, and H. B. Gu. Charge/Discharge Characteristics of SnO_2 Electrodes for Lithium Polymer Batteries. In *Materials Science Forum*, volume 486-487, pages 606–609, Virtual Event, 6 2005. Trans Tech Publications, Ltd.
- [62] M. Kothari, Y. Jeon, D. N. Miller, A. E. Pascui, J. Kilmartin, D. Wails, S. Ramos, A. Chadwick, and J. T. S. Irvine. Platinum incorporation into titanate perovskites to deliver emergent active and stable platinum nanoparticles. *Nature Chemistry*, 5 2021.
- [63] D. Krejci, A. Woschnak, M. Schiebl, C. Scharlemann, K. Ponweiser, R. Brahmi, Y. Batonneau, and C. Kappenstein. Assessment of catalysts for hydrogen-peroxide-based thrusters in a flow reactor. *Journal of Propulsion and Power*, 29(2):321–330, 3 2013.
- [64] B. Lafuente, R. T. Downs, H. Yang, and N. Stone. 1. The power of databases: The RRUFF project. In *Highlights in Mineralogical Crystallography*, pages 1–30. DE GRUYTER, 11 2015.
- [65] C. Lahousse, A. Bernier, P. Grange, B. Delmon, P. Papaefthimiou, T. Ioannides, and X. Verykios. Evaluation of $\gamma\text{-MnO}_2$ as a VOC Removal Catalyst: Comparison with a Noble Metal Catalyst. *Journal of Catalysis*, 178(1):214–225, 8 1998.
- [66] S. Landi, I. R. Segundo, E. Freitas, M. Vasilevskiy, J. Carneiro, and C. J. Tavares. Use and misuse of the Kubelka-Munk function to obtain the band gap energy from diffuse reflectance measurements. *Solid State Communications*, 341, 1 2022.
- [67] W. J. Larson and J. R. Wertz, editors. *Space Mission Analysis and Design*. Microcosm, Inc., El Segundo, third edition, 1999.
- [68] J. Lee and S. Kwon. Evaluation of ethanol-blended hydrogen peroxide monopropellant on a 10 N class thruster. *Journal of Propulsion and Power*, 29(5):1164–1170, 2013.
- [69] Y. N. Lee, R. M. Lago, J. L. G. Fierro, and J. González. Hydrogen peroxide decomposition over $\text{Ln}_{1-x}\text{A}_x\text{MnO}_3$ ($\text{Ln} = \text{La}$ or Nd and $\text{A} = \text{K}$ or Sr) perovskites. *Applied Catalysis A: General*, 215(1-2):245–256, 7 2001.
- [70] A. G. Leigh. Stabilisation of hydrogen peroxide, 9 1978.
- [71] J.-Y. Lestrade, P. Prévot, J. Messineo, J. Anthoine, S. Casu, B. Geiger, J.-Y. Lestrade, P. Prévot, J. Messineo, J. Anthoine, S. Casu, B. Geiger, and J.-Y. Lestrade. Development of a catalyst for highly concentrated hydrogen peroxide. In *Space Propulsion*, Rome, 5 2016.
- [72] F. Li, X. Yu, L. Chen, H. Pan, and Q. Xin. Solid-State Synthesis of LaCoO_3 Perovskite Nanocrystals. *Journal of the American Ceramic Society*, 85(9):2177–2180, 9 2002.
- [73] J. Li, W. Fan, X. Weng, C. Tang, X. Zhang, Z. Huang, and Q. Zhang. Experimental observation of hypergolic ignition of superbase-derived ionic liquids. *Journal of Propulsion and Power*, 34(1):125–132, 1 2018.

- [74] J. H. Lienhard IV and J. H. Lienhard V. *A Heat Transfer Textbook*. Phlogistron Press, Cambridge, Massachusetts, 5 edition, 2020.
- [75] S. Y. Lim. Bimodal porous structure tin oxide anode materials for lithium ion batteries. *Journal of Industrial and Engineering Chemistry*, 78:284–294, 10 2019.
- [76] C. Lin, A. C. Foucher, Y. Ji, C. D. Curran, E. A. Stach, S. McIntosh, and R. J. Gorte. "intelligent" Pt Catalysts Studied on High-Surface-Area CaTiO₃ Films. *ACS Catalysis*, 9(8):7318–7327, 8 2019.
- [77] U. Lohbauer, M. Zipperle, K. Rischka, A. Petschelt, and F. A. Müller. Hydroxylation of dental zirconia surfaces: characterization and bonding potential. *Journal of biomedical materials research. Part B, Applied biomaterials*, 87(2):461–467, 11 2008.
- [78] MAESNET. Anemometer calibration procedure. Technical report, MAESNET, 2009.
- [79] F. Magalhães, F. Cristina, C. Moura, J. Domingos Ardisson, and R. Montero Lago. LaMn_{1-x}FeO₃ and LaMn_{0.1-x}Fe_{0.90}Mo_xO₃ Perovskites: Synthesis, Characterization and Catalytic Activity in H₂O₂ Reactions. *Materials Research*, 11(3):307–312, 2008.
- [80] X. Mao, A. C. Foucher, E. A. Stach, and R. J. Gorte. "Intelligent" Pt catalysts based on thin LaCoO₃ films prepared by atomic layer deposition. *Inorganics*, 7(9):113, 9 2019.
- [81] X. Mao, C. Lin, G. W. Graham, and R. J. Gorte. A Perspective on Thin-Film Perovskites as Supports for Metal Catalysts. *ACS Catalysis*, 10(15):8840–8849, 8 2020.
- [82] C. J. Martinez, B. Hockey, C. B. Montgomery, and S. Semancik. Porous tin oxide nanostructured microspheres for sensor applications. *Langmuir*, 21(17):7937–7944, 8 2005.
- [83] B. J. McBride and S. Gordon. Computer Program for Calculation of Complex Chemical Equilibrium Compositions and Applications. Technical report, NASA, 6 1996.
- [84] L. Micoli, G. Bagnasco, M. Turco, M. Trifuoggi, A. Russo Sorge, E. Fanelli, P. Pernice, and A. Aronne. Vapour phase H₂O₂ decomposition on Mn based monolithic catalysts synthesized by innovative procedures. *Applied Catalysis B: Environmental*, 140-141:516–522, 8 2013.
- [85] A. J. Musker, J. J. Rusek, C. Kappenstein, and G. T. Roberts. Hydrogen peroxide - From bridesmaid to bride. In *3rd ESA International Conference on Green Propellants for Space Propulsion*, Poitiers, 9 2006.
- [86] M. S. Naseem, B. V. Jyoti, S. W. Baek, H. J. Lee, and S. J. Cho. Hypergolic Studies of Ethanol Based Gelled Bi-Propellant System for Propulsion Application. *Propellants, Explosives, Pyrotechnics*, 42(6):676–682, 6 2017.
- [87] Y. Nishihata, J. Mizuki, T. Akao, H. Tanaka, M. Uenishi, M. Kimura, T. Okamoto, and N. Hamada. Self-regeneration of a Pd-perovskite catalyst for automotive emissions control. *Nature*, 418(6894):164–167, 7 2002.
- [88] T. M. Onn, M. Monai, S. Dai, E. Fonda, T. Montini, X. Pan, G. W. Graham, P. Fornasiero, and R. J. Gorte. Smart Pd catalyst with improved thermal stability supported on high-surface-area LaFeO₃ prepared by atomic layer deposition. *Journal of the American Chemical Society*, 140(14):4841–4848, 4 2018.
- [89] S. Ono. Structure and Growth Mechanism of Anodic Oxide Films Formed on Aluminum and Their Gas Emission Property in Vacuum. *Journal of the Vacuum Society of Japan*, 52(12):637–644, 2009.
- [90] P. Pal, S. Saha, A. Banik, A. Sarkar, and K. Biswas. All-Solid-State Mechanochemical Synthesis and Post-Synthetic Transformation of Inorganic Perovskite-type Halides. *Chemistry – A European Journal*, 24(8):1811–1815, 2 2018.
- [91] R. K. Palmer and J. J. Rusek. Low toxicity reactive hypergolic fuels for use with hydrogen peroxide. In *2nd Int. Conference on Green Propellants for Space Propulsion*, Cagliari, 10 2004. ESA.
- [92] N. K. Park, T. H. Lee, Y. B. Sung, Y. S. Kim, and T. J. Lee. Preparation of macro-porous tin oxide for sensing of sulfur compound. *Journal of Nanoscience and Nanotechnology*, 16(3):3062–3066, 3 2016.

- [93] N. Pearson, T. Pourpoint, and W. Anderson. Vaporization and decomposition of hydrogen peroxide drops. In *39th AIAA/ASME/SAE/ASEE Joint Propulsion Conference and Exhibit*, Huntsville, 7 2003. AIAA.
- [94] P. Pędziwiatr, F. Mikołajczyk, D. Zawadzki, K. Mikołajczyk, A. Bedka, S. Koło, and N. Oktan. Decomposition of hydrogen peroxide - kinetics and review of chosen catalysts. *Acta Innovations*, 45(26):45–52, 2018.
- [95] S. Peter, S. Kabelac, M. Kind, D. Mewes, K. Schaber, and T. Wetzel, editors. *VDI-Wärmeatlas*. Springer-Verlag GmbH, Düsseldorf, 12 edition, 2019.
- [96] A. P. Philipse. *Brownian Motion*. Undergraduate Lecture Notes in Physics. Springer International Publishing, Cham, 1 edition, 2018.
- [97] L. Pirault-Roy, C. Kappenstein, M. Guérin, R. Eloirdi, and N. Pillet. Hydrogen peroxide decomposition on various supported catalysts effect of stabilizers. *Journal of Propulsion and Power*, 18(6):1235–1241, 2002.
- [98] J. E. Post, D. A. McKeown, and P. J. Heaney. Raman spectroscopy study of manganese oxides: Tunnel structures. *American Mineralogist*, 105(8):1175–1190, 8 2020.
- [99] S. Pugh. *Total Design: Integrated Methods for Successful Product Engineering*. Addison-Wesley, 1991.
- [100] K. Radimer. Stabilization of high purity hydrogen peroxide, 1983.
- [101] A. Rao, H. Long, A. Harley-Trochimczyk, T. Pham, A. Zettl, C. Carraro, and R. Maboudian. In situ localized growth of ordered metal oxide hollow sphere array on microheater platform for sensitive, ultra-fast gas sensing. *ACS Applied Materials and Interfaces*, 9(3):2634–2641, 1 2017.
- [102] G. Rarata, K. Rokicka, and P. Surmacz. Hydrogen peroxide as a high energy compound optimal for propulsive applications. *Central European Journal of Energetic Materials*, 13(3):778–790, 2016.
- [103] J. Richter, A. E. Peter, H. Ae, T. Graule, A. E. Tetsuro, N. Ae, and L. J. Gauckler. Materials design for perovskite SOFC cathodes. *Monatsh Chem*, 140:985–999, 2009.
- [104] T. G. Roberts. Space Launch to Low Earth Orbit: How Much Does It Cost?, 5 2021. URL <https://aerospace.csis.org/data/space-launch-to-low-earth-orbit-how-much-does-it-cost/>.
- [105] L. Romeo, L. Torre, A. Pasini, A. Cervone, L. D’Agostino, and F. Calderazzo. Performance of different catalysts supported on alumina spheres for hydrogen peroxide decomposition. In *Collection of Technical Papers - 43rd AIAA/ASME/SAE/ASEE Joint Propulsion Conference*, volume 5, pages 4457–4469, 2007.
- [106] L. Romeo, L. Torre, A. Pasini, A. SpA, and F. Calderazzo. Comparative Characterization of Advanced Catalytic Beds for Hydrogen Peroxide Thrusters. In *44th AIAA/ASME/SAE/ASEE Joint Propulsion Conference & Exhibit 21*, Hartford, 7 2008.
- [107] G. Rothenberg. *Catalysis*. Wiley, 1 2008.
- [108] A. Russo Sorge, M. Turco, G. Pilone, and G. Bagnasco. Decomposition of hydrogen peroxide on $\text{MnO}_2/\text{TiO}_2$ catalysts. *Journal of Propulsion and Power*, 20(6):1069–1075, 2004.
- [109] W. C. Schumb, C. N. Satterfield, and R. L. Wentworth. *Hydrogen Peroxide*. Reinhold Publishing Corporation, London, 1955.
- [110] R. Serra-Maia, M. Bellier, S. Chastka, K. Tranhuu, A. Subowo, J. D. Rimstidt, P. M. Usov, A. J. Morris, and F. M. Michel. Mechanism and Kinetics of Hydrogen Peroxide Decomposition on Platinum Nanocatalysts. *ACS Applied Materials & Interfaces*, 10(25), 6 2018.
- [111] R. K. Shah and D. P. Sekuli. *Fundamentals of Heat Exchanger Design*. John Wiley & Sons, Inc., Hoboken, NJ, USA, 7 2003.
- [112] M. N. Shoaib, B. V. Jyoti, S. W. Baek, and J. Huh. Effect of alcohol carbon chain on enthalpy of combustion and ignition delay time for gelled hypergolic propellant system. *Propellants, Explosives, Pyrotechnics*, 43(5):453–460, 5 2018.

- [113] M. Soleymani, A. Moheb, and D. Babakhani. Hydrogen Peroxide Decomposition over Nanosized $\text{La}_{1-x}\text{Ca}_x\text{MnO}_3$ ($0 < x < 0.6$) Perovskite Oxides. *Chemical Engineering and Technology*, 34(1):49–55, 1 2011.
- [114] D. Song, X. Shao, M. Yuan, L. Wang, W. Zhan, Y. Guo, Y. Guo, and G. Lu. Selective catalytic oxidation of ammonia over $\text{MnO}_x\text{-TiO}_2$ mixed oxides. *RSC Advances*, 6(91):88117–88125, 2016.
- [115] M. Stevenson. Anodizing. In C. Cotell, J. Sprague, and F. Smidt, editors, *ASM Handbook*, volume 5, pages 482–493. ASM International, 1994.
- [116] P. Surmacz, M. Kostecki, Z. Gut, and A. Olszyna. Aluminum Oxide-Supported Manganese Oxide Catalyst for a 98% Hydrogen Peroxide Thruster. *Journal of Propulsion and Power*, 35(3):614–623, 2019.
- [117] G. P. Sutton and O. Biblarz. *Rocket propulsion elements*. John Wiley & Sons, Inc., Hoboken, 8th edition, 2010.
- [118] H. Tanaka, M. Taniguchi, M. Uenishi, N. Kajita, I. Tan, Y. Nishihata, J. Mizuki, K. Narita, M. Kimura, and K. Kaneko. Self-regenerating Rh- and Pt-based perovskite catalysts for automotive-emissions control. *Angewandte Chemie - International Edition*, 45(36):5998–6002, 9 2006.
- [119] M. Tepluchin, M. Casapu, A. Boubnov, H. Lichtenberg, D. Wang, S. Kureti, and J.-D. Grunwaldt. Fe and Mn-Based Catalysts Supported on $\gamma\text{-Al}_2\text{O}_3$ for CO Oxidation under O_2 -Rich Conditions. *Chem-CatChem*, 6(6):1763–1773, 6 2014.
- [120] K. Thulukkanam. *Heat Exchanger Design Handbook*. CRC Press, 5 2013.
- [121] J. M. Tran and E. Y. Kenig. Condensation. In *Ullmann's Encyclopedia of Industrial Chemistry*. Wiley-VCH Verlag GmbH & Co. KGaA, Weinheim, Germany, 11 2017.
- [122] S. V. Tsybulya, G. N. Kryukova, T. A. Kriger, and P. G. Tsyru'nikov. Structural Aspect of a Thermal Activation Effect in the $\text{MnO}_x/\gamma\text{-Al}_2\text{O}_3$ System. *Kinetics and Catalysis 2003 44:2*, 44(2):287–296, 3 2003.
- [123] US Department of Defense. Performance specification: propellant, hydrogen peroxide (MIL-PRF-16005F), 1967.
- [124] M. Ventura and G. Garboden. A brief history of concentrated hydrogen peroxide uses, 1999. URL https://www.hydrogen-peroxide.us/history-US-General-Kinetics/AIAA-1999-2739_A_Brief_History_of_Concentrated_Hydrogen_Peroxide_Uses_pitch.pdf.
- [125] M. C. Ventura. Long Term Storability of Hydrogen Peroxide. In *41st AIAA/ASME/SAE/ASEE Joint Propulsion Conference & Exhibit*, Tucson, 7 2005. AIAA.
- [126] Virgin Galactic. Safety - the North star, 2013. URL <http://www.virgingalactic.com/overview/safety>.
- [127] D. Watling, C. Ryle, M. Parks, and M. Christopher. Theoretical Analysis of the Condensation of Hydrogen Peroxide Gas and Water Vapour as Used in Surface Decontamination. *PDA Journal of Pharmaceutical Science and Technology*, 56(6), 2002.
- [128] R. C. Weast, editor. *CRC Handbook of Chemistry and Physics*. CRC Press, Inc., Boca Raton, 60th edition, 1979.
- [129] H. Wu, X. Xu, L. Shi, Y. Yin, L. C. Zhang, Z. Wu, X. Duan, S. Wang, and H. Sun. Manganese oxide integrated catalytic ceramic membrane for degradation of organic pollutants using sulfate radicals. *Water Research*, 167, 12 2019.
- [130] Y. Wu, L. Lu, Z. Yu, and X. Wang. Electrochemical sensor based on the $\text{Mn}_3\text{O}_4/\text{CeO}_2$ nanocomposite with abundant oxygen vacancies for highly sensitive detection of hydrogen peroxide released from living cells. *Analytical Methods*, 13(14):1672–1680, 2021.
- [131] H. Yang, T. Zhang, H. Tian, J. Tang, D. Xu, W. Yang, and L. Lin. Effect of Sr substitution on catalytic activity of $\text{La}_{1-x}\text{Sr}_x\text{MnO}_3$ ($0 < x < 0.8$) perovskite-type oxides for catalytic decomposition of hydrogen peroxide. *Reaction Kinetics and Catalysis Letters*, 73(2):311–316, 2001.

-
- [132] H. Yinyan and B. Amiram. Method for washcoating a catalytic material onto a monolithic structure , 7 2004.
- [133] S. Zhai, Y. Yin, S. R. Shieh, Y. Y. Chang, T. Xie, and W. Xue. Raman spectroscopic study of MnAl_2O_4 galaxite at various pressures and temperatures. *Physics and Chemistry of Minerals*, 44(3):163–170, 3 2017.

Appendices

A

Hydrogen peroxide properties

Table A-1: All conditions are given for anhydrous hydrogen peroxide at 298K and atmospheric conditions, unless otherwise indicated;¹ at 293K;[‡] at 7MPa chamber pressure, [†] over 50°C supercooling possible [51].

Molar mass	M_w	g/mol	34.018	[109]
Heat of formation	$\Delta_f^0 H$	kJ/mol	-187.80	
		kJ/kg	-5520.6	
Reduction potential	ΔV	V	1.776	[128, pp. D-158]
Acidity	pK_a	-	11.75 ¹	[33, 51]
Dipole moment	m	D	2.26 (water 1.8546)	[109]
Dielectric constant	ϵ_r	-	60(water 80.2 ¹)	[109, 128]
Heat of reaction (liquid state)	$\Delta_r^0 H$	kJ/mol	98.20	[33]
		kJ/kg	2888	
Heat of reaction (gaseous state)	$\Delta_r^0 H$	kJ/mol	105.26	[33]
		kJ/kg	3094	
Decomposition activation energy (auto-thermal)	E_a	kJ/mol	188-230	[42]
		kJ/kg	5526-6761	
Auto-ignition temperature	T_{auto}	°C	>400	[49]
Decomposition activation energy (catalyzed)	E_a	kJ/mol	30-50	[42, 93]
		kJ/kg	881.9-1470	
Decomposition temperature	T_{dec}	°C	1000	[22, 108]
Density	ρ	kg/L	1.4425	[30, 33, 128]
Volume coefficient of thermal expansion	β	10^{-6} 1/K	750.2	[30]
Solidification point	T_s	°C	-0.43 [†]	[30, 109, 128]
Boiling point	T_b	°C	150.0	[30]
Specific heat, liquid	C_p	J/kg/K	2629	[33]
Specific heat, gas	C_p	J/kg/K	1352	[33]
Heat of vaporization	$\Delta_{vap}^0 H$	kJ/mol	51.61	[33]
		kJ/kg	1517	
Vapor pressure	p_0	Pa	660	[109]
Surface tension	γ_{lg}	N/m	80.4 ¹	[109]
Specific impulse	I_{sp}	s	165 [‡]	[34, pp. 183]

B

Rocket theory

The following is based on the book *Rocket Propulsion Elements* by G.P. Sutton [117].

Simply put, rocket engines operate by mass expulsion. The required energy is stored in the propellants, either in physical (pressure) or chemical form. In chemical systems, the energy is stored in molecules and is released by combustion, whereas for e.g. pressure-based systems it is readily available. The available energy is then transformed in the rocket motor's nozzle by expanding and accelerating the exhaust gasses to high velocities, and hence generating a high impulse. A common factor that to compare different propellants and rocket motor designs is the mass-normalized specific impulse ($I_{sp,m}$, or in usually in short: I_{sp}), which is defined as

$$I_{sp,m} = \frac{F}{\dot{m}g_0} \quad (\text{B-1})$$

Here, F represents the thrust (N), \dot{m} the mass flow through the nozzle (kg/s) and g_0 the gravitational acceleration at sea level (m/s). It can be easily understood that, when assuming a constant mass flow, a higher specific impulse implies a higher thrust per mass of propellant. In addition to the mass-normalized specific impulse, also sometimes the density-based I_{sp} is used, $I_{sp,\rho}$. This can be calculated from the mass-normalized specific impulse by multiplication with the (stored) specific density of the propellant mixture. A higher $I_{sp,\rho}$ thus indicates that for an equal total delivered impulse less propellant volume is required. This means that the storage tanks on board of the spacecraft can be smaller, which not only reduces the total system size, but also its mass.

The thrust itself then depends on many factors, for instance combustion chamber temperature and pressure, average exhaust gas composition and nozzle geometry. The simplest definition for thrust is given below, while neglecting the effects of under- and overexpansion.

$$F = \dot{m}I_{sp}g_0 = \dot{m}U_{eff} \approx \dot{m}U_{exit} \quad (\text{B-2})$$

From this formula it is clear that the exit velocity of the nozzle U_{exit} (m/s) has a large effect on the thrust generation. It can be split up in a part independent of the nozzle geometry (U_{lim} , the limit velocity) and the nozzle expansion factor. The limit velocity is largely determined by exhaust gas properties (the specific heat ratio γ and their molecular weight M_w in g/mol), but is also heavily dependent on the combustion chamber temperature T_c (K). Finally, the total exhaust velocity can be calculated from the limit velocity and the pressure inside the combustion chamber ($P_{chamber}$ in Pa) and at the nozzle exit (P_{exit}).

$$U_{lim} = \sqrt{2 \frac{\gamma}{\gamma-1} \frac{R_A}{M_w} T_c} \quad (\text{B-3})$$

$$U_{exit} = U_{lim} \sqrt{1 - \left(\frac{P_{exit}}{P_{chamber}} \right)^{\frac{\gamma-1}{\gamma}}} \quad (\text{B-4})$$

Close inspection of [Equation B-3](#) learns that the limit velocity increases when the exhaust gasses have a lower molecular weight. Concretely, light combustion products will result in higher rocket performance. Additionally, [Equation B-4](#) shows that performance can be improved as well when the chamber pressure is increased. Alternatively, this chamber pressure can be converted to combustion chamber temperature with the isentropic relations. In practice this means that, while keeping the same performance, the chamber temperature can be lowered if the exhaust gas composition is lowered accordingly. A stoichiometrically operating HP - ethanol engine would merely produce water and CO_2 ; when the engine would be operated lean, the exhaust will contain more O_2 resulting from HP decomposition. It is obvious that a larger concentration of O_2 in the exhaust gas will lower its average mass, hence increasing the limit velocity, and thus performance. Simultaneously though, running lean will generally lead to a lower combustion temperature, which is beneficial

for propulsion system design from a thermomechanical point of view. Yet, it should be considered that lean operation of the engine results in large amounts of high temperature, and thus highly reactive oxygen. This means that there is a higher need for oxygen-resistant materials.

Metal oxide perovskite catalysts

A support that has a stronger interaction than conventional metal oxide supports with the catalytic phase is essential to the success of HP in space propulsion. Many materials have been investigated over the years for their support interaction with Mn and Pt active phases, primarily in industry for instance for automotive catalytic converters. A class of materials that has recently attracted increased interest are metal oxide perovskites (MOPs). MOPs are a structure group of minerals consisting of at least two different cations and oxide ions with general formula ABO_3 . Here A can be a lanthanide or an alkaline Earth metal ion, whereas the (usually smaller) B is generally a transition metal cation. Both A and B can also be composed of multiple different ions, e.g. $X\%$ of A_1 and $100-X\%$ of A_2 . The catalytic performance and stability of the MOP can be tuned by meticulous choice of the A and B species.

Metal oxide perovskitic materials have been the subject of elaborate research efforts. As an example, some MOPs investigated for use in solid oxide fuel cells have proven to be functional at temperatures over 1000°C for 1000 hours, while continuously exposed to an oxygen atmosphere [26, 103]. Other MOPs have been tested for catalytic conversion of HP with mixed results [69, 79, 113, 131]. Due to the additional degrees of freedom in the composition of a MOP catalyst when compared to single metal (oxide) catalysts, optimization of MOP catalytic performance is very challenging. The high stability of these MOPs can also be exploited in another manner: they can serve as a stabilizing support for catalytically active NPs [45]. Certain compositions of MOP can show poor compatibility with NPs on the first sight: Nishihata and coworkers noticed that under oxidative atmosphere palladium NPs would disappear from the surface of the MOP. Yet, when the catalyst was exposed to a reductive atmosphere the nanoparticles would re-form on the surface, i.e. they had not been stripped of the support. This process is illustrated in Figure C-1. Moreover, it was shown that the metal particles would instead atomically dissolve in the support material while being exposed to oxidative conditions [76, 87, 118]. Later research on these regenerative MOPs (ReMOPs) demonstrated both the exceptionally high thermal and long-term stability of this process, without having an impact on the catalytic performance of the NPs [88]. Kothari and coworkers showed that this regenerative behavior was not limited to palladium, but could also be noticed for platinum-based catalysts, without affecting the catalyst's thermal performance [62]. Unfortunately, at this time no research was conducted to investigate the catalytic activity of these platinum-based ReMOPs with HP.

Therefore, because of the promising behavior of these ReMOPs, such a platinum-containing ReMOP (LCT(Pt), or $\text{La}_{0.4}\text{Ca}_{0.3925}\text{Ba}_{0.0075}\text{Ti}_{0.995}\text{Pt}_{0.005}\text{O}_3$ from Kothari et al. [62]) was synthesized in this research in order to verify its reactivity with HP. Due to the proven stability of this catalyst under harsh conditions (no degradation for 350 hours under continuous airflow of 800°C [62]), it was expected that this catalyst material would offer good long-term performance in the catalytic decomposition of concentrated HP. Preparation details of this catalyst can be found in subsection D.1.1 and characterization efforts can be found in subsection E.2.1.

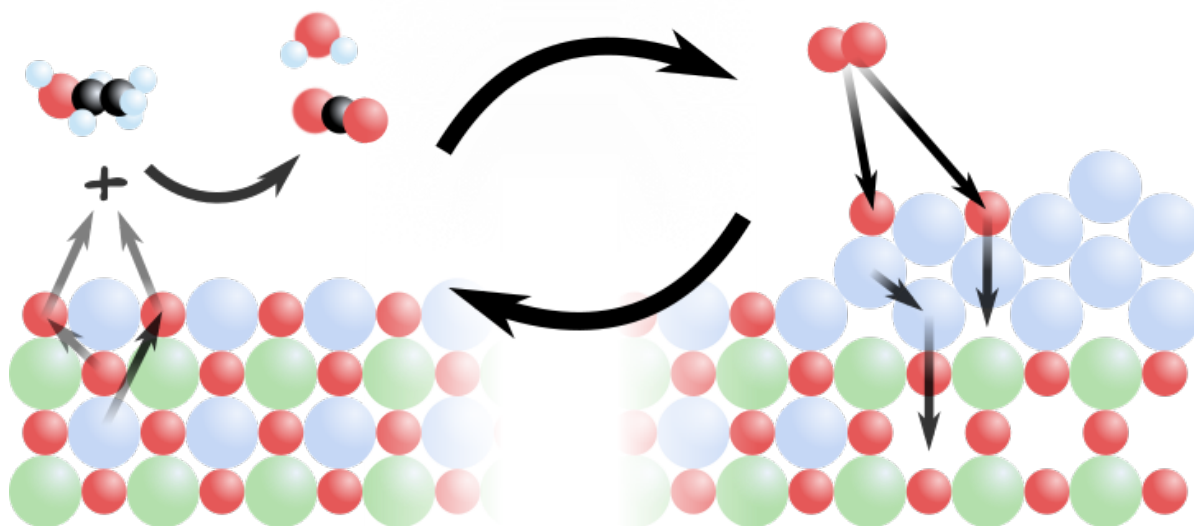


Figure C-1: Schematic representation of the exsolution process. When the catalyst is exposed to ethanol (left), oxygen ions from the crystal lattice are liberated to oxidize the ethanol molecule to water and CO_2 . Simultaneously, because of the resulting lattice instability, the platinum ions are exsolved from the crystal lattice and reduced to atomic platinum, which forms NPs on the surface. The opposite happens under an oxidizing atmosphere (right): the platinum atoms react with the present oxygen and both the platinum and oxygen ions are dissolved in the crystal lattice.

Materials and methods

This chapter will first describe the efforts made to synthesize the catalysts as used during decomposition testing, as described in [chapter 3](#). In addition, it will present the checklists used during testing and a flow diagram of the testing procedure. Then, it will touch upon the methods of calibration for the instruments used during the diverse measurements.

D.1. Support effect on the decomposition of H₂O₂ over MnO_x catalysts

This section will supply the methodology related to the synthesis and testing of the various catalysts in this research.

D.1.1. LCT(Pt) synthesis

For synthesis of the LCT(Pt) catalyst, all precursors were dried at 300°C; La₂O₃ was prepared by decomposing La₂(CO₃)₃ in air in a muffle oven at 750°C for 4 hours, followed by 9 hours calcination at 800°C with a heating rate of 8°C per minute. BaCO₃ (Alfa Aesar, 99%) and PtO₂ (Sigma Aldrich, 99%) were mixed in appropriate amounts, and heated in a muffle oven to 1000°C for 12 hours with a heating rate of 5°C per minute to form Ba₃Pt₂O₇. It was found that standard crucibles were heavily affected by the BaCO₃. Thereto a quartz crucible was coated with a BaCO₃-water paste and calcined (8 hours at 1100°C); this was used for further synthesis of Ba₃Pt₂O₇. It is important to note that the BaO from the liner might also react with the PtO₂, hence possibly changing the stoichiometry of the barium platinate.

Consequently, La_{0.4}Ca_{0.3925}Ba_{0.0075}Ti_{0.995}Pt_{0.005}O₃ (0.577 wt.% Pt), or LCT(Pt), was synthesized by mixing the appropriate amounts of La₂O₃, CaCO₃, Ba₃Pt₂O₇ and TiO₂ in acetone. In addition, 1.4 wt.% of polyester dispersant (Croda KD-1 Hypermer) was added. The dispersion was sonicated for 2 hours. The acetone was removed using centrifugation (3500 rpm, 3 minutes), and the samples were dried at 120°C prior to calcination. Different calcination conditions were tested; the best results were given by a two-step calcination in pure oxygen (20 mL/min). After the first calcination (1000°C, 12 hours) the powder was crushed and sonicated in acetone for two hours; the conversion to LCT(Pt) was complete after the second calcination (24 hours at 1150°C).

Then it was attempted to reduce the catalyst and hence exsolve the platinum by reduction with H₂. Thereto 250 mg of LCT(Pt) was heated to 250°C (with 5°C/min ramp rate) for 2 hours in a 50 vol-% hydrogen atmosphere, balanced with N₂ to 100 mL/min. After cooling, the sample was partially passivated by exposure to air (100 mL/min, 30 minutes). Since this proved not to be sufficient to exsolve the platinum, another approach was attempted. Based on the successful reduction of a similar catalyst (La₃Fe₂O(Pt)), it was attempted to perform reduction of 250 mg of LCT(Pt) with a stronger reductant, CO (10% in nitrogen, balanced to 150 mL/min), at 500°C for 5 hours (with heating and cooling rate of 2°C/min). Yet, even with this strong reductant no metallic platinum could be found.

D.1.2. Manganese dioxide on YSZ synthesis

For the preparation of MnO₂ on YSZ (Mn/YSZ, 10 wt.% MnO₂) the protocol from Bonifacio and coworkers was followed [7–9]. The YSZ support was coated with manganese dihydroxide using deposition precipitation, which was subsequently calcined to the active phase, manganese oxide.

The synthesis was carried out by dissolution of manganese(II) acetate tetrahydrate (Sigma Aldrich, 99%) in DI water to give a 0.23 M solution. The solution was heated to 45°C while being stirred and kept at this temperature for one hour. Then YSZ powder (Alfa Aesar, 99%) was added while stirring giving an opaque white solution; using a syringe pump, 1.0 mL of 24% ammonia was added in an hour. The addition of the ammonia caused the formation of a dark layer on top and a beige layer at the bottom with a brown layer in between. The solution was centrifuged (2500 rpm, 3 minutes) and washed with distilled water three times.

Afterwards the powder was dried overnight at 120°C. The catalyst was calcined in air (10 mL/min) in a quartz crucible at 500°C, with a heating and cooling rate of 10°C/min.

D.1.3. Support development

Initially, 20-30 mg Mn/YSZ was pressed into pellets with 400 MPa pressure into 1/2 inch diameter discs. Additionally, two pellets were pressed with 219 mg of Mn/YSZ with 800 MPa pressure; one of these was calcined at 600°C for 2 hours. Testing with 87% HP showed that the mechanical integrity of these pellets was too low.

To that end, different supports and support types were tried, which were coated by dropcasting. The dropcasting was carried out by sonicating a mixture of Mn/YSZ and ethanol until a stable dispersion was formed. This was then applied dropwise to the surface, only adding the next droplet when all previously applied ethanol had evaporated. Afterwards, the coated support would be calcined (600°C, for 2 hours with 10°C/min heating and cooling rate). Fused alumina, YSZ, silica and silicon surfaces were thus coated with Mn/YSZ, giving a total catalyst loading of 3 mg per cm². Before application of the Mn/YSZ onto the YSZ slide, it was first etched for 5 days in concentrated phosphoric acid to increase adhesion, following Lobhauer et al. [77]

It was verified that dropcasting of Mn/YSZ had no effect on the decomposition of HP by treating an inert borosilicate glass surface.

D.1.3.1. Washcoating

Washcoats were prepared and applied to alumina following the method by Yinyan for SiO₂ [132]. Thereto one part nanoparticulate silica (Davicat SI 1302, mean particle size 14.5 nm) was mixed with six parts water and sonicated until a uniform gel was formed, which was consequently applied onto the alumina slides. A thick layer would be formed due to the high viscosity of the gel. Since this was undesired, it was partially wiped off of the surface using a razor; blowing with compressed air or spincoating would remove either too much or too little of the gel. Other washcoating materials were prepared similarly, being TiO₂ (Aeroxide P25, Dagussa) and YSZ (Alfa Aesar). After deposition of the washcoats, the samples were left to dry overnight at 80°C. Afterwards, they were calcined at 1100°C for 6 hours (5°C/min heating rate). Subsequently, part of the washcoated alumina supports was coated with Mn/YSZ as described above to give catalyst loadings of 5 mg per cm². The remaining washcoated supports were loaded with MnOx using deposition precipitation as elaborated upon in [subsection D.1.2.](#)

D.1.4. Chemical list

Table D-1: Summary of all chemicals used during the catalytic synthesis. All chemicals have 99% purity unless otherwise indicated.

Name	Formula	CAS	Supplier	Remarks
LCT(Pt)				
Titania	TiO ₂	13463-67-7	Dagussa	P25
Calcium carbonate	CaCO ₃	471-34-1	Sigma Aldrich	
Lanthanum Carbonate hydrate	La ₂ (CO ₃) ₃	54451-24-0	Sigma Aldrich	99.9%, calcined at 800°C to give La ₂ O ₃
Platinum oxide hydrate	PtO ₂ · xH ₂ O	52785-06-5	Sigma Aldrich	
Barium Carbonate	BaCO ₃	513-77-9	Alfa Aesar	
KD-1 dispersant	-	-	Croda	Polyester polymer
Acetone	C ₃ H ₆ O	67-64-1	VWR	Rectapur
Mn/YSZ catalysts				
Manganese acetate tetrahydrate	MnAc · 4 H ₂ O	6156-78-1	Sigma Aldrich	
Ytria-stabilized zirconia	ZrO ₂ · 0.1 - 0.15 Y ₂ O ₃	1314-23-4	Alfa Aesar	Hf 4% max
Mn/YSZ - washcoats				
Titania	TiO ₂	13463-67-7	Dagussa P25	
Silica	SiO ₂	7631-86-9	Davicat	Davisil Si-1302
Ytria-stabilized zirconia	ZrO ₂ · 0.1 - 0.15 Y ₂ O ₃	1314-23-4	Alfa Aesar	Hf 4% max
Nitric acid	HNO ₃	7697-37-2	VWR	Emplura; 65% concentration
Phosphoric acid	H ₃ PO ₄	7664-38-2	Sigma Aldrich	ACS Reagent
Cercaps				
Titania	TiO ₂	13463-67-7	Dagussa P25	
Silica	SiO ₂	7631-86-9	Davicat	Davisil Si-1302
Alumina	Al ₂ O ₃	1344-28-1	Sigma Aldrich	γ-alumina, activated, neutral, Brockmann I
Hydrotalcite	Mg ₆ Al ₂ CO ₃ (OH) ₁₆ · 4 H ₂ O	11097-59-9	Honeywell Fluka	α-alumina, purum
Kaolin	Al ₂ (OH) ₄ Si ₂ O ₅	Al2(OH)4Si2O5	BASF Sasol	Pural MG 30; calcined at 600°C to give MgAl ₂ O ₄
Ytria-stabilized zirconia	ZrO ₂ · 0.1 - 0.15 Y ₂ O ₃	1314-23-4	Sigma Aldrich	
PVA	(C ₂ H ₄ O) _n	9002-89-5	Alfa Aesar	Hf 4% max
Glycerol	HOCH ₂ CH(OH)CH ₂ OH	56-81-5	Sigma Aldrich	98%
Manganese dioxide	MnO ₂	1313-13-9	Sigma Aldrich	99.5%

D.1.5. Test checklists

Table D-2: Pre-testing procedures

#	Action	Check
1	Characterize the sample using XRD (powder diffraction) to validate material composition	<input type="checkbox"/>
2	Characterize the sample using UV-Vis and Raman spectroscopy	<input type="checkbox"/>
3	Use SEM to validate topography	<input type="checkbox"/>
4	Carry out EDX to validate material composition	<input type="checkbox"/>
	All tests complete?	<input type="checkbox"/>

Table D-3: Pre-testing precautionary procedures

#	Action	Check
0	Work in a well ventilated area to prevent build-up of H ₂ O ₂ fumes	<input type="checkbox"/>
0	Use only compatible materials, such as pure aluminum, stainless steel, silicone, borosilicate glass	<input type="checkbox"/>
1	Clean workspace of unnecessary items/equipment.	<input type="checkbox"/>
2	Cover workspace with aluminum foil to prevent damage or ignition in case of undesired contact	<input type="checkbox"/>
3	Clean all materials meticulously with DI water to remove contaminants. Finally rinse with HP to remove remaining contaminants.	<input type="checkbox"/>
4	Clear area of people.	<input type="checkbox"/>
	Area safe?	<input type="checkbox"/>

Table D-4: Testing procedures

#	Action	Check
1	Measure and adjust the initial HP concentration	<input type="checkbox"/>
2a	Load the syringe with HP	<input type="checkbox"/>
2b	Adjust the flow rate to 2.4 mL/h, or equivalently 1 drop per 10 seconds	<input type="checkbox"/>
2c	Flush the HP system into a thoroughly cleaned receptacle	<input type="checkbox"/>
3	Put the catalyst pellet in the center of the receptacle; take care to properly align the pellet with the HP outflow	<input type="checkbox"/>
4	Start data-logging (thermocouples and camera)	<input type="checkbox"/>
5	Check whether data is recording	<input type="checkbox"/>
6	Start dropping of HP	<input type="checkbox"/>
7	When the dropping has stopped, stop the data-logging.	<input type="checkbox"/>
7a	Wait 2 minutes for the reaction to stop and the materials to cool down	<input type="checkbox"/>
8	Visually inspect the catalyst for changes	<input type="checkbox"/>
9	Remove the pellet from the receptacle and put in a closed container for further analysis.	<input type="checkbox"/>
10	Measure the final HP concentration in the syringe to check for degradation effects during the testing.	<input type="checkbox"/>
	Testing complete?	<input type="checkbox"/>

Table D-5: Post-testing analyses

#	Action	Check
1	Visually inspect the catalyst for changes.	<input type="checkbox"/>
2	Characterize the sample using XRD to validate material composition.	<input type="checkbox"/>
3	Characterize the sample using UV-Vis and Raman spectroscopy.	<input type="checkbox"/>
4	Use SEM to validate topographic stability.	<input type="checkbox"/>
5	Carry out EDX to validate material composition.	<input type="checkbox"/>
	All characterization conducted?	<input type="checkbox"/>

D.1.6. Test flow representation

This section will represent the flowcharts that represent the logic flow during the reactivity testing.

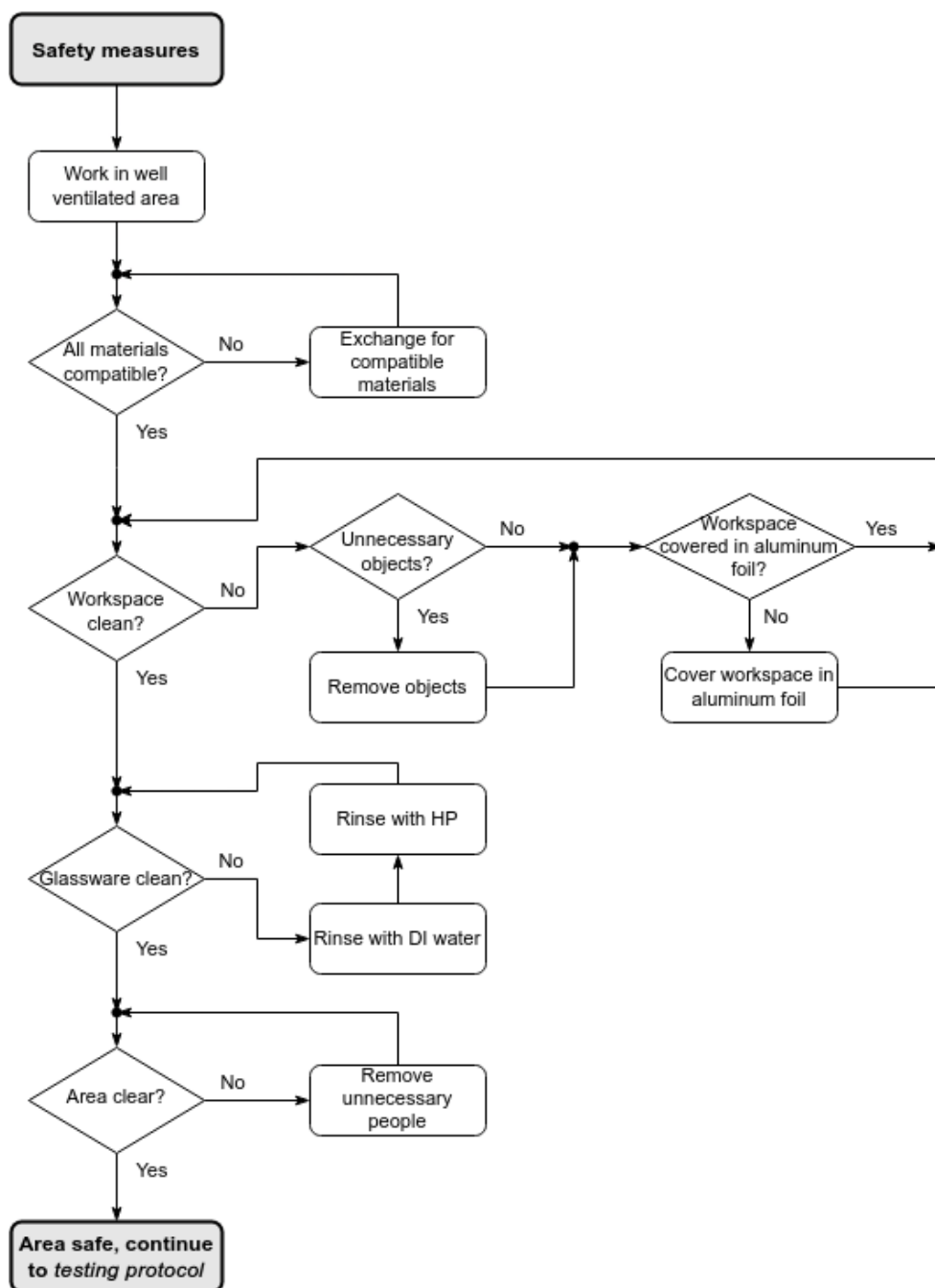
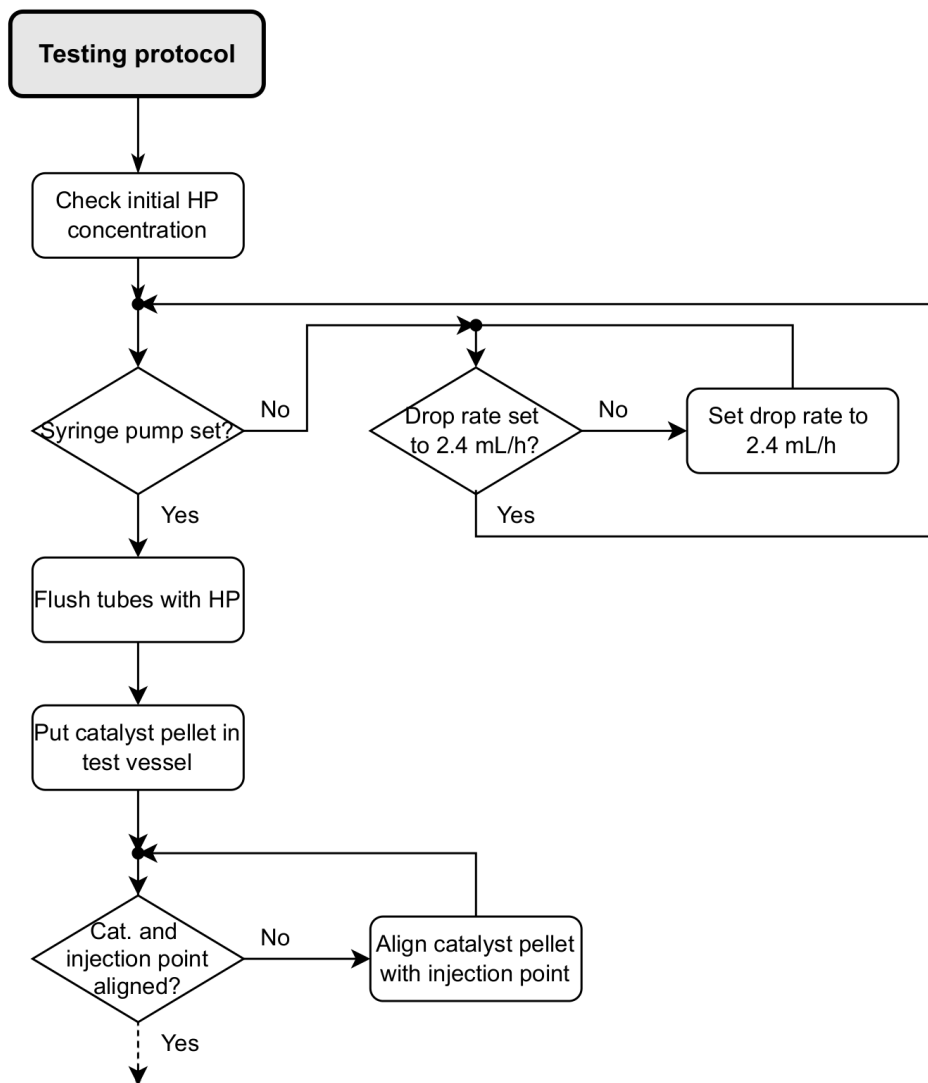


Figure D-1: Functional flow representation of safety precautions as taken during the experiments.



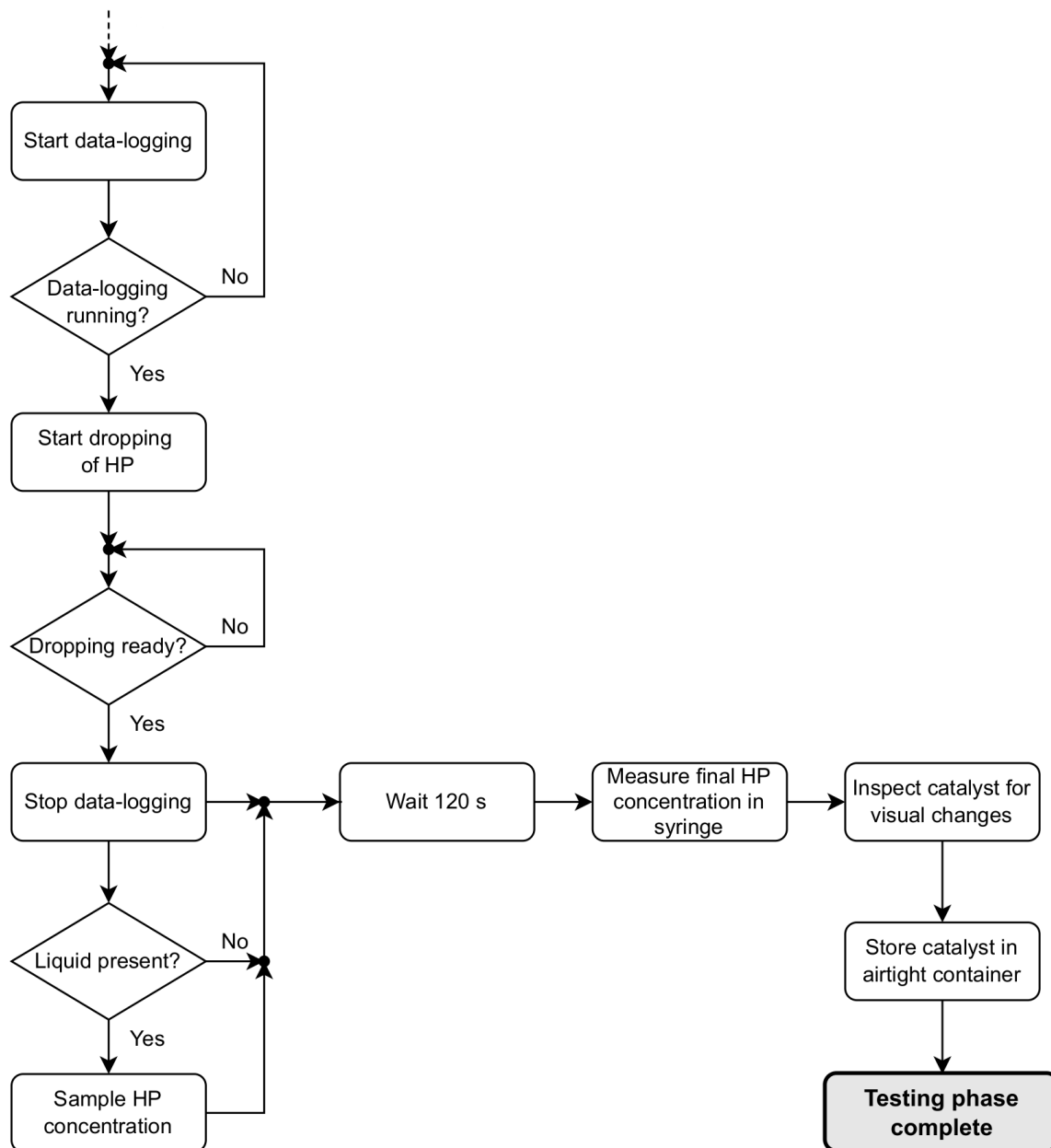


Figure D-2: Functional flow representation of the testing.

D.2. Calibration

This section summarizes all the calibration efforts that have been carried out over the course of this research. Standard laboratory equipment, such as scales, are yearly calibrated by an external party. The same applies to analysis equipment, such as the XRD and Raman spectrometer. In addition, these are inspected on a regular basis by the responsible technicians. Further, reference data were used to validate the obtained results from the Crystallography Open Database [41] or the RRUFF Project [64].

Some of the used sensors however need user calibration: thermocouples (subsection D.2.1), refractometers (subsection D.2.2), the anemometer (subsection D.2.3) and the syringe pumps.

D.2.1. Thermocouple calibration

During the condensation experiments, two thermometers have been used. One thermocouple was attached to the power controller, while the other was attached to a handheld digital thermometer unit. The latter unit is calibrated yearly by the supplier. The thermometer attached to the power controller was validated against this handheld thermometer, giving readings within 0.1°C . The readings of both thermometers were verified in an ice-water bath (0°C).

For the drop-testing, the conversion from the voltage drop over the thermocouple wires to the actual temperature was carried out automatically by the DataQ data recorder, which was calibrated before shipment. Nevertheless, the thermal readings were validated in the lab. Due to the technical difficulties with calibrating a sensor up until the decomposition temperature of HP (1000°C for anhydrous HP [108]), it was chosen to validate using water of 0°C and 100°C . These data were used to further calibrate the thermocouple readings, the result of which can be found in Figure D-4. With the use of a propane torch (with a flame temperature of approximately 2000°C) the thermocouples were aligned; this also showed that the thermal readings at high temperature were correct (the maximum readout temperature could be achieved, i.e. 1363°C). Decomposition tests showed that the (once) maximum attained temperature was 462°C for 98% HP at 20 mm from the reaction surface, which is lower than what could be expected. However, during most decomposition experiments the maximum temperature achieved was around 120°C . Adjustment of the thermocouple positions did not lead to improved thermal readings. For reference, decomposition experiments were also performed with MnAc_2 , which is used in literature as means to induce hypergolicity [53]. The maximum temperatures achieved while decomposing HP with manganese acetate were comparable to those achieved with the cer-caps, as can be seen in Figure D-3. This figure also shows the frequent absence of peaks at h_2 and h_3 , and also the spread in peak intensities.

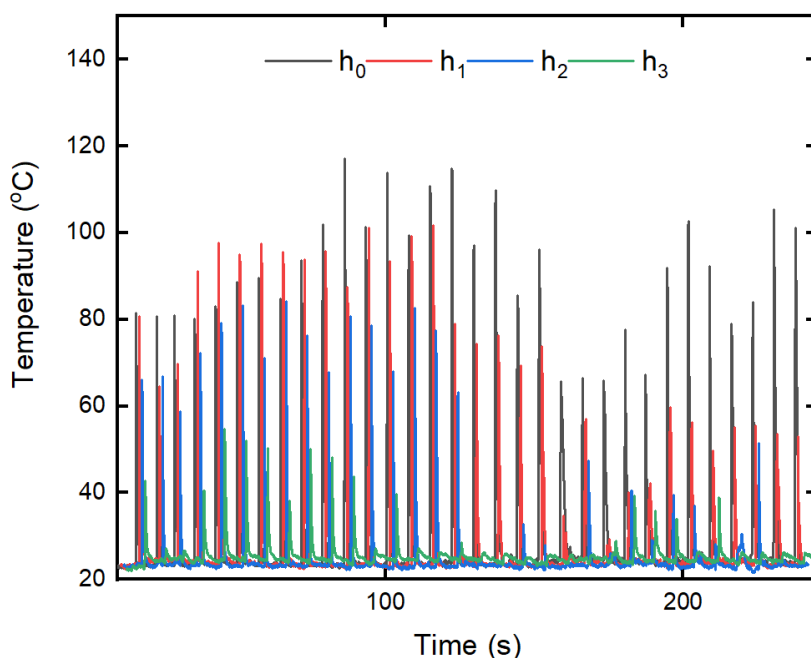


Figure D-3: Heat trace showing the decomposition of 87% HP using manganese acetate. The temperature traces from higher locations are shifted horizontally for clarity.

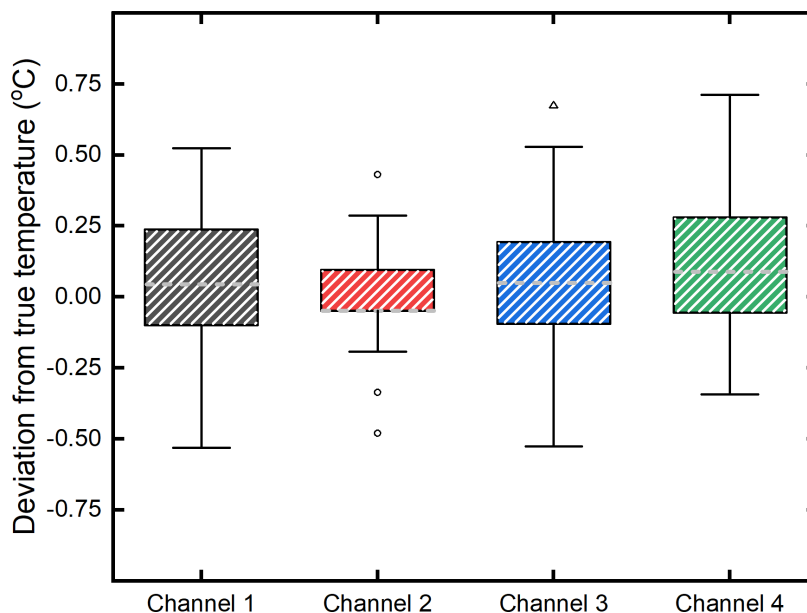


Figure D-4: Thermocouple temperature recording measurement after calibration. The offset with respect to the actual temperature is shown for each channel.

D.2.2. Refractometer calibration

The refractometers had been calibrated using manufacturer supplied calibration solutions, and were checked before each experiment by means of a measurement of 30% HP. The scale on the refractometer is in brix-%, a direct measure for sugar mass-percentage. With a conversion chart as supplied by SolvGE these concentrations can be converted directly into mass percent hydrogen peroxide ($C_{HP} = 2.2518 \text{ brix} - \% + 0.4968$; $r^2 = 0.99995$). The reading accuracy of the analog refractometer is 0.5 brix percent point, which translates to a standard error in the concentrations of 1.13 mpp. At the end of the research, a digital refractometer (Mettler Toledo Refractometer 30PX, with an accuracy of 0.45 mpp HP) became available. This was used to cross-calibrate the analog refractometer to validate the results obtained during the research. This led to the calibration data as can be found in Figure D-5. Linear regression on these data showed a constant offset in the measurements of 1.52 mpp ($\sigma=1.04$ mpp) and a correlation of 0.956 ($\sigma=0.012$). The shown outlier is illustrative of the difficulties associated with operation of the analog refractometer: the fluid should be evenly distributed over the window without entrapped air and the inclination of the apparatus with respect to the eye can result in a shift of the measured values. Nevertheless, the distribution of the error (defined as the digitally measured concentration minus the analogically measured concentration) shows a normal distribution, which indicates that all measurements are most likely independent.

Additionally, a clear bias is present, which seems to increase with concentration (bottom, circles). Hence, care must be taken to interpret the analogically measured concentrations as the true concentration. However, in this research concentrations were merely used to mutually compare different samples. In this realm, it should be considered that small concentration differences (up to 2.1 mpp) can occur with 95% probability and hence do not necessarily indicate a true concentration difference.

D.2.3. Anemometer calibration

Due to sparse resources, an anemometer was used to measure the flow rate of the nitrogen coming out of the fumehood connection for the condensation experiments. Already during these experiments it was noticed that the readings varied over a wide range (e.g. from 10 to 13 m/s), strongly dependent on the orientation of the anemometer with respect to the gas outlet. In order to partly counter this uncertainty, all possible orientations were probed and the maximum reading was used. The use of the maximum value proved to be highly reproducible over multiple experiments. According to the leading cooperation group of wind measurement institutes (MAESNET), calibration of anemometers can only be carried out successfully in a wind tunnel [78]; this was deemed unfeasible for this research and therefore the manufacturer set calibration was used.

After the research had been completed, a calibrated mass flow controller was purchased; this controller

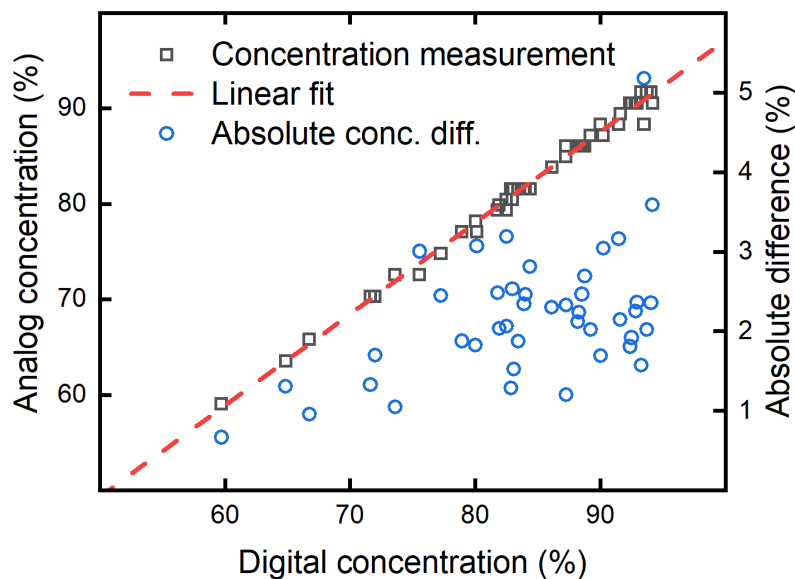


Figure D-5: Cross-calibration data of the analog refractometer. The cross-correlation between the analog and digital refractometer is shown, together with a clear linear relation ($A = 0.956D + 1.515$, $r^2 = 0.996$). Also shown is the distribution of the concentration error, which appear to increase with increasing concentration.

showed that the flow rates as determined with the anemometer were off by approximately a factor 5. This large factor can be explained considering that the gas would emanate from a small tube (3.5 mm inner diameter), whereas the anemometer is intended for undisturbed air flows.

D.2.4. Drop volume calibration

The drop size, which is important to assess the conversion power of the catalyst, should be as uniform as possible. The drop size was controlled to a large extent by the needle selection. The consistency in drop volume was checked before the experiments by administering drops of deionized water onto a yearly ISO-calibrated analytic balance with 0.1 mg resolution. This yielded an average drop mass of 10.82 mg ($\sigma = 0.40$ mg, $n = 90$), or equivalently a water drop volume of 0.0108 mL, please refer to Figure D-6. This consistency has been checked later with pure ethanol (3.84 mg, $\sigma = 0.12$ mg, $n = 50$). Due to the dangers associated with concentrated HP, no drop masses have been measured on the balance. Instead, it has been assumed that due to the highly similar viscosity and surface tension of water and HP drop volumes would be similar. During the experiments it was found that 100 drops would be approximately equal to 1 mL, showing that the average volume of a HP drop is roughly equal to that of water.

Instead, in order to determine the drop volume during the experiments, a ruler was placed at the border of the image. Afterwards the drop volumes were estimated using image editing software. For each experiment the five first drops of every video file were analyzed. The drop size was then determined in three subsequent video frames, right after the drop entered the field of view to limit flattening effects due to air resistance. This resulted in a estimated drop volume of 0.67 mL ($\sigma_{avg} = 0.07$ mL, $n=60$) with less than 2% variation between experiments (see Figure D-7). The large error margin can be explained considering the fact that a drop would occupy only some 20 pixels. Additionally, the drop size resulting from the video footage is about 60 times higher than the actual drop volume. One major factor contributing hereto is the short focal distance of the camera (14 mm), which causes large deformations of the image, including the ruler. Additionally, the lensing effect of the droplet may have caused the droplets to appear enlarged.

Next to the drop volume, also the delay between subsequent drops was monitored. This was investigated by comparing the moment of impact of each drop, during each experiment. This showed that the average time between drops was 10.64 seconds ($\sigma = 0.42$ s, $n = 210$) for the YSZ experiments and 10.55 ($\sigma = 0.48$ s, $n = 210$) for the yAl experiments, as can be seen below in Figure D-7.

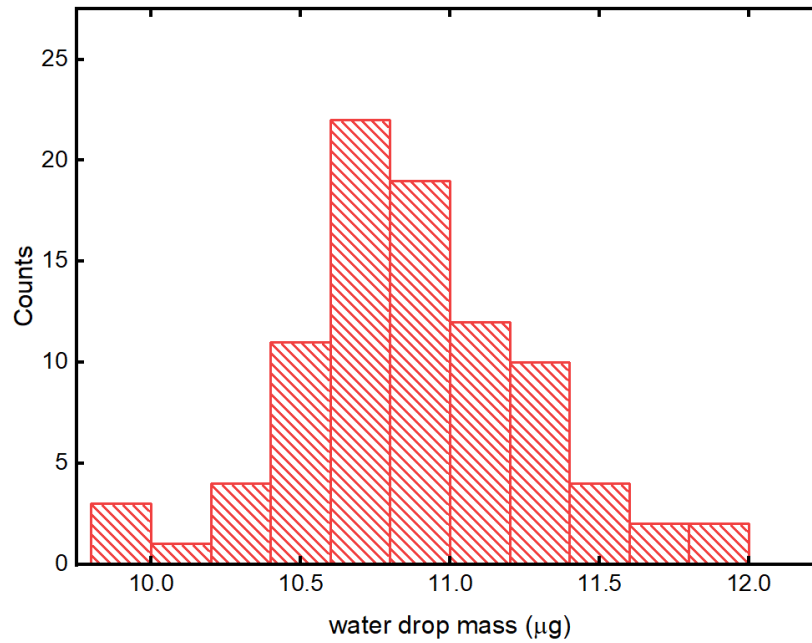


Figure D-6: Spread of the drop volumes as measured with water.

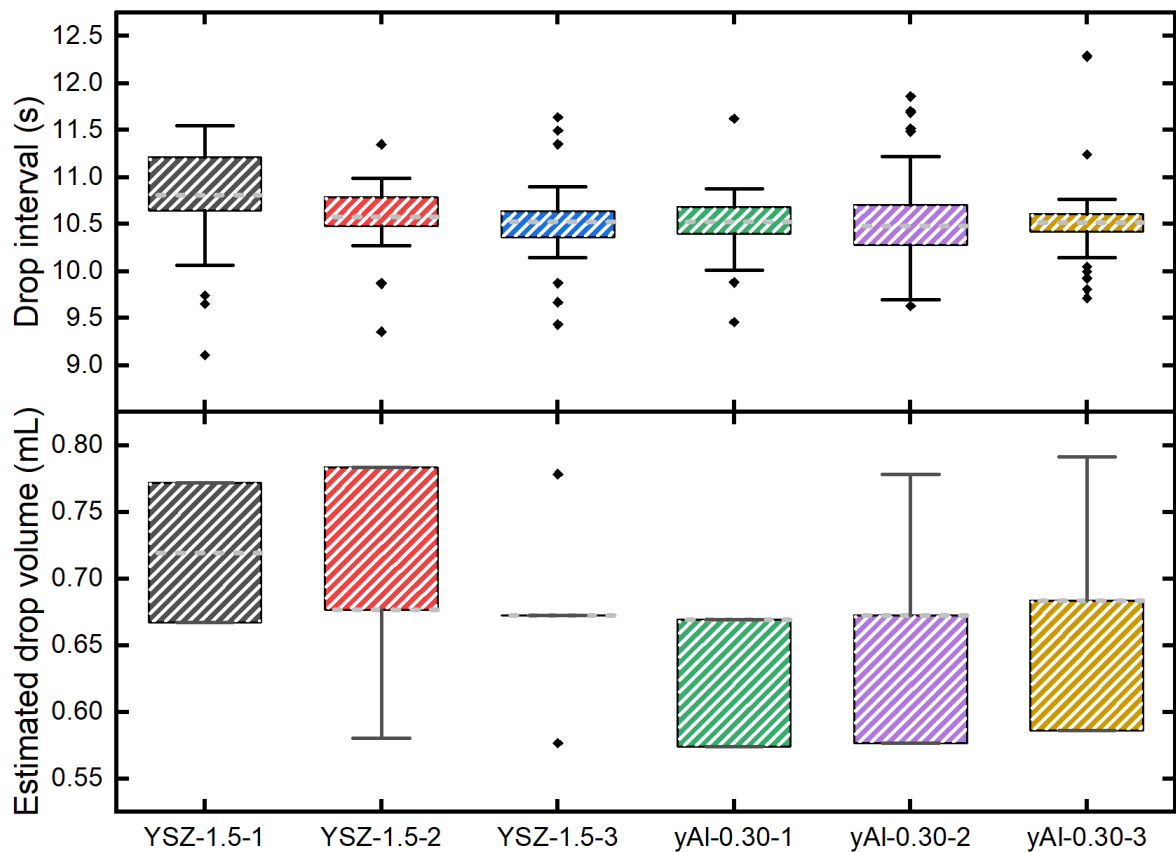


Figure D-7: Top: spread in drop timing as determined from camera data. Bottom: spread of the drop volumes during the decomposition experiments as determined from the camera data. The median is indicated by the pink dashed line.

D.2.5. Bubble detection

The presence of noise made the detection of bubbles difficult, since these would both have approximately the same size. This was worsened by the relatively high noise level of the camera. Therefore, a certain light pixel would only be judged as a bubble if it would persist in at least three subsequent image frames (total 13 ms). In addition, some events would not show bubble formation, but merely the retraction of fluid, as can be seen in [Figure D-8](#). As was verified by comparison with water, this retraction could only be explained by decomposition of HP. If no bubble could be detected, this latter behavior was used instead.



Figure D-8: Example of a typical drop evolution event, showing two subsequent frames. The encircled area shows the formation of a drop. Further the retraction of liquid can be seen at the borders of the wetted area.

Supporting information

This appendix supplies information supporting the claims made in the respective chapters. Further data are available upon request.

E.1. Purification of propellant-grade H_2O_2

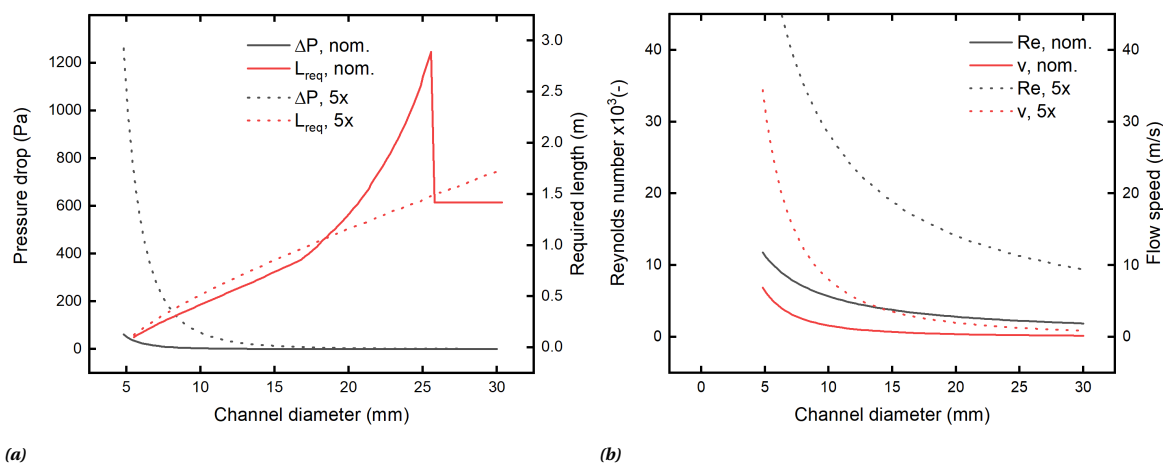


Figure E-1: Results of model calculations for both the nominal case ("nom") and the sensitivity analysis, with a five times higher flow rate ("5x"). For clarity the results below 5 mm channel diameter have been removed. a) Results showing the predicted pressure drop (ΔP) over the condenser and minimally required condenser length (L_{req}). b) Figure showing the predicted maximum occurring Reynolds number (Re) and flow speed (v).

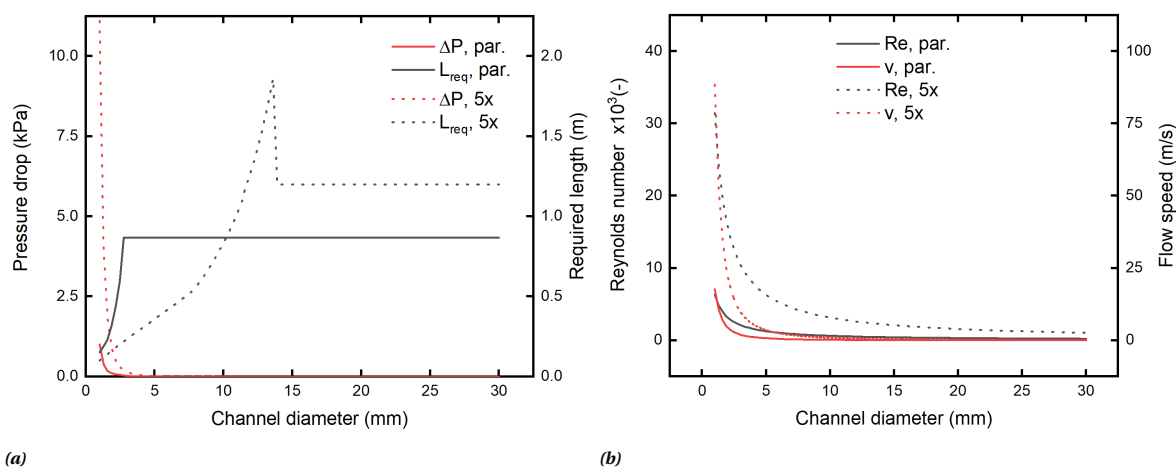


Figure E-2: Results of model calculations performed for the parallel condenser, i.e. with a 89% lower flow rate than the earlier presented results. The results are shown for both the nominal case ("par.") and the sensitivity analysis, with a five times higher flow rate ("5x"). a) Results showing the predicted pressure drop (ΔP) over the condenser and minimally required condenser length (L_{req}). b) Figure showing the predicted maximum occurring Reynolds number (Re) and flow speed (v).

E.2. Support effect on the decomposition of H_2O_2 over MnO_x catalysts

E.2.1. Regenerative LCT(Pt) perovskite

Different crucibles were tested for their compatibility with the synthesis of $\text{Ba}_3\text{Pt}_2\text{O}_7$; it was found that a quartz crucible lined with BaO was most suitable for this synthesis. XRD shows the successful conversion into $\text{Ba}_3\text{Pt}_2\text{O}_7$; the relevant patterns are displayed in Figure E-3 and are compared with reference spectrum PDF 01-070-0618. It should be noted that the peaks at $2\theta = 59$ and 68° are known artifacts of the XRD, as well as that all the amounts analyzed are between 40 and 50 mg.

The same figure shows the almost full conversion of the precursors into the perovskite crystal phase. However, in order for the platinum to catalyze the decomposition of HP, it needs to be reduced to the metallic form, the exsolution stage. As it turned out, the reduction conditions as described by Kothari et al. were not sufficient to exsolve the platinum from the perovskitic matrix; not even the stronger reductant CO was able to release (all) platinum from the perovskitic matrix, as can be seen in Figure E-3. To that extent it was tried to synthesize the LCT(Pt) catalyst with a higher (i.e. 5 wt.-%) platinum loading, yet this caused failure of the formation of the perovskite crystals. Hence, despite much effort, it appeared that the platinum atoms in LCT(Pt) showed a too high affinity with the LCT matrix, due to which it would not form metallic nanoparticles on the surface. In order to verify whether such perovskitic matrix supported platinum catalysts would even react with HP, 8 mg of the comparable (reduced) Pt/LaFeO₃ was exposed to 87% HP; no sign of reactivity could be noticed. It appears as if the perovskitic matrix has a too strong stabilizing interaction with the platinum, causing it to be unreactive with concentrated HP, whereas yet unpublished research demonstrates the reactivity of this Pt/LaFeO₃ in CO reduction.

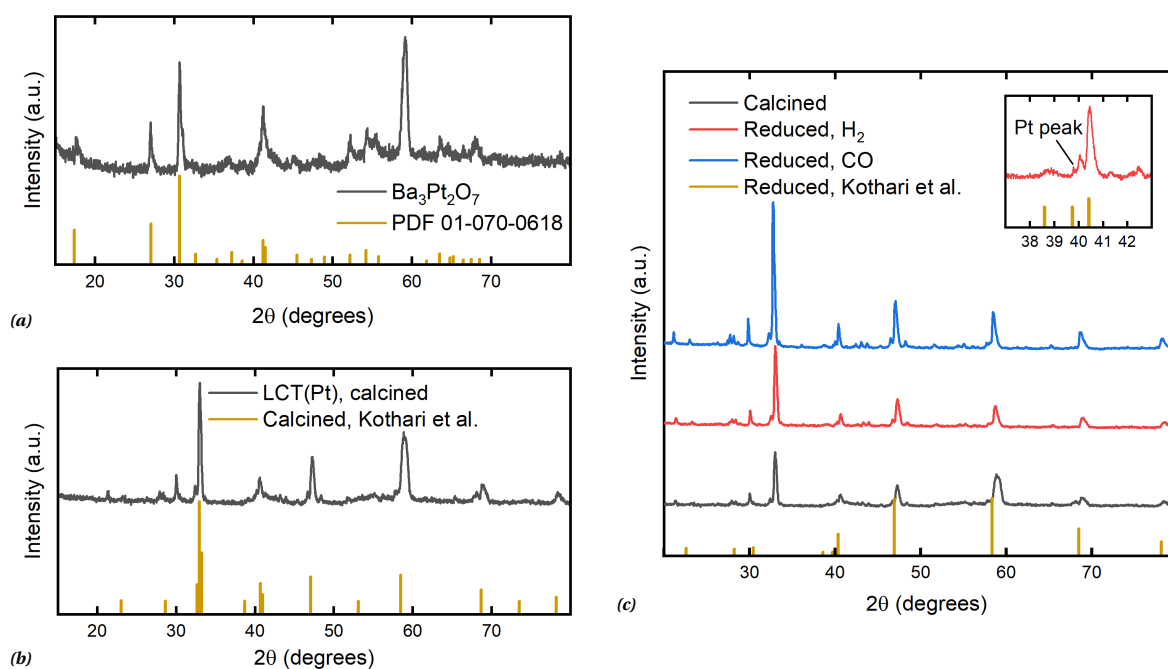


Figure E-3: a) XRD patterns showing the success of $\text{Ba}_3\text{Pt}_2\text{O}_7$ synthesis and b) the large conversion into the perovskite crystal phase for LCT(Pt). c) The effects of different reduction conditions on the emergence of platinum from the perovskite matrix. All reference signals are based on the work by Kothari et al. [62].

E.2.2. Mn/YSZ catalysts

Manganese oxide was precipitation deposited on powdered YSZ (Mn/YSZ, 10 w/w%) as explained in subsection D.1.2. After calcination, no MnO_2 was formed (as is claimed by Bonifacio et al. [7, 9]), but Mn_3O_4 , as can be seen in Figure E-4. Its reactivity was tested with by exposing a 30 mg catalyst pellet to 87% HP in drop-testing, which resulted in immediate disintegration. Neither an increase of the pellet mass to 250 mg, nor an additional calcination step resulted in enhanced mechanical integrity of the pellet.

As the mechanical integrity of the catalyst appeared to be the culprit, it was tried to support the Mn/YSZ

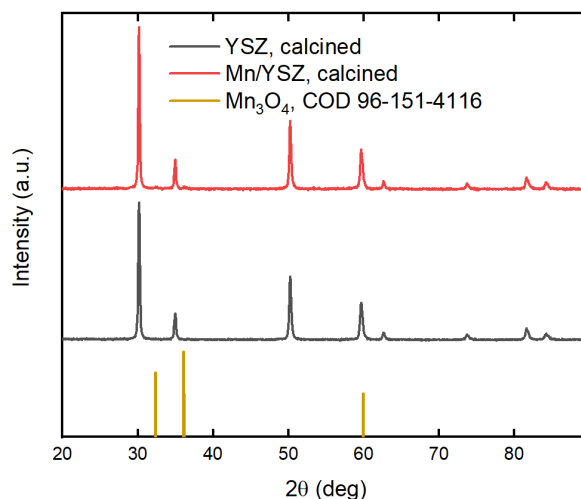


Figure E-4: XRD patterns of calcined YSZ and calcined Mn/YSZ. In addition a reference spectrum of Mn₃O₄ is shown.

itself on different support materials. First, it was tried to dropcast the catalyst powder onto fused alumina slides due to its widespread use as catalyst carrier. It was chosen not to use deposition precipitation directly onto the aluminum slides due to the limited stabilization of alumina of the manganese active phase [2, 47]. Surprisingly though, calcination of the dropcasted alumina resulted into complete deactivation of the catalyst; no reactivity could be noticed upon exposure to up to 98% HP. Chemical characterization could not supply a clear explanation, as can be seen from Figure E-5; though, Raman spectroscopy showed a shift in the peak wavenumber (belonging to Mn₃O₄) of 1.6 cm⁻¹. It thus appears that calcination on alumina increases the stability of the MnOx. Perhaps the calcination step after dropcasting creates an interaction between the YSZ and the alumina, which on its turn negatively influences the reactivity of manganese.

Subsequently, Mn/YSZ was dropcasted onto other support materials, specifically silica, titania and fused YSZ. While these supports did not cause deactivation of the catalyst, the Mn/YSZ would be removed by drop-testing with 87% HP within a couple of drops. In order to increase its adherence, deposition precipitation was carried out directly on these supports; yet, no measurable amounts of manganese hydroxide would deposit on the supports. In this context especially the poor performance of the YSZ support was surprising, considering the promising results as demonstrated by Russo Sorge's group (i.a. [9]). A thorough investigation of all the research works by this group showed that the high physical stability of the manganese phase could be explained by the high (macroscopic and microscopic) porosity of the used YSZ monolithic support.

E.2.2.1. Washcoats

In order to replicate the enhanced surface roughness as featured in the research by Russo Sorge's group, it was tried to apply washcoats onto fused alumina slides. A washcoat is a common method in catalyst development to change surface properties of a support material. A washcoat is a thin layer of a (often) inert metal oxide which binds strongly with the support material as well as with the catalytic phase. It can be used to, for instance, increase the active surface area of the catalyst support, or as in this case to insulate the support from the catalytic phase. Different washcoats (titania, silica, YSZ) were prepared on fused alumina slides as is described in subsection D.1.3.1. As was the case for the bare supports, deposition precipitation was not able to deposit measurable amounts of MnOx onto the washcoated alumina supports. While preparing the washcoated slides for application of the catalytic phase, the poor adhesion of the silica and YSZ washcoats was demonstrated by spontaneous splintering of the washcoats. XRD data (as displayed in Figure E-9) clearly shows the incomplete coverage (least prominently of titania) of the alumina surface by the washcoat materials. Immediately visible is that the YSZ signal dominates the diffraction pattern after dropcasting the Mn/YSZ.

The activity of all these washcoated specimens was evaluated using 87% HP. The poor adhesion of the YSZ washcoats led to complete removal of both the washcoat and the Mn/YSZ within several drops. The silica and titania washcoat showed similar signs of deterioration, yet part of the applied washcoats adhered very well to the alumina. In addition, part of the catalytic phase would remain bonded to the washcoat. Perhaps the (relatively rough) surface of these two washcoats (see e.g. Figure E-6) reduced the direct effects of the drop

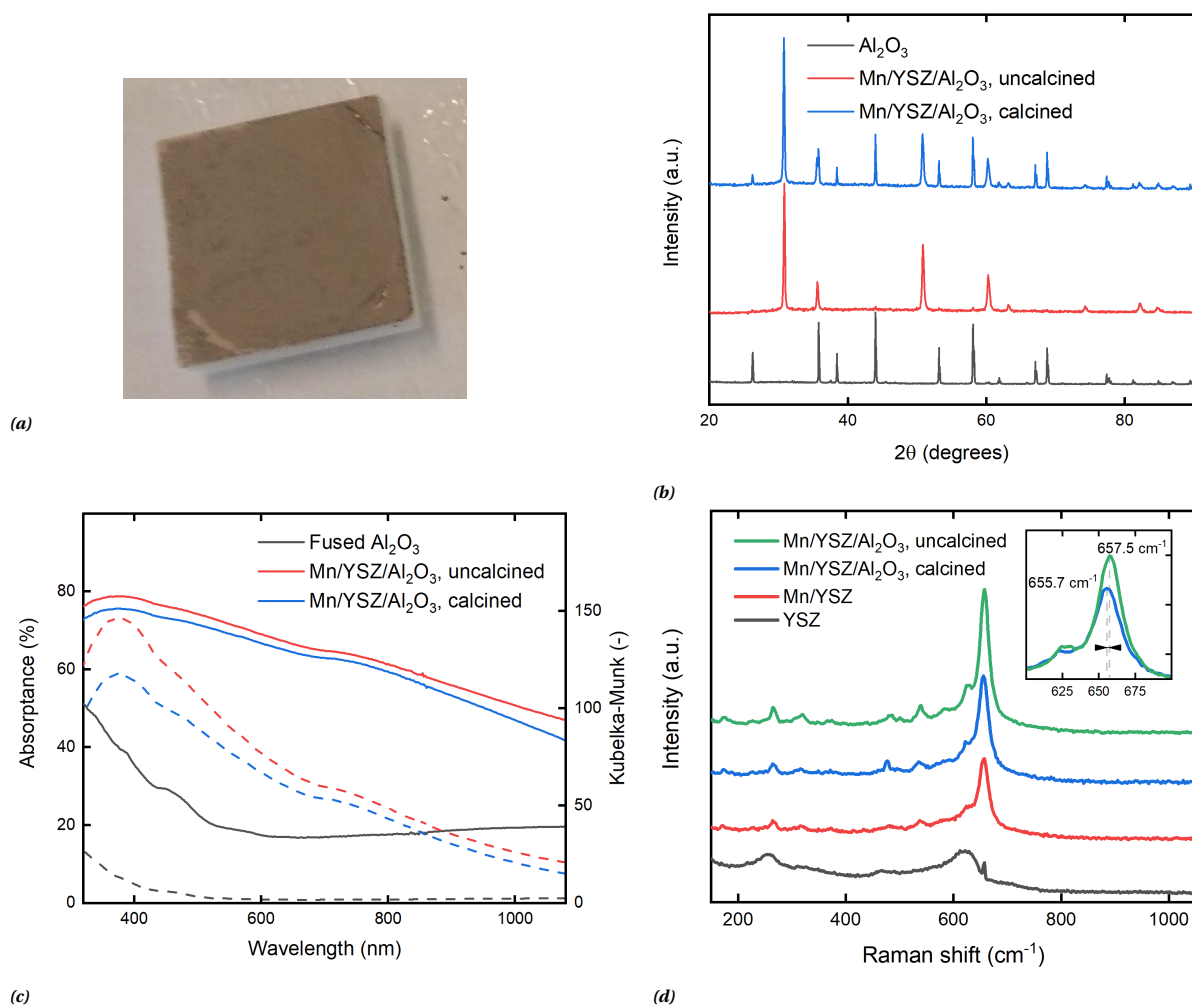


Figure E-5: Characterization of Mn/YSZ, dropcasted on fused alumina. *a)* Typical dropcasted sample prior to testing. *b)* XRD patterns for Mn/YSZ on alumina, showing the emergence of alumina peaks after calcination. *c)* TDR spectrum showing the effect of calcination of Mn/YSZ/ Al_2O_3 . Also the effect of the KM transform (dashed lines) is shown. *d)* Raman spectrum (532 nm) of Mn/YSZ on alumina. Calcination results in a 1.8 cm^{-1} peak shift, or equivalently 0.223 meV .

impact on the Mn/YSZ layer, and maybe also confined the reaction into a larger number of more isolated areas, which on its turn leads to a higher spread of the reaction heat. This tenacity allowed long-term activity testing, as can be seen in [Figure E-6](#) and [Figure E-8](#), for silica and titania, respectively. Note that in these experiments the bottom thermocouple could not be fitted due to physical constraints.

Despite the toughness of the silica washcoat, it would still be gradually removed from the alumina. This steady removal of both the washcoat and the Mn/YSZ is evident from the continuous decrease in temperature, up to the moment that the vast majority is removed (after 600 seconds).

For the drop-testing experiments conducted with titania washcoats (see [Figure E-8](#)), the effects of poor alignment with respect to the thermocouples (at the start of TiO_2 -1 and at the end of the first measurement for TiO_2 -2) are evident. Since the recording interval for the DAQ was limited, the administering of dropping was stopped during the required resetting hereof. It can be seen that the restarting resulted in induction behavior, even though the catalyst surface had remained covered in HP. Perhaps this is caused by the presence of a layer of (low concentration) HP on and around the catalyst. Addition of the first few drops then increases the local concentration again up until sufficiently high levels. When TiO_2 -1 was left to dry for 40 minutes, all reactivity had gone, even though still 2 mg of Mn/YSZ was present (as is hinted by [Figure E-7b](#)). This behavior was confirmed with TiO_2 -2; here the lateral movements are visible in the second half of the first measurement. After the first part of the experiment, drop-testing was halted for 2 minutes. It can be seen that, even though reactivity was slowly restored, the catalyst nevertheless would quickly become inactive. A heat treatment

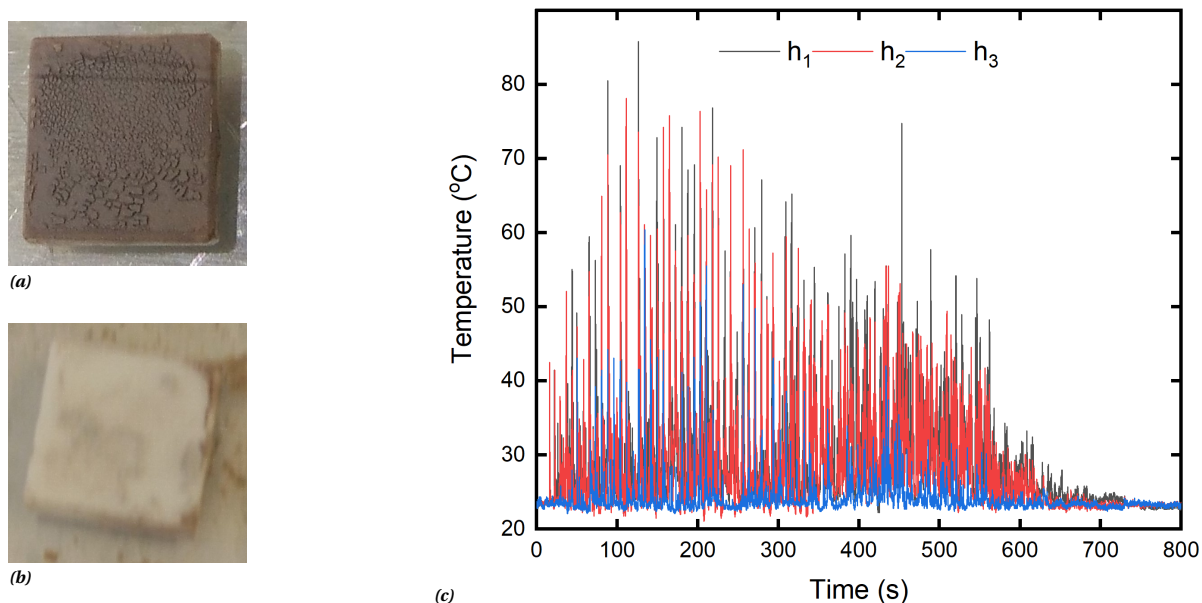


Figure E-6: a) Dropcasted SiO_2 sample prior to testing. b) Spent silica washcoated sample. Clearly no Mn/YSZ is left. c) Temperature trace of a drop-testing experiment of a SiO_2 washcoated alumina slide. The decreasing activity of catalyst is evident from the continuously decreasing maximum temperatures.

conducted at 120°C proved the possibility of reactivation. Also, this indicates that water is indeed a possible cause for deactivation. After successfully conducting a drop-testing experiment on the heat treated TiO_2 -2 sample, the catalyst was left to dry for one hour. Afterwards, the reactivity was quenched again. At the end of these experiments, still 2 mg of Mn/YSZ was present on this sample.

Due to the alignment issues, no conclusions can be drawn with respect to chemical deactivation phenomena. Nevertheless, evident from Figure E-7b is the near complete removal of the washcoat at the place of impact. This shows the (still) limited adherence of the washcoat to the fused alumina. Unfortunately, after the experiments the video data turned out to be corrupted further hampering the analysis of these experiments. Thus, even though the method of washcoating yielded promising results, it did not deliver the required rigidity. Due to the complexity of washcoat development, a different catalyst supporting method was sought.

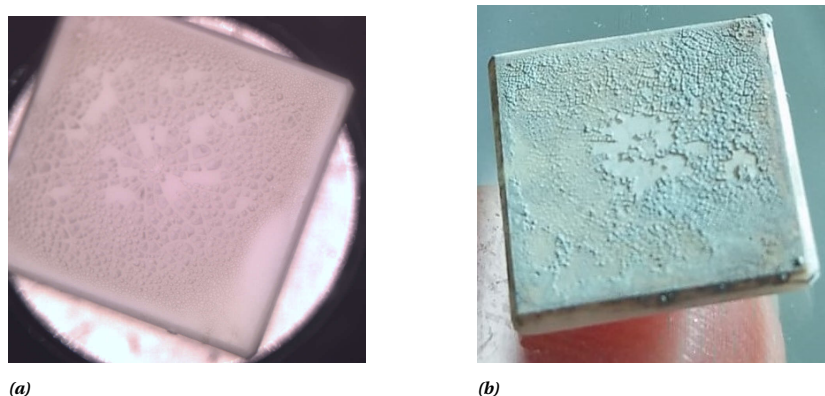


Figure E-7: Pristine and spent titania washcoated samples. a) TiO_2 washcoated alumina catalyst, prior to dropcasting with Mn/YSZ. The surface roughness displayed by the washcoat is apparent. b) Spent TiO_2 -1 washcoated alumina catalyst. As is indicated by the color, still some 2 mg of Mn/YSZ was present. Note the bare spot in the center, coinciding with the drop impact area.

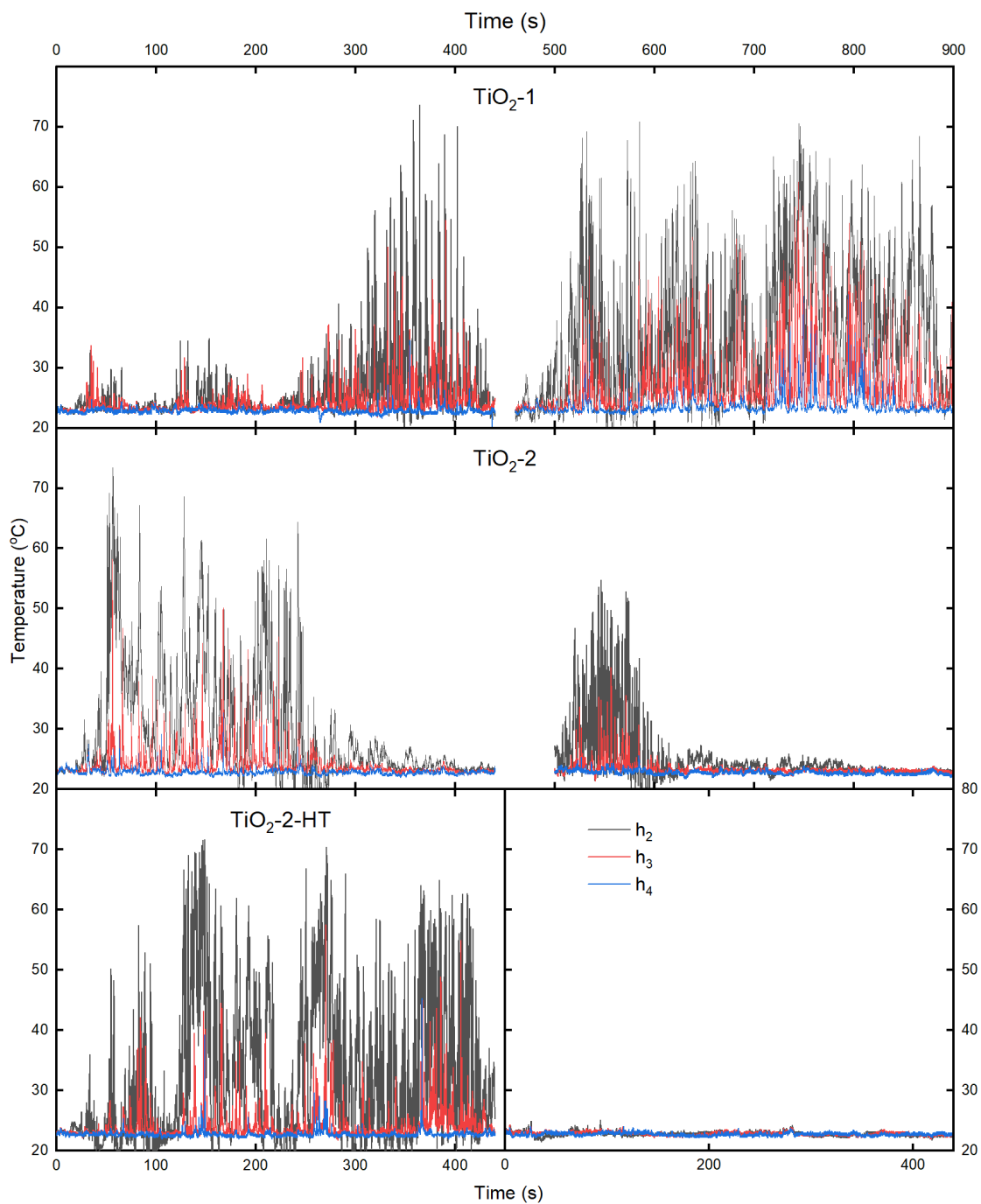


Figure E-8: Thermal traces of experiments conducted with titania washcoats. Decreases in attained temperatures can be largely attributed to inconsistent alignment of the catalyst with respect to the thermocouples. Deactivation behavior can be clearly seen when halting decomposition for a longer duration. As can be seen in TiO₂-2-HT, heat treatment at 120°C can regain reactivity, until dropping is stopped again.

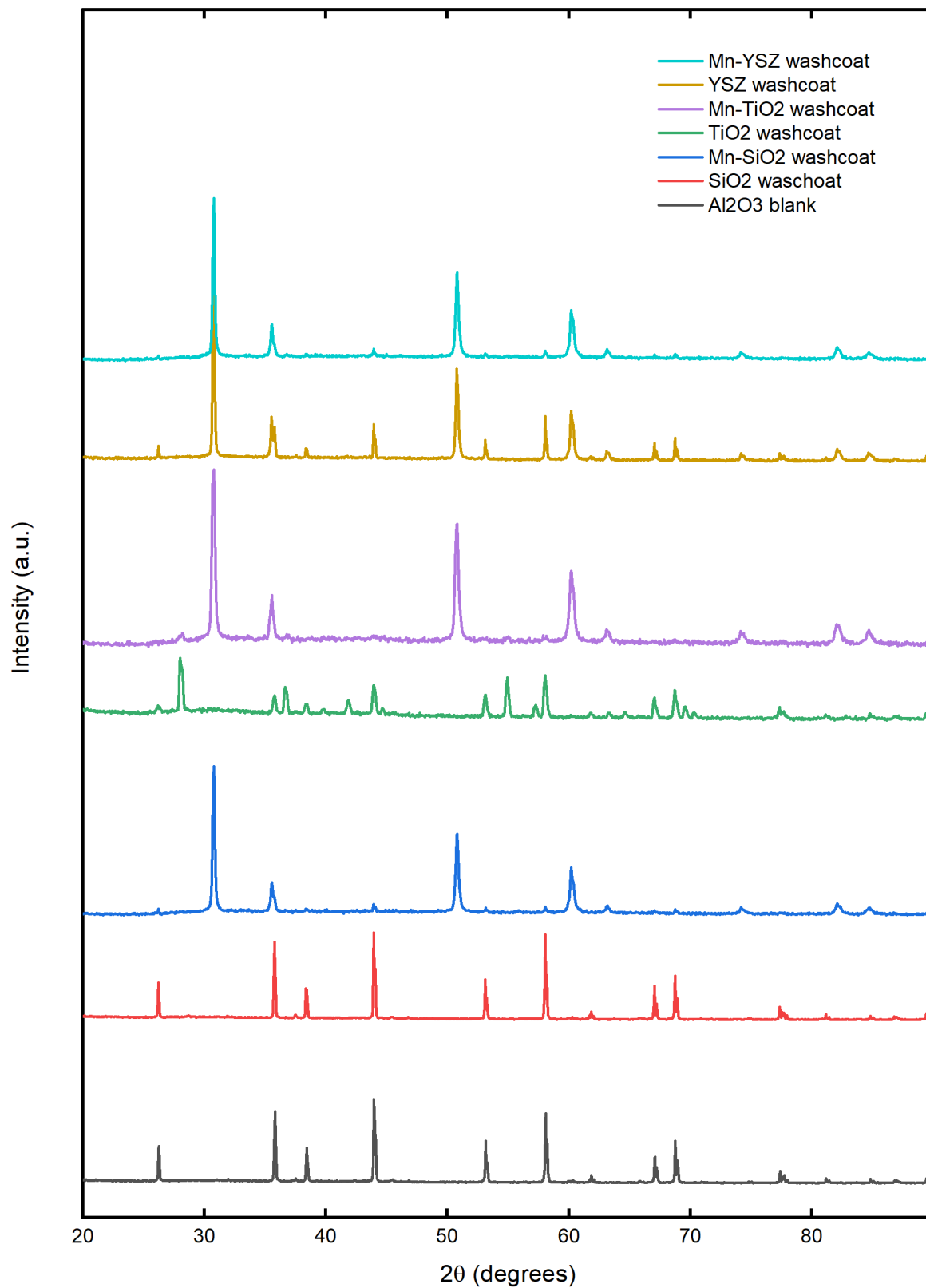


Figure E-9: XRD patterns of the washcoated and dropcasted alumina slides. The incomplete surface coverage of the washcoats is evident from the alumina diffractions. The dropcasted samples primarily show the presence of Mn/YSZ.

E.2.3. MnO_x cercaps

Supplementary information with respect to all synthesized cercaps can be found below. This ranges from additional reaction characterization to detailed chemical characterization.

E.2.3.1. Catalyst characterization

This section will present additional characterization for all synthesized cercaps. All Raman spectra have been obtained at 785 nm wavelength (5% power, 30 s total acquisition time) on a Renishaw inVia confocal microscope, equipped with Leica 50x objective and 1200 lines diffractive grating.

The Raman spectrum obtained for YSZ-1.5, as shown in Figure E-10, does not reveal the presence of any manganese phase. When analyzing the peak locations, it can be calculated that the yttria-content of this YSZ is between 15 and 17 wt.%, whereas it should contain between 10 and 15 wt.% [44]. The same can be concluded from XRD data when these are compared with reference patterns (e.g. COD 96-152-8645 [41]).

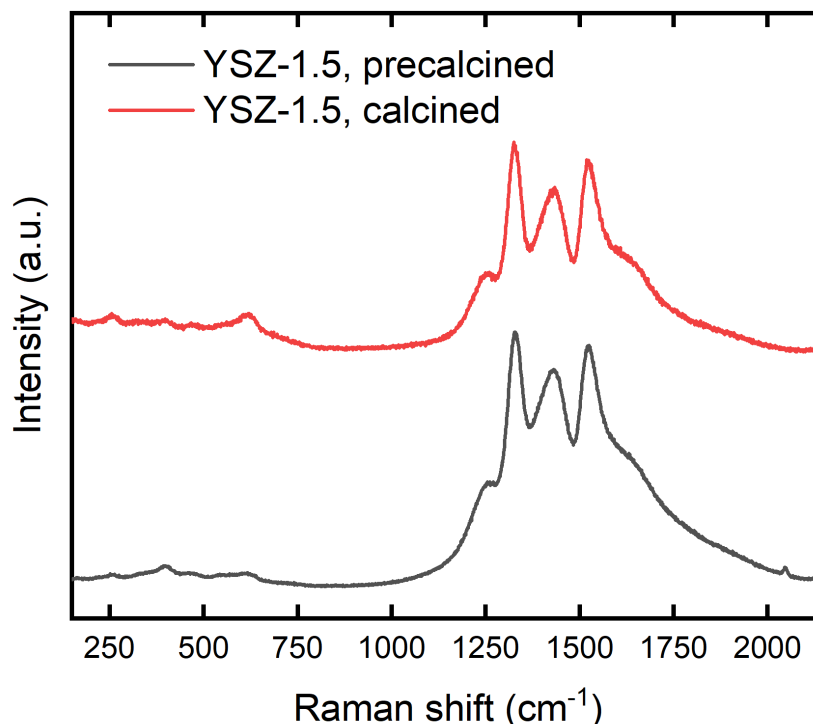


Figure E-10: Raman spectrum obtained of both precalcined and calcined YSZ-1.5 cercap. No peak shifts can be noticed. The peak in the precalcined signal at 2050 cm⁻¹ is the remnant of a cosmic ray event.

While TDR spectra can be very informative in absorption, the so-called Kubelka-Munk transform (the inverse square of the measured signal) is often used to amplify the (often) weak variations in signal intensity. In addition, correct implementation of this transform will show the band energies of the analyzed compound [66]. Yet, here it will merely be used to allow easier comparison with literature, if applicable.

Detection of manganese compounds with TDRS is challenging, according to Baldi and Kijlstra and coworkers [4, 60]. Detection of MnO is realistically impossible due to the forbidden electronic transition, resulting in very low signal strength. Additional complications in TDRS in the determination of the oxidation state of manganese are the overlapping (broad) signals from Mn₂O₃ (around 470 nm) and MnO₂ (around 485 nm). According to Baldi et al., the presence of hausmannite should give rise to a peak around 330 nm, which is not visible in any of the acquired spectra. This is clear when inspecting the TDR spectra as visible in Figure E-12a, Figure E-13 and Figure E-12b. (Note for all spectra the noise induced by the lamp change at 840 nm.) Especially the non-reactive cercaps share peaks at 460 and 508 nm. Yet, due to the absence of proper reference spectra and the complications associated with the determination of manganese phases from TDRS, no conclusions can be drawn from Figure E-13. Further, Figure E-12a shows that the quantity of α -alumina increases with increasing manganese loading.

Lastly, XRD patterns are presented here of all cercaps as can be seen in Figure E-14. Comparison of all spectra with suitable references for all (over 30) possible manganese phases does not result in determination

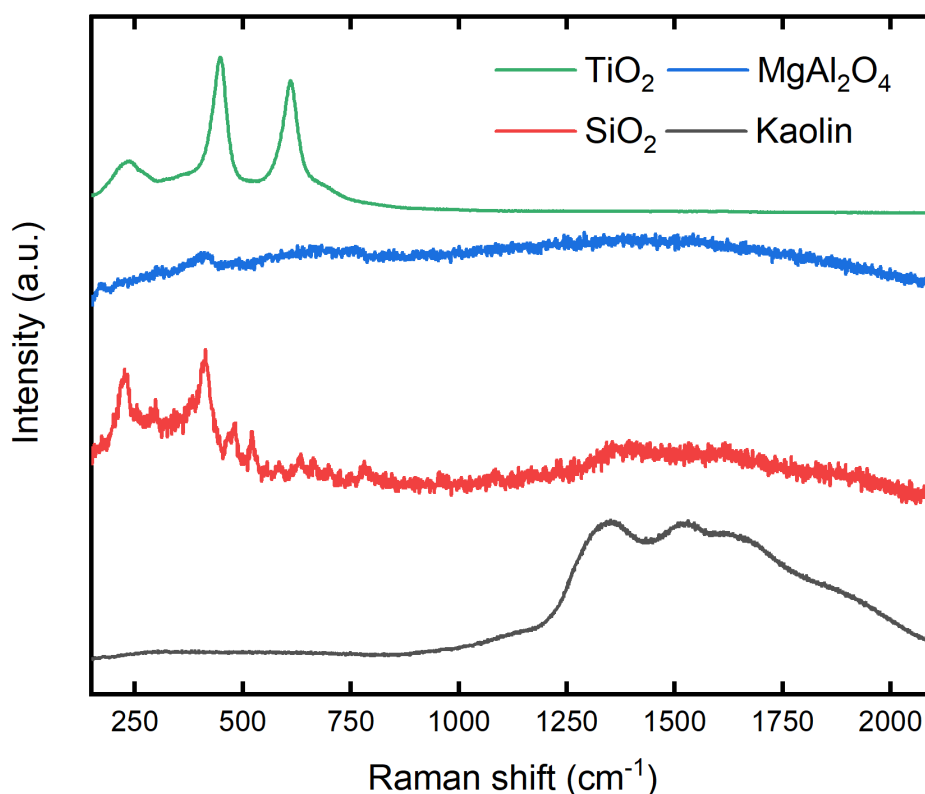


Figure E-11: Raman shifts as measured for the inactive cerceps, all with 1.5 wt.% MnO₂. Note: the signal for SiO₂ has been scaled with 20 times, whereas the signal for MgAl₂O₄ has been scaled 3x.

of the here present MnOx. This is most likely caused by several phenomena. First of all, the concentration of manganese in the cerceps is relatively low. Further, as had been discussed for γ -alumina and YSZ, manganese oxides are known to dissolve in other metal oxides. This leads to a high dispersion and low crystallinity, which results in very low signal (especially in XRD and Raman). For TiO₂-1.5, this migration should have led to the formation of MnTiO₃ [4]; yet the currently carried out characterization cannot confirm its presence. What can be discerned from the diffraction data are the phase transitions the host metal oxide undergoes. For titania it is evident that all anatase as present prior to calcination is converted to rutile (as was already evident from TDRS and Raman). The silica precursors, consisting primarily of cristoballite and coesite, are fully converted into quartz. The transformation from kaolinite to mullite is apparent; the unavailability of Raman spectra with the correct (laser) wavelength and spectral range makes verification of this observation impossible. Further, the here shown XRD data confirm the formation of a notably more crystalline MgAl₂O₄. Due to the high fluorescent background, Raman cannot be used to identify the formed compounds. For completeness, X-ray diffraction data have been included for α -alumina, calcined under the same circumstances as all earlier mentioned cerceps. It can be seen that the peak at 28.8° 2 θ belonging to MnO₂ disappears upon calcination. Minute inspection of the diffraction data does not result in identification of any manganese compound.

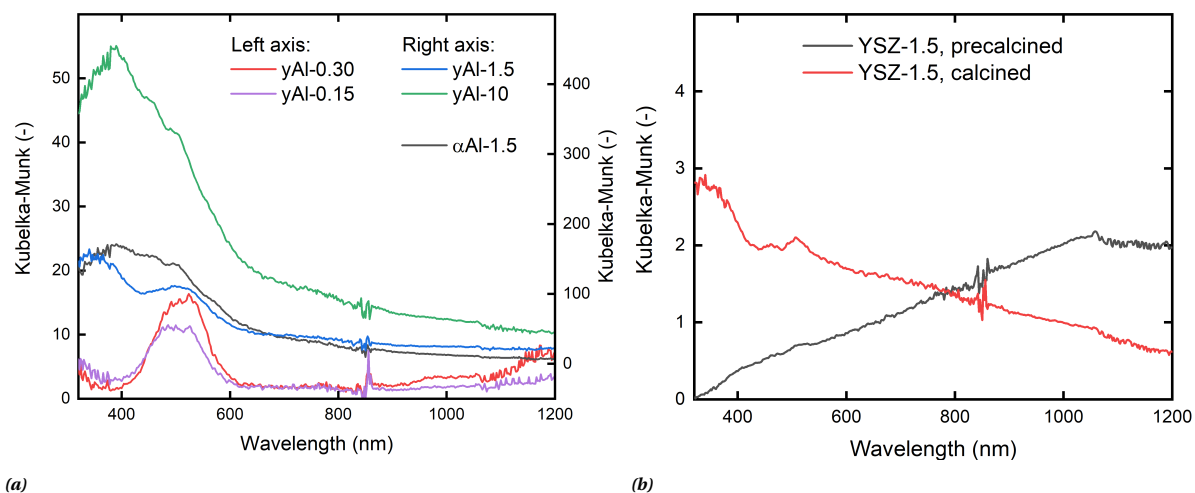


Figure E-12: Total diffuse reflectance spectrum of γ Al and YSZ-1.5 cercaps. a) Total diffuse reflectance spectrum of γ Al cercaps with different manganese loading. As reference a cercap synthesized from α -alumina (α Al-1.5) is included. b) Total diffuse reflectance spectrum of YSZ-1.5 cercap, both precalcined and calcined. For the calcined spectrum the same peak around 380 nm can be found as for γ Al-1.5. Note that all other peaks have remained in place.

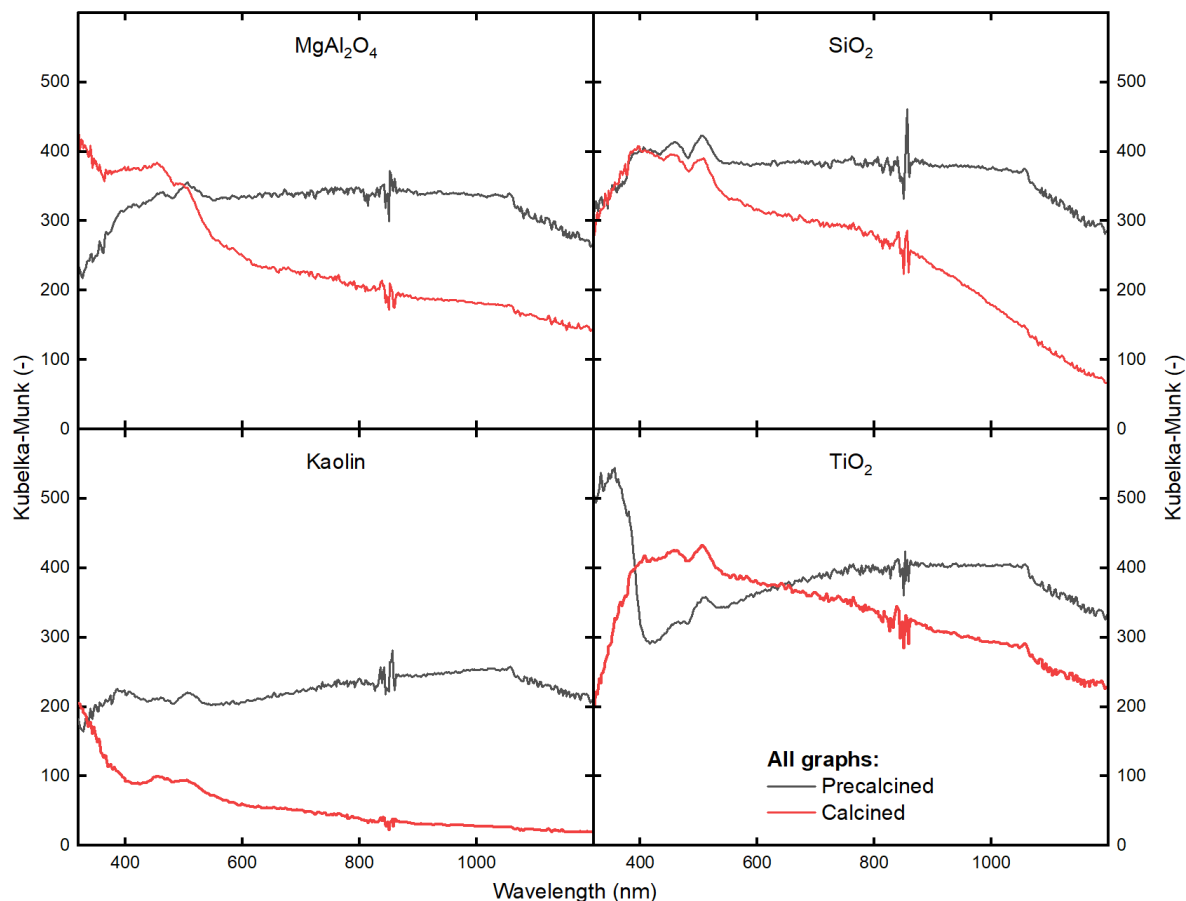


Figure E-13: Total diffuse reflectance spectra of all inactive cercaps, both precalcined and calcined.

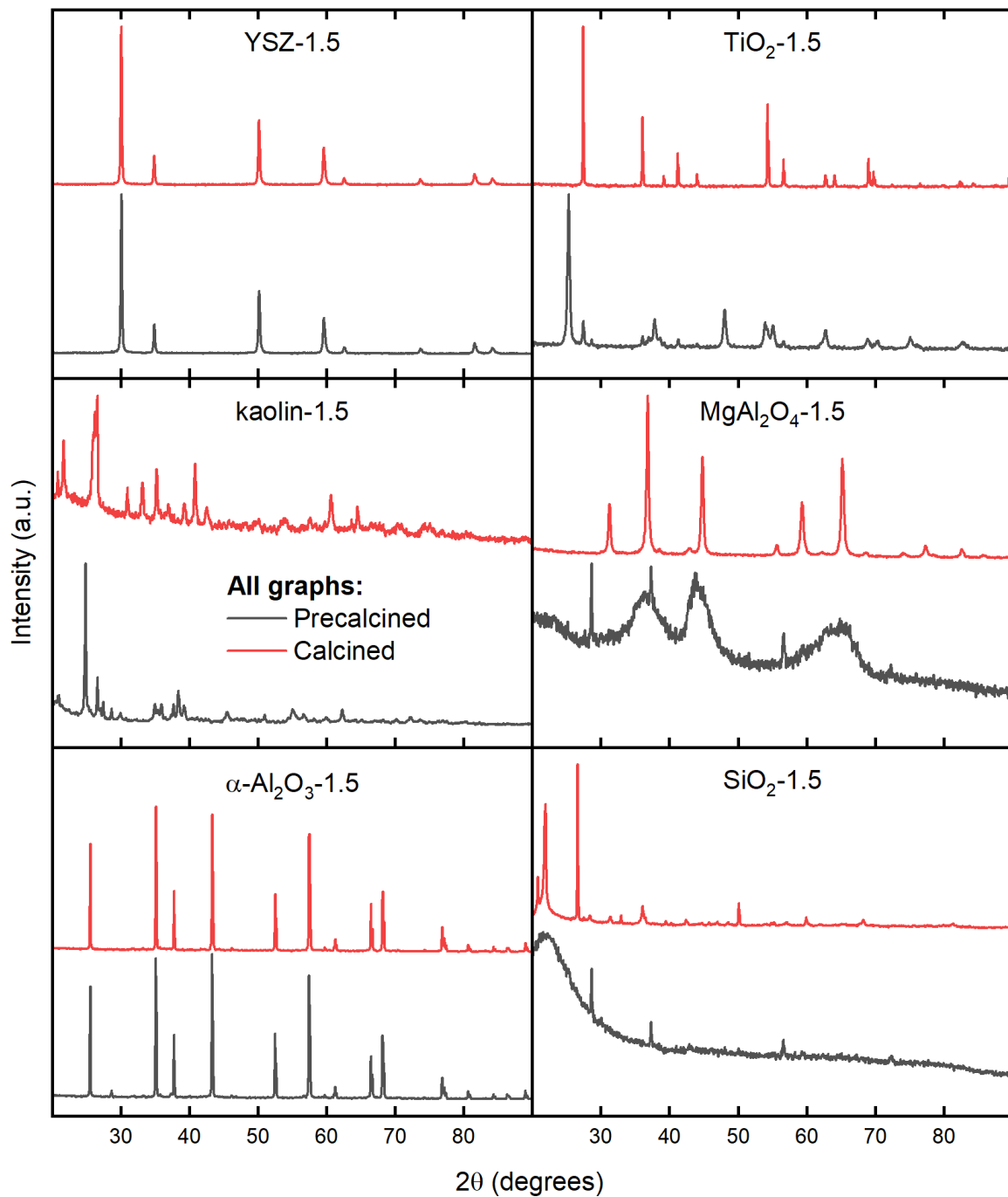


Figure E-14: Powder X-ray diffraction data for all ceria supports except for $\gamma\text{-Al}_2\text{O}_3$ -1.5.

E.2.3.2. γ Al-0.30 cercap decomposition event

Figure E-15: Typical decomposition event of 98% HP over γ Al-0.30, for the sixth administered drop.

E.2.3.3. Reaction characterization

This section provides additional visualizations of the temporal evolution of the decomposition behavior of all YSZ-1.5 and γ Al-0.30 catalysts.

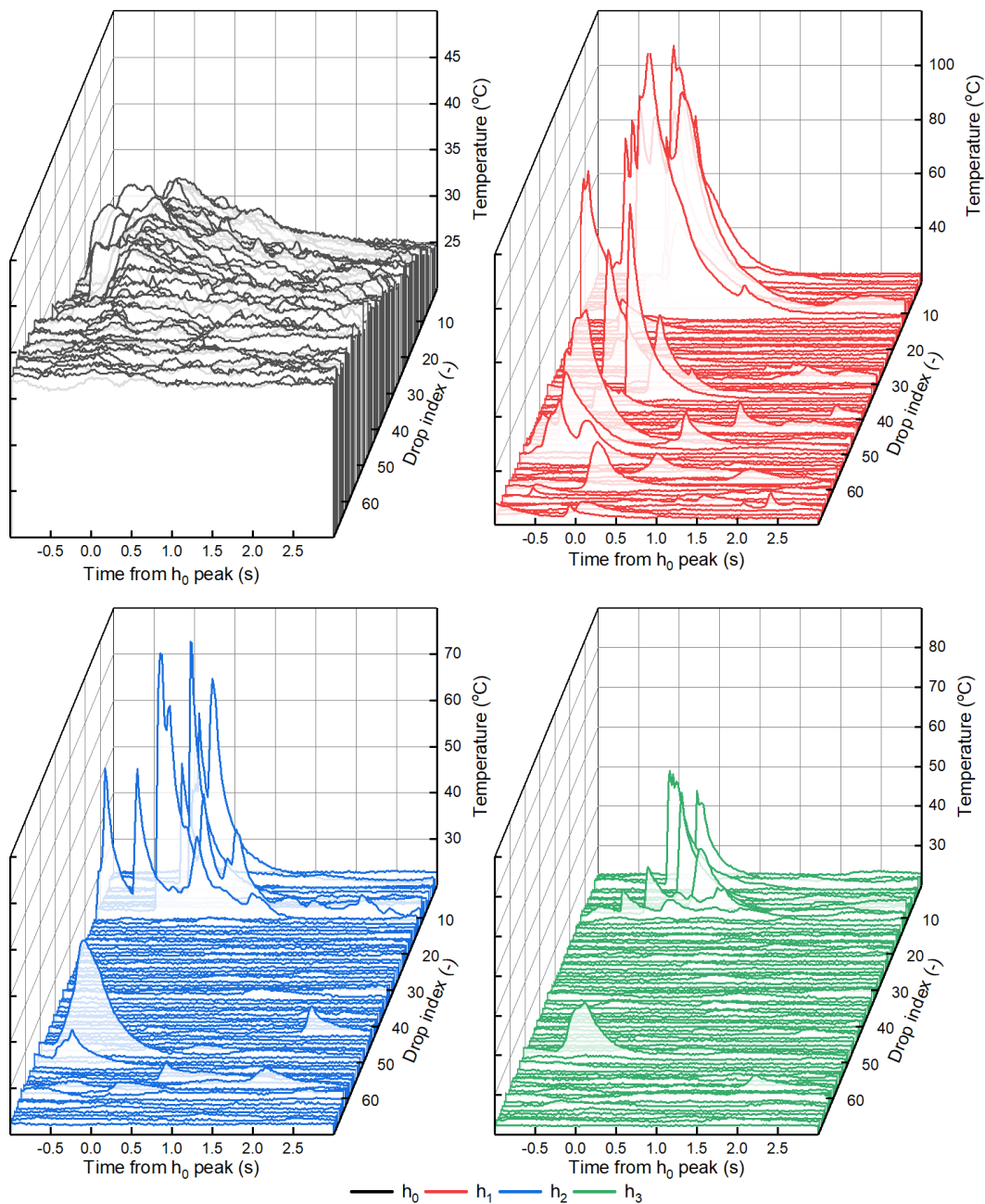


Figure E-16: Peak temperature development for γ Al-0.30-1 during drop-testing.

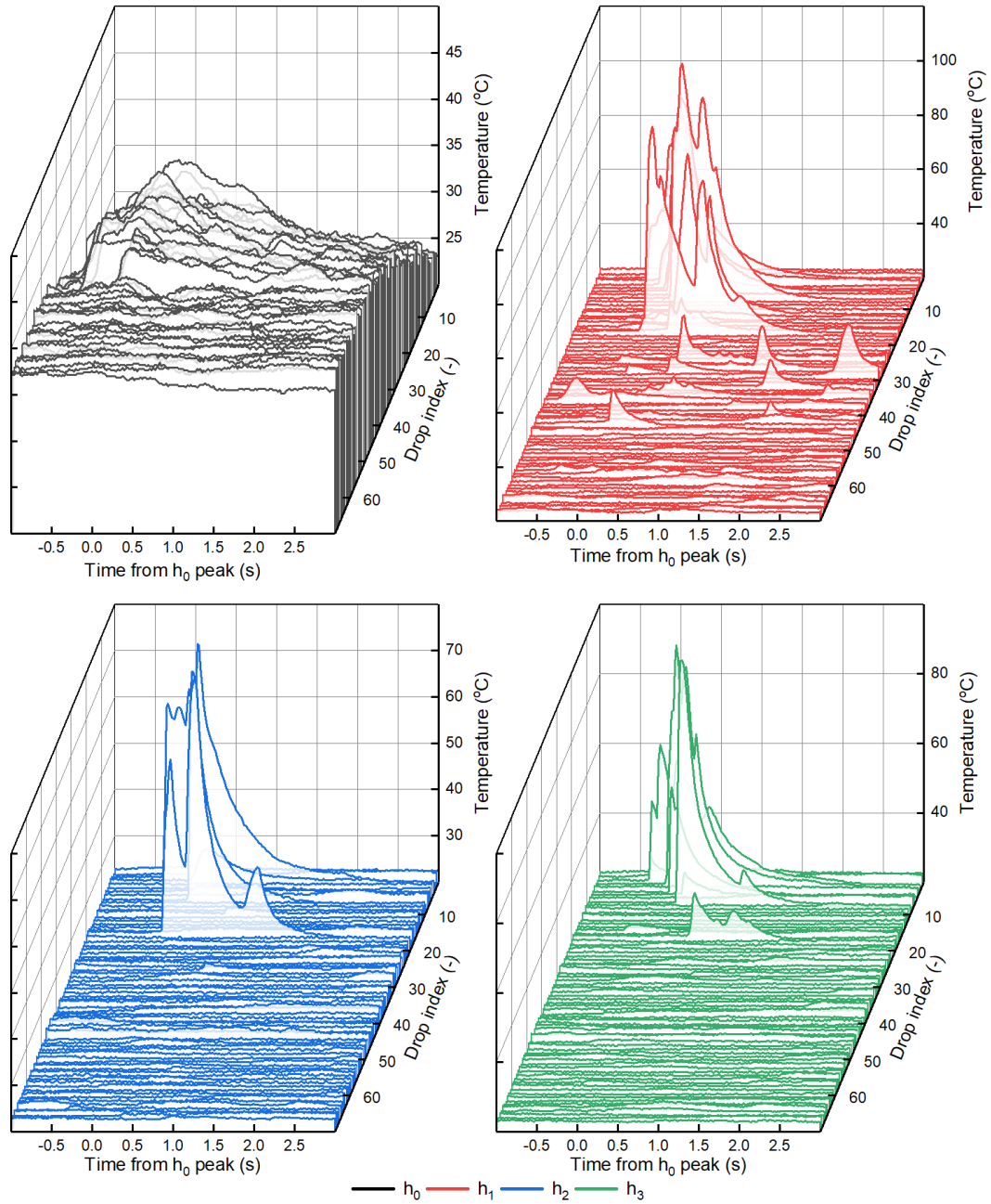


Figure E-17: Peak temperature development for yAl-0.30-2 during drop-testing.

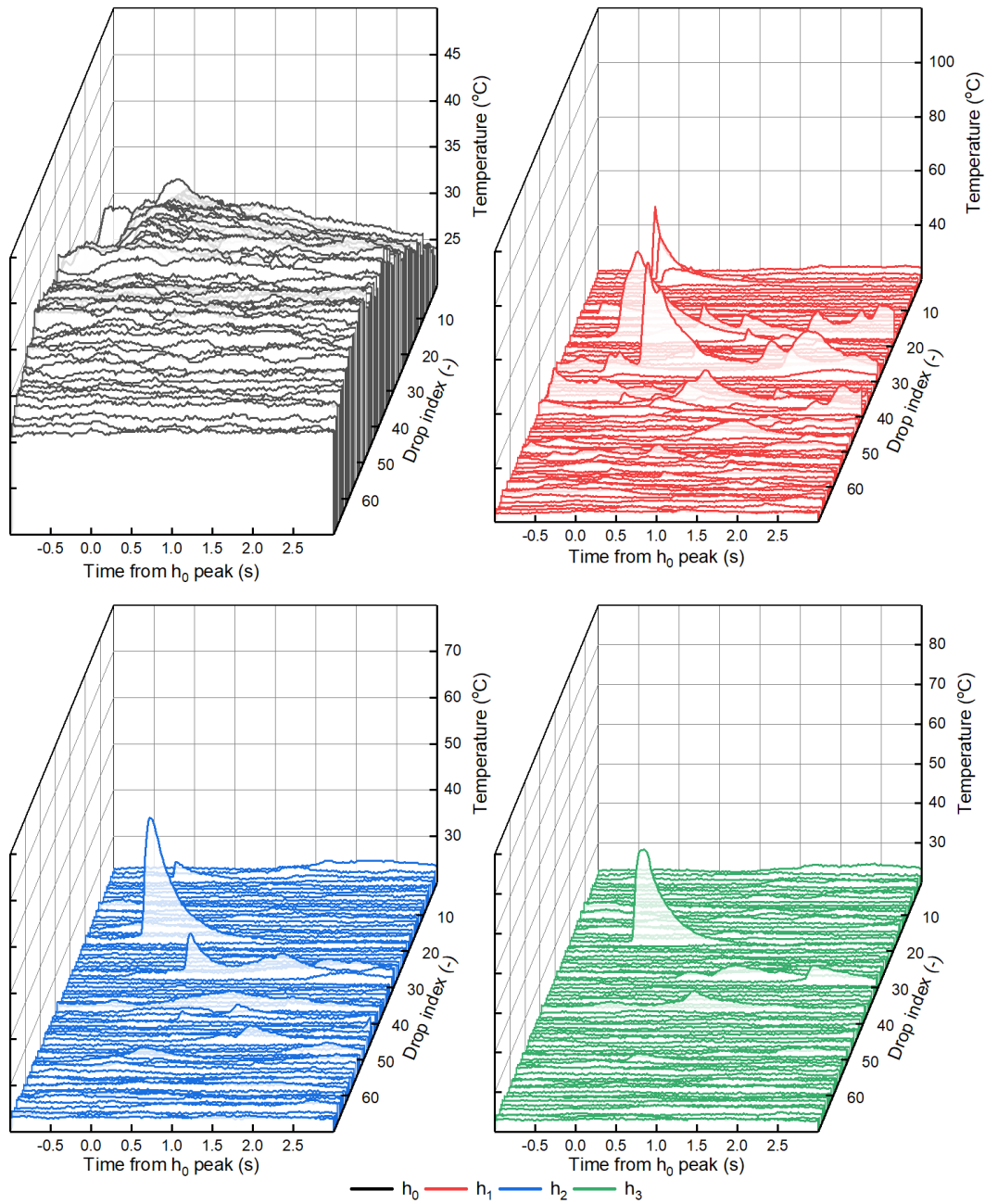


Figure E-18: Peak temperature development for γ Al-0.30-3 during drop-testing.

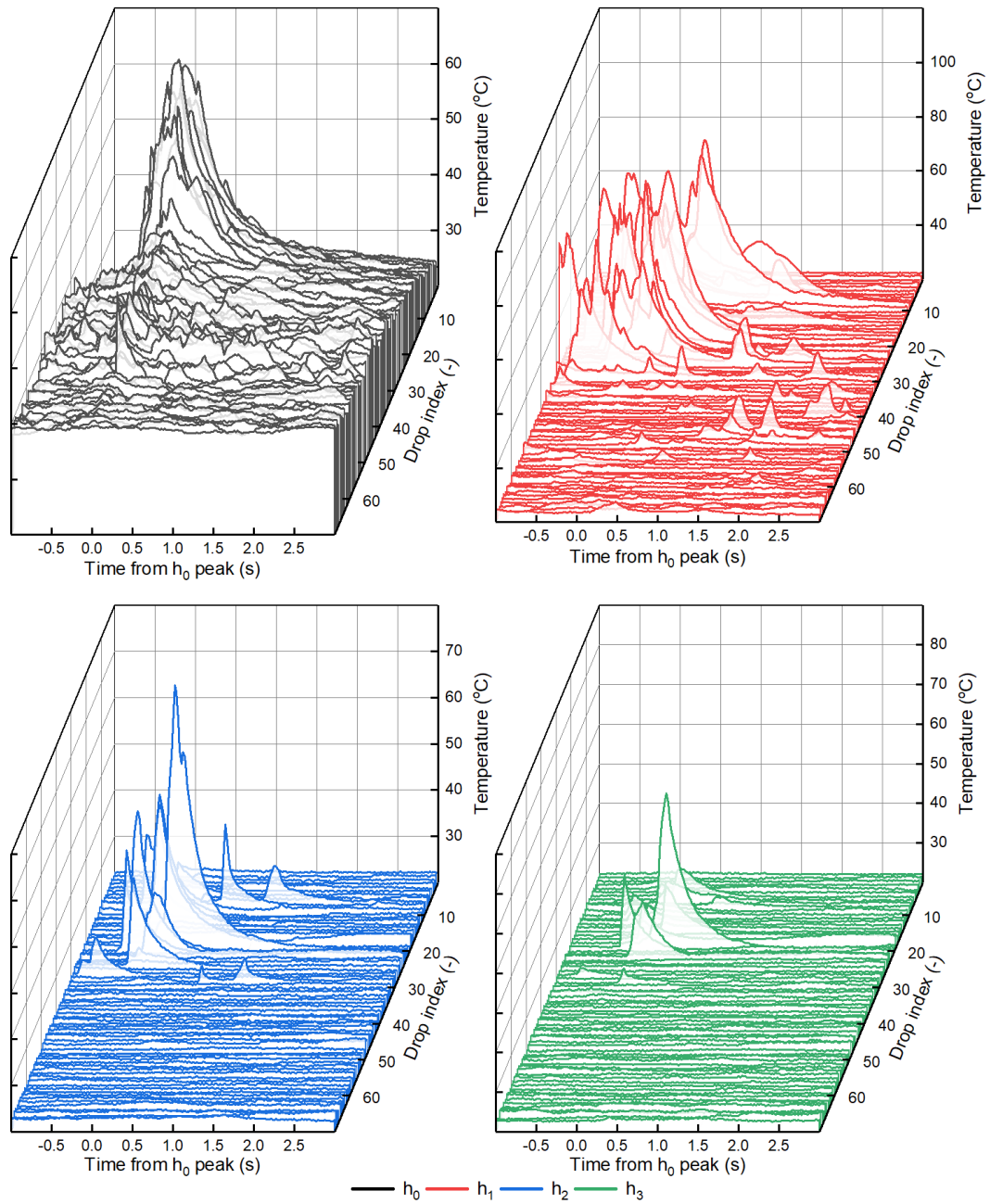


Figure E-19: Peak temperature development for YSZ-1.5-1 during drop-testing.

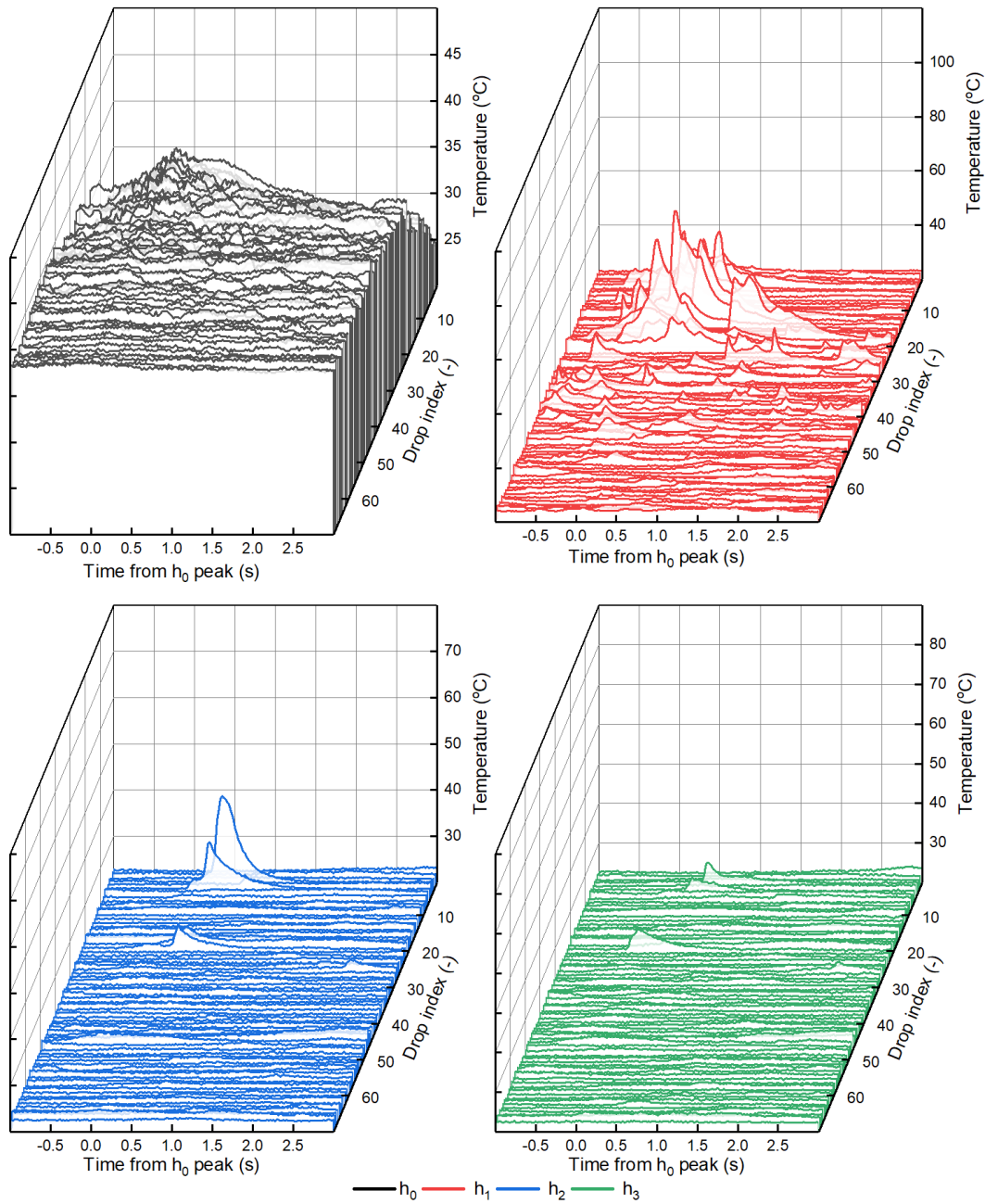


Figure E-20: Peak temperature development for YSZ-1.5-2 during drop-testing.

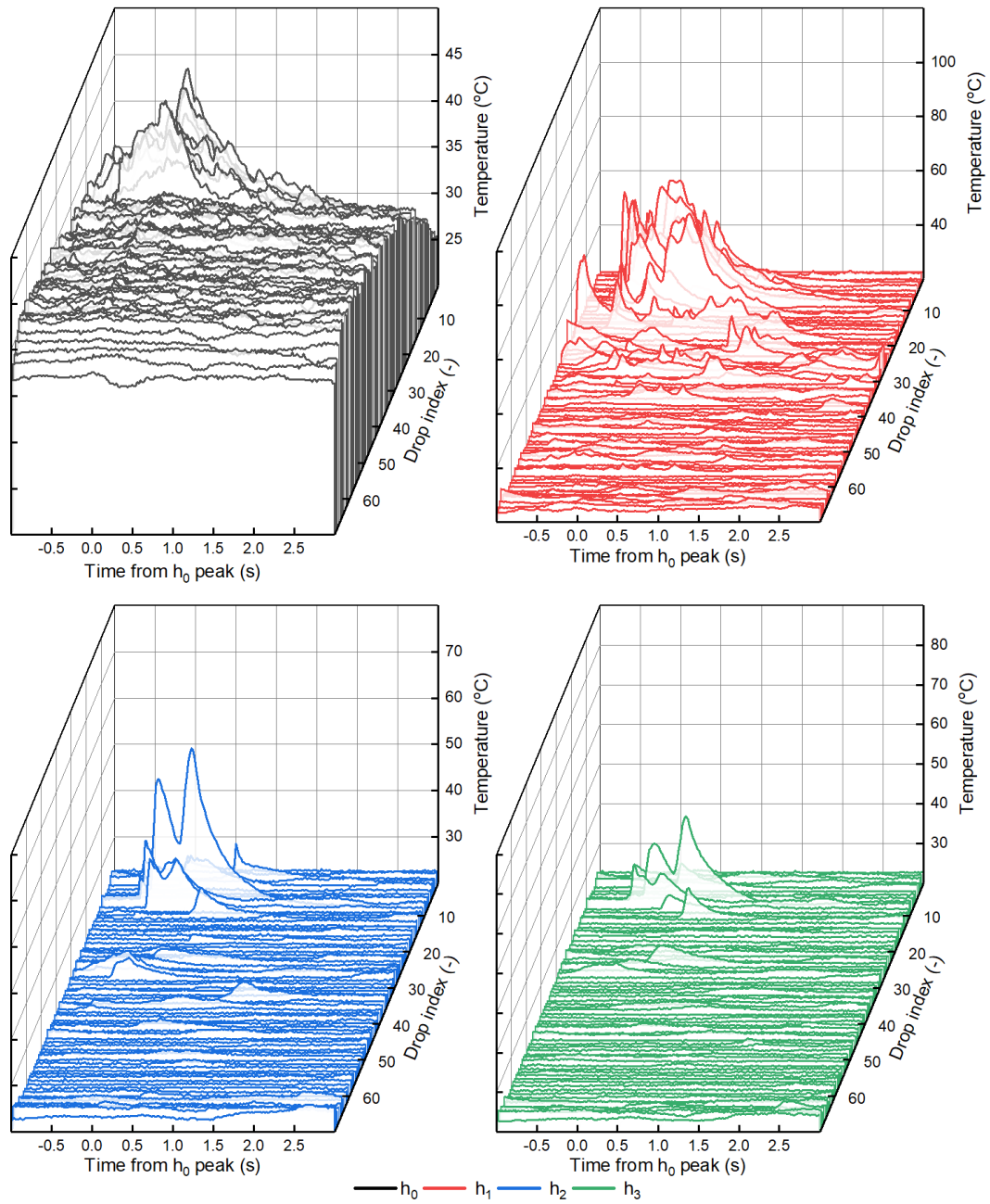


Figure E-21: Peak temperature development for YSZ-1.5-3 during drop-testing.

E.2.3.4. Catalyst summary table

Table E-1: Summary table with all tested catalysts, comparing reactivity, lifetime, and difficulty or proposed area of improvement.

	Active phase content (wt.%)	Reactivity	Lifetime	Direction of improvement	Comments
ICT(Pt)	0.5	-	?	More vigorous reduction	Challenging synthesis, could not be reduced
MnO₂/YSZ					
Powder pressed pellet	10	++	-	Decrease reactivity, increase cohesion	
Thick pellet, calcined	10	++	-	Decrease reactivity, increase cohesion	Calcined at 600°C
	10	0	?	Increase reactivity	Calcined at 1050°C; very rigid
Supported:					
Deposition precipitated	0			Increase porosity of support	Supports: YSZ, Al ₂ O ₃ , calcined Si, SiO ₂
Dropcasted	10	+/-	-	Change physico-chemical surface properties	Supports: YSZ, Al ₂ O ₃ , calcined Si, SiO ₂ ; calcined at 600°C
Washcoat:	10	0.5		Increase adhesion of washcoat to Al ₂ O ₃	Poor adhesion of washcoats to Al ₂ O ₃ , poor adhesion of catalyst to washcoat; brittle.
Silica		++	0		
Titania		++	+		
MnOx cercaps					
Silica, titania, spinel, kaolin	1.5	3.75	-	Change calcination conditions	More spectroscopy needed
γAl	0.3	0.750	++	Lower porosity, increase cohesion	Rigid, but brittle
YSZ	1.5	3.75	++	Increase reactivity	Rigid, forms cracks during calcination

E.3. Stabilizing propellant-grade H_2O_2

This section displays the fitting results as resulting from the least-squares fitting of the SA decomposition data, performed using OriginPro 2018.

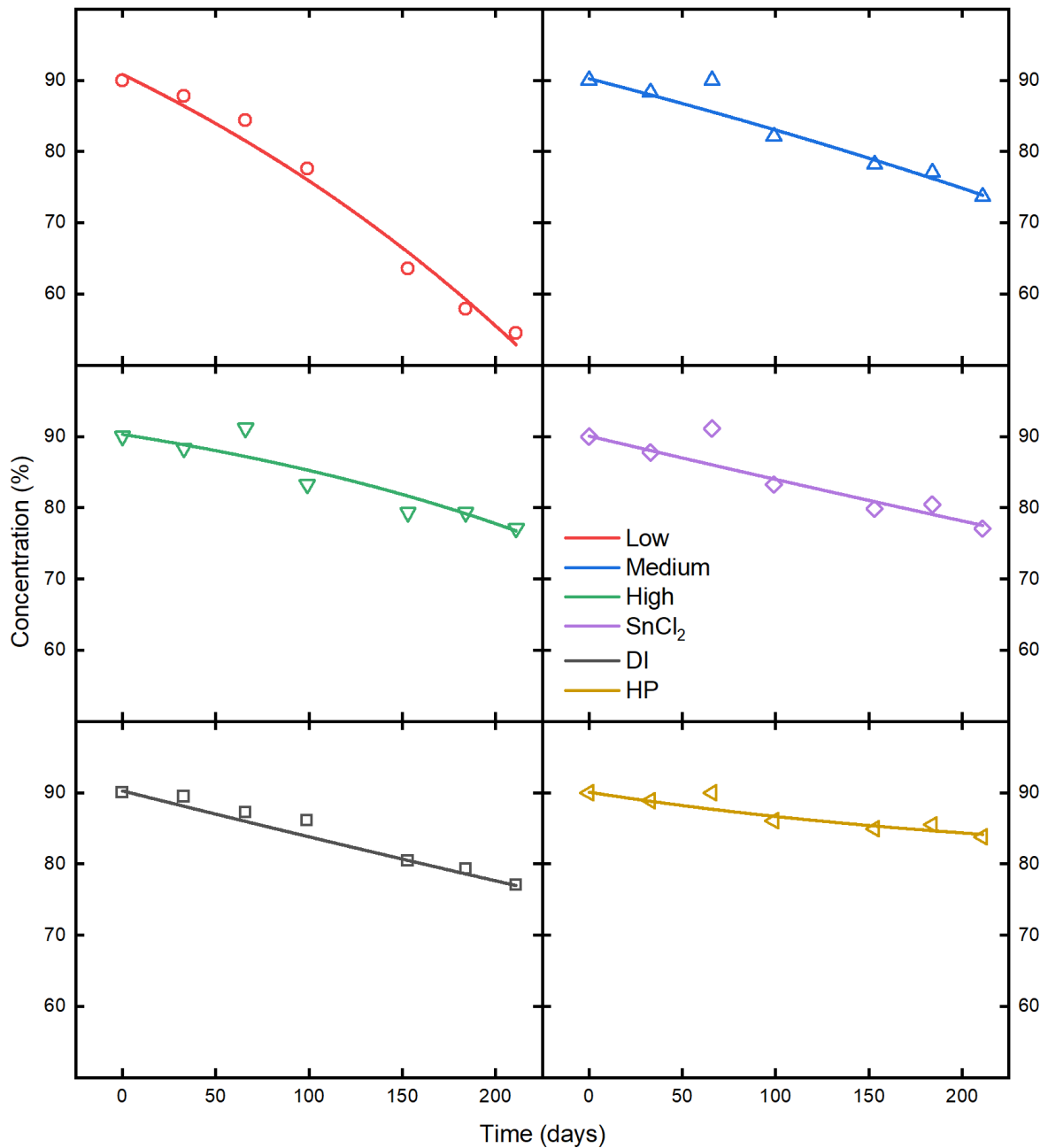


Figure E-22: Comparison of measurements with results from least-square fit using Origin Pro 2016 for SA-90-S.

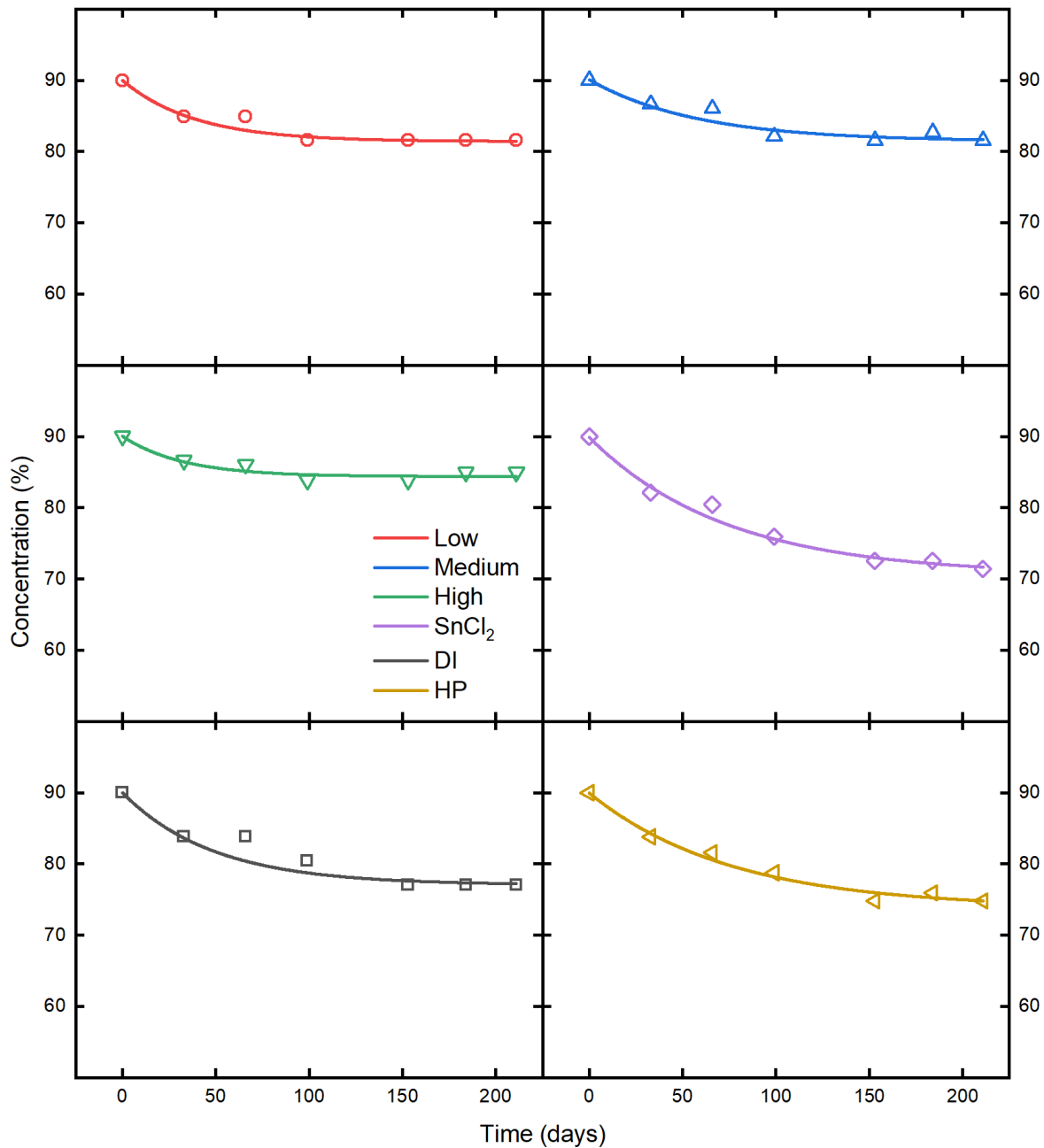


Figure E-23: Comparison of measurements with results from least-square fit using Origin Pro 2016 for SA-90-D.

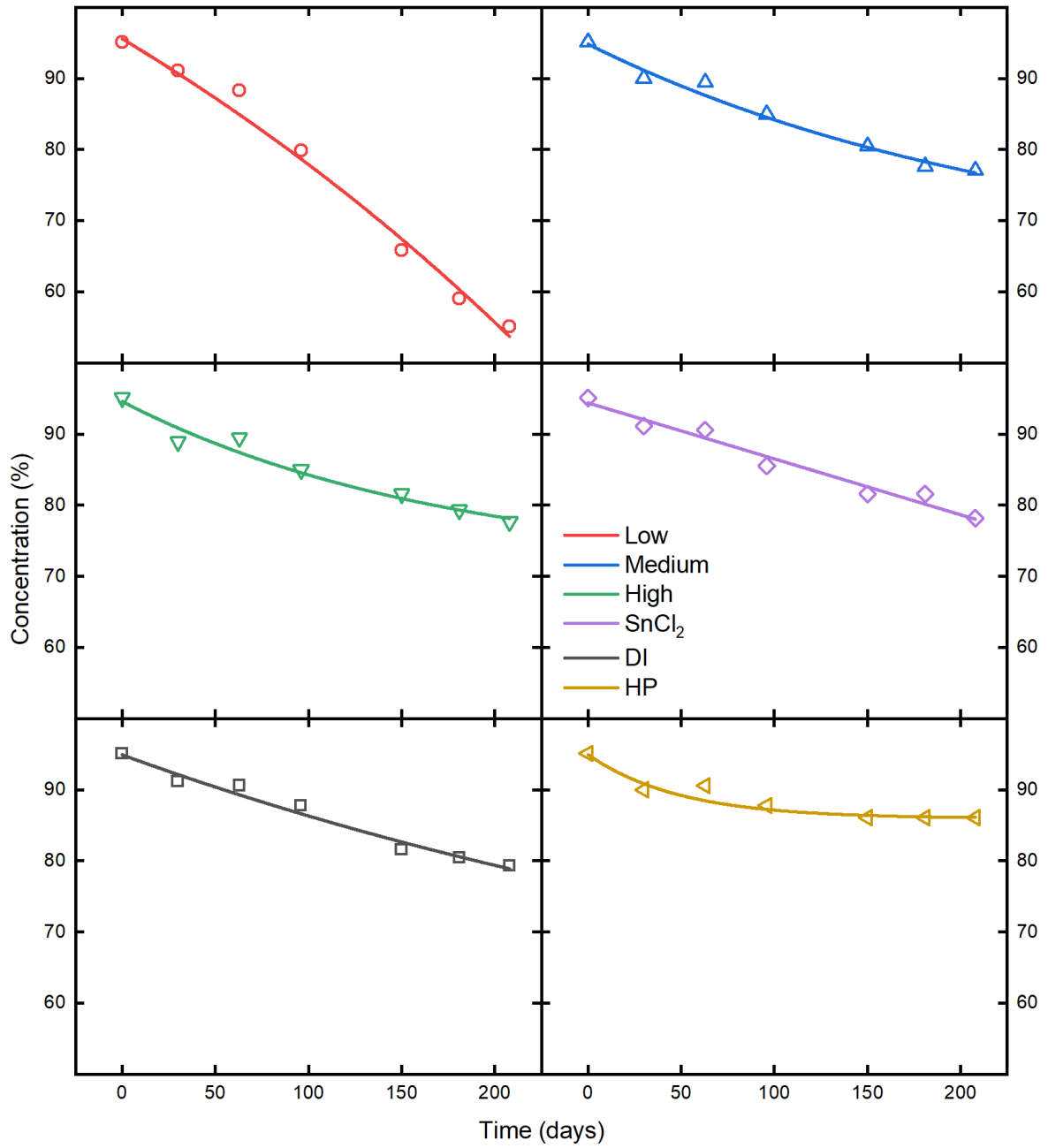


Figure E-24: Comparison of measurements with results from least-square fit using Origin Pro 2016 for SA-95-S.

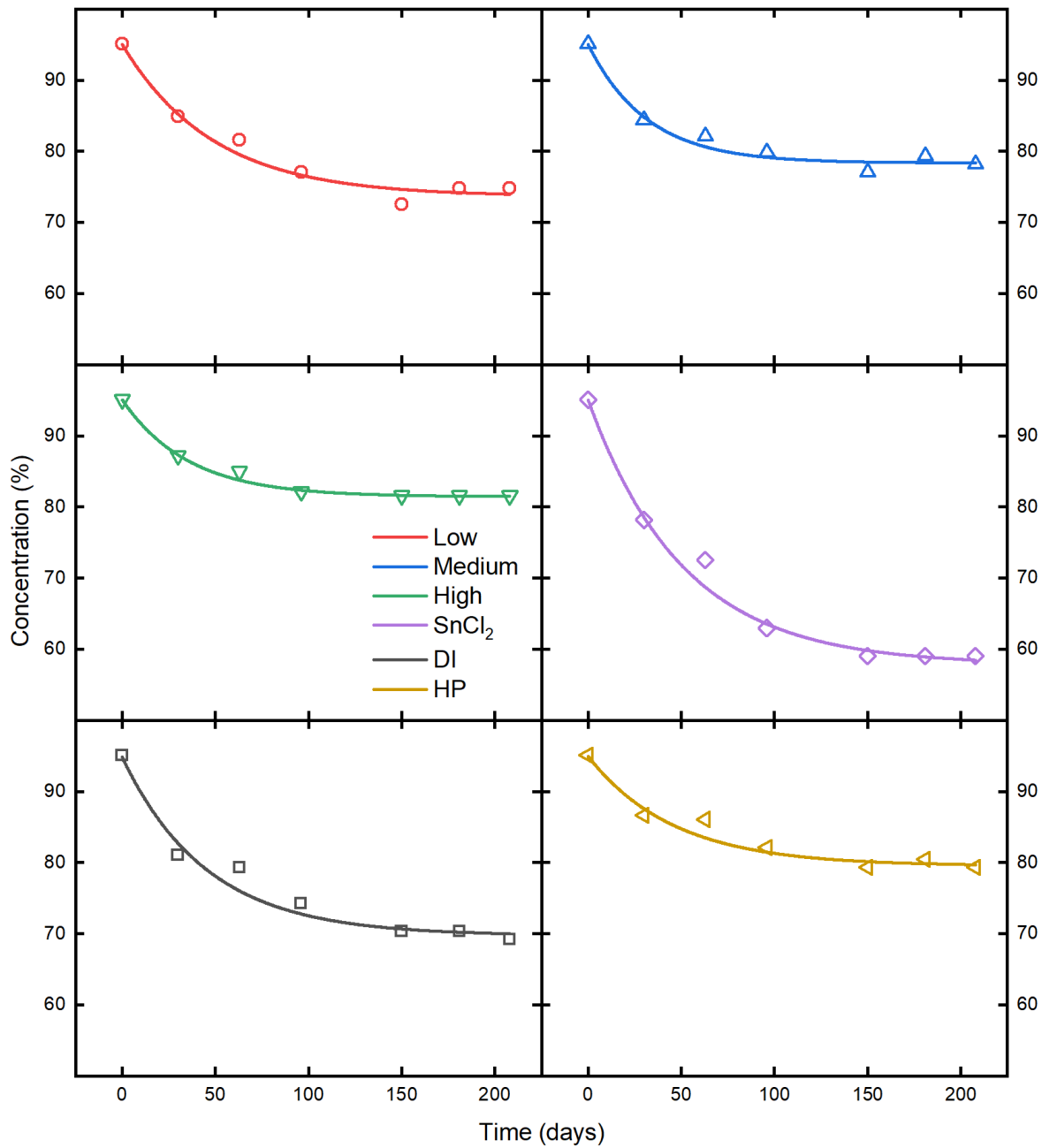


Figure E-25: Comparison of measurements with results from least-square fit for SA-95-D.

Table E-2: Fitting parameters for SA-90-S. Included are both the fitted values and the associated standard errors. The last column shows the overall adjusted r^2 for the fitting.

	y_0 Value [%]	Std. error [%]	A_1 Value [%]	Std. error [%]	t_1 Value [days]	Std. error [days]	K Value [1/days]	$\tau_{1/2}$ Value [days]	Reduced ξ^2	Adj. r^2
SA-90-DI-S	101.0	9.446	-10.67	9.149	-257.3	152.4	-0.00389	-178.3	0.6717	0.9785
SA-90-L-S	132.4	38.70	-41.52	37.96	-324.9	220.8	-0.00308	-225.2	4.404	0.9822
SA-90-M-S	144.8	153.9	-54.58	153.4	-805.1	2002.1	-0.00124	-558.0	1.807	0.9619
SA-90-H-S	-60.15	1407.8	150.4	1407.4	2280.0	22292.	4.386E-4	1580.4	2.288	0.9300
SA-90-CI-S	-49.58	1443.0	139.6	1443.4	2241.4	24226.	4.461E-4	1553.7	2.576	0.9126
SA-90-HP-S	79.54	10.03	10.53	9.830	255.6	355.1	0.00391	177.2	0.6820	0.9008

Table E-3: Fitting parameters for SA-90-D. Included are both the fitted values and the associated standard errors. The last column shows the overall adjusted r^2 for the fitting.

	y_0 Value [%]	Std. error [%]	A_1 Value [%]	Std. error [%]	t_1 Value [days]	Std. error [days]	K Value [1/days]	$\tau_{1/2}$ Value [days]	Reduced ξ^2	Adj. r^2
SA-90-DI-D	77.06	0.9345	12.95	1.204	48.65	14.63	0.02055	33.72	1.557	0.955
SA-90-L-D	81.41	0.3539	8.586	0.5128	38.82	7.575	0.02576	26.91	0.3173	0.9800
SA-90-M-D	81.43	0.7587	8.647	0.8808	58.23	18.85	0.01717	40.36	0.6954	0.9538
SA-90-H-D	84.38	0.3999	5.654	0.6197	32.64	11.90	0.03064	22.62	0.4844	0.9334
SA-90-CI-D	70.58	0.9163	19.30	0.9496	73.55	10.79	0.0136	50.98	0.5347	0.9920
SA-90-HP-D	73.84	1.046	16.11	1.073	75.53	14.84	0.01324	52.36	0.6425	0.9861

Table E-4: Fitting parameters for SA-95-S. Included are both the fitted values and the associated standard errors. The last column shows the overall adjusted r^2 for the fitting.

	y_0 Value [%]	Std. error [%]	A_1 Value [%]	Std. error [%]	t_1 Value [days]	Std. error [days]	K Value [1/days]	$\tau_{1/2}$ Value [days]	Reduced ξ^2	Adj. r^2
SA-95-L-S	50.15	42.28	44.75	42.01	469.1	544.6	0.00213	325.1	1.040	0.9779
SA-95-M-S	164.9	58.92	-69.35	58.35	-440.2	297.9	-0.00227	-305.2	2.817	0.9907
SA-95-H-S	63.70	9.571	31.13	9.367	238.9	109.3	0.00419	165.6	0.7543	0.9876
SA-95-CI-S	71.01	7.371	23.57	7.122	173.6	93.00	0.00576	120.4	1.533	0.9705
SA-95-DI-S	8.215E6	3.034E7	-8.215E6	3.034E7	-1.044E8	3.858E8	-9.574E-9	-7.240E7	1.729	0.9642
SA-95-HP-S	85.96817	0.5725	8.982	0.7238	48.91	12.88	0.02045	33.90	0.5586	0.9668

Table E-5: Fitting parameters for SA-95-D. Included are both the fitted values and the associated standard errors. The last column shows the overall adjusted r^2 for the fitting.

	y_0 Value [%]	Std. error [%]	A_1 Value [%]	Std. error [%]	t_1 Value [days]	Std. error [days]	K Value [1/days]	$\tau_{1/2}$ Value [days]	Reduced ξ^2	Adj. r^2
SA-95-DI-D	69.74	1.058	25.07	1.394	45.50	8.287	0.02198	31.54	2.181	0.9835
SA-95-L-D	73.67	0.9931	21.39	1.257	48.78	9.373	0.0205	33.81	1.690	0.9821
SA-95-M-D	78.36	0.5846	16.68	0.9078	31.63	5.721	0.03161	21.93	1.049	0.9829
SA-95-H-D	81.44	0.1979	13.63	0.2941	35.65	2.534	0.02805	24.71	0.1074	0.9973
SA-95-CI-D	57.83	0.9051	37.22	1.114	51.18	4.992	0.01954	35.48	1.272	0.9955
SA-95-HP-D	79.54	0.7468	15.40	0.9769	46.09	9.579	0.0217	31.95	1.063	0.9786